

Volume 6, Issue 1 (XIX)
January - March 2019

ISSN 2394 - 7780



International Journal of
Advance and Innovative Research
(Conference Special)
Part – 1

Indian Academicians and Researchers Association
www.iaraedu.com

**NATIONAL CONFERENCE
ON
FUNCTIONAL MATERIALS SYNTHESIS AND
CHARACTERIZATION TECHNIQUES**

SPONSORED BY



Dr. Babasaheb Ambedkar Marathwada University
Aurangabad (M.S)

ORGANIZED BY
Department of Physics,
Vaidyanath College, Parli-Vaijnath, Dist. Beed
Saturday, 2nd March 2019

With Support and Inspirations From
RUSA Centre for Advanced Sensor Technology
Dr. Babasaheb Ambedkar Marathwada University, Aurangabad

In association with



Indian Academicians and Researcher's Association



Jawahar Education Society's

Vaidyanath College

Parli-Vaijnath, Dist. Beed - 431515, Maharashtra

Affiliated to Dr. Babasaheb Ambedkar Marathwada University, Aurangabad

NAAC Accredited a 'B' level with CGPA (2.53)

Guest Editors of Special Issue

Dr. Madhav N Rode

Dr. Dilipkumar Meshram

ABOUT COLLEGE

Jawahar Education Society's Vaidyanath College (ARTS, SCIENCE & COMMERCE) was established on June 15, 1968 to cater higher education in rural area of Marathwada region. It is affiliated to Dr. Babasaheb Ambedkar Marathwada University, Aurangabad. It is accredited by NAAC at B level. The college offers UG and PG courses and has been contributing to churn out good human resource through academic process. Vaidyanath College is one of the leading institutions in the Marathwada region. It imparts education to the needy students from backward and rural areas. In the 20th century, the social workers put forward a new and life turning avenue before the society by establishing this reputed institution with a motto "Satyam Dnyanamnam Brahma". It means "The truth, full of knowledge is the principle known as Brahma". Since 1968 it has been constantly serving to the society in various ways. The institution is focusing on the holistic development of the students by enriching adequate learning resources. In the past few years, Vaidyanath College has established a distinctive position among leading College in the Marathwada region.

ABOUT IARA

Indian Academicians and Researchers Association (IARA) is an educational and scientific research organization of Academicians, Research Scholars and practitioners responsible for sharing information about research activities, projects, conferences to its members. IARA offers an excellent opportunity for networking with other members and exchange knowledge. It also takes immense pride in its services offerings to undergraduate and graduate students. Students are provided opportunities to develop and clarify their research interests and skills as part of their preparation to become faculty members and researcher. Visit our website www.iaraedu.com for more details.

ABOUT THE CONFERENCE

National Conference on Functional Materials Synthesis and Characterization Techniques (NCFMSCT-2019) is organized by Department of Physics, Vaidyanath College, Parli - Vajinath considering vital role of functional materials in the development of indigenous technology the present deliberation has the objective of creating a national forum for academics, researchers, scientists and students. The conference will include participation of renowned keynote speakers, oral presentation.

A BRIEF ABOUT ORGANIZING COMMITTEES

CHIEF PATRONS

Hon'ble. Jugalkishorji Lohiya

Chairman, Jahwahar Education Society's

Hon'ble. Dattapp Itke

Secretary, Jahwahar Education Society's

Hon'ble. Fulchand Karad

Vice Chairman, Jahwahar Education Society's

Hon'ble. Dr. D. G. Munde

Vice Chairman, Jahwahar Education Society's

Hon'ble. Dr. Sureshji Chaudhari

Joint Secretary, J. E. Society's

Hon'ble. Sureshji Agrawal

Treasurer, Jahwahar Education Society's

PATRON

Dr. R. K. Ippar

Principal, Vaidyanath College, Parli

ORGANIZING SECRETARY

Dr. D. V. Meshram

CONVENER

Dr. Madhav N. Rode

CO-CONVENER

Dr. V. B. Kawade

JOINT SECRETARY

Dr. B. V. Kendre

Dr. B. R. Chavan

MEMBERS

Dr. J. V. Jagatkar, Vice Principal

Asst. Prof. D. K. Andhale, JES, Director

Dr. T. A. Gitte

Asst. Prof. B. S. Satpute,

Asst. Prof. B. P. Gajbhare

Asst. Prof. M. M. Kamble

Asst. Prof. U. R. Kande

Asst. Prof. S. A. Dhande
Asst. Prof. Milind V. Sonkamble
Dr. C. T. Birajdar, SMP College, Murum
Dr. Ravindra Katre, KMJ College, Washi
Dr. R. J. Topre, Yogeshori College, Ambajogai
Dr. Mahendra Shinde, M.J.M. College, Karanjali, Nashik
Dr. Swapil Arsad, M. F. M Warad College

NATIONAL ADVISORY COMMITTEE

Prof. Dr. Aswal Dinesh, Director- CSIR-NPL, New Delhi
Prof. Dr. V. N.Mani, Scientist-F at C-MET, Govt. of India, Hyderabad
Prof. Dr.B.N.Gajbhiye, Scientist-G, DRDO, Hyderabad
Prof. Dr.GanesanV. , Centre Director-UGC,DAE,CSR,Indore
Prof. Dr. N. L. Singh, M. S. University, Vadodara, Gujrat, India
Prof. Dr. M. D. Shirsat, Director, RUSA CAST, Dr. B. A. M.University, Aurangabad
Prof. Dr.R.B.Sharma, Head & BOS Chariman , Dr.B.A.M.University, Aurangabad
Prof. Dr. G. G. Muley , Dept. of Phycis, S.G.B. University, Amaravati
Prof. Dr. M. K. Patil, MC Member & Director, School of Physical Science, S.R.T. University, Nanded
Dr. S. D. Deshpande, Dept. of Physics, Dr. B. A. M. University, Aurangabad
Prof. Dr. K. M.Jadhav, Dept. of Physics, Dr. B. A. M. University, Aurangabad
Prof. Dr. Pravina P.Pawar, Dept. of Physics Dr. B. A. M. University, Aurangabad
Prof. Mahajan A.M., Dept. of Physics, N.M.Univeristy, Jalgaon, India
Dr. Dilip Garud, Principal Adarsh College, Omerga (MS), India
Dr. Bhaskar Munde, Principal KKM College, Manwat.
Dr.Jai shri Kumar, Government college, Kharkhra (Rewari), Haryana
Dr. Aurn Kumar Gautam, C.S.A. Government P.G.College, Sehore, (M.P)
Anil Das, Dept of Physics, ST John College, Agra
Dr. K. B. Bogle, School of Physical Science, S.R.T. Univeristy, Nanded
Dr. S. S. Hussaini, Milliya College, Beed

Dr. Babasaheb Ambedkar Marathwada University,
Aurangabad - 431 004 Maharashtra (India)

Re- accredited by NAAC with 'A' Grade in 2013

Professor B.A. Chopade

M.Sc., Ph.D (Nottingham University, England)
Fogarty Fellow (Illinois University, Chicago, USA)

Vice-Chancellor



EPABX 0240 - 2403399, 2403400
Direct 0240 - 2403111
Fax No. 0240 - 2403113/2403335
E-mail vc@bamu.ac.in
Website www.bamu.ac.in

Ref. No. VC.Sec./2019/340

Date: 20 February 2019



Message

I am delighted to pen greetings to this truly significant National Conference devoted to Functional Materials Synthesis and Characterization Techniques (Physics-NCFMSCT-2019) on 2nd March 2019 sponsored by Our Dr.Babasaheb Ambedkar Marathwada University, Aurangabad.

I congratulate Convener Dr.Madhav Rode and his entire team colleagues at Vaidyanath College, Parli Vajinath. organising such fruitful program.

I consider the program to be one of my most significant contributions to Physics researchers, academicians and students.

My best wishes to the conference.

B.A. Chopade

Professor B. A. Chopade
Vice Chancellor

DR. PRITAM GOPINATH MUNDE-KHADE

Member of Parliament (Lok Sabha)

Beed, Maharashtra

Member:

- Standing Committee on Health and Family Welfare
- Committee on Welfare of OBC's



सत्यमेव जयते

डॉ. प्रितम गोपीनाथ मुंडे-खाडे

संसद सदस्य (लोक सभा)

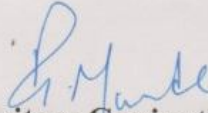
बीड, महाराष्ट्र

MESSAGE

I am pleased to know that, Jawahar Education Society's Vaidyanath College, Parli Vajinath is organizing National Conference on Functional Materials Synthesis and Characterization Techniques (Physics-NCFMSCT-2019) on 2nd March 2019 sponsored by Dr.Babasaheb Ambedkar Marathwada University, Aurangabad.

I hope all the participants will enjoy this academic fest.

I extend my greetings and best wishes to organizing committee, participants.


(Dr.Pritam Gopinath Munde)

Delhi Off.: 601, Narmada, Dr. B.D. Marg, New Delhi-110 001 • Telefax: 011-23312110

Resi.: 'Yashshree', Tal. Parali, Distt. Beed-431 515 • Telefax: 02446-222054

Mumbai Off.: 'Shubhada', Opp. Police Officers' Mess, Sir Pochkhanwala Marg, Worli, Mumbai-400 030 • Ph.: 022-24900993 • Fax: 022-24951493

Beed Off.: BJP Beed District Office, Opp. Superintendent Office, Vidhyanagar (W), Beed-431 122 • Telefax: 02442-225177/233377



Chairman's Message

I am pleased to know that department of physics is organizing national conference on functional materials synthesis and characterization techniques on 2nd March 2019.

The progress of nation depends on the progress of science and technology and the higher education is effective medium to incubate the essential foundation and envisage future technological development. To create suitable surround through such national conference that provide a platform for the scientific discussion and recent development in research areas is essential.

Functional materials are now essential part of our everyday life. Development in functional materials has been improving our life. These materials are being used in various areas such as energy conversion, energy storage, and solar energy conversion and in surgery etc. The materials with improved functionality are highly demanded in the market. In such situation creating awareness among teachers and students in the rural area is very important. The present national conference organized by Department of Physics for functional materials in which eminent scientists and researchers are going to exchange their known and ideas, is really useful. I hope the deliberation will be really helpful to enhance knowledge and engrave vision of the national progress according to skill India approach of government of India. I welcome to all delegates and wish the conference a great success.

Hon'ble Jugalkishorji Lohiya
Chairman Jawahar Education Society's



Message from the Principal

Department of physics is really worthy of appreciation for organizing a National conference on functional materials synthesis and characterization techniques. This conference is sponsored by Dr. Babasaheb Ambedkar Marathwada University Aurangabad. It is my pleasure to invite the scientists, academia & researchers as well as students from all over nation to attend the NCFMSCT-2019.

All of you are acutely aware of growing interests in functional material for indigenous technological progress. This conference ensures to share an insight in recent research and cutting edge technologies as far as functional materials are concerned. I am sure that each of you will benefit from fruitful and enriching discussion in the conference.

I welcome you to this conference and look forward to your participation. Wishing the conference a grand success.

Dr. R. K. Ippar
Principal
Vaidyanath College, Parli-Vaijnath



Message from HOD

It is my great delight and proud privilege to welcome you all delegates and extend my warm welcome to the distinguished scientists, authorities and dignitaries in the national conference on functional materials, synthesis and characterization techniques going to be held on 2nd March 2019. The college has established a distinctive position among leading colleges in Marathwada region by imparting education to needy students from rural and backward areas. This year it commemorates its gold jubilee. The present conference which sponsored by Dr. Babasheb Ambedkar Marathwada University, Aurangabad is one of the special events on the eve of the gold jubilee celebration as department of physics is inherent part of the college since its establishment.

125th birth year of Prof. Meghnad Saha and birth centenary of Prof. Richard Feynman are being commemorated also. The famous visionary statement of Prof. Feynman, “There is plenty of room at the bottom” is now being realized in form of nanomaterial development which contributes excellently the functional materials development. The present conference really includes reminiscences of those great contributions which helped to develop today’s functional material area. This deliberation is a small leap to create awareness and provide platform for functional materials synthesis and characterization techniques, so that it will contribute to incubate the future process of skill India for indigenous technological development for national prosperity. I really appreciate to the researchers across the country for sending the research papers for publication on call for research paper for the conference and extend my gratitude to the publisher International Journal of Advance and Innovative Research.

I am thankful to the university as well as RUSA centre for Advanced Sensor technology for support and movition for the conference

I sincerely hope the deliberation from various distinguished speakers will benefit the delegates to update their knowledge. Hope you will find the conference valuable and enjoyable. Wishing you the best for your involvement to make the event successful.

Dr. Dilipkumar V. Meshram
Head of Department
Department of Physics
Vaidyanath College, Parli-Vaijnath

International Journal of Advance and Innovative Research

Volume 6, Issue 1 (XIX): January - March 2019 : Part - 1

Editor- In-Chief

Dr. Tazyn Rahman

Members of Editorial Advisory Board

Mr. Nakibur Rahman

Ex. General Manager (Project)
Bongaigoan Refinery, IOC Ltd, Assam

Dr. Alka Agarwal

Director,
Mewar Institute of Management, Ghaziabad

Prof. (Dr.) Sudhansu Ranjan Mohapatra

Dean, Faculty of Law,
Sambalpur University, Sambalpur

Dr. P. Malyadri

Principal,
Government Degree College, Hyderabad

Prof.(Dr.) Shareef Hoque

Professor,
North South University, Bangladesh

Prof.(Dr.) Michael J. Riordan

Professor,
Sanda University, Jiashan, China

Prof.(Dr.) James Steve

Professor,
Fresno Pacific University, California, USA

Prof.(Dr.) Chris Wilson

Professor,
Curtin University, Singapore

Prof. (Dr.) Amer A. Taqa

Professor, DBS Department,
University of Mosul, Iraq

Dr. Nurul Fadly Habidin

Faculty of Management and Economics,
Universiti Pendidikan Sultan Idris, Malaysia

Dr. Neetu Singh

HOD, Department of Biotechnology,
Mewar Institute, Vasundhara, Ghaziabad

Dr. Mukesh Saxena

Pro Vice Chancellor,
University of Technology and Management, Shillong

Dr. Archana A. Ghatule

Director,
SKN Sinhgad Business School, Pandharpur

Prof. (Dr.) Monoj Kumar Chowdhury

Professor, Department of Business Administration,
Guahati University, Guwahati

Prof. (Dr.) Baljeet Singh Hothi

Professor,
Gitarattan International Business School, Delhi

Prof. (Dr.) Badiuddin Ahmed

Professor & Head, Department of Commerce,
Maulana Azad Nationl Urdu University, Hyderabad

Dr. Anindita Sharma

Dean & Associate Professor,
Jaipuria School of Business, Indirapuram, Ghaziabad

Prof. (Dr.) Jose Vargas Hernandez

Research Professor,
University of Guadalajara, Jalisco, México

Prof. (Dr.) P. Madhu Sudana Rao

Professor,
Mekelle University, Mekelle, Ethiopia

Prof. (Dr.) Himanshu Pandey

Professor, Department of Mathematics and Statistics
Gorakhpur University, Gorakhpur

Prof. (Dr.) Agbo Johnson Madaki

Faculty, Faculty of Law,
Catholic University of Eastern Africa, Nairobi, Kenya

Prof. (Dr.) D. Durga Bhavani

Professor,
CVR College of Engineering, Hyderabad, Telangana

Prof. (Dr.) Shashi Singhal

Professor,
Amity University, Jaipur

Prof. (Dr.) Alireza Heidari

Professor, Faculty of Chemistry,
California South University, California, USA

Prof. (Dr.) A. Mahadevan

Professor
S. G. School of Business Management, Salem

Prof. (Dr.) Hemant Sharma

Professor,
Amity University, Haryana

Dr. C. Shalini Kumar

Principal,
Vidhya Sagar Women's College, Chengalpet

Prof. (Dr.) Badar Alam Iqbal

Adjunct Professor,
Monarch University, Switzerland

Prof.(Dr.) D. Madan Mohan

Professor,
Indur PG College of MBA, Bodhan, Nizamabad

Dr. Sandeep Kumar Sahratia

Professor
Sreyas Institute of Engineering & Technology

Dr. S. Balamurugan

Director - Research & Development,
Mindnotix Technologies, Coimbatore

Dr. Dhananjay Prabhakar Awasarikar

Associate Professor,
Suryadutta Institute, Pune

Dr. Mohammad Younis

Associate Professor,
King Abdullah University, Saudi Arabia

Dr. Kavita Gidwani

Associate Professor,
Chanakya Technical Campus, Jaipur

Dr. Vijit Chaturvedi

Associate Professor,
Amity University, Noida

Dr. Marwan Mustafa Shamot

Associate Professor,
King Saud University, Saudi Arabia

Prof. (Dr.) Aradhna Yadav

Professor,
Krupanidhi School of Management, Bengaluru

Prof.(Dr.) Robert Allen

Professor
Carnegie Mellon University, Australia

Prof. (Dr.) S. Nallusamy

Professor & Dean,
Dr. M.G.R. Educational & Research Institute, Chennai

Prof. (Dr.) Ravi Kumar Bommiseti

Professor,
Amrita Sai Institute of Science & Technology, Paritala

Dr. Syed Mehartaj Begum

Professor,
Hamdard University, New Delhi

Dr. Darshana Narayanan

Head of Research,
Pymetrics, New York, USA

Dr. Rosemary Ekechukwu

Associate Dean,
University of Port Harcourt, Nigeria

Dr. P.V. Praveen Sundar

Director,
Shanmuga Industries Arts and Science College

Dr. Manoj P. K.

Associate Professor,
Cochin University of Science and Technology

Dr. Indu Santosh

Associate Professor,
Dr. C. V.Raman University, Chhattisgarh

Dr. Pranjal Sharma

Associate Professor, Department of Management
Mile Stone Institute of Higher Management, Ghaziabad

Dr. Lalata K Pani

Reader,
Bhadrak Autonomous College, Bhadrak, Odisha

Dr. Pradeepta Kishore Sahoo

Associate Professor,
B.S.A, Institute of Law, Faridabad

Dr. R. Navaneeth Krishnan

Associate Professor,
Bharathiyar College of Engg & Tech, Puducherry

Dr. Mahendra Daiya
Associate Professor,
JIET Group of Institutions, Jodhpur

Dr. G. Valarmathi
Associate Professor,
Vidhya Sagar Women's College, Chengalpet

Dr. Parbin Sultana
Associate Professor,
University of Science & Technology Meghalaya

Dr. M. I. Qadir
Assistant Professor,
Bahauddin Zakariya University, Pakistan

Dr. Kalpesh T. Patel
Principal (In-charge)
Shree G. N. Patel Commerce College, Nanikadi

Dr. Brijesh H. Joshi
Principal (In-charge)
B. L. Parikh College of BBA, Palanpur

Dr. Juhab Hussain
Assistant Professor,
King Abdulaziz University, Saudi Arabia

Dr. Namita Dixit
Associate Professor,
ITS Institute of Management, Ghaziabad

Dr. V. Tulasi Das
Assistant Professor,
Acharya Nagarjuna University, Guntur, A.P.

Dr. Nidhi Agrawal
Assistant Professor,
Institute of Technology & Science, Ghaziabad

Dr. Urmila Yadav
Assistant Professor,
Sharda University, Greater Noida

Dr. Ashutosh Pandey
Assistant Professor,
Lovely Professional University, Punjab

Dr. M. Kanagarathinam
Head, Department of Commerce
Nehru Arts and Science College, Coimbatore

Dr. Subha Ganguly
Scientist (Food Microbiology)
West Bengal University of A. & F Sciences, Kolkata

Dr. V. Ananthaswamy
Assistant Professor
The Madura College (Autonomous), Madurai

Dr. R. Suresh
Assistant Professor, Department of Management
Mahatma Gandhi University

Dr. S. R. Boselin Prabhu
Assistant Professor,
SVS College of Engineering, Coimbatore

Dr. V. Subba Reddy
Assistant Professor,
RGM Group of Institutions, Kadapa

Dr. A. Anbu
Assistant Professor,
Achariya College of Education, Puducherry

Dr. R. Jayanthi
Assistant Professor,
Vidhya Sagar Women's College, Chengalpattu

Dr. C. Sankar
Assistant Professor,
VLB Janakiammal College of Arts and Science

Dr. Manisha Gupta
Assistant Professor,
Jagannath International Management School

Copyright @ 2019 Indian Academicians and Researchers Association, Guwahati
All rights reserved.

No part of this publication may be reproduced or transmitted in any form or by any means, or stored in any retrieval system of any nature without prior written permission. Application for permission for other use of copyright material including permission to reproduce extracts in other published works shall be made to the publishers. Full acknowledgment of author, publishers and source must be given.

The views expressed in the articles are those of the contributors and not necessarily of the Editorial Board or the IARA. Although every care has been taken to avoid errors or omissions, this publication is being published on the condition and understanding that information given in this journal is merely for reference and must not be taken as having authority of or binding in any way on the authors, editors and publishers, who do not owe any responsibility for any damage or loss to any person, for the result of any action taken on the basis of this work. All disputes are subject to Guwahati jurisdiction only.



Journal - 63571

UGC Journal Details

Name of the Journal : International Journal of Advance & Innovative Research

ISSN Number :

e-ISSN Number : 23947780

Source: UNIV

Subject: Multidisciplinary

Publisher: Indian Academicians and Researchers Association

Country of Publication: India

Broad Subject Category: Multidisciplinary

CONTENTS

Research Papers

- GREEN SYNTHESIS OF RARE-EARTH DOPED SPINEL FERRITE AND FERRITE /PANI NANO COMPOSITE TO MICROWAVE ABSORPTION IN RADAR FREQUENCY RANGE** 1 – 7
Ravindra N. Kambale, Akhilesh Kumar Patel, K. G. Suresh, Sandeep Kumar and Vaishali Bambole
- DFT STUDY ON NONLINEAR OPTICAL (NLO) PROPERTIES OF BORAZINE** 8 – 12
Vinayak Deshmukh and Shivshankar Mitkari
- MAGNETIC PROPERTIES AND MAGNETOELECTRIC (ME) EFFECT IN FERROELECTRIC RICH (1-X) $\text{Co}_{1.2}\text{Mn}_{0.2}\text{Fe}_{1.6}\text{O}_4$ + (X) BaTiO_3 ME COMPOSITES** 13 – 18
Dr. Sandipan Shrirang Sawant
- ELECTRICAL AND ELECTROCHEMICAL PERFORMANCE OF (1-x) $\text{La}_{0.8}\text{Sr}_{0.2}\text{MnO}_3$: (x) $\text{Ce}_{0.8}\text{Gd}_{0.2}\text{O}_2$ COMPOSITE CATHODE FOR INTERMEDIATE TEMPERATURE SOLID OXIDE FUEL CELL APPLICATION** 19 – 26
K. R. Nagde
- M-POLYNOMIALS, ECCENTRICITY AND DEGREE-BASED TOPOLOGICAL INDICES OF CHALCONE** 27 – 32
N. K. Raut and S. N. Ipper
- DIELECTRIC PROPERTIES OF NANOSCALE COMPOSITE JUNCTION** 33 – 37
G. G. Patil, Khirade P. W. and Sayyad S. B.
- DETERMINATION OF RADIOLOGICAL DATA OF LIPIDS USING GAMMA RAY SPECTROMETRY** 38 – 43
Prashant S. Kore, Ram Bhosale, Dr. Jai Shri Kumar, Madhav Rode and Pravina P. Pawar
- STUDY THE MASS ATTENUATION COEFFICIENT OF ALCOHOL SOLUBLE COMPOUND AT ENERGY 511eV** 44 – 48
Mitkari S R and Deshmukh V. P.
- SYNTHESIS OF NANO-COMPOSITE CERIUM-ALUMINA: ADVANCED MATERIAL FOR CATALYTIC SUPPORT** 49 – 51
R. M. Belekar and B. A. Shingade
- EFFECT OF Zn^{++} ION SUBSTITUTION ON DIELECTRIC BEHAVIOUR OF MAGNESIUM FERRITE WITH VARYING FREQUENCY** 52 – 54
C. T. Birajdar
- ENERGY DISPERSIVE X-RAY [EDAX] SEM AND INFRARED SPECTROSCOPY STUDY OF Cd^{2+} SUBSTITUTED TO NICKEL FERRITE NANO PARTICAL** 55 – 57
M. B. Solunke and B. H. Devmunde

INVESTIGATION OF PHYSICOCHEMICAL PROPERTIES USING LCR METER TECHNIQUE	58 – 59
P. T. Sonwane and S. R. Gaur	
SYNTHESIS AND CHARACTERISATION OF POLYCRYSTALLINE Mn^{4+} DOPED Cu-Zn FERRITE	60 – 64
Padampalle A. S., Labde B. K., Suryawanshi A. D. and Suryawanshi D. D.	
STUDY OF MAGNETIC PROPERTIES OF $MgZn_xMn_xFe_{2-2x}O_4$ SPINEL FERRITE SYSTEMS	65 – 67
S. V. Kshirsagar, S. S. Raut, P. R. Maheshmalkar, S. J. Shukla and K. M. Jadhav	
GREEN SYNTHESIS OF GOLD AND COPPER NANOPARTICLES USING CINNAMOMUM TAMALA STEAM EXTRACTS	68 – 73
Zuber H. Mapkar, Surbhi Benjamin and Manohar V Lokhande	
SYNTHESIS, STRUCTURAL AND DIELECTRIC PROPERTIES OF $Ni_{0.3}Zn_{0.7-x}Co_xFeCrO_4$ FERRITE	74 – 78
D. L. Navgare, U. B. Tumberphale, Shyam K. Gore, V. B. Kawade	
POLYANILINE MATRIX FOR BIOELECTRONICS DEVICES	79 – 81
P. D. Gaikwad	
MEASUREMENT OF ATTENUATION DATA OF VITAMINS USING Na(I) DETECTOR	82 – 86
Amol Mandle, Anil Gachhe, Prashant S. Kore, Madhav Rode and Pravina P. Pawar	
DEVELOPMENT OF NANO-TiO_2/AI ELECTRODE FOR NON-ENZYMATIC GLUCOSE BIO-SENSING APPLICATION	87 – 92
Kiran D. More, Nilesh S. Shinde, Jagdish W. Dadge, Megha P. Mahabole, Rajendra S. Khairnar and Kashinath A. Bogle	
STRUCTURAL PROPERTIES OF RARE EARTH DOPED COBALT FERRITE	93 – 96
P. K. Gaikwad	
TEMPERATURE DEPENDENT GAS DETECTION OF SPRAY DEPOSITED ZNO THIN FILMS	97 – 100
E. U. Masumdar and M. A. Barote	
SURFACE WATER LEVEL ESTIMATION FROM MICROWAVE SIR-C SAR IMAGE: A HYDROLOGICAL STUDY USING CLASSIFICATION TECHNIQUES	101 – 105
Shaikh M. A, Sonawane D K, Karle S. C., Momin R. K, Sayyad S. B	
STRUCTURAL, MORPHOLOGICAL AND OPTICAL PROPERTIES OF $Zn_{1-x}Fe_xS$ NANOPARTICLES PREPARED BY CO-PRECIIPITATION METHOD	106 – 110
V. V Jadhavar, V. D. Mote1 and B. S. Munde	
ELECTROCHEMICAL IMPEDANCE SPECTROSCOPIC STUDY OF DYE SENSITIZED SOLAR CELL WITH AL DOPED TiO_2 NANOPARTICLES PHOTO ANODE SENSITIZED BY EOSIN Y DYE	111 – 116
Swati S. Kulkarni, Gajanan A. Bodkhe, Nikesh Ingle, S. S. Hussaini, N. N. Shejwal and Mahendra D. Shirsat	
SYNTHESIS, GROWTH MECHANISM AND PHYSICAL OBSERVATIONS OF In_2Se_3	117 – 119
R. V. Suryawanshi	
FLUORESCENCE CHARACTERISTICS OF BREAST CANCER TISSUES	120 - 122
Sanjay Awadhane and D. K. Kendre	

STUDY OF STRUCTURAL PROPERTIES OF Ni-Zn FERRITE AND APPLICATION FOR SYNTHESIS OF PYRANO PYRAZOLE 123 – 127

U. M. Mandle, B. L. Shinde, L. A. Dhale and K. S. Lohar

STRUCTURAL AND ELASTIC PROPERTIES OF CADMIUM SUBSTITUTED Ni –Cu FERRITES 128 – 130

R. B. Kavade, R. G. Vidhate, J. M. Bhandari, K. H Katke, S. J. Shukla and K. M. Jadhav

INVESTIGATION OF CRYSTAL STRUCTURE AND D.C. ELECTRICAL RESISTIVITY OF In^{3+} SUBSTITUTED YTTRIUM IRON GARNET 131 – 134

Vidhate R. G., Kavade R. B., Bhandari J. M., Katke K. H, and Jadhav K. M.

GREEN SYNTHESIS OF RARE-EARTH DOPED SPINEL FERRITE AND FERRITE /PANI NANO COMPOSITE TO MICROWAVE ABSORPTION IN RADAR FREQUENCY RANGE**Ravindra N. Kambale¹, Akhilesh Kumar Patel², K. G. Suresh², Sandeep Kumar³, and Vaishali Bambole⁴**^{1,4}Department of Physics, University of Mumbai, Vidyanagari Campus Kalin Santacruz Mumbai²Department of Physics, Indian Institute of Technology Bombay, Powai, Mumbai³Magnetics and Advanced Ceramics Lab, Department of Physics, Indian Institute of Technology Delhi, Delhi**ABSTRACT**

Er doped Ni-Zn (Ni_{0.5} Zn_{0.5}Fe_{1.9}Er_{0.1}O₄) ferrite nanoparticles have been synthesized by sol- gel auto combustion technique and ferrite /polyaniline (PANI) nanocomposite was synthesized by in-situ polymerization. The structural and morphological properties of the prepared samples were characterized by X- ray diffraction (XRD), Field emission scanning electron microscopy (FEG-SEM), Field emission gun transmission electron microscopy (FEG-TEM) and magnetic properties of the samples at room temperature were studied by Vibrating Sample Magnetometer (VSM). X-ray patterns confirmed the formation of single phase cubic structure with space group Fd-3m. The crystallite size of prepared sample is found to be in the range of 20-75 nm. While adding PANI in ferrite, the saturation magnetization was decreased due to nonmagnetic polyaniline. To investigate microwave absorbing properties of prepared samples, vector Network Analyser is used in the frequency range 2 GHz to 18 GHz. The minimum value of reflection loss was -18dB at the frequency of 10.64 GHz for Ni_{0.5} Zn_{0.5}Fe_{1.9}Er_{0.1}O₄ ferrite nanoparticles (thickness 1.9mm) and -25.58dB at frequency of 15.12GHz for PANI/ Ni_{0.5} Zn_{0.5}Fe_{1.9}Er_{0.1}O₄ ferrite nanocomposite (thickness 1.7mm). The microwave absorbing properties increase drastically and significant absorption frequency shifting in higher level by forming a nanocomposite with conducting polyaniline due to its high electric conductivity and controllable dielectric loss.

Keywords: Spinel structure, ferrite nanoparticles, polyaniline, nanocomposites, microwave absorbing property, reflection loss.

1. INTRODUCTION

The fast development of internet system and wireless technology brings many benefits like in telecommunication system, medical field, and industry. On the other hand, there is creation of one more type of pollution that is known as electromagnetic pollution. This is due to electromagnetic interference (EMI). The effect of EMI on human being and functionally of equipment is one of the serious problem, because of it decreases the electronic or electrical circuit functionality or damages the electronic equipment's in military and civil uses. Most of the electronic devices working on few MHz to 300 GHz In order to solve this problem there is need to develop good microwave absorbing materials. This material play an important role in controlling EM pollution[1-5]. An ideal microwave absorbing materials should have the properties of low density, tiny thickness, wide bandwidth and flexibility simultaneously [6-9]. Microwave absorbers should have properties of high electric loss and high magnetic loss [10-13]. Spinel ferrites with the properties of large magnetic losses and resistivity have been widely used as microwave absorbing materials in the Giga hertz range [14 -15].

In order to fabricate low density and flexible microwave absorbing materials extensive research is underway where carbonaceous fillers with ferrite nanoparticles are in a polymer matrix. Composite materials like ferrites and conducting polymers enhances microwave absorption properties [19-23]. Among all conducting polymer, polyaniline (PANI) has been studied extensively in recent year because of its environmental stability and variety of oxidation states [24-28]. The material like Er doped Ni-Zn ferrite/ polyaniline nanocomposite having maximum reflection loss is enhance the microwave absorbing properties

In this work we report, Ni_{0.5}Zn_{0.5}Fe_{1.9}Er_{0.1}O₄ ferrite nanoparticles (NZE) and Ni_{0.5}Zn_{0.5}Fe_{1.9}Er_{0.1}O₄ ferrite/Polyaniline (NZE/PANI) nanocomposite were successfully synthesized by lemon juice sol-gel auto comparison method and the in-situ polymerization method. The prepared NZE and NZE/ PANI were characterized by various technique. The morphology and structure-size dependent microwave absorption performance of the NZE and NZE/ PANI were investigated details by X-ray diffraction (XRD), Field emission gun scanning electron microscopy (FEG-SEM), Field emission gun transmission electron microscopy FEG-TEM. Magnetic properties investigated by M-H plot from Vibrating Sample Magnetometer and microwave absorption properties of the samples studied by measuring complex permittivity and complex permeability from vector network analyzer. The NZE/ PANI nanocomposite have high efficient and light weight microwave absorber.

2. EXPERIMENTAL DETAILS

2.1 Green synthesis of $\text{Ni}_{0.5}\text{Zn}_{0.5}\text{Fe}_{1.9}\text{Er}_{0.1}\text{O}_4$ Ferrite Nanoparticles

$\text{Ni}_{0.5}\text{Zn}_{0.5}\text{Fe}_{1.9}\text{Er}_{0.1}\text{O}_4$ ferrite powder was synthesized by a sol-gel auto-combustion method. The detail process can be described as follows. The stoichiometric amount of Ni $(\text{NO}_3)_2 \cdot 6\text{H}_2\text{O}$, Zn $(\text{NO}_3)_2 \cdot 6\text{H}_2\text{O}$, $\text{Er}(\text{NO}_3)_3 \cdot 5\text{H}_2\text{O}$, and $\text{Fe}(\text{NO}_3)_3 \cdot 9\text{H}_2\text{O}$ were first dissolved separately in 50ml of deionized water. This obtained solutions were mixed and stirred continuously for 60min. and certain amount of lemon juice is added in the mixture as a chelating agent. Ammonium hydroxide was then added dropwise to make a neutral solution and this solution was heated at 80°C with constant stirring to form a dried gel burned in a self-propagating combustion until all gels were burned completely out to form loose precursors. Finally, $\text{Ni}_{0.5}\text{Zn}_{0.5}\text{Fe}_{1.9}\text{Er}_{0.1}\text{O}_4$ crystalline powder was obtained after calcining the loose precursors at 850°C for 6 hours [20].

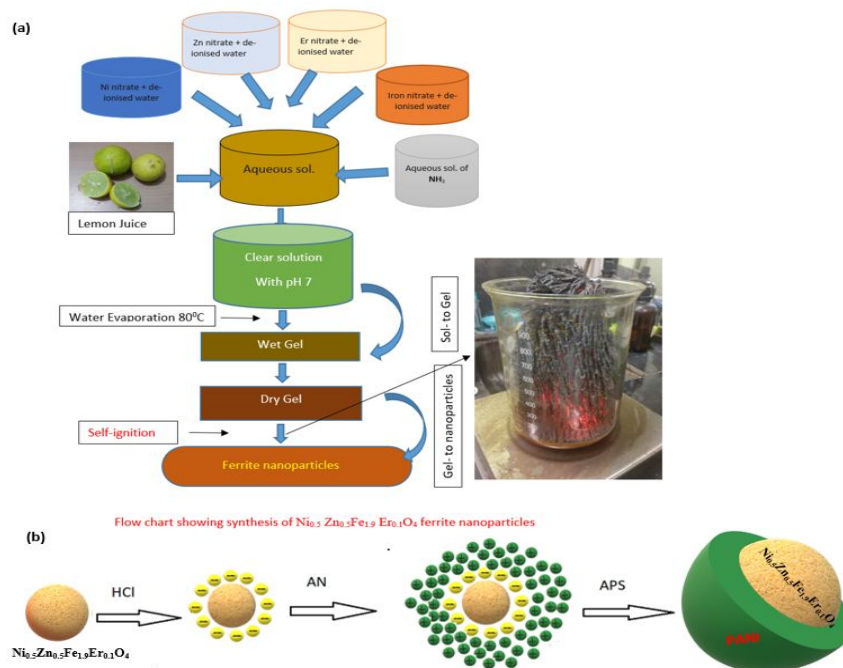


Fig-1 (a) Flow chart for the synthesis of $\text{Ni}_{0.5}\text{Zn}_{0.5}\text{Fe}_{1.9}\text{Er}_{0.1}\text{O}_4$ ferrite nanoparticles (b) possible reaction in the synthesis of ferrite/PANI nanocomposite

2.2 Synthesis of Polyaniline / $\text{Ni}_{0.5}\text{Zn}_{0.5}\text{Fe}_{1.9}\text{Er}_{0.1}\text{O}_4$ Ferrite Nano Composite

Polyaniline/ $\text{Ni}_{0.5}\text{Zn}_{0.5}\text{Fe}_{1.9}\text{Er}_{0.1}\text{O}_4$ ferrite composite was synthesized by in situ polymerization method. Firstly, a certain amount $\text{Ni}_{0.5}\text{Zn}_{0.5}\text{Fe}_{1.9}\text{Er}_{0.1}\text{O}_4$ Ferrite particle were suspended in a 70ml, 1M HCl solution and stirred for one hour to get well dispersed. Two millilitre aniline monomer was then added to the suspension and stirred for 30min. Ammonium peroxydisulfate (ASP) of 4.98gm (the molar ratio of ASP to aniline was 1:1) in a 40ml 1M HCl solution was then slowly dropped to the suspension mixture with a constant stirring. The polymerization was allowed to proceed for 12 hours at 0°C to 5°C . The composite of ferrite/ PANI was obtained by filtering and washing the suspension with 1M HCl and deionized water and dried under the vacuum at 60°C for 48hours.

3. RESULTS AND DISCUSSION

3.1 X- ray Diffraction Analysis

Figure 1 (a) shows the XRD pattern of PANI, $\text{Ni}_{0.5}\text{Zn}_{0.5}\text{Fe}_{1.9}\text{Er}_{0.1}\text{O}_4$ ferrite nanoparticles and $\text{Ni}_{0.5}\text{Zn}_{0.5}\text{Fe}_{1.9}\text{Er}_{0.1}\text{O}_4$ / PANI(Composite). PANI shows the amorphous nature in partially crystalline state with two diffraction peak $2\theta = 20.41^\circ$ and 25.61° due to the densely packed phenyl rings those exhibit an extensive inter chain π - π orbital overlap and parallel and perpendicular periodicity of the PANI. $\text{Ni}_{0.5}\text{Zn}_{0.5}\text{Fe}_{1.9}\text{Er}_{0.1}\text{O}_4$ and composite showed the polycrystalline nature as shown in fig. 1(a), we can see the intensity of composite sample is decreased as compared $\text{Ni}_{0.5}\text{Zn}_{0.5}\text{Fe}_{1.9}\text{Er}_{0.1}\text{O}_4$ sample, which is due to reduction of ferrite content. The room temperature Rietveld refined x-ray diffraction of $\text{Ni}_{0.5}\text{Zn}_{0.5}\text{Fe}_{1.9}\text{Er}_{0.1}\text{O}_4$ compound is as shown fig. 1 (b). The ferrite compound crystallizes in cubic structure having space group $\text{Fd-}3\text{m}$ with lattice parameter $\sim 8.39 \text{ \AA}$ and the Wyckoff positions are (0.125, 0.125, 0.125), (0.5, 0.5, 0.5) and (0.252, 0.252, 0.252) for Ni/Zn, Fe/Er and O respectively. The unit cell structure is shown in fig.1 (c), In the unit cell structure Fe/Er comprises with octahedral surrounding and Ni/Zn with tetrahedral surrounding, which are shown in Fig. 1(d). The Average crystallite size (D) of $\text{Ni}_{0.5}\text{Zn}_{0.5}\text{Fe}_{1.9}\text{Er}_{0.1}\text{O}_4$ ferrite nanoparticles has been calculated from XRD data using Scherer's equation

$$D = \frac{k\lambda}{\beta \cos \theta} \quad (1)$$

Where k is the grain shape factor (0.9) and λ , θ , and β are the X-ray wavelength, Bragg diffraction angle, and full-width at half-maximum of the diffraction peak, respectively. The value of average crystallite size $\text{Ni}_{0.5}\text{Zn}_{0.5}\text{Fe}_{1.9}\text{Er}_{0.1}\text{O}_4$ ferrite nanoparticles was found to be 26 nm.

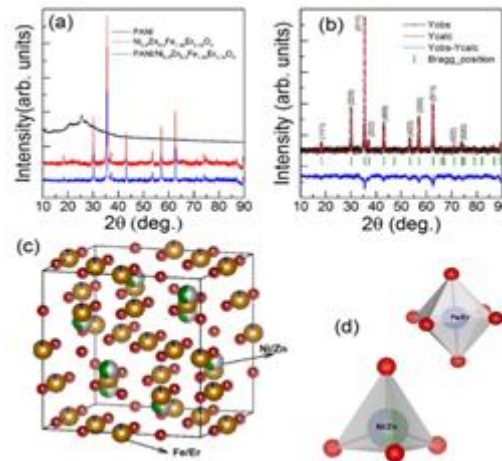


Fig-2 (a) XRD Patterns of PANI, $\text{Ni}_{0.5}\text{Zn}_{0.5}\text{Fe}_{1.9}\text{Er}_{0.1}\text{O}_4$ and PANI/ $\text{Ni}_{0.5}\text{Zn}_{0.5}\text{Fe}_{1.9}\text{Er}_{0.1}\text{O}_4$ (b) Rietveld refined x-ray diffraction of $\text{Ni}_{0.5}\text{Zn}_{0.5}\text{Fe}_{1.9}\text{Er}_{0.1}\text{O}_4$ (c) unit cell structure Fe/Er comprises with octahedral surrounding and Ni/Zn with tetrahedral surrounding. (d) Unit cell structure Fe/Er comprises with octahedral and Ni/Zn with tetrahedral.

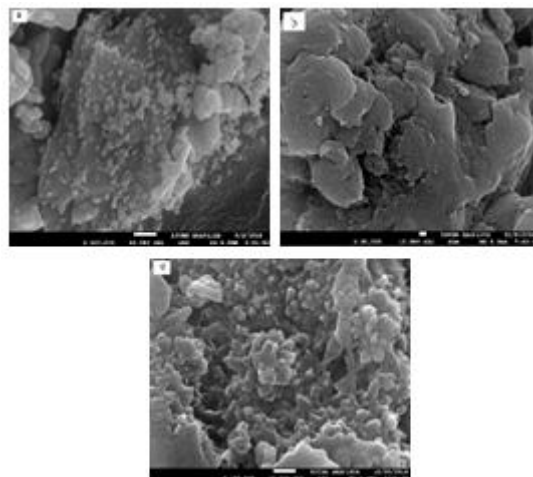


Fig-3: FEG-SEM images of (a) $\text{Ni}_{0.5}\text{Zn}_{0.5}\text{Fe}_{1.9}\text{Er}_{0.1}\text{O}_4$ ferrite nanoparticles (b) PANI (c) PANI/ $\text{Ni}_{0.5}\text{Zn}_{0.5}\text{Fe}_{1.9}\text{Er}_{0.1}\text{O}_4$ nanocomposite.

3.2 Morphology Investigation

Fig.3 (a) shows the cubic structure of $\text{Ni}_{0.5}\text{Zn}_{0.5}\text{Fe}_{1.9}\text{Er}_{0.1}\text{O}_4$ ferrite nanoparticles of size is about 12-56 nm. Fig.3 (b) shows the PANI as amorphous and Fig. 3(c) shows PANI/ $\text{Ni}_{0.5}\text{Zn}_{0.5}\text{Fe}_{1.9}\text{Er}_{0.1}\text{O}_4$ nanocomposite still retains the morphology of PANI shape and it can be observed that ferrites nanoparticles coated with PANI. The FEG-SEM images show that the particle size of Er doped Ni-Zn ferrite nanoparticles were uniformly distributed. Er doped Ni-Zn ferrite nanoparticles were distributed homogeneously in the polymer matrix.

The average particle size of the $\text{Ni}_{0.5}\text{Zn}_{0.5}\text{Fe}_{1.9}\text{Er}_{0.1}\text{O}_4$ ferrite nanoparticles and PANI coated $\text{Ni}_{0.5}\text{Zn}_{0.5}\text{Fe}_{1.9}\text{Er}_{0.1}\text{O}_4$ nanocomposite were calculated using FEG-TEM images, which are shown in Fig.4 (a, b). The average particle size were found in the range of 20-68 nm, which is calculated using Image-J software and matched with XRD and SEM images. Fig.4 b) shows that $\text{Ni}_{0.5}\text{Zn}_{0.5}\text{Fe}_{1.9}\text{Er}_{0.1}\text{O}_4$ ferrite nanoparticles were embedded in the conducting PANI matrix forming the core – shell structure. Fig. 4(c) shows the HR-TEM image, which clearly indicates the coating of PANI over ferrite nanoparticles. Dark core indicates the $\text{Ni}_{0.5}\text{Zn}_{0.5}\text{Fe}_{1.9}\text{Er}_{0.1}\text{O}_4$ ferrite nanoparticles of diameter 20 – 68 nm and the bright coloured shells distinctly different from $\text{Ni}_{0.5}\text{Zn}_{0.5}\text{Fe}_{1.9}\text{Er}_{0.1}\text{O}_4$ ferrite nanoparticles which were non-crystal conducting PANI layer were formed on the surface $\text{Ni}_{0.5}\text{Zn}_{0.5}\text{Fe}_{1.9}\text{Er}_{0.1}\text{O}_4$ ferrite nanoparticles. Fig. 4 d) shows SAED patterns of

$\text{Ni}_{0.5}\text{Zn}_{0.5}\text{Fe}_{1.9}\text{Er}_{0.1}\text{O}_4$ ferrite nanoparticles which reveal that the polycrystalline diffraction rings with many diffraction spots which indicates $\text{Ni}_{0.5}\text{Zn}_{0.5}\text{Fe}_{1.9}\text{Er}_{0.1}\text{O}_4$ ferrite is highly crystalline.

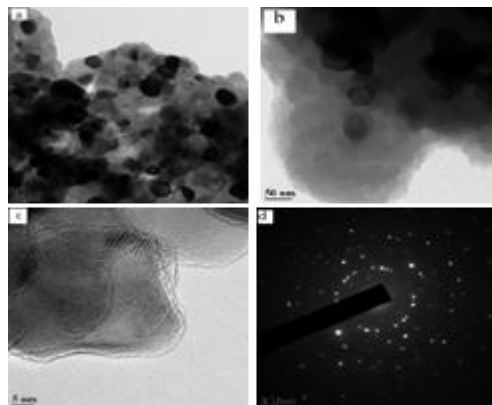


Fig-4 (a) $\text{Ni}_{0.5}\text{Zn}_{0.5}\text{Fe}_{1.9}\text{Er}_{0.1}\text{O}_4$ ferrite nanoparticles (b) $\text{Ni}_{0.5}\text{Zn}_{0.5}\text{Fe}_{1.9}\text{Er}_{0.1}\text{O}_4/\text{PANI}$ nanocomposite (c) H-R Image of $\text{Ni}_{0.5}\text{Zn}_{0.5}\text{Fe}_{1.9}\text{Er}_{0.1}\text{O}_4/\text{PANI}$ Nanocomposite. (d) SEAD pattern of $\text{Ni}_{0.5}\text{Zn}_{0.5}\text{Fe}_{1.9}\text{Er}_{0.1}\text{O}_4$ ferrite nanoparticles.

3.3 Magnetic Properties

The magnetic properties of the $\text{Ni}_{0.5}\text{Zn}_{0.5}\text{Fe}_{1.9}\text{Er}_{0.1}\text{O}_4$ ferrite nanoparticles and $\text{Ni}_{0.5}\text{Zn}_{0.5}\text{Fe}_{1.9}\text{Er}_{0.1}\text{O}_4 / \text{PANI}$ nanocomposite were analysed at room temperature by using a vibrating sample magnetometer (VSM) with an applied field $-20 \text{ kOe} \leq H \leq 20 \text{ kOe}$.

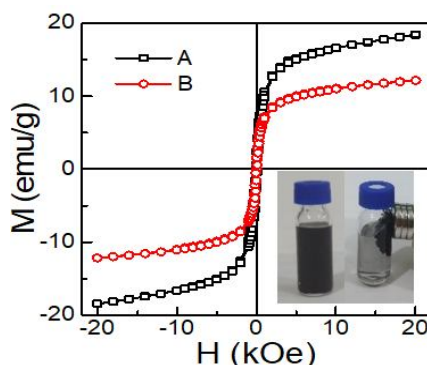


Fig-5: Magnetic hysteresis loops of (A) $\text{Ni}_{0.5}\text{Zn}_{0.5}\text{Fe}_{1.9}\text{Er}_{0.1}\text{O}_4$ (B) $\text{Ni}_{0.5}\text{Zn}_{0.5}\text{Fe}_{1.9}\text{Er}_{0.1}\text{O}_4/\text{PANI}$ Nanocomposite

Fig.5 shows the magnetization (M) versus the applied magnetic field (H) for $\text{Ni}_{0.5}\text{Zn}_{0.5}\text{Fe}_{1.9}\text{Er}_{0.1}\text{O}_4$ ferrite nanoparticles and $\text{PANI}/\text{Ni}_{0.5}\text{Zn}_{0.5}\text{Fe}_{1.9}\text{Er}_{0.1}\text{O}_4$ ferrite nanocomposite (B). The value of saturation magnetization (M_s) for $\text{Ni}_{0.5}\text{Zn}_{0.5}\text{Fe}_{1.9}\text{Er}_{0.1}\text{O}_4$ ferrite is about 18.38 emu/g, and remnant magnetization (M_r) and coercivity field are 2.47 emu/g and 0.12 kOe respectively. It can be seen that this ferrite material belongs to soft magnetic material due to the area of the hysteresis loop and residual magnetism is small.

The value of saturation magnetization (M_s) for $\text{Ni}_{0.5}\text{Zn}_{0.5}\text{Fe}_{1.9}\text{Er}_{0.1}\text{O}_4 / \text{PANI}$ nanocomposite is about 12.21 emu/g, and remnant magnetization (M_r) and coactivity field are 1.57 emu/g and 0.073 kOe respectively, these values are lower than pure $\text{Ni}_{0.5}\text{Zn}_{0.5}\text{Fe}_{1.9}\text{Er}_{0.1}\text{O}_4$ ferrite nanoparticles. This could be due to surface pinning of ferrite nanoparticle spin in easy axis of the magnetization. Pinning of spin in easy axis of the magnetization leads to decrease in coercivity of the materials which has been reflected in our composite sample. So the magnetization curve of the composite shows weak ferromagnetic behaviour. The Magnetic properties of nanocomposites containing $\text{Ni}_{0.5}\text{Zn}_{0.5}\text{Fe}_{1.9}\text{Er}_{0.1}\text{O}_4$ ferrite nanoparticles have been observed to be highly dependent on the value of magnetic particles, sample shape and crystallinity.

3.4 Microwave Absorbing Properties

Microwave absorption properties material depend on complex permittivity and complex permeability. The real parts of complex permittivity and permeability shows the storage capability of electric and magnetic energy, whereas imaginary parts of complex permittivity and complex represent the dissipation of electric and magnetic energy. Dielectric loss commonly results from electron polarization and electric dipolar polarization. The dielectric and magnetic loss factor $\tan \delta_E = \frac{\epsilon''}{\epsilon'}$ and $\tan \delta_M = \frac{\mu''}{\mu'}$ provides the measure of power lost in the materials versus the amount of power stored.

The frequency dependence of the real part (ϵ') and imaginary part (ϵ'') of complex permittivity for ferrite and composite are shown in Fig. 6 a) and b) respectively. For $\text{Ni}_{0.5}\text{Zn}_{0.5}\text{Fe}_{1.9}\text{Er}_{0.1}\text{O}_4$ ferrite nanoparticles, the real part (ϵ') of permittivity are almost constant up to 13GHz with one broad peak of value 8.362 at 13.89GHz, then it shows reducing tendency in the rest range. Imaginary part (ϵ'') of complex permittivity is constant for all frequency expect two peaks value 1.868 and 1.62 at 13.87GHz and 17.11 respectively. For composite, the real part of permittivity (ϵ') decreasing with frequency expect two broad peaks of vale 7.19 and 7.27 at 12.22 GHz and 13.81GHz respectively. It indicates that dielectric storage decreases with frequency. But Imaginary part of complex permittivity almost constant. Ferrites coating with PANI is greatly increases the electric conductivity of the sample and help to the increase the permittivity of sample, Because of the conducting properties of the shell, electrons can travel freely and accumulate on ferrite interface, forming a structure similar to a boundary layer capacitor and generating interfacial electric dipolar polarization. The frequency dependence of the real part (μ') and imaginary part (μ'') of permeability for ferrite and composite are shown in Fig. 6 (c) and (d) respectively. The real part (μ') of permeability for $\text{Ni}_{0.5}\text{Zn}_{0.5}\text{Fe}_{1.9}\text{Er}_{0.1}\text{O}_4$ ferrite nanoparticles and composite shows the decreasing tendency with some peaks with increase in frequency. The imaginary part (μ'') of permeability for $\text{Ni}_{0.5}\text{Zn}_{0.5}\text{Fe}_{1.9}\text{Er}_{0.1}\text{O}_4$ ferrite nanoparticles decreases with one broad peak of value 0.97 at 10.77GHz which indicates the maximum reflection loss at 10.77GHz. The imaginary part (μ'') of permeability for composite is almost same with two broad peaks of value 0.52 and 0.74 at 11.12GHz and 14.95GHz respectively which shows maximum reflection loss these frequencies.

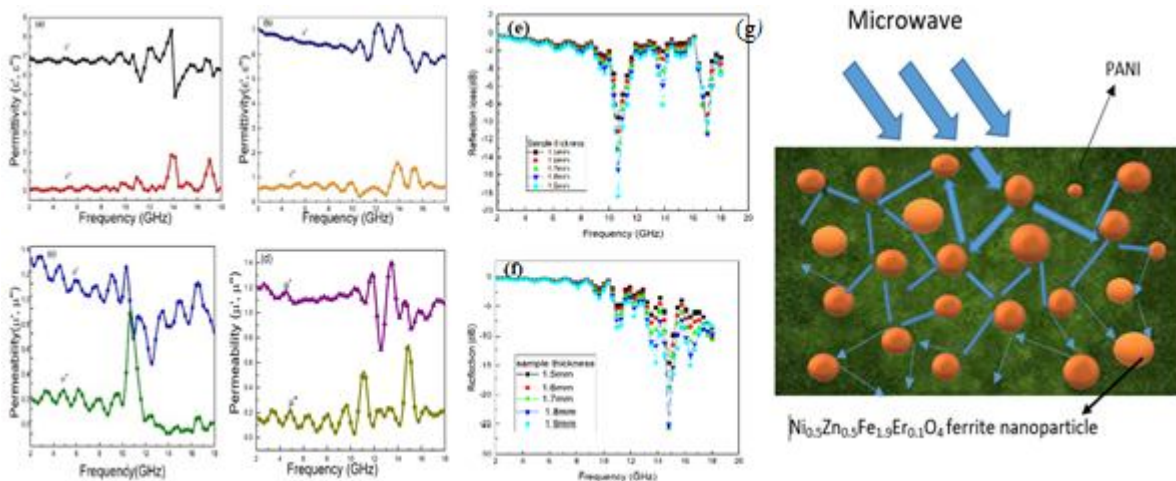


Fig-6 (a) Frequency dependence of complex relative permittivity of $\text{Ni}_{0.5}\text{Zn}_{0.5}\text{Fe}_{1.9}\text{Er}_{0.1}\text{O}_4$ ferrite nanoparticles (b) Frequency dependence of complex relative permittivity of $\text{Ni}_{0.5}\text{Zn}_{0.5}\text{Fe}_{1.9}\text{Er}_{0.1}\text{O}_4$ / PANI nanocomposite (c) Frequency dependence of complex relative permeability of $\text{Ni}_{0.5}\text{Zn}_{0.5}\text{Fe}_{1.9}\text{Er}_{0.1}\text{O}_4$ ferrite nanoparticles (d) Frequency dependence of complex relative permeability of $\text{Ni}_{0.5}\text{Zn}_{0.5}\text{Fe}_{1.9}\text{Er}_{0.1}\text{O}_4$ / PANI nanocomposite (e) Reflection loss curves of $\text{Ni}_{0.5}\text{Zn}_{0.5}\text{Fe}_{1.9}\text{Er}_{0.1}\text{O}_4$ (f) Reflection loss curves of $\text{Ni}_{0.5}\text{Zn}_{0.5}\text{Fe}_{1.9}\text{Er}_{0.1}\text{O}_4$ / PANI nanocomposite (g) Schematic illustration of the single-layer absorber.

The measured permittivity and permeability of samples by vector network analyser are used to calculate the reflection loss (RL) by using following equation [21]

$$RL = 20 \log \left| \frac{Z_{in} - 1}{Z_{in} + 1} \right| \quad (2)$$

Where the impedance (Z_{in}) of medium is

$$Z_{in} = \sqrt{\frac{\mu_r}{\epsilon_r}} \tanh \left(-i \frac{2\pi f}{\lambda} t \sqrt{\mu_r \epsilon_r} \right)$$

Here μ_r and ϵ_r are the measured relative complex permeability and complex permittivity, respectively. λ is wavelength of the incident wave in free space and t is a thickness of the absorber. Calculated RL curves of $\text{Ni}_{0.5}\text{Zn}_{0.5}\text{Fe}_{1.9}\text{Er}_{0.1}\text{O}_4$ ferrite nanoparticles and $\text{Ni}_{0.5}\text{Zn}_{0.5}\text{Fe}_{1.9}\text{Er}_{0.1}\text{O}_4$ / PANI nanocomposite with different thickness are shown in Fig. 6 (e) and Fig.6(f) respectively. The minimum value of reflection loss was -18dB at the frequency of 10.64 GHz for $\text{Ni}_{0.5}\text{Zn}_{0.5}\text{Fe}_{1.9}\text{Er}_{0.1}\text{O}_4$ ferrite nanoparticles (thickness 1.9mm) and -25.58dB at frequency of 15.12GHz for $\text{Ni}_{0.5}\text{Zn}_{0.5}\text{Fe}_{1.9}\text{Er}_{0.1}\text{O}_4$ / PANI nanocomposite (thickness 1.7mm). It seen from Fig. 6 (e) and (f) minimum RL values of composite are stronger than those of $\text{Ni}_{0.5}\text{Zn}_{0.5}\text{Fe}_{1.9}\text{Er}_{0.1}\text{O}_4$ ferrite nanoparticles.

4. CONCLUSION

Er doped Nickel Zinc ferrite nanoparticles and $\text{Ni}_{0.5}\text{Zn}_{0.5}\text{Fe}_{1.9}\text{Er}_{0.1}\text{O}_4$ / PANInanocomposite exhibiting microwave absorption properties were successfully synthesized by lemon juice sol-gel auto combustion method using lemon juice and in situ polymerization method. The cubic structure of $\text{Ni}_{0.5}\text{Zn}_{0.5}\text{Fe}_{1.9}\text{Er}_{0.1}\text{O}_4$ ferrite nanoparticles was confirmed by XRD, FEG-SEM and TEM images. SEM and Tem images shows PANI layer was formed on the surface of $\text{Ni}_{0.5}\text{Zn}_{0.5}\text{Fe}_{1.9}\text{Er}_{0.1}\text{O}_4$ ferrite nanoparticles. The studies of complex permittivity and complex permeability shows the better impedance matching and the combined effect between magnetic loss of core $\text{Ni}_{0.5}\text{Zn}_{0.5}\text{Fe}_{1.9}\text{Er}_{0.1}\text{O}_4$ ferrite nanoparticles and dielectric loss pf PANI shell contributed to the enhancement of microwave absorption performance. The absorption properties of the nanocomposite has been significantly enhanced more $\text{Ni}_{0.5}\text{Zn}_{0.5}\text{Fe}_{1.9}\text{Er}_{0.1}\text{O}_4$ ferrite nanoparticles.

ACKNOWLEDGMENT

Authors acknowledged to Magnetism and Advanced Ceramics Lab, Department of Physics, India Institute of Technology Delhi, Delhi 110016, India for providing Vector Network Analyser facility.

REFERENCES

1. Juua Luo, Yue Zuo, Pan Shen , Zhu Yun , King Zhang, excellent microwave absorption properties by tuned electromagnetic parameters in polyaniline coated $\text{Ba}_{0.9}\text{La}_{0.1}\text{Fe}_{1.9}\text{Ni}_{0.1}\text{O}_{19}$ / reduced graphene oxide nano composites. RSC Adv. 7 (2017) 36433-36443.
2. Ridham Dhawan, Saroj Kumari, Rajeew Kumar, S.K. Dhawan, Sanjay R Dhakate, Mesocarbon, microsphere composites with Fe_3O_4 nanocomposites for outstanding electromagnetic interference shielding effectiveness RSC Adv. 5, (2015) 43279- 43289.
3. Xiao Hu Ren, Guang Liang Xu, Electromagnetic and microwave absorbing properties of NiCoZn- ferrite doped with La^{3+} . J. Magn. Magn. Mater, vol. 354 pp. 44-48, 2014.
4. Pan Shen Juhua Luo, Yue Zuo, Zhu Yan, Kang Zhang, Effect of La-Ni substitution on structural, magnetic and microwave absorption properties of barium ferrite Ceramics Internation 43 (2017) 4846 – 4851
5. Liqiu Wei, Ruxin Che,, Yijun Jiang Bing Yu, Study on preparation and microwave absorption property of the core- nano shell composite materials doped with La, J. environment sciences 25 (2013) 527-531.
6. K.K Gupta, S M Abhas, T. H. Goswami, A. C. Abhyankar, Microwave absorption in X and Ku band frequency of cotton fabric coated NiZn ferrite and carbon formulation in polyurethane, J. Magn. Magn. Materials, vol. 362, pp. 216-225, 2014
7. Seema, Joon, Rakesh Kumar, Avanish Pratap Singh, Rajni Shukla, S. K. Dhawan, Fabrication and mrowave shielding properties of free standing polyaniline-carbon fibre thin sheets, Mat. Chem. Phys., vol. xxx pp.1-9, 2015.
8. M. A. Popov, O P fedorchuk, S.O Solopan, I. V. Zavislyak, A. G. Belous, Microwave composite structured on the base of nickel – zinc ferrite $\text{Ni}_{1-x}\text{Zn}_x\text{Fe}_2\text{O}_4$ nanoparticles in the photopolymer matrix, J. Magn. Magn. Mater, 469 (2019) 398-404.
9. L.L.Wang P.K.Tay. K.Y. See, Z. Sun, L. K Tan, D. L. Ua, Electromagnetic interference shielding effectiveness of carbon base materials prepared by screen printing, Carbon, Vol.47 pp. 1905-1910, 2009.
10. Gopal datt, Chetan Kotabage, A C Abhyankar, Ferromagnetic resonance of Ni Co Fe_2O_4 nanoparticles and microwave absorption properties of flexible Ni Co Fe_2O_4 - Carbon block/poly(vinyl alcohol composites , Phys. Chem, chem. Phys. 19 (2017) 20699-20712
11. P. Sambyal, A. P. Singh, M. Verma, M. Farukh , B. P. Singh, S. K. Dhavan, Tailored Polyaniline/ Barium strontium titanate / expanded grate multiphase composite for efficient radar absorption, RAC Advance, vol. 4 pp. 12614-12624, 2014..
12. Cong Chen, shouzhen Bao, Baoshun Zhang, Yuanyuan Zhou, Shimei Li, Development of sulphide – doped graphene/ Fe_2O_4 absorber with wide band electromagnetic absorption performance, J. alloys. Comps. 770 (2019) 90-97
13. Muhammed Waqas, Muktar, Muhammad Irfan, Synthesis and properties of Pr substituted Mg-Zn ferrites of core materials and high frequency applications, J. Magn. Magn. Mater. vol. 381, pp. 173-178, 2015.
14. Yi Liu, Shicheng, Effect of heat treatment on microwave absorption properties of Ni-Zn-Mg–La ferrite nanoparticle, J. Magn. Magn. Mater, vol. 349, pp. 57-62, 2014.

15. C.A. Stergiou, G. Litsardakis, Electromagnetic properties of Ni and La doped strontium hex ferrites in the microwave region, *J. Alloys Comp.*, vol 509 pp. 6609-6615, 2011
16. Majid Niaz Akhtar, Muhammad Saleem, Muhammad Azhar Khan, Al doped spinel and garnet nanostructured ferrites for microwave frequency C and X- band application, *J. Phys and Chem Solids* 123 (2018) 260–265
17. A. I. Lorgu, F. Maxim, C. Matel, Liliana Pines, Ferreira, P. Ferreira, M. M Cruz, D. Berger, Fast synthesis of rare earth (Pr^{3+} , Sm^{3+} , Eu^{3+} and Gd^{3+}) doped bismuth ferrite powders with enhanced magnetic properties, *J. Alloys Comp.*, V. 629, 62-68, 2015.
18. M. K., Tehrani, A Ghasemi, m Moradi, R. S Alam, Wideband , electromagnetic wave absorption using doped barium hexferrite in Ku band, *J. Alloys Comp.*, vol. 509 pp. 8398-8400, 2011.
19. E. Lahiff, T. Woods, w. Blau, G.G.Wallace, Synthesis and characterization of controllably functionalized polyaniline nanofiber, *Synth. Met.* vol. 159 pp. 0741-0748, 2009.
20. Ravindra N. Kambale, Akhilesh Patel, K G Suresh, Vaishali Bambole , Magnetic and enhanced microwave absorption properties of NiCoZn ferrite /Polyaniline nanocomposite , *Int. J. Engg. Tech. Sci. Research*, vol. 5 Issue. 2, 147-154, 2018.
21. E.F. Fang , H. J. Choi,W. S. Ahn, Electroactive response of mesoporous silica and its nanocomposites with conducting polymers. *Compos. Sci. tech.* vol. 69, pp. 2088-2093, 2009.
22. S.Geeta, K.K.S. Kumar, S. Meenaxi, Synergetic effect of conducting polymer composites reinforced E-Glass fabric for the control of electromagnetic radiation. *Compos. Sci. Tech.*, vol. 70,pp. 1017-1022, 2010.
23. Pablo Hernández-Gómez, José María Muñoz, and Manuel A. Valente, Field-Induced Microwave Absorption in Ni Ferrite Nanoparticles, *IEEE Trans. Magn.*, vol. 46, no. 2, pp. 475-478, Feb. 2010.
24. Yan Wang, Ying Huang, Qiufen Wang, Wang, Qian He, Lin Chen, Preparation and electromagnetic properties of polyaniline (polypyrrole)- Ba $\text{Fe}_{12}\text{O}_{19}/\text{Ni}_{0.8}\text{Zn}_{0.2}\text{Fe}_2\text{O}_4$ ferrite nanocomposites, vol. 259 pp. 486-493, 2012.
25. Juhua, Lao, Yang Xu, Honkai Mao, magnetic and microwave absorption properties of rare earth ions(Sm^{3+} , Er^{3+}) doped strontium ferrite and its nanocomposites with polypyrrole,*J. Magn. Magn. Mater.*, vol. 381, pp. 365-371, 2015.
26. Polyaniline composite, vol 332, pp. 10-14, 2013.
27. C. L. Yaan, Y. S. Hang, Microwave absorption of core shell structure polyaniline / $\text{Sr Fe}_{12}\text{O}_{19}$ composites, *J. Mater. Sci.*, vol. 45, pp. 3470-3476, 2010.
28. Zhong Zhy, Wang, Hong Bi, Jian liu, Tao Sun, Xian Liang Wu, Magnetic and microwave absorbing properties of polyaniline / $\gamma\text{-Fe}_2\text{O}_3$ nanocomposite, *J. Magn. Magn. Mater.*, vol 320, pp. 2132-2139, 2008.

DFT STUDY ON NONLINEAR OPTICAL (NLO) PROPERTIES OF BORAZINE

Vinayak Deshmukh and Shivshankar Mitkari

Shri Siddheshwar Mahavidyalaya, Majalgaon Dist. Beed

ABSTRACT

*In this work, density functional theory (DFT) and finite field (FF) approach has been adopted to study nonlinear optical (NLO) properties of borazine. The geometrical parameters and NLO properties obtained at B3LYP/6-311++G** level of theory. For the calculations of first (β) and second (γ) hyperpolarizabilities, the finite field approach has been used. The geometrical parameters and vibrational frequencies for borazine at this level of theory are in excellent agreement with the available experimental determinations. Systematic changes in the β and γ values are obtained.*

Keywords: Borazine, DFT, Finite field approach, NLO properties.

INTRODUCTION

There is growing attention in materials with high non-linear optical (NLO) properties due to their potential application in technologies such as lasers, telecommunications, photovoltaic cells, organic light emitting diodes, and semiconductor layers in field-effect transistors [1] information processing and holography. Nonlinear optical (NLO) phenomena have been extensively studied over the last decades; molecules exhibiting large hyperpolarizabilities have a strong NLO potential and could be used, under conditions, for optoelectronics and a variety of optical devices [2-5].

Borazine, the inorganic analogue of benzene, is obtained by replacing the carbon atoms with alternating boron and nitrogen atoms and shares many similarities with the benzene both in structures and characteristics [6-8]. Planar structure, equal bond lengths and the similarity in physical properties to benzene entitle borazine to be named as 'inorganic benzene' [9]. However, the chemical properties of borazine are entirely different from those of benzene [10-13]. Borazine readily undergo several polar addition reactions that are difficult with benzene. Theoretical studies have shown that six p electrons are significantly localized on nitrogen atoms due to the large electronegativity difference between boron and nitrogen [14-16]. Although borazine is aromatic it remains still in controversy [17-19], but it is the fact that borazine is considerably less aromatic as compared to benzene. In this work, we have studied the change in nonlinear properties in terms of a , b , and c values of borazine upon derivatisation with electron donating and withdrawing groups in the form of D-p-A system. Many studies have reported that organic NLO chromophores, especially those demonstrating high b values, typically have large dipole moments [20-21].

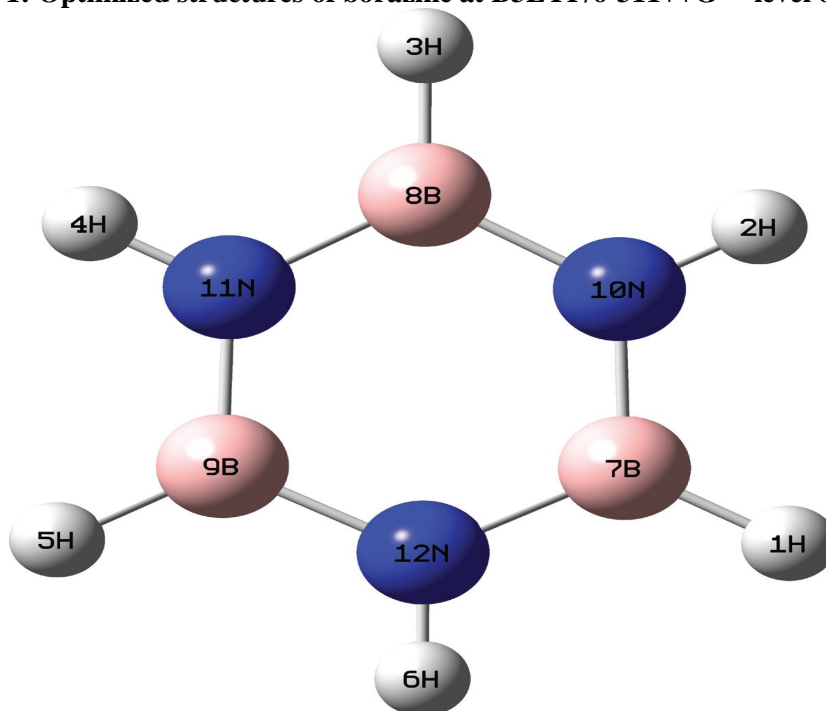
The aim of this work is to study nonlinear optical properties (NLO) using density functional theory method. We compare the geometrical properties and nonlinear optical properties of borazine with available experimental values.

COMPUTATIONAL DETAILS

We first optimized the geometries of borazine with the density functional theory (DFT) method with different exchange and correlation functional. We compared the geometrical parameters with the experimental values and found that the geometries of borazine at B3LYP/6-311++G** level of theory. The geometrical parameters of borazine at this level are compared with the available experimental determinations [22]. The vibrational frequencies are also obtained at the same level of theory. To obtain the first and second hyperpolarizabilities of these molecules the Finite-Field approach has been used [23]. The hyperpolarizabilities viz. β and γ can be calculated using the total energy E of a molecule in presence of an applied field. The field is applied either in X, Y or Z direction. The static hyperpolarizabilities are obtained using different field strengths to avoid numerical instability. The static hyperpolarizabilities β and γ are also obtained for various methods and basis sets for the fixed field strength. All the calculations are carried out using Gaussian 03 suit of programme [24].

RESULT AND DISCUSSION

Figure 1 shows the optimized structures of borazine at B3LYP/6-311++G** level of theory. The bond lengths, angles and dipole moment for these molecules are reported in Table 1 along with the available experimental values [22]. It can be seen that the geometrical parameters for borazine are in good agreement with the experimental determinations at this level of theory.

Figure-1: Optimized structures of borazine at B3LYP/6-311++G level of theory****Table-1: Optimized geometries for borazine molecule at B3LYP/6-311++G** level alongwith experimental values. Bond lengths in Å, angle in degrees and dipole moment in debye**

Parameters	Expt.*	Borazine(B3N3H6)
B-N	1.436 ±0.004	1.431
B-H	1.258 ±0.020	1.191
N-H	1.050 ±0.020	1.008
<N-B-N	117.7 ±2.0	117.0
<B-N-B	121.1 ±2.0	122.9
<H-B-N	----	121.4
<H-N-B	----	118.5
Dipole moment	----	0.01D

Abbreviation: B- $B_3N_3H_6$ * Experimental values from ref [22].

NONLINEAR OPTICAL PROPERTIES

There are several techniques to calculate the hyperpolarizabilities. The dipole moment or total energy based equation of a molecule can be used to calculate the hyperpolarizabilities. The hyperpolarizabilities by the energy and dipole moment based equations do not give the same result. The energy based equations give more stable result with respect to the field strength than the dipole moment based equation. We have obtained the NLO properties of borazine using the Finite-Field approach. We confine our attention to β and γ of borazine. The Finite-Field method is a derivative method, so numerical problem can't be avoided. For the calculation of NLO properties one can prevent numerical instability by choosing the value of appropriate field strength by obtaining β and γ at various field strengths.

We have used B3LYP/6-311++G** level to obtain NLO properties of borazine. We first applied Finite-Field of different field strength either in X, Y or Z direction to decide the suitable field strength in order to obtain the numerical stable hyperpolarizabilities. We then obtained the hyperpolarizabilities of borazine using different methods for the fixed field strength.

The variation of β and γ of borazine with field strength applied either in X, Y or Z direction is shown in Fig.2. As can be seen from Fig.2, borazine show numerically stable hyperpolarizabilities at a certain range of field strength applied along Y direction. From Fig.2, we choose the field strength of 0.006a.u. to calculate the hyperpolarizabilities of borazine using different methods with 6-311++G** basis set to see the effect of level of theory on hyperpolarizabilities.

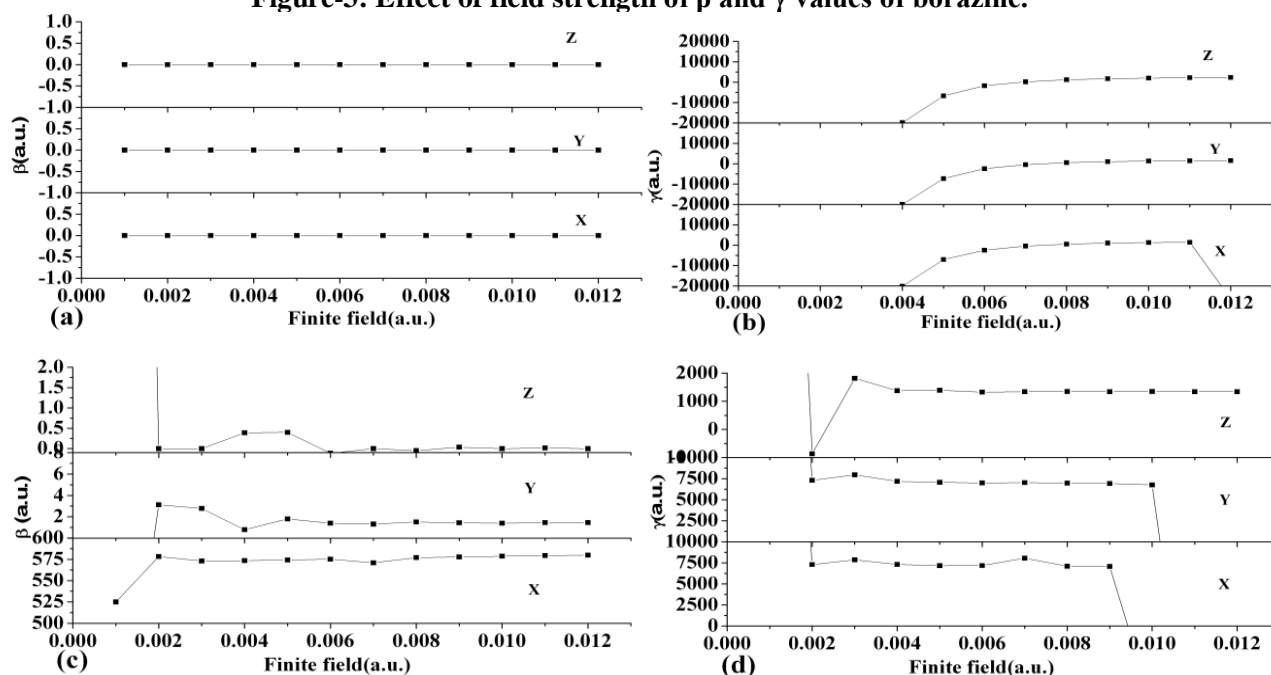
Figure-3: Effect of field strength of β and γ values of borazine.

Fig. 3.

The variation of β and γ of borazine obtained using different methods and 6-311++G** basis set with field strength of 0.006a.u. applied in Y direction is shown in Fig. 4. It appears clearly from Fig. 4 that the magnitude of calculated β values for borazine is around 1 a.u. for all the methods used here. The calculated γ values for borazine is in a range of 300-400 a.u. using different methods used here. The magnitude of β is higher where there is no inclusion of diffuse function in the basis set. The values of β obtained using MP2 are slightly higher than the DFT method. The correlation effect by the MP2 method increases the β at the HF level. The β values using DFT with different exchange and correlation functional viz. PBE1PBE, PBEPBE, B3PW91 and BLYP are nearly equal for all the basis sets with the same method. As seen in Fig. 4(b) when diffuse functions are added to the split valence triple zeta basis set (6-311G), the magnitude of γ obtained using different methods changes significantly.

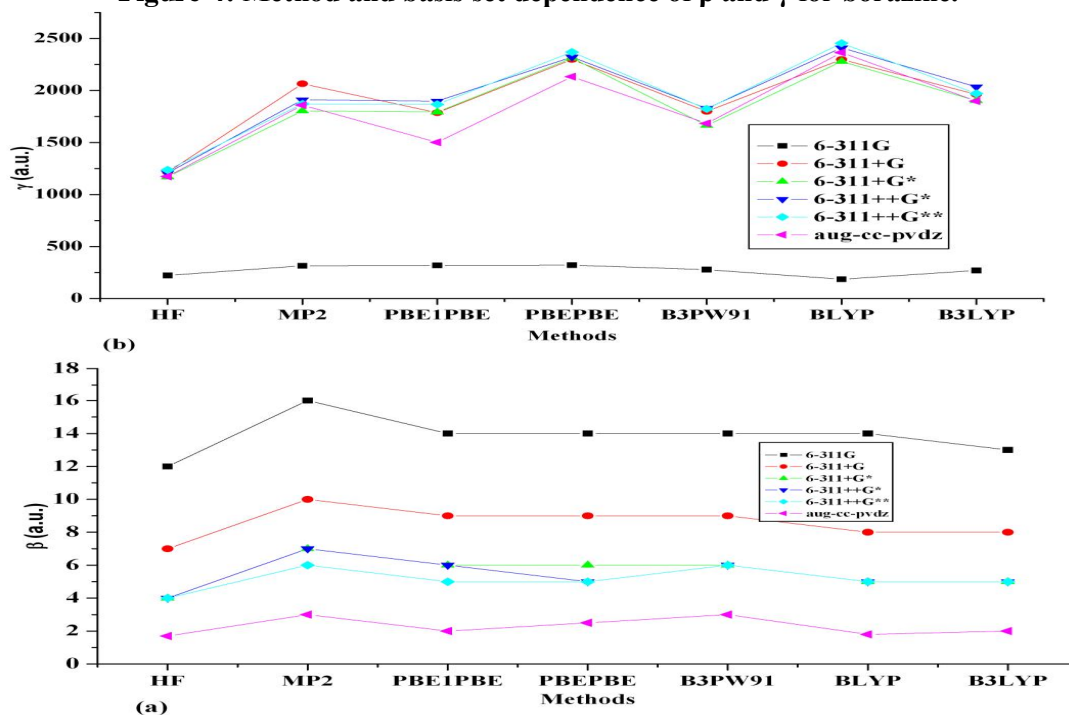
Figure-4: Method and basis set dependence of β and γ for borazine.

Figure 4.

CONCLUSIONS

We have performed DFT calculations for the study of first and second hyperpolarizabilities (β and γ) of borazine. The optimized geometries and vibrational frequencies for borazine are in excellent agreement with the available experimental determinations. The substituent effect on NLO properties of borazine has been investigated by using finite field method. The β and γ values are calculated at field strength of 0.006 a.u. for borazine and substituted borazines using different methods and different basis sets. A large change in dipole moment is observed in borazine.

REFERENCES

1. C.D. Dimitrakopoulos, P. Malenfant, Adv. Mater. 14, 29, (2002).
2. M. Albota, D. Beljonne, J.L. Brédas, J.E. Ehrlich, J.Y. Fu, A. A. Heikal, S. E. Hess, T.Kogej, M. D. Levin, S. R. Marder, D. McCordmaughon, J. W. Perry, H. Rockel, M. Rumi, C.Subramaniam, W. W. Webb, I. L. Wu and C. Xu, Science, 281 (1998) 1653.
3. A. M. McDonagh, M. G. Humphrey, M. Samoc and B. Luther-Davies, Organometallics, 18 (1999) 5195.
4. C. E. Powell, J. P. Morrall, S. A. Ward, M. P. Cifuentes, E. G. A. Notaras, M. Samoc and M. G. Humphrey, J. Am. Chem. Soc., 126 (2004) 12234.
5. X. Zhou, J. K. Feng and A. M. Ren, Chem. Phys. Lett., 403 (2005) 7.
6. R.J. Doerksen, A.J. Thakkar, Quadrupole and octopole moments of heteroaromatic rings, J. Phys. Chem. A 103 (1999) 10009–10014.
7. E. Wiberg, A. Bolz, Das “anorganischeBenzol” B₃N₃H₆, Ber.Dtsch. Chem. Ges. 73 (1940) 209–232.
8. A.F. Holleman, E. Wiberg, N. Wiberg, Lehrbuch der Anorganischen Chemie, vol. 102, de Gruyter, Berlin, 2007.
9. A.L. Korich, P.M. Iovine, Boroxine chemistry and applications: a perspective, Dalton Trans. 39 (2010) 1423–1431.
10. K.P. Loh, S.W. Yang, J.M. Soon, H. Zhang, P. Wu, Ab initio studies of borazine and benzene cyclacenes and their fluoro-substituted derivatives, J. Phys. Chem., A 107 (2003) 5555–5560.
11. C. Tçnshoff, M. Mller, T. Kar, F. Latteyer, T. Chass, K. Eichele, H.F. Bettinger, B₃N₃ borazine substitution in hexa-peri-hexabenzocoronene: computational analysis and scholl reaction of hexaphenylborazine, Chem. Phys. Chem. 13(2012) 1173–1181.
12. H.F. Bettinger, T. Kar, E. Sanchez-Garcia, Borazine and benzene homo- and heterodimers, J. Phys. Chem. A 113 (2009) 3353–3359.
13. N.A.A. Zwaneveld, R. Pawlak, M. Abel, D. Catalin, D. Gimes, D. Bertin, L. Porte, Organized formation of 2D extended covalent organic frameworks at surfaces, J. Am. Chem. Soc. 130 (2008) 6678–6679.
14. E.F. Archibong, A.J. Thakkar, Polarizabilities of aromatic six-membered rings: azines and inorganic benzenes, Mol. Phys. 81 (1994) 557–567.
15. D.L. Cooper, S.C. Wright, J. Gerratt, P.A. Hyams, The electronic structure of heteroaromatic molecules. Part 3. A comparison of benzene, borazine, and boroxine, J. Chem. Soc., Perkin Trans. 2 (1989) 719–724.
16. P.W. Fowler, E. Steiner, Ring currents and aromaticity of monocyclic p-electron systems C₆H₆, B₃N₃H₆, B₃O₃H₃, C₃N₃H₃, C₅H₅-, C₇H₇+, C₃N₃F₃, C₆H₃F₃, and C₆F₆, J. Phys. Chem. A 101 (1997) 1409–1413.
17. D.W. Lamb, R.I. Keir, G.L.D. Ritchie, Polarizability and magnetizability anisotropies of trimethylboroxine, Me₃B₃O₃: comparison of boroxine and benzene ring systems, Chem. Phys. Lett. 291 (1998) 197–201.
18. N. Islam, A.H. Pandith, Analysis of vibrational spectra (FT-IR and VCD) and nonlinear optical properties of [Ru(L)₃]²⁺ complexes, J. Coord. Chem. 67 (2014) 3288–3310.
19. M. Cho, S.Y. An, H. Lee, Nonlinear optical properties of tetrahedral donor–acceptor octupolar molecules: effective five-state model approach, J. Chem. Phys. 116 (2002) 9165–9173.
20. C. Coluccini, A.K. Sharma, N. Caricato, A. Sironi, E. Cariati, S. Righetto, E. Tordin, C. Botta, A. Forni, D. Pasini, Switching of emissive and NLO properties in push–pull chromophores with crescent PPV-like structures, Phys. Chem. Chem. Phys. 15 (2013) 1666–1674.

-
21. Y. Dai, Z. Li, J. Yang, Density functional study of nonlinear optical properties of grossly warped nanographene C₈₀H₃₀, *J. Phys. Chem. C* 118 (2014) 3313–3318.
 22. R. J. Boyd, S. C. Choi, C. C. Hale, *Chem. Phys. Lett.* **1984**, 112, 2.
 23. L. Turker, S. Erkoc, *J. Mol. Struct.: Theochem.* **2000**, 531, 401.
 24. M. J. Frisch, G. W. Trucks, H. B. Schlegel, et al., Gaussian 03 Revision E.01 Gaussian Inc., Wallingford, CT, **2004**.

MAGNETIC PROPERTIES AND MAGNETOELECTRIC (ME) EFFECT IN FERROELECTRIC RICH (1-X) $\text{Co}_{1.2}\text{Mn}_{0.2}\text{Fe}_{1.6}\text{O}_4$ + (X) BaTiO_3 ME COMPOSITES**Dr. Sandipan Shirang Sawant**

Assistant Professor Department of Physics, Shri Chhatrapati Shivaji College, Omerga

ABSTRACT

Magnetoelectric composites with composition $(1-x)\text{Co}_{1.2}\text{Mn}_{0.2}\text{Fe}_{1.6}\text{O}_4 + (x)\text{BaTiO}_3$ (ME) composite have been prepared using conventional double sintering ceramic process where x varies as 0.00, 0.25, 0.50, 0.75 and 1.00. The X-ray diffraction pattern of the composites reveals the formation of spinel structure for the piezomagnetic phase and tetragonal perovskite structure for the piezoelectric phase without any other phase formation. The micro-structure of composites were characterized by scanning electron microscopy. The average grain size of ferrite, ferroelectric and their composites was determined using linear intercept method. The saturation magnetization (M_s), coercive field (H_c), remanance magnetization (M_r) etc. magnetic properties are measured using pulse field magnetic hysteresis loop tracer. The measurements were carried out at room temperature. The magnetoelectric voltage coefficient $(dE/dH)H$ was studied as a function of intensity of the magnetic field. A large ME voltage coefficient of about $647 \text{ Vcm}^{-1}\text{Oe}^{-1}$ was observed for 25% $\text{CoMnFe}_2\text{O}_4$ + 75% BaTiO_3 composite.

Keywords: XRD; SEM; Hysteresis; and Magnetoelectric effect.

1 INTRODUCTION

The development of composite materials has been a subject of intensive research today. The composite material is a mixture of at least two chemically distinct materials combined three dimensionally having a distinct interface separating the constituent phases which have repeated geometry for large enough scale [1, 2]. The ME composite materials consist of piezomagnetic and piezoelectric phases mechanically coupled in equilibrium. Magnetoelectricity is a product properties in which the material gets magnetized after applying electric field and electrically polarized in a magnetic field.

In 1978, Boomgard et al. have outlined following conceptual points inherent to ME effect in composite to obtain good ME effect the two phase must be equilibrium, the mechanical coupling between the two phases must be perfect, the value of magnetostriction coefficient of piezomagnetic phase and piezoelectric coefficient of piezoelectric phase must be high, the resistivity of the constituent phases must high to avoid the leakage current during poling are required to be satisfied to get good ME output[3]. Such magnetoelectric composites find many applications in ME data storage and switching, radio electronic device, Modulation of amplitudes, optoelectronic, microelectronic, Spin wave generation, frequency conversion, amplification, transducers, etc [3, 4]. The ME effect occurs due to the interaction between the magnetic and electric dipoles.

In the present communication, we have chosen $\text{Co}_{1.2}\text{Mn}_{0.2}\text{Fe}_{1.6}\text{O}_4$ as a piezomagnetic phase and BaTiO_3 as the piezoelectric phase. Such composite to show high magnetoelectric effect, which in turn suggests that, the magnetoelectric interaction in these composites may lead to interesting results in their structural and magnetic properties [5, 6].

2 EXPERIMENTAL TECHNIQUES**2.1 Preparation of ME composites**

The piezomagnetic material chosen as a ferromagnetic phase $\text{Co}_{1.2}\text{Mn}_{0.2}\text{Fe}_{1.6}\text{O}_4$ has been prepared by standard double sintering ceramic method using AR grade oxides. The oxides were mixed in stoichiometric proportion and wet ground for about 2-3 hours in an agate mortar and pestle. The mixed fine powder is pre-sintered at 925°C for 9 hours. The sintered powder is again reground and finally sintered at 1080°C for 16 hours followed by slow cooling to room temperature to obtain pure single phase piezomagnetic samples. The single phase cubic spinel structure formation of piezomagnetic was confirmed by X-ray diffraction technique. The piezoelectric phase Barium Titanate (BaTiO_3) was prepared by standard double sintering ceramic method using AR grade oxides/carbonate. Barium carbonate (BaCO_3) and Titanium-dioxide (TiO_2) were taken in molar proportion. The mixed powder of Barium carbonate (BaCO_3) and Titanium-dioxide (TiO_2) was ground using agate mortar and pestle and pre-sintered at 900°C for 12 hours. In the final sintering the material was held at 1050°C for 16 hours. The sintered samples were allowed to cool to room temperature. Analysis of XRD pattern of BaTiO_3 revealed the formation of single phase tetragonal perovskite structure [7].

The composite of piezomagnetic and piezoelectric phase $(1-x)\text{CoMnFe}_2\text{O}_4 + (x)\text{BaTiO}_3$ with ($x = 0.25, 0.50$ and 0.75 mole %) was prepared by standard double sintering ceramic method using prepared piezomagnetic and

piezoelectric phases. The fine powders of piezomagnetic ($\text{CoMnFe}_2\text{O}_4$) and piezoelectric phase (BaTiO_3) were mixed thoroughly in molar proportion and ground for above 3 hours. The composite phase of piezomagnetic and piezoelectric was pre-sintered at 925°C for 12 hours and is cooled at room temperature. The composite powder is then reground again and finally sintered at 1080°C for 24 hours. The magnetoelectric composites of piezomagnetic and piezoelectric prepared by mixing the constituent phase were ground for 2-3 hours and mixed with 2-3 drops of polyvinyl alcohol as a binder. The composite powder is then pressed into pellets of thickness around 2-3 mm and diameter 10mm using a hydraulic press. A pressure of 6 ton / cm^2 was applied for 10 to 15 minute. The pellets are finally heated up to 600°C for 6 hours to remove the binder and cooled at room temperature. The prepared composite of piezomagnetic $\text{Co}_{1.2}\text{Mn}_{0.2}\text{Fe}_{1.6}\text{O}_4$ and piezoelectric BaTiO_3 was characterized by X- ray diffraction technique and was used for further investigations of structural, magnetic properties of piezomagnetic, piezoelectric and their composites [8, 9].

2.2 Characterization

The presence of constituent phases in the composites as well as the crystal structure of constituent phases and their composites was determined by X-ray diffraction using a Rigaku Miniflux-II and $\lambda=1.5406\text{\AA}$.

3. RESULTS AND DISCUSSION

3.1. Structural analysis

The XRD pattern of the representative composite is shown in figure 1. The pattern reveals the presence of both ferroelectric as well as ferrite phases. All the peaks are indexed and no additional peaks were observed. This indicates the absence of impurities or intermediate phases in the composite. Ferroelectric phase has tetragonal perovskite structure and ferrite phase has a cubic spinel structure. The lattice parameters of ferroelectric phase are $a=4.001$ and $c=4.005$ and c/a ratio is 1.001 the lattice parameter for ferrite phase is $a=8.366\text{\AA}$. are given in Table 1. As all the peaks of the composites are identified it conforms the formation of composites with two distinct phases. Increased molar percentage of ferroelectric in composites leads to increase in the intensity of (110) ferroelectric peaks. From XRD pattern it observed that with increase in ferroelectric percent in composite, number of ferroelectric peaks increases also the intensity of most intense ferroelectric peak (110) also increases. The XRD pattern shows the presence of two phases i.e. piezomagnetic and piezoelectric, no single phase formation of composite material is observed, further it can be observed from figure that the intensity of all the reflections of piezomagnetic and piezoelectric phases decreases as compared to their individual phases [10, 11].

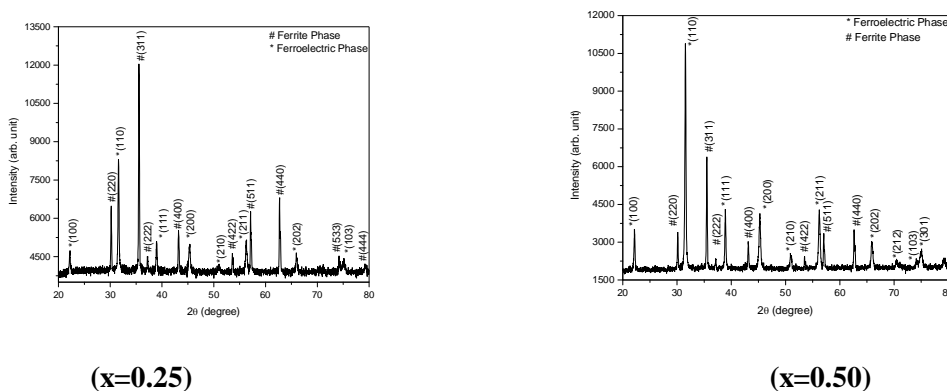


Fig-1: X-Ray Diffraction pattern of $(1-x) \text{Co}_{1.2}\text{Mn}_{0.2}\text{Fe}_{1.6}\text{O}_4 + (x) \text{BaTiO}_3$ composite

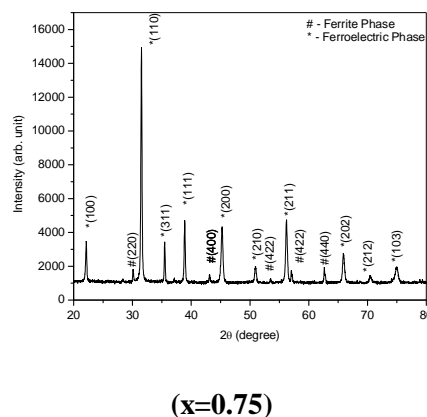


Fig-1: X-Ray Diffraction pattern of $(1-x) \text{Co}_{1.2}\text{Mn}_{0.2}\text{Fe}_{1.6}\text{O}_4 + (x) \text{BaTiO}_3$ composite

Table 1 contains the values of lattice constant for piezomagnetic phase and piezoelectric phase. It is evident from Table 1 that lattice constant of piezomagnetic phase increases from $x=0.00$ to $x=0.75$. The increase in lattice constant of the piezoelectric phase $x=0.25$ to $x=1.00$ found to increase marginally. The slight increase in lattice constant is attributed to increase in piezoelectric contents in the composite.

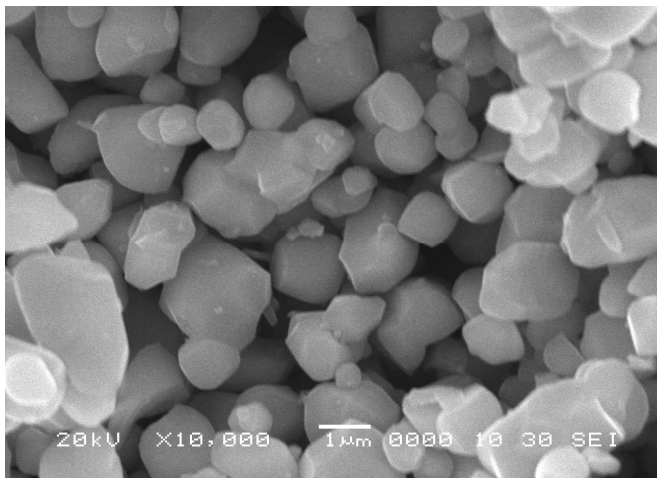
The values of average grain size are also given in Table 1 and found to increase with ferroelectric contents x . The grain size lies between 1.11 to $2.56\mu\text{m}$. The grain size of composites is found to increase with increasing ferroelectric content.

Comp 'x'	Lattice parameters (Å)				Particle size 't' (Å)		Average grain size(μm)
	Piezomagnetic		Piezoelectric		Piezomagnetic Phase	Piezoelectric Phase	
	a	a	c	c/a			
0.00	8.366	---	---	---	245	---	1.11
0.25	8.376	4.000	4.000	1.000	231	158	1.25
0.50	8.387	4.000	4.006	1.002	208	175	1.68
0.75	8.389	4.001	4.005	1.001	185	192	2.19
1.00	---	4.002	4.003	1.003	---	211	2.56

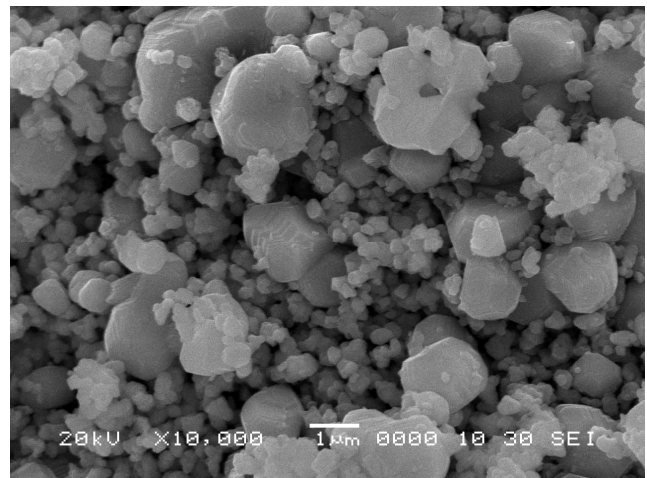
Table 1: Lattice constant of piezomagnetic, piezoelectric phase and Variation of average grain size and particle size of $(1-x)\text{Co}_{1.2}\text{Mn}_{0.2}\text{Fe}_{1.6}\text{O}_4 + (x)\text{BaTiO}_3$, ($x=0.00-1.00$) composite.

3.2 Scanning Electron Microscopy (SEM)

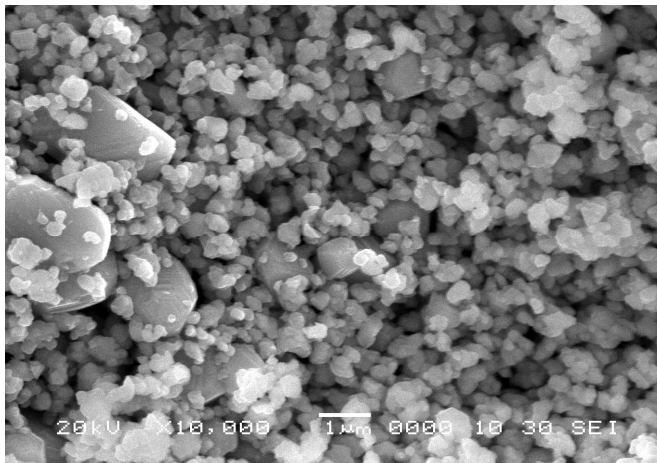
Fig.2 represents the scanning electron micro graphs of the ferrite, ferroelectric and their composites. The grain size of the ferrite, ferroelectric and their composites was also estimated from Scanning electron microscope technique (SEM)[12, 13]. The average grain size of pure piezoelectric phase is high as compared to pure piezomagnetic phase. In case of composites the grain size decreases as mole percentage of piezomagnetic phase increases.



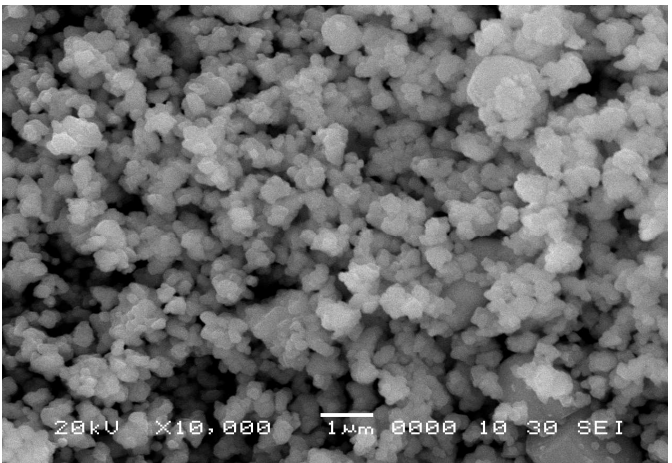
(X = 0.00)



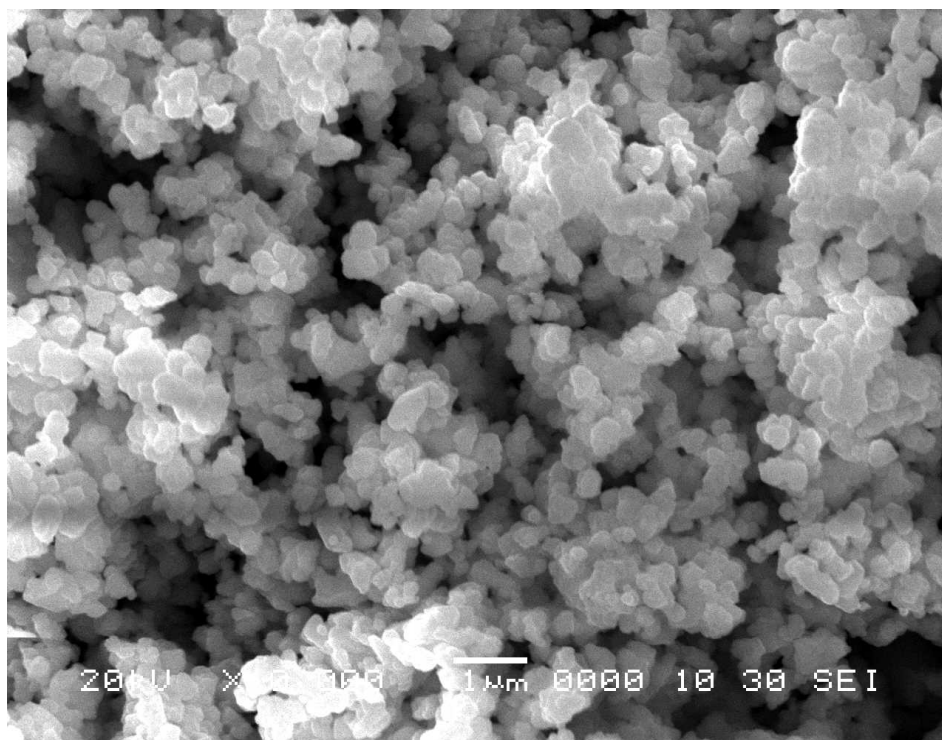
(X=0.25)



(X = 0.50)



(X = 0.75)



(X =1.00)

Fig-2: SEM micrograph of (1-x) $\text{Co}_{1.2}\text{Mn}_{0.2}\text{Fe}_{1.6}\text{O}_4$ + (x) BaTiO_3 . (X = 00 to 1.00)

4. MAGNETIC STUDIES

4.1 Magnetic Hysteresis

The magnetic properties of (1-x) $\text{Co}_{1.2}\text{Mn}_{0.2}\text{Fe}_{1.6}\text{O}_4$ + (x) BaTiO_3 composite materials were investigated using pulse field hysteresis loop technique. The hysteresis loop for all the samples of composite material under investigations are shown in Fig 3. It is seen that the hysteresis loops for the composites shift towards the field axis with decreasing piezomagnetic content. The saturation magnetization and magnetic moment of the composites increases with piezomagnetic content, however individual piezomagnetic grains acts as a centers of magnetization and the saturation magnetization of the composites is due to the vector sum of all these individual grains of piezomagnetic [14, 15]. The increase of magnetic contacts with piezomagnetic content results in the increase of net magnetization. Piezoelectric phase incorporated with the piezomagnetic phase acts as pores in the presence of applied magnetic field, which breaks the magnetic circuits resulting in the decrease of saturation magnetization with increasing piezoelectric content [16, 17].

The hysteresis loop for x= 0.00, 0.25, 0.50 and 0.75 at room temperature for x = 0.00 the saturation magnetization is 70.67 emu/gm and for x=0.25, 0.50 and 0.75 the values are 54.95 emu/gm, 35.59 emu/gm and 19.90emu/gm respectively. This indicates that the magnetic moment decreased with increasing ferroelectric content in the composite. It is clear from Fig 3that all the sample exhibit typical magnetic hysteresis of the magnetic materials, indicating that the composites are magnetically ordered.

The saturation magnetization of the composites decreases linearly with increasing ferroelectric BaTiO_3 content. This is because the ferroelectric phase incorporated with the ferrite phase acts as pores in the presence of applied magnetic field which breaks the magnetic circuits resulting in the decrease of saturation magnetization with increasing ferroelectric content. The decrease in saturation magnetization is due to non magnetic nature of BaTiO_3 . Similar behaviour of the saturation magnetization (M_s) with composition 'x' is reported in the literature [18, 19]. The remanent magnetization (M_r) values obtained from M-H plots shows decreasing nature with increase in ferroelectric content. For x = 1.0 (pure ferroelectric), the M-H plot is not seen.

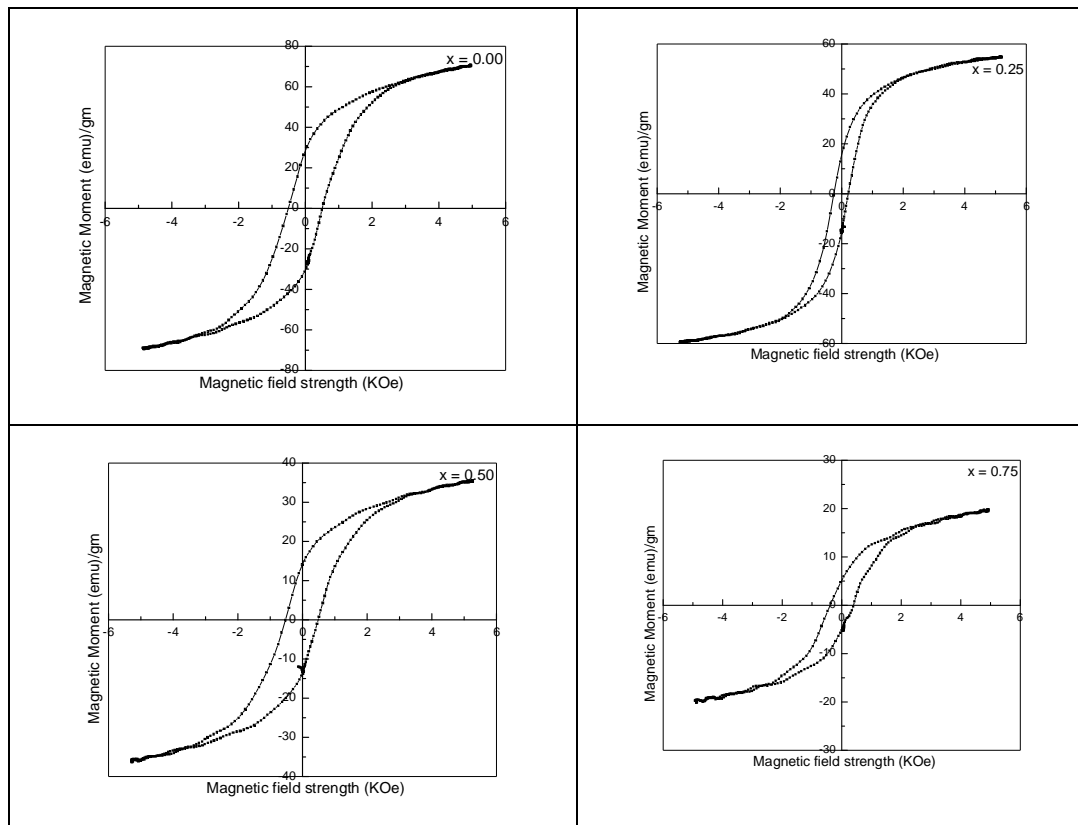


Fig-3: Hysteresis loop for $(1-x) \text{Co}_{1.2}\text{Mn}_{0.2}\text{Fe}_{1.6}\text{O}_4 + (x) \text{BaTiO}_3$. ($X = 0.00$ to $X=0.75$) Composite.

4.2 ME output

The magnetoelectric effect is characterized by a variation of the electrical magnetization by an external electrical field E . The ME effect is defined as an induced dielectric polarization of a material in an applied magnetic field or an induced magnetization in an external electric field. The composite, which exhibit ME effect are known as the “Magneto-electric composites”. Composite material containing piezoelectric and piezomagnetic phases exhibit ME effect. It is due to the strain induced in the piezomagnetic phase by the applied magnetic field, being mechanically coupled stress induced in the piezoelectric/ ferroelectric phase, the coupling resulting in an electric voltage.

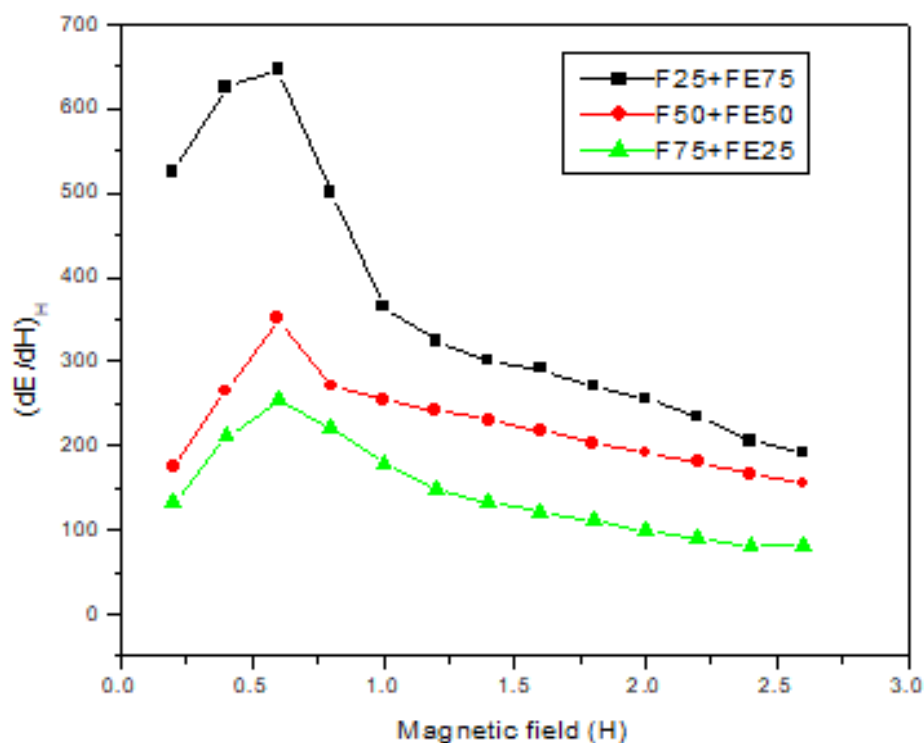


Fig-4: Variation of magneto-electric conversion factor with magnetic field for $(1-x) \text{Co}_{1.2}\text{Mn}_{0.2}\text{Fe}_{1.6}\text{O}_4 + (x) \text{BaTiO}_3$.

Fig. 4 shows the magnetoelectric effect voltage coefficient as a function of d. c. magnetic bias for all composites under investigation. The magnetoelectric (ME) effect is measured by changes in the resulting electric field in the magnetoelectric (ME) composites due to the applied external magnetic field. It is observed that magnetoelectric (ME) coefficient initially increases to a certain applied magnetic field (0.5KOe) and then start decreasing as applied field increases [20, 21].

The magnetoelectric (ME) effect is found to be maximum for $x=0.75$ (i.e. for 25% $\text{Co}_{1.2}\text{Mn}_{0.2}\text{Fe}_{1.6}\text{O}_4$ + 75% BaTiO_3). The magnetoelectric (ME) effect in composites is due to the strain induced in ferrite phase by the applied magnetic field which being mechanically coupled to induce a stress in surrounding ferroelectric phase.

4 CONCLUSIONS

The composites of ferrite and ferroelectric with formula $(1-x) \text{Co}_{1.2}\text{Mn}_{0.2}\text{Fe}_{1.6}\text{O}_4 + (x) \text{BaTiO}_3$ has been successfully synthesized by ceramic technique with the presence of two distinct phases of ferrite and ferroelectric as evidenced by the X ray diffraction techniques. The intensity of piezomagnetic peak increases with in piezomagnetic contents in the composite. The saturation magnetization, remanent magnetization, coercivity, Curie temperature of the composites decreases with decrease in ferrite content of the composites. The composite under investigation in the present study exhibits better values of magnetoelectric conversion factor. A large ME voltage coefficient of about $647 \text{ Vcm}^{-1}\text{Oe}^{-1}$ was observed for 25% $\text{CoMnFe}_2\text{O}_4$ + 75% BaTiO_3 composite

REFERENCES

1. R.S. Devan, B.K. Chougule, J. Appl. Phys, 101 (2007)014109.
2. J. V. Suchtelen, Philips Res. Rep. 27, 28 (1972)
3. J. Zhai, N. Cai, Z. Shi, Y. Lin, C. W. Nan, J. Phys. D., Appl. Phys. 37, 823 (2004)
4. J. V. Boomgaard, R. A. J. Born, J. Mater. Sci. 13, 1538 (1978)
5. G. A. Smolenski, I. E. Chupis, Sovt. Phys. Usp. 25, 475 (1989)
6. K. K. Patankar, P.D. Dombale, V.L. Mathe, S.A. Patil, R.N.Patil, Mater. Sci. and Engg. B 87, 53–58 (2001)
7. Y. Liou, J. Electroceram. 12, 187–190 (2004)
8. K. W. Wagner, Ann Phys 40 (1993) 818.
9. C. G. Koops, Phy. Rev 83 (1951) 121.
10. K. K. Pathankar, S. S. Joshi, B. K. Chougule, Phys Lett A 346 (2005)337.
11. J. Zhai, N. Cai, Z. Shi, Y. Lin, C. W. Nan, J. Phys. D: Appl Phys 37 (2004) 823.
12. S.A. Lokare, D. R. Patil, B. K. Chougule, J. of Alloys and Componds 453 (2008) 58.
13. S.L. Kadam, K.K. Patanakar, V.L. Mathe, M.B. Kothale, R.B. Kale, B.K. Chougule, Mater. Chem. Phys. 78, 684–690(2003)
14. S. S. Chougule and B. K. Chougule, Smart Mater. Struct 16 (2007) 493
15. Dandanwu, Weihua Gong, Haijin Deng and Ming Li., J. Phys. D. Appl. Phys 40 (2007) 5002.
16. K. K. Patankar, P. D. Dombale, V. L. Mathe and R. N. Patil, Mater. Sci. Engg. B87 (2001) 53'
17. Hongmei An, Paul J, M. C. Ginn, Appl. Cata. B: Env 62 (2006) 46
18. Giap V. Duonga, R. Groessingera and R. Sato Turtelli, J. Magn. Magn. Matter 310 (2007) 36.
19. Y. H. Tang, X. M. Chen, Y. J. Li, X. H. Zheng., Mater. Sci. Engg. B. 116 (2005) 150.
20. N. Ponpandian, P. Balaya and A. Narayanasamy. J. Phys. Cond. Mater 14 (2002) 3221.
21. G. Arlt and N. A. Perstev, J. App. Phys. 70 (1991) 2286.

ELECTRICAL AND ELECTROCHEMICAL PERFORMANCE OF (1-x)La_{0.8}Sr_{0.2}MnO₃: (x)Ce_{0.8}Gd_{0.2}O₂ COMPOSITE CATHODE FOR INTERMEDIATE TEMPERATURE SOLID OXIDE FUEL CELL APPLICATION

K. R. Nagde

Department of Physics, Government Vidarbha Institute of Science & Humanities Amravati

ABSTRACT

(1-x)La_{0.8}Sr_{0.2}MnO₃:(x)Ce_{0.8}Gd_{0.2}O₂ (x = 30, 40, 50 and 60 wt%) composite cathodes were investigated in order to enhance the electrochemical performance from intermediate temperature solid oxide fuel cell (IT-SOFC) application view point. Composite cathode showed decrease in electronic conductivity with increased Ce_{0.8}Gd_{0.2}O₂ content. The parameters of constant phase element (CPE) corresponding to electrode varied with decreased temperature. The sintering temperature of the cells was optimized to 1000 °C in terms of lowest area specific resistance (0.30 Ω cm² at 800 °C). The polarization resistance is minimum for 60La_{0.8}Sr_{0.2}MnO₃:40Ce_{0.8}Gd_{0.2}O₂ composite cathode.

Keywords: Solid oxide fuel cells, Composite cathode, Electrical conductivity, Electrochemical impedance spectroscopy, Area specific resistance (ASR), Symmetric cell.

1. INTRODUCTION

Solid oxide fuel cells, SOFCs, have been exhibiting two prominent advantages over the conventional power sources viz. high-energy efficiency and low emission level. Additionally, they have attracted a great deal of attention due to their operation in a two - phase (gas/solid) system. LaMO₃ based perovskites, where M represents transition metal elements, have been the typical functional ceramics useful for SOFC application. ABO₃ perovskite type structure permits the formation of vacancies on oxygen lattice site to a large extent, and most transition elements can take more than one valence states. The perovskite, therefore, exhibited oxygen non-stoichiometry depending on composition, temperature and oxygen partial pressure [1].

In near recent past, to improve the performance of cathode for intermediate-temperature solid oxide fuel cells (IT-SOFC) mixed ionic-electronic conductor as cathode has been proposed [1]. In this regard, a new structure has been proposed, in which the cathode comprised of two continuous parts. One part has been the framework made of the porous electrolyte. The other part consisted electronic-conducting particles embedded in the framework. The contact area between the electronically and ionically conductive phases, thus, increased significantly [2]. Concurrently, the use of the composite cathode has allowed spreading of the electrochemical reaction zone from the electrode/electrolyte interface into the electrode. The chemical reactivity between lanthanum strontium manganite, LSM, and yttria stabilized zirconia, YSZ, led to the formation of low conducting pyrochlore La₂ZrO₇ (LZO) phase in case of LSM-YSZ composite that prohibited its use in SOFC [3]. However, LSM is chemically stable at high temperature with gadolinia doped ceria (GDC) electrolyte [4]. Composite cathode have proven to exhibit high electrochemical performance and considered to be feasible for SOFC application.

Perry and Barnett prepared (1-x)La_{0.8}Sr_{0.2}MnO₃:(x)Ce_{0.8}Gd_{0.2}O₂ (x = 0 to 60 wt%) composite cathode system to measure the oxygen reaction kinetics. However, they have used La_{0.8}Sr_{0.2}MnO₃ and Ce_{0.8}Gd_{0.2}O₂ powders (Seattle Specialty Ceramics) having particle size 2.3 and 3 μm, respectively [5]. Also no DC conductivity is reported.

In the present study nano crystallite (425 nm) La_{0.8}Sr_{0.2}MnO₃ (LSM) was prepared using combustion technique, without using fuel and Ce_{0.8}Gd_{0.2}O₂ (GDC) nanopowder procured from Sigma Aldrich to see the effect of particle size on electrical and electrochemical performance of composite cathode. Various compositions belonging to the (1-x)LSM:(x)GDC composite system were prepared and subsequently characterized. The effect of the sintering temperature on the cell performance was also evaluated using electrochemical impedance spectroscopy.

2. EXPERIMENTAL

The La_{0.8}Sr_{0.2}MnO₃ was prepared using combustion synthesis as described elsewhere [6]. Nano powder of Ce_{0.8}Gd_{0.2}O₂ procured from Aldrich (USA) was used as an electrolyte. The La_{0.8}Sr_{0.2}MnO₃, electronic conductor used to obtain composite cathode was selected on the basis of lowest area specific resistance ASR observed in previous study [4]. The LSM and GDC in 70:30, 60:40, 50:50 and 40:60 weight ratios were taken to optimize the composition of composite. Each composite mixture mentioned above was ball milled at 300

revolution per minute, rpm, for 1 h under acetone using Pulversitte-6 planetary monomil (Fritsch, Germany). Finally, the pellets of well ground composite mixture were sintered at 1000 °C for 4 h.

The microstructures of sintered samples were examined with the help of scanning electron microscope, JEOL JSM-6380A. The thin platinum film on both the flat surfaces of sintered pellet was obtained by dc sputtering to ensure good ohmic contacts during dc electrical conductivity measurements. Prior to the conductivity measurement, the sample was heated to 800 °C for 1 h so as to homogenize the charge carriers. The resistance as a function of temperature, during the cooling cycle, was measured using four-probe method with the help of computer controlled Keithley 6221 current source and 2182A nanovoltmeter in delta mode. The temperature of the sample, during the conductivity measurement, was controlled with an accuracy of ± 1 °C with the help of Eurotherm 2216e temperature controller. The tip of a calibrated thermocouple was kept in the vicinity of the sample to measure the actual sample temperature.

For electrochemical investigations, initially the slurry / ink of each cathode composition was obtained as follows. Specifically, 1g batch of composite cathode mixture as described above was mixed with polyvinyl buteral binder, sodium free corn oil and methyl ethyl ketone and ball milled for 5 h at 300 rpm. On the other hand, GDC nano-powder as procured was fired at 800 °C for 2 h. Subsequently, GDC electrolyte was obtained in the form of a circular disc (pellet) of 9 and 1 - 2 mm diameter and thickness, respectively. Later, they were sintered at 1400 °C for 6 h. The density of GDC pellet was about 96% of the theoretical value. Both the flat surfaces of the disc were then roughened with # 60 grid paper and cleaned with an acetone. The slurry / ink of cathode material was then spin coated on both the flat surfaces of sintered GDC electrolyte at 3000 rpm for 60 s so as to obtain the symmetric cell of configuration given below: composite cathode / GDC / composite cathode

The symmetric cells were initially baked at 600 °C for 2 h so as to burn out the organic binders, and then finally sintered at 800, 1000 and 1200 °C for 2 h so as to optimize the sintering temperature. The details of symmetric cells are summarized in Table 1.

Table-1: Details of composition of composite cathode, cell sintering temperature (t_s), cell abbreviation and activation energies of symmetric cells.

LSM: GDC (wt %)	t_s (°C)	Cell abbreviation	E_a (eV)	E_a' (eV)
70:30	1000	Cell 73-10	1.670	1.601
60:40	1000	Cell 64-10	1.092	1.121
50:50	1000	Cell 55-10	1.960	1.955
40:60	1000	Cell 46-10	1.362	1.321
60:40	800	Cell 64- 8	1.671	1.701
60:40	1200	Cell 64-12	1.616	1.597

t_s - Sintering temperature.

E_a - Activation energy determined from temperature dependent conductivity plots.

E_a' - Activation energy determined from peak frequency temperature dependent plots

Experimental procedure adopted for electrochemical impedance spectroscopy as a function of temperature and oxygen partial pressure on composite cathode was similar to that described elsewhere [7].

3. RESULTS AND DISCUSSION

3.1. Scanning electron microscopy

The SEM photographs of cathode surface of Cell 64-8, Cell 64-10 and Cell 64-12 are shown in Figs. 1 (a), (b) and (c), respectively. A close look at the Fig. 1 (a) revealed the agglomeration of nano-sized grains with a large number of nano pores. The cells sintered at 1000 °C resulted in increased grain size with adequate porosity (Fig. 1 (b)). Evidently, a considerable grain growth took place when the cell was sintered at 1200 °C. The grain growth considerably reduced agglomeration thereby less pores (Fig. 1 (c)). Fig. 1 (d) revealed intimate contact between cathode and electrolyte. Moreover, the electrode / electrolyte interface was found to be homogeneous. Despite thermal cycles at 800 °C neither cracks nor separations between the electrode and electrolyte was found at the interface. The electrode layer thickness was approximately 17.1 μm .

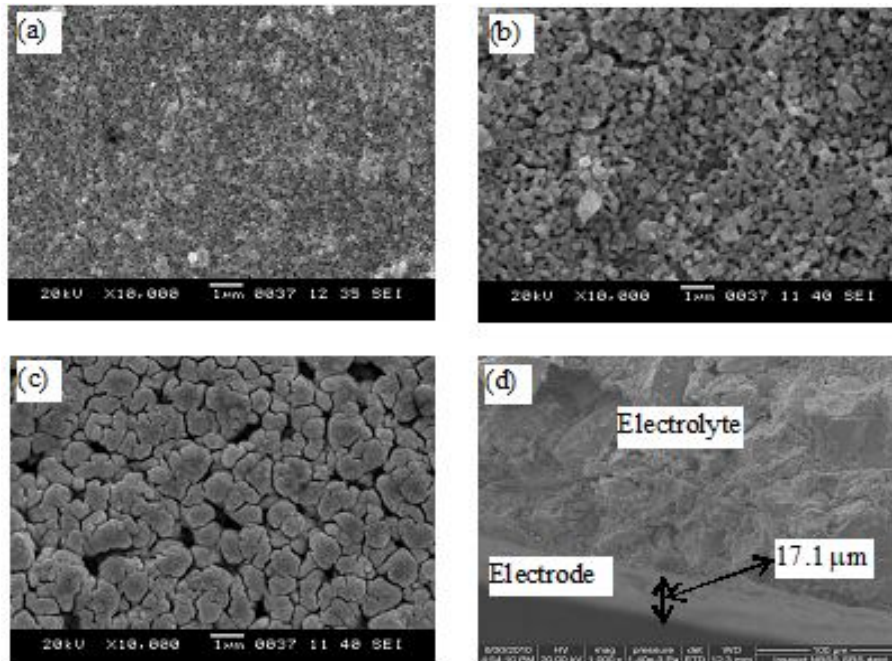


Fig-1: Scanning electron microphotographs of cathode surface of (a) Cell 64-8 (b) Cell 64-10 and (c) Cell 64-12 and (d) fractured electrode / electrolyte interface of Cell 64-10.

3.2. DC conductivity

The variation of DC conductivity with temperature for all the composites (70:30, 60:40, 50:50 and 40: 60 wt%) under study is depicted in Fig. 2. As seen, the electronic conductivity, in general, of all composites obeyed Arrhenius law described in eq. (A.1). A close scrutiny of the Fig. 2 revealed lower electronic DC conductivity in case of composites compared to that of in pure LSM. The decreased electronic dc conductivity of composites was due to an addition of electronically insulating GDC into them. The addition of such electronically insulating phase reduced considerably the electron-conducting parallel paths in the sample thereby the conductivity [8]. Nevertheless, all composites exhibited requisite electronic conductivity from cathode viewpoint due to a large number of parallel electronically conducting paths. The semiconductor to pseudo-metal phase transition at about 680 °C observed in all the composites was due to presence of LSM.

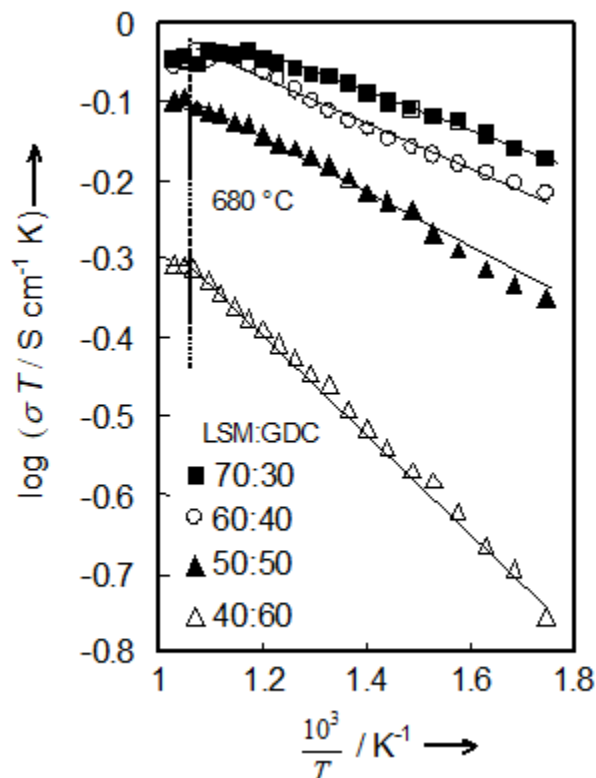


Fig-2: Arrhenius plots of $\log(\sigma T / S \text{ cm}^{-1} \text{ K})$ versus $10^3/T / \text{K}^{-1}$ for (1-x) LSM: (x) GDC ($x=30$ to 60 wt%) composite system sintered at 1000 °C for 4 h.

3.3. Electrochemical impedance spectroscopy

Typical complex impedance plots for Cell 64-10 at different temperatures are depicted in Fig. 3 (a) and (b). In general, the convoluted impedance spectra are observed. The impedance spectra were analyzed using computer programme revealed two overlapped semicircular distorted arcs in the low frequency region. The presence of two semicircular arcs (dotted curves in the low and the mid frequency regimes) suggested at least two different electrode processes that limited the oxygen reduction reaction. The low and mid frequency arcs were due to oxygen ion diffusion and charge transfer process, respectively. Similar interpretation was done by Suzuki et al [9]. The absence of semicircular arc in the high - frequency region was attributed to the limitations of high frequency of FRA 1255B ($\leq 1\text{MHz}$). Similar behavior was observed for Cell 73-10, Cell 55-10 and Cell 46-10. The activation energy $E_a = 0.91 \pm 0.003$ eV determined from the Arrhenius plot ($\log \sigma T$ Vs $10^3/T$) due to bulk electrolyte (R_b) estimated from high frequency domain, is in good agreement with the value for GDC electrolyte reported earlier [10, 11]. The real axis intercepts of all semicircular arcs, as expected, increased with decreased temperature; indicated increased ASR as well as bulk electrolyte resistance. Hence, observed semicircular arc at low frequency domain was not due to the GDC electrolyte but correspond to electrode.

The simulated curve (dotted line shown in Fig. 3 (b)) obtained from the electrical equivalent model, depicted in insert of Fig. 3 (b), fitted well with the experimental data (solid circular points).

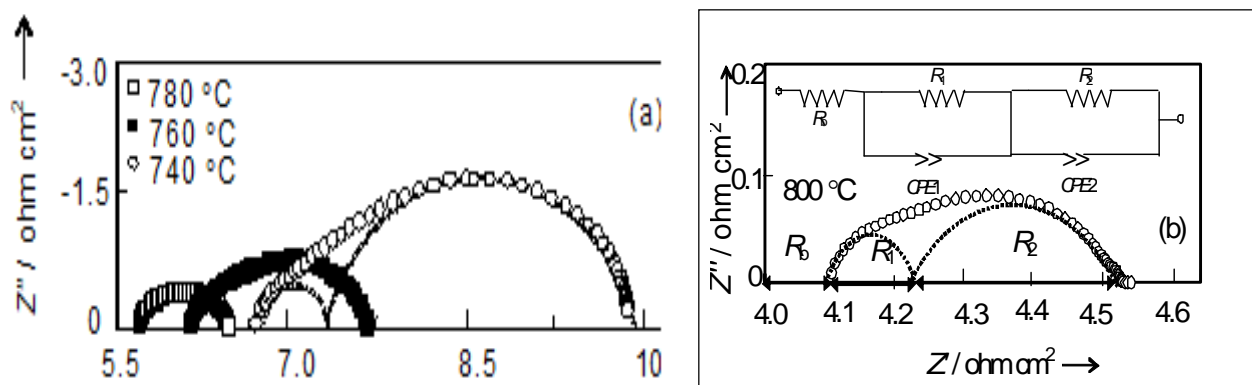


Fig-3: Complex impedance plots of Cell 64-10(a) at different temperatures and (b) at 800 °C.

Constant phase element (CPE) in circuit takes care of depression in the semicircular arc due to the distributed relaxation time. The R_b was the bulk resistance due to GDC electrolyte. The R_2 and R_1 were the resistances corresponding to low- and -mid-frequency semicircles, respectively. The values of the simulated circuit elements at various temperatures are displayed in Table 2.

Table-2: The values of fitted circuit elements corresponding to electrochemical impedance spectra of Cell 64 -10 at various temperatures.

Sr#	T (°C)	R_b (Ω)	CPE1 -T	CPE1 -P	R_1 (Ω)	CPE2-T	CPE2 -P	R_2 (Ω)
1	800	9.27	9.770E-5	1.0	0.373	0.224	0.66	1.375
2	780	10.84	4.130 E-5	0.85	0.969	0.178	0.77	1.517
3	760	12.33	4.933 E-5	0.87	1.41	0.162	0.75	3.503
4	740	14.04	4.068 E-4	0.68	3.765	0.133	0.82	7.148
5	720	16.19	1.091 E-4	0.74	5.268	0.108	0.79	18.79

Evidently, the parameters ($CPE-T$ and $CPE-P$) of $CPE1$ as well as $CPE2$ varied with decreased in temperature, such behavior indicated thermally activated electrode process.

Plots of \log (ASR) against $10^3/T$ for Cell 64-8, Cell 64-10 and Cell 64-12 sintered at 800, 1000 and 1200 °C are displayed in Fig. 4. The ASR, in general, obeyed the Arrhenius law. The activation energies for all cells determined from temperature dependent ASR plots are compared in Table 1. A close scrutiny of the insert of Fig. 4 revealed relatively higher ASR for the cell sintered at 800 °C. The ASR reduced on sintering the cell at 1000 °C, which was attributed to the improved contact between LSM and GDC grains of composite cathode (Fig. 1 (b)). When the sintering temperature increased to 1200 °C, however, the ASR increased (Fig. 4). Here, GDC as well as LSM grains grew further ((Fig. 1 (c)) after sintering. The grain growth decreased the cathode porosity (Fig. 1(C)), and eventually reduced the triple phase boundary, TPB, or electrochemical reaction sites whereby ASR. Since, the cell sintered at 1000 °C offered lowest ASR as well as activation energy (Table 1); all other cells under study were sintered at this (1000 °C) temperature for further study.

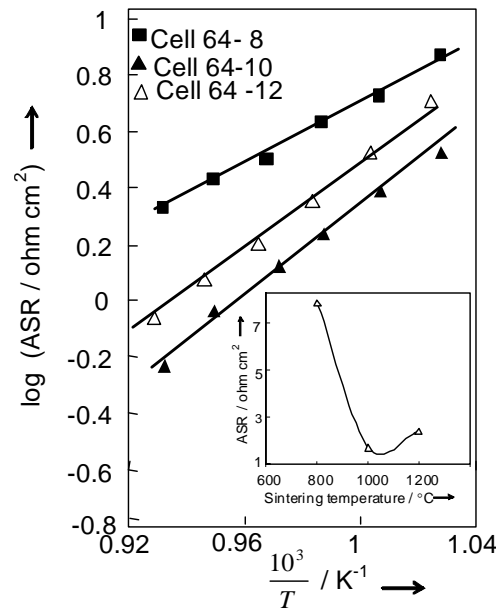


Fig-4: Variation of log (ASR) with temperature for Cell 64-8, Cell 64-10 and Cell 64-12; insert shows

The variation of peak frequency (f_p) corresponding to the low frequency semicircle in complex impedance plane with temperature, depicted in Fig. 5, suggested Arrhenius like behavior. The activation energy (E_a) determined using Eq. (A.2). A comparison of activation energies determined using eq. (A.2) and from temperature dependent ASR (Table 1) revealed close matching. These results suggested hopping mechanism of the charge transport via oxy ion diffusion within the electrode as well as across the electrode- electrolyte interface. Similar results have also been reported in literature [7].

Plots of log (ASR) against $10^3/T$ for cells having different cathode compositions and sintered at 1000 °C for 2 h are displayed in Fig. 6. Evidently, amongst all the cells, Cell 64-10 exhibited lowest ASR as well as activation energy (Table 1). The variation of ASR for cell with GDC content in composite cathode, depicted in insert of Fig. 6, suggested lowest ASR for cell having 60LSM:40GDC cathode. The initial decrease in ASR with GDC content was due to increased TPB. The increased ASR with GDC content beyond 40 wt% was attributed to the decreased continuity of the LSM phase in the composite, thereby, decreased electronic conductivity. Lowest ASR for 60LSM:40GDC composite cathode was due to maximum TPB resulting from optimum dispersion of GDC in LSM. In fact, the high ionic conductivity of electrolyte reduced the cathodic polarization resistance in composite cathode. The reduction in the cathode polarization resistance due to an addition of high ionically conducting electrolyte in composite has also been reported in literature [12, 13]. The 60LSM :40GDC composite cathode, cell sintered at 1000 °C for 2 h, selected on the basis of lowest ASR for further study.

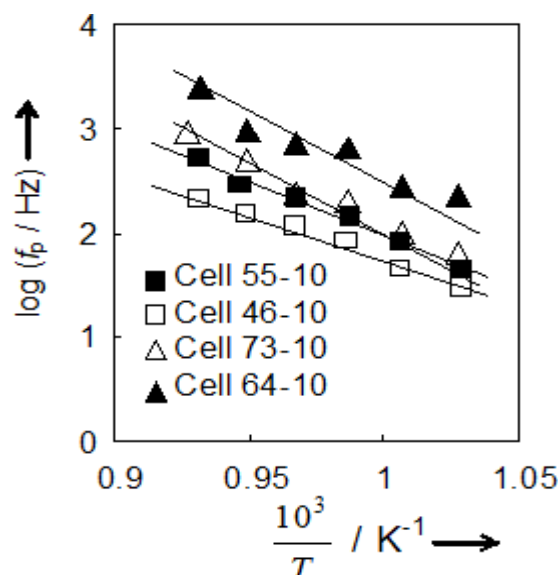


Fig-5: Variation of log (f_p) with $10^3/T$, corresponding to low frequency semicircular arcs (cathode), for cells with different cathode compositions.

The electrochemical impedance plots at 800 °C for different oxygen partial pressures (P_{O_2}) around optimized Cell 64-10 are depicted in Fig. 7. In general, x -axis intercept of low frequency semicircular arc increased with decrease in P_{O_2} . On the other hand, the electrolytic bulk resistance / conductivity was least affected in spite of variation in P_{O_2} . Similar behavior was observed for Cell 64-10 at 700 °C. The variation of $\log (ASR)$ at 700 and 800 °C with $\log (P_{O_2})$ shown in insert of Fig.7 suggested a linear dependence of the former on the latter. In other words, the ASR varies with the oxygen partial pressure according to the eq. (A.3)

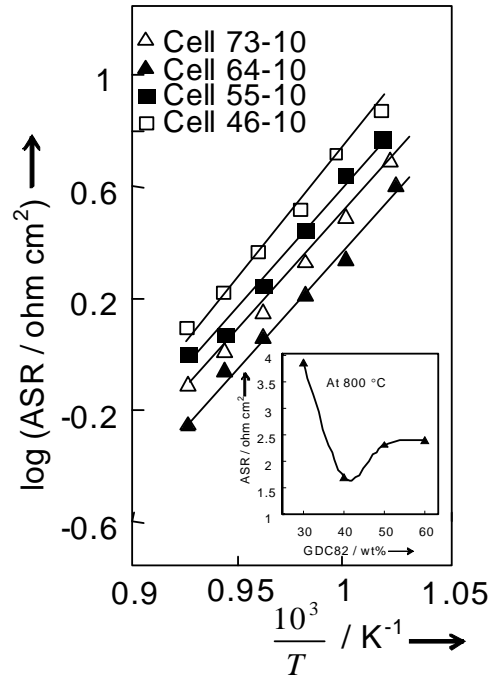


Fig-6: Variation of $\log (ASR)$ with $10^3 / T$ for cells with different composite cathode and sintered at 1000 °C for 2 h; insert shows effect of GDC content in composite on ASR at 800 °C.

The value of n is useful to understand the type of species and electrochemical reactions involved in electrode reactions [13].

The $n = 0.20$, $n = 0.18$ at 700 and 800 °C, respectively (estimated from insert of Fig. 7) indicated adsorption of oxygen in oxide lattice. The oxygen, thus adsorbed, resulted into the change in concentration of electron and vacancy for oxygen according to eq. (A.6). The changed concentration of such created defects in the oxide lattice with increased P_{O_2} reduced the ASR.

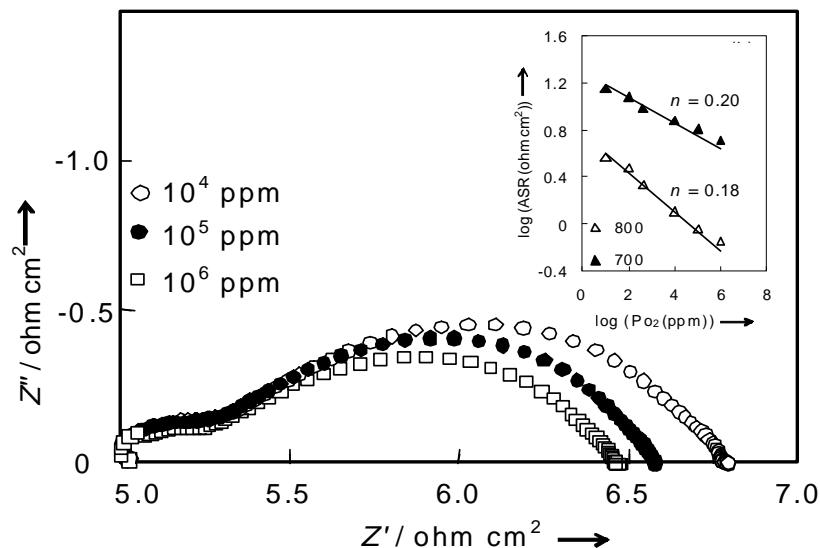


Fig-7: Complex impedance plots at different oxygen partial pressures for Cell 64-10 at 800 °C and insert shows variation of ASR with oxygen partial pressure at 700 and 800 °C.

CONCLUSIONS

The cellsintering temperature was optimizedto 1000 °C to obtained smaller grain with adequate porosity. Electrode polarization decreased considerably due to addition of oxy-ion conducting second phase in LSM. Amongst all composite cathodes60LSM:40GDC gave lowest ASR ($0.30\Omega\text{ cm}^2$) with minimum activation enthalpy (1.092eV). Impedance analysis and oxygen partial pressure dependence study indicated charge transport process as the rate limiting step for the oxygen reduction. The charge transport process within the electrode and across the electrode-electrolyte interface was via charge hopping mechanism.

ACKNOWLEDGEMENTS

Ms. K. R. Nagde is thankful to MSRL lab, Department of Physics, RTMNU for research facility.

APPENDIX A

$$\sigma T = (\sigma T)_0 \exp\left(\frac{-E_a}{kT}\right) \quad (\text{A.1})$$

Where, E_a is the activation energy and k is Boltzmann constant.

$$f_p = f_0 \exp\left(\frac{-E_a}{kT}\right) \quad (\text{A.2})$$

Here, f_p and f_0 are jump and attempt frequencies, respectively.

$$\text{ASR} = \text{ASR}_0 (P_{\text{O}_2})^{-n} \quad (\text{A.3})$$

$$n = 1, \quad \text{O}_2(\text{g}) \rightleftharpoons \text{O}_{2,\text{ads}} \quad (\text{A.4})$$

$$n = 0.5, \quad \text{O}_{2,\text{ads}} \rightleftharpoons 2\text{O}_{\text{ads}} \quad (\text{A.5})$$

$$n = 0.25, \quad \text{O}_{\text{ads}} + 2e' + V_{\text{O}}^{\bullet\bullet} \rightleftharpoons \text{O}_{\text{O}}^{\times} \quad (\text{A.6})$$

$$n = 0, \quad \text{O}_{\text{TPB}}^{2-} + V_{\text{O}}^{\bullet\bullet} \rightleftharpoons \text{O}_{\text{O}}^{\times} \quad (\text{A.7})$$

REFERENCES

- NieH, WenT, WangS, WangY, GuthU, VashookV. Preparation, thermal expansion, chemical compatibility, electrical conductivity and polarization of $\text{A}_{2-\alpha}\text{A}'_{\alpha}\text{MO}_4$ ($\text{A} = \text{Pr, Sm}$; $\text{A}' = \text{Sr}$; $\text{M} = \text{Mn, Ni}$; $\alpha = 0.3, 0.6$) as a new cathode for SOFC. Solid State Ionics 2006; 117(19-25):1929-1932.
- AdlerSB. Factors governing oxygen reduction in solid oxide fuel cell cathodes. Chem Rev 2004; 104:4791-4843.
- ChervinC, GlassRS, KauzlarichSM. Chemical degradation of $\text{La}_{1-x}\text{Sr}_x\text{MnO}_3/\text{Y}_2\text{O}_3$ -stabilized ZrO_2 composite cathodes in the presence of current collector pastes. Solid State Ionics 2005; 176(1-2):17-23.
- NagdeKR, BhogaSS. Effect of preparative methods on electrical and electrochemical performance of lanthanum strontium manganite. J Solid State Electrochem 2011; 16:1605-1613.
- MurrayEP, BarnettSA. $(\text{La, Sr})\text{MnO}_3-(\text{Ce, Gd})\text{O}_{2-x}$ composite cathodes for solid oxide fuel cells. Solid State Ionics 2001; 143(3-4):265-273.
- NagdeKR, BhogaSS. Effect of Sr content on structure and electrical properties of $\text{La}_{1-x}\text{Sr}_x\text{MnO}_3$ from IT-SOFC cathode view point. Ionics 2009; 15:571-578.
- Khandale, Bhoga. Combustion synthesized $\text{Nd}_{2-x}\text{Ce}_x\text{CuO}_4$ ($x = 0-0.25$) cathode materials for intermediate temperature solid oxide fuel cell applications. J Power Sources 2010; 195:7974-7982.
- LiQ, FanY, ZhaoH, SunLP, HuoLH. Preparation and electrochemical properties of a $\text{Sm}_{2-x}\text{Sr}_x\text{NiO}_4$ cathode for an IT-SOFC. J Power Sources 2007; 167(1):64-68.
- SuzukiT, AwanoM, JasinskiP, PetrovskyV, AndersonH. Composite $(\text{La, Sr})\text{MnO}_3$ -YSZ cathode for SOFC. Solid State Ionics 2006; 177(19-25):2071-2074.
- KhandaleAP, BhogaSS. Electrochemical performance of a mechanochemically prepared submicron-sized crystalline $\text{Nd}_{1.8}\text{Ce}_{0.2}\text{CuO}_{4\pm 1}$ cathode for intermediate temperature solid oxide fuel cells. Electrochimica Acta 2011; 56:9219-9223.
- SinghK, AcharyaSA, BhogaSS. Nanosized ceria-based ceramics: Ionics 2006; 12(4-5):295-301.

-
12. LiJ, WangS, WangZ, LiuR, WenT, WenZ. $(\text{La}_{0.74}\text{Bi}_{0.10}\text{Sr}_{0.16})\text{MnO}_{3-\delta}-(\text{Bi}_2\text{O}_3)_{0.7}(\text{Er}_2\text{O}_3)_{0.3}$ composite cathodes for intermediate temperature solid oxide fuel cells J Power Sources 2008;179:474-480.
 13. PingS, QiangL, HuaH, HuiZ, YingZ, NanL, ViricelleJ, PijolatC. Synthesis and performance of $\text{Sr}_{1.5}\text{La}_x\text{MnO}_4$ as cathode materials for intermediate temperature solid oxide fuel cell. J Power Sources 2011; 196(14):5835-5839.

M-POLYNOMIALS, ECCENTRICITY AND DEGREE-BASED TOPOLOGICAL INDICES OF CHALCONE

N. K. Raut¹ and S. N. Ipper²Department of Physics¹, Sunderrao Solanke Mahavidyalaya Majalgaon, District Beed
Department of Chemistry², Sunderrao Solanke Mahavidyalaya Majalgaon, District Beed

ABSTRACT

Chalcones are a class of α, β unsaturated carbonyl compounds that form the central core for a variety of naturally occurring biologically active compounds. They exhibit tremendous potential to act as a pharmacological agent. A molecular graph is constructed by representing each atom of a molecule by a vertex and bonds between atoms by edges. The M-polynomial of G is introduced with $M(G; x, y) = \sum_{i \leq j} m_{ij}(G) x^i y^j$, Where $m_{ij}(G)$, ($i, j \geq 1$) be the number of edges $e = uv$ of G such that $(d_u, d_v) = (i, j)$. In this paper M-polynomials, degree-based Zagreb indices, new versions of Zagreb indices and redefined Zagreb indices of chalcone are investigated.

Keywords: Chalcone, molecular graph, M-polynomial, topological index, redefined Zagreb index, Zagreb index,.

1. INTRODUCTION

Let G be a connected graph with vertex set $V(G)$ and edge set $E(G)$. The edge connecting the vertices u and v will be denoted by uv. The degree of a vertex u belong to $E(G)$ is denoted by d_u and is the number of vertices that are adjacent to u [1]. A topological index is a numerical value associated with the chemical constitution of a certain chemical compound aiming to correlate various physical and chemical properties or some biological activity in it [2]. The degree-based topological indices in the form of function $f(x, y)$ are defined by Gutman [3]. The M-polynomials, degree-based polynomials and topological indices of different molecular graphs are studied by [4-14]. Some degree-based topological indices and polynomials of silicate and oxide networks are studied by [15].

Chalcones are group of compounds with two aromatic rings connected by a keto-vinyl chain, constitute an important class of naturally occurring flavonoids exhibiting a wide spectrum of biological activities [16-17]. Chalcones are a class of α, β unsaturated carbonyl compounds that form the central core for a variety of naturally occurring biologically active compounds. They exhibit tremendous potential to act as a pharmacological agent [18]. Chalcones, either natural or synthetic, are known to exhibit various biological activities, such as antioxidant, antiinflammatory, antimalarial, antileishmanial, anticancer and antitumor [19]. The degree-based topological indices, first Zagreb (M_1), second Zagreb (M_2), second modified Zagreb (mM_2), general Randić' (R_α), reciprocal general Randić' (RR_α) and symmetric division deg (SDD) indices are computed from the M-polynomials. In addition, the Harmonic index (H), inverse sum index (IS) and the augmented Zagreb index (AZI) for different molecular graphs are also studied.

The formulas of standard degree-based topological indices are defined in the literature. The new versions of Zagreb indices are defined in [20-22] and are given table (1). The redefined first, second and third Zagreb indices are defined by [23]. The eccentricities of vertices of simple graph are represented in figure (1) [24]. The notations used in this paper are standard and mainly taken from [25-29]. In this paper M-polynomials, degree-based Zagreb indices ($M_1(G)$, $M_2(G)$, ${}^mM_2(G)$), new versions of Zagreb indices ($M_2^*(G)$,

$M_1^*(G)$, $M_1^{**}(G)$) and redefined Zagreb indices ($ReZG_1(G)$, $ReZG_2(G)$) of chalcone are investigated. The first and second Zagreb indices are defined as:

$M_1(G) = \sum_{uv \in E(G)} (d_u + d_v)$ and $M_2(G) = \sum_{uv \in E(G)} (d_u d_v)$ respectively. The second modified Zagreb index is defined as: ${}^mM_2(G) = \sum_{uv \in E(G)} \frac{1}{d_u d_v}$.

The eccentricity of a vertex v in a graph G, denoted $ecc(u)$, is the distance from u to a vertex farthest from u that is $ecc(u) = \varepsilon(u) = \max\{d(x, u) \mid x \in V(G)\}$, The eccentricity of all the vertices of simple connected graph with $n = 5$ can be seen from figure (1) as:

$$\varepsilon[1] = [2]; \varepsilon[2] = [2]; \varepsilon[3] = [3]; \varepsilon[4] = [2]; \varepsilon[5] = [3].$$

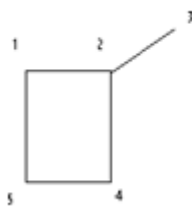
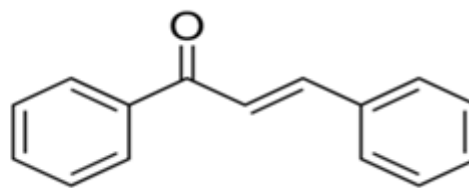


Fig-1: Molecular graph with $n = 5$ and Fig-2: Molecular graph of chalcone.



2. EXPERIMENTAL PROCEDURE

A molecular graph is constructed by representing each atom of a molecule by a vertex and bonds between atoms by edges. Molecular graphs are hydrogen suppressed graphs i.e. vertices of the graph correspond to non-hydrogen atoms [30-31]. The degree-based topological indices $D=D(G) = \sum_{u,v} F(d_u, d_v)$, where summation goes over all pairs adjacent vertices u, v of the molecular graph G and d_u denotes the degree of vertex u is the number of edges that are incident to u . The notation in the form of function $f(x, y)$ for degree-based topological indices is used by [32] to discuss special cases as:

$$(1) f(x, y) = \frac{1}{\sqrt{xy}}, \text{ for the Randic index.}$$

$$(2) f(x, y) = x + y, \text{ for the first Zagreb index, etc.}$$

The function $f(x, y)$ for $M_1^{**}(G)$ can be expressed as [33]:

$$\text{The alternative form of } M_1(G) = M_1(G) \sum_{e=uv \in E(G)} (d_u + d_v) \text{ is } M_1(G) = \sum_{v \in V(G)} d_v^2, \\ \text{Likewise } M_1^{**}(G) \text{ can be defined as:}$$

$$M_1^{**}(G) = \sum_{v \in V(G)} \epsilon_v(G)^2 = \sum_{e=uv \in E(G)} (\epsilon_G(u) + \epsilon_G(v)) \text{ and so } f(x, y) = \epsilon_G(u) + \epsilon_G(v).$$

The M-polynomial of G is introduced with

$$M(G; x, y) = \sum_{i \leq j} m_{ij}(G) x^i y^j$$

Where $m_{ij}(G)$, $(i, j \geq 1)$ be the number of edges $e=uv$ of G such that $(d_u, d_v) = (i, j)$.

Redefined first and second Zagreb indices are defined as:

$$\text{ReZG}_1(G) = \sum_{uv \in E(G)} \frac{d_u + d_v}{d_u d_v} \text{ and}$$

$$\text{ReZG}_2(G) = \sum_{uv \in E(G)} \frac{d_u d_v}{d_u + d_v}.$$

The new versions of Zagreb indices are defined as:

$$M_2^*(G) = \sum_{uv \in E(G)} [\epsilon_G(u) \epsilon_G(v)],$$

$$M_1^*(G) = \sum_{uv \in E(G)} [\epsilon_G(u) + \epsilon_G(v)] \text{ and}$$

$$M_1^{**}(G) = \sum_{v \in V(G)} \epsilon_G(v)^2.$$

3. RESULTS AND DISCUSSION

It is possible to use molecular graphs to construct descriptors of molecular shape and size that correlate to properties of substances. The hydrogen suppressed molecular graph of chalcone is shown in figure (2). The degree-based topological indices such as $M_1(G)$, $M_2(G)$, $^m M_2(G)$, $R_\alpha(G)$, $R_\alpha(G)$, $SDD(G)$, $IS(G)$, $AZI(G)$ are discussed in the literature. It can be observed from molecular graph of chalcone figure (2), there are 18 vertices and 17 edges. Let $G = (V, E)$ be a graph with V vertices and E edges. The distance $d(u, v)$ between two nodes u and v is the length of the shortest path between them [32]. The eccentricity $\epsilon(u)$ of a graph vertex u in connected graph G is the maximum distance between u and any other vertex v of G i.e. $\max\{d(x, u) \mid x \in V(G)\}$. Redefined Zagreb indices $\text{ReZG}_1(G)$ and $\text{ReZG}_2(G)$ are degree-based topological indices. The new versions of Zagreb indices, third Zagreb eccentric index ($M_2^*(G)$), first Zagreb eccentric index ($M_1^*(G)$), second Zagreb eccentric index

($M_1^{**}(G)$) are eccentricity-based topological indices. The eccentricity of all the vertices of simple connected graph with $n = 5$ can be seen from figure (1) as:

$$\varepsilon[1] = [2]; \varepsilon[2] = [2]; \varepsilon[3] = [3]; \varepsilon[4] = [2]; \varepsilon[5] = [3].$$

3.1 M-polynomial

In this section we compute Zagreb indices for chalcone. The M-polynomial of G is introduced with $M(G; x, y) = \sum_{i \leq j} m_{ij}(G) x^i y^j$ where $m_{ij}(G)$, $(i, j \geq 1)$ be the number of edges $e = uv$ of G such that $(d_u, d_v) = (i, j)$. It can be observed from figure (2) that there are four types of edge partitions as: $E_{(2,2)}$, $E_{(2,3)}$, $E_{(2,4)}$, and $E_{(3,4)}$.

The M-polynomial of the chalcone is

$$\begin{aligned} M(G; x, y) &= \sum_{i \leq j} m_{ij}(G) x^i y^j \\ &= \sum_{i=j=2} m_{22}(G) x^2 y^2 + \sum_{2 \leq 3} m_{23}(G) x^2 y^3 + \sum_{2 \leq 4} m_{24}(G) x^2 y^4 + \sum_{3 \leq 4} m_{34}(G) x^3 y^4. \\ &= \sum_{uv \in E_{(2,2)}} m_{22}(G) x^2 y^2 + \sum_{uv \in E_{(2,3)}} m_{23}(G) x^2 y^3 + \sum_{uv \in E_{(2,4)}} m_{24}(G) x^2 y^4 + \sum_{uv \in E_{(3,4)}} m_{34}(G) x^3 y^4. \\ &= |E_{(2,2)}| x^2 y^2 + |E_{(2,3)}| x^2 y^3 + |E_{(2,4)}| x^2 y^4 + |E_{(3,4)}| x^3 y^4. \end{aligned}$$

Now, from M-polynomial equation we compute the D_x , D_y , J , S_x and S_y :

$$\begin{aligned} M(G; x, y) &= 9x^2 y^2 + 5x^2 y^3 + 2x^2 y^4 + x^3 y^4 \\ D_x &= 18x^2 y^2 + 10x^2 y^3 + 4x^2 y^4 + 3x^3 y^4 \\ D_y &= 18x^2 y^2 + 15x^2 y^3 + 8x^2 y^4 + 4x^3 y^4 \\ D_y D_x &= 36x^2 y^2 + 30x^2 y^3 + 16x^2 y^4 + 12x^3 y^4 \\ S_y &= \frac{9}{2} x^2 y^2 + \frac{5}{3} x^2 y^3 + \frac{1}{2} x^2 y^4 + \frac{1}{4} x^3 y^4. \\ S_x &= \frac{9}{2} x^2 y^2 + \frac{5}{2} x^2 y^3 + x^2 y^4 + \frac{1}{3} x^3 y^4 \\ J &= 9x^4 + 5x^5 + 2x^6 + x^7. \\ S_x J &= \frac{9}{4} x^4 + x^5 + \frac{1}{3} x^6 + \frac{1}{7} x^7. \\ S_x S_y &= \frac{9}{4} x^2 y^2 + \frac{5}{6} x^2 y^3 + \frac{1}{4} x^2 y^4 + \frac{1}{12} x^3 y^4. \end{aligned}$$

The first Zagreb, second Zagreb and second modified Zagreb indices are computed as:

3.2 First Zagreb index

First Zagreb index: $f(x, y) = (x + y)$, As $D_x = 18x^2 y^2 + 10x^2 y^3 + 4x^2 y^4 + 3x^3 y^4$

and $D_y = 18x^2 y^2 + 15x^2 y^3 + 8x^2 y^4 + 4x^3 y^4$

$$\begin{aligned} M_1(G) &= (D_x + D_y)(M(G; x, y))_{x=y=1} \\ &= ((18x^2 y^2 + 10x^2 y^3 + 4x^2 y^4 + 3x^3 y^4) + (18x^2 y^2 + 15x^2 y^3 + 8x^2 y^4 + 4x^3 y^4))_{x=y=1} \\ &= (36x^2 y^2 + 25x^2 y^3 + 12x^2 y^4 + 7x^3 y^4)_{x=y=1} = 36 + 25 + 12 + 7 = 80. \end{aligned}$$

3.3 Second Zagreb index

Second Zagreb index: $f(x, y) = xy$, As $D_x = 18x^2 y^2 + 10x^2 y^3 + 4x^2 y^4 + 3x^3 y^4$,

$$\begin{aligned} M_2(G) &= (D_y D_x)(M(G; x, y))_{x=y=1} = D_y (18x^2 y^2 + 10x^2 y^3 + 4x^2 y^4 + 3x^3 y^4)_{x=y=1} \\ &= (36x^2 y^2 + 30x^2 y^3 + 16x^2 y^4 + 12x^3 y^4)_{x=y=1} = 36 + 30 + 16 + 12 = 94. \end{aligned}$$

3.4 Second modified Zagreb index

Second modified Zagreb index: $f(x, y) = \frac{1}{xy} = (S_x S_y)(M(G; x, y))_{x=y=1}$

$$\text{As } S_x (S_y) = \frac{9}{4} x^2 y^2 + \frac{5}{6} x^2 y^3 + \frac{1}{4} x^2 y^4 + \frac{1}{12} x^3 y^4.$$

$${}^m M_2(G) = \left(\frac{9}{4} x^2 y^2 + \frac{5}{6} x^2 y^3 + \frac{1}{4} x^2 y^4 + \frac{1}{12} x^3 y^4 \right)_{x=y=1}.$$

$$= 3.4166.$$

3.5 Redefined second Zagreb index

$$\text{ReZG}_2(G):f(x,y)=\frac{xy}{x+y}$$

$$\text{As } J = 9x^4 + 5x^5 + 2x^6 + x^7.$$

$$S_x J(M(G; x, y))_{x=1} = \left(\frac{9}{4}x^4 + x^5 + \frac{1}{3}x^6 + \frac{1}{7}x^7 \right)_{x=y=1}.$$

$$= \frac{9}{4} + 1 + \frac{1}{3} + \frac{1}{7}.$$

$$= 3.726.$$

The computed values of $\text{ReZG}_1(G)$, $M_2^*(G)$, $M_1^*(G)$ and $M_1^{**}(G)$ from M-polynomials are represented in table number (2). The eccentricity based M-polynomials and new versions of Zagreb indices can be studied by studying the eccentricity of each vertex of a molecular graph of chalcone (fig.2). The eccentricity-based M-polynomials are expressed and eccentricity-based Zagreb indices are computed and given in table number (2).

Table-1: Derivation of Zagreb indices from M-polynomial for chalcone.

Zagreb indices	f(x,y)	Derivation from M(G;x,y)
$M_1(G)$	$x+y$	$(D_x+D_y)(M(G;x,y))_{x=y=1}$
$M_2(G)$	xy	$(D_x D_y)(M(G;x,y))_{x=y=1}$
${}^m M_2(G)$	$\frac{1}{xy}$	$(S_x S_y)(M(G;x,y))_{x=y=1}$
$\text{ReZG}_1(G)$	$\frac{x+y}{xy}$	$1/S_x J(M(G;x,y))_{x=1}$
$\text{ReZG}_2(G)$	$\frac{xy}{x+y}$	$S_x J(M(G;x,y))_{x=1}$
$M_2^*(G)$	$\epsilon_G(u) \epsilon_G(v)$	$(D_{\epsilon_G(u)} D_{\epsilon_G(v)})(M(G;x,y))_{x=y=1}$
$M_1^*(G)$	$\epsilon_G(u) + \epsilon_G(v)$	$(D_{\epsilon_G(u)} + D_{\epsilon_G(v)})(M(G;x,y))_{x=y=1}$
$M_1^{**}(G)$	$(\epsilon_G(u) + \epsilon_G(v))^2 = \epsilon_G(u)^2 + \epsilon_G(v)^2 + 2\epsilon_G(u)\epsilon_G(v)$	$(D_{\epsilon_G(u)}^2 + D_{\epsilon_G(v)}^2 + 2D_{\epsilon_G(u)} D_{\epsilon_G(v)})(M(G;x,y))_{x=y=1}$

$$\text{Where } D_x = \frac{\partial(f(x,y))}{\partial x}, D_y = \frac{\partial(f(x,y))}{\partial y}, S_x = \int_0^x f(t,y) \frac{dt}{t}, S_y = \int_0^y f(x,t) \frac{dt}{t}, J=f(x,x).$$

Table-2: The values of Zagreb indices for chalcone.

Zagreb indices	Derivation from M(G;x,y)
$M_1(G)$	80
$M_2(G)$	94
${}^m M_2(G)$	3.4166
$\text{ReZG}_1(G)$	0.2684
$\text{ReZG}_2(G)$	3.726
$M_2^*(G)$	1414
$M_1^*(G)$	306
$M_1^{**}(G)$	306

4. CONCLUSION

The M-polynomials, degree-based, new versions and redefined Zagreb indices are computed for chalcone. The chalcone is widely used in pharmacology experimentation. Chalcones are known to exhibit various biological activities, such as antioxidant, antiinflammatory and antimalarial, antileishmanial, anticancer and antitumor. These results can play an important role in preparation of new drugs and QSPR/QSAR study.

REFERENCES

- Kanna, M.R.R., & Jagadeesh, R. (2018). *International Journal of Mathematics and its Applications*, 6(1-B), 271-279.
- Farahani, M.R., Baig, A.Q., & Sajjad, W. (2017). The second Zagreb index of the N^{TH} growth nanostar dendrimer $D_3[N]$, *Journal of Mathematical Nanoscience*, 7(1-2), 23-28.
- Gutman, I. (2013). Degree-based topological indices, *Croat.Chem.Acta* 86(4), 351-361.

4. Raut, N.K., (2014). Schultz, modified Schultz and Hosoya polynomials and their indices in 2,3-dimethyl hexane and isomers of octane, *International Journal of Mathematics and Computer Research*, Vol.2, Issue 8, 587-592.
5. Riyaz, M., Gao, W., & Baig, A.Q. (2018). M-polynomials and degree-based topological indices of some families of convex polytopes, *Open Journal Math.Sci.*, Vol.2, No.1, 18-28.
6. Deutsch, E. (2014). M-polynomial and degree-based topological indices, *arXiv: 1407.1592v1, [math.CO]*, 1-10.
7. Lokesh, V., Deepika, T., & Gangul, I.N. (2017). Computing the M-polynomials for 2D-lattice, Nanotube and Nanotorus by operating the semitotal line and points groups via degree-based indices, *Tamap, Journal of Mathematics and Statistics*, Article ID 23, 01-22.
8. Ajmal, M., Nazeer, W., Munir, M., Kang, S.M., & Jung, C.Y. (2017). The Polynomials and topological indices of Toroidal polyhex network, *International Journal of Mathematical Analysis*, Vol.11, No.7, 305-315.
9. Suwito, H. et.al. (2014). Chalcones: Synthesis, structure diversity and pharmacological aspects, *Journal Chem.Pharm.Research*, 6(5), 1076-1088.
10. Thayamathy, P.J.N., Elango P., & Koneswaran, M. (2018). M-polynomials and degree-based indices of silicon oxide, *Int. Jou. Of Pure and Applied Chemistry*, 16(4): 1-9.
11. Gao, Y., Jamil, M.K., Aslam, A., & Farahani, M.R. (2017). *Journal of Optoelectronics and Biomedical Materials*, Vol.9, No.3, 135-142.
12. Kulli, V.R. (2017). Certain topological indices and their polynomials of Dendrimer nanostars, *Annals of Pure and Applied Mathematics*, Vol.14, No.2, 263-268.
13. N.M.Soleimani, M.J.Nikmehr, H.A.Tavallae, (2015). Computation of different topological indices of nanostructures, *Journal of National Foundation of Shri Lanka*, 43(2); 127-133.
14. Deutsch, E., & Klavzar, S. (2015). M-polynomial and degree-based topological indices, *Iranian J.Math.Chem.*, 6, 93-102.
15. Javaid, M., & Jung, C.J., (2017). M-polynomials and topological indices of silicate and oxide networks, *Int.Journal of Pure and Applied Mathematics*, Vol.115, No.1, 129-152.
16. Pararathi, P.K., & Namasivayam, E. (2013). Synthesis and Biological Evaluation of Chalcones from 2-Acetyl-5-Methylfuran, *IJPSR*, Vol.4, Issue-7, ISSN:0975-8232, 2629-2638.
17. Berar, U. (2012). Chalcones: Compounds possessing a diversity in applications, *Journal of Pharmacy Research*, 5(8), 4236-4241.
18. Ceyan, M., & Gezezen, H. (2008). Preparation of 1,5-Diketones by addition of Cyclohexane chalcones under Solvent-free phase transfer catalyst condition, *Turk J.Chem.* 32, 55-61.
19. Bukhari, N.A., Jasamai, S., Jantan, M., & Ibrahim, (2012). Synthesis and Biological Evaluation of Chalcone Derivatives, *Mini Reviews in Medicinal Chemistry*, 12; 1394-1403.
20. Ghorbani, M., & Hosseinzadeh, M.A. (2012). A new version of Zagreb indices, *Filomat, University of Nis, Serbia*, 26:1, 93-100.
21. Farahani, M.R., Jamil, M.K., Kanna, M.R.R., & Kumar, R.P. (2016). The multiplicative Zagreb eccentricity index of polycyclic aromatic hydrocarbon (PAHs), *International Journal of Scientific and Engineering Research*, Vol.7, Issue 2, 1132-1135.
22. Zahid, M.A., Baig, A.Q., Naeem, M., & Azhar, M.R. (2018). Eccentricity-based topological indices of a cyclic octahedron structure, *Mathematics-MDPI*, 141, 01-15.
23. Noreen, S., & Mahmood, A. (2018). Zagreb polynomials and redefined Zagreb indices for the line graph of carbon nanocones, *Open Journal Math.Anal.* Vol.2, 67-76.
24. Balasubramanian K. et.al., (2017). Computing eccentric distance sum of dendrimers sum of and nanotubes, *International Journal of Pharmacy and Technology*, Vol.9, Issue no.1, 28728-28738.
25. Vasudev, C. (2006). *Graph theory with applications*, New Age, International Publishers, New Delhi.

-
26. Balakrishnan, R., & Renganathan, K. (2000). *A textbook of Graph theory*, Springer-Verlag, New York.
 27. Diudea, M.V., Gutman, I., & Lorentz, J. (1999). *Molecular Topology*, NOVA, Science Publishers Inc..
 28. Deo, N. (2007). *Graph theory*, Prentice – Hall of India Private Limited, New Delhi
 29. Harary, F. (1971). *Graph theory*, Addison, Wesley, Reading MA.
 30. Dworakowska, Sylwia., & Dariusz Bo. (2012). Application of connectivity indices in polymer chemistry, *16th International Electronic Conference on Synthetic Organic Chemistry*, 1-30,pcbogdal@cyf-kr.edu.pl,1-3.
 31. Raut, N.K. (2016).The Zagreb group indices and polynomials, *International Journal of Modern Engineering Research*, Vol.6, Issue 10, 84-87.
 32. Gutman, I.,& Tosovic, J. (2013). Testing the quality of molecular structure descriptors, Vertex-degree topological indices, *J.Serb.Chem.Soc.*78(6) JSCS, 805-810.
 33. Farahani, M.R., & Gao, W. (2016). On multiplication and redefined version of Zagreb indices of V-Phenylenic nanotubes and nanotorous, *British Journal of Mathematics and Computer science*,13(5):Article no.BJMCS.22752,1-8.

DIELECTRIC PROPERTIES OF NANOSCALE COMPOSITE JUNCTION

G. G. Patil¹, Khirade P. W.² and Sayyad S. B.³¹Department of Electronic Science, K. T. H. M. College, Nashik²Department of Physics, Dr. Babasaheb Ambedkar Marathwada University, Aurangabad³Department of Physics, Milliyya Arts, Science & Management Science College, Beed

ABSTRACT

Due to the increasing demands of metal oxide nanocomposite materials in the electronic industry, it is necessary to investigate the dielectric properties of nanocomposite under various frequency and temperature conditions. In this work we reported the synthesis of CuO/ZnO nanoscale composite junction by mechanical milling method. The XRD was used to analyse the nanocomposite sample. The dielectric properties such as permittivity, loss tangent, AC conductivity and capacitance was investigated using broadband dielectric spectroscopy(BDS) at frequency 1MHz, 10MHz and 100MHz respectively under temperature range from 0°C to 100°C. The result revealed that the permittivity of CuO/ZnO nanoscale composite junction at 1MHz frequency goes on increasing with increasing temperature. It is relatively constant at 10 MHz and 100 MHz frequency. The Loss tangent, AC conductivity and capacitance also showed the significant variation with temperature.

1. INTRODUCTION

The metal oxide nanocomposites are attracting the attention of scientific community due to their strange properties as compared to their bulk material counterpart. The structural, mechanical, electrical and optical properties of nanocomposite are useful in electronic devices fabrication [1-5]. In this work we used the CuO and ZnO research grade powder for the synthesis of CuO/ZnO nanoscale composite junction. The CuO is narrow bandgap p-type semiconductor with band gap energy about 1.7eV [6-9]. The ZnO is n-type wide band gap semiconductor with band gap energy about 3.37eV [10, 11]. The CuO/ZnO nanoscale composite junction is formed by simple mechanical milling of the research grade powder taken in equal weight ratio. The milling was done at room temperature. This is the simplest method of forming the nanocomposite junction. In this process, the lattice crystal of CuO and ZnO undergoes strong plastic deformation, result in stresses and strains. During the mechanical milling process the collision between the grains of powder increases the interface temperature, which creates the nanocomposite [12]. When the interface of p-CuO and n-ZnO contact each other, the p-CuO/n-ZnO nanoscale composite junction could be formed. The formation of nanocomposite junction is confirmed from the XRD of the sample. The synthesis part of this nanocomposite junction is published in my earlier publication [13].

The dielectric properties of CuO/ZnO nanoscale composite junction were studied using broadband dielectric spectroscopy (BDS). The pellets of the synthesized nanocomposite junction in powder form were prepared using hydraulic press. The pellets were about 10mm in diameter and 1mm to 2mm in thickness. The prepared pellets were heated at 300°C temperature for two hour for hardening purpose. These pellet sample were placed in sample holder of NOVOCONTROL BDS at metallurgical Department, IIT Mumbai. The dielectric parameters such as permittivity, loss tangent delta, AC conductivity and capacitance were investigated at 1MHz, 10 MHz and 100MHz frequency respectively in temperature range from 0°C to 100°C.

2. EXPERIMENTAL**2.1 Material**

The CuO and ZnO research grade powder was used for synthesis CuO/ZnO nanoscale composite junction.

2.2 Sample preparation

The CuO/ZnO nanoscale composite junction was prepared by mechanical crushing of the CuO and ZnO powder taken in equal weight ratio.

2.3 Characterization

The synthesized CuO/ZnO nanocomposite was characterized by using XRD. The synthesis of nanoscale composite of CuO/ZnO is confirmed from XRD.

3. RESULT and DISCUSSION

3.1 XRD

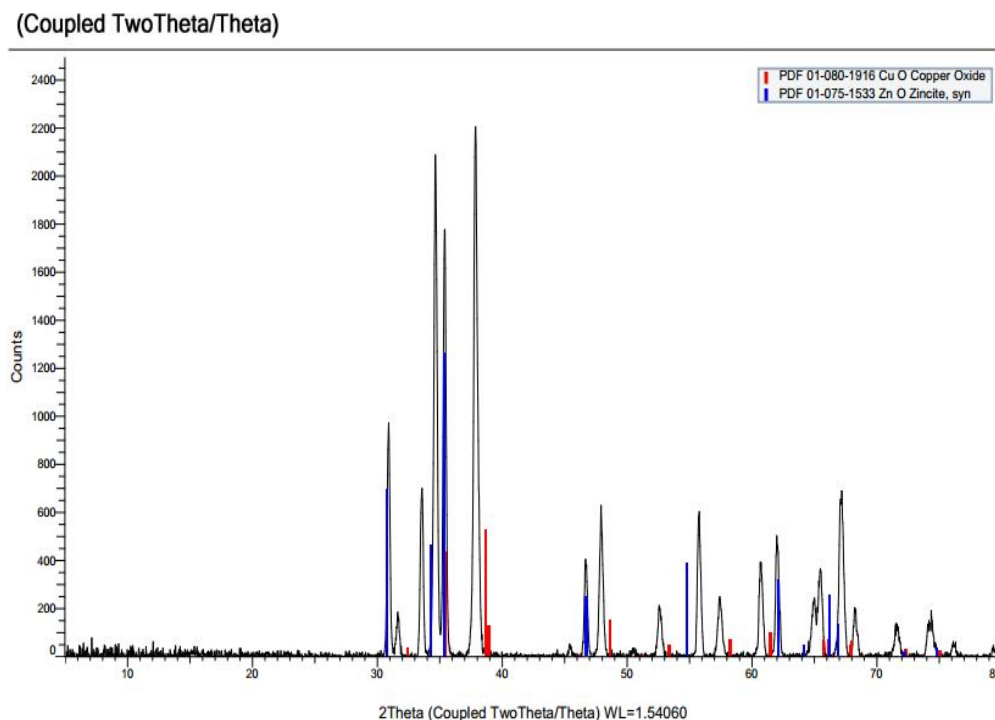


Fig-1: XRD of CuO/ ZnO nanoscale composite junction

Figure 1 represents the XRD of CuO/ ZnO nanoscale composite junction. The XRD was matched to JCPDS shown in figure1.

3.2 Real Permittivity ϵ'

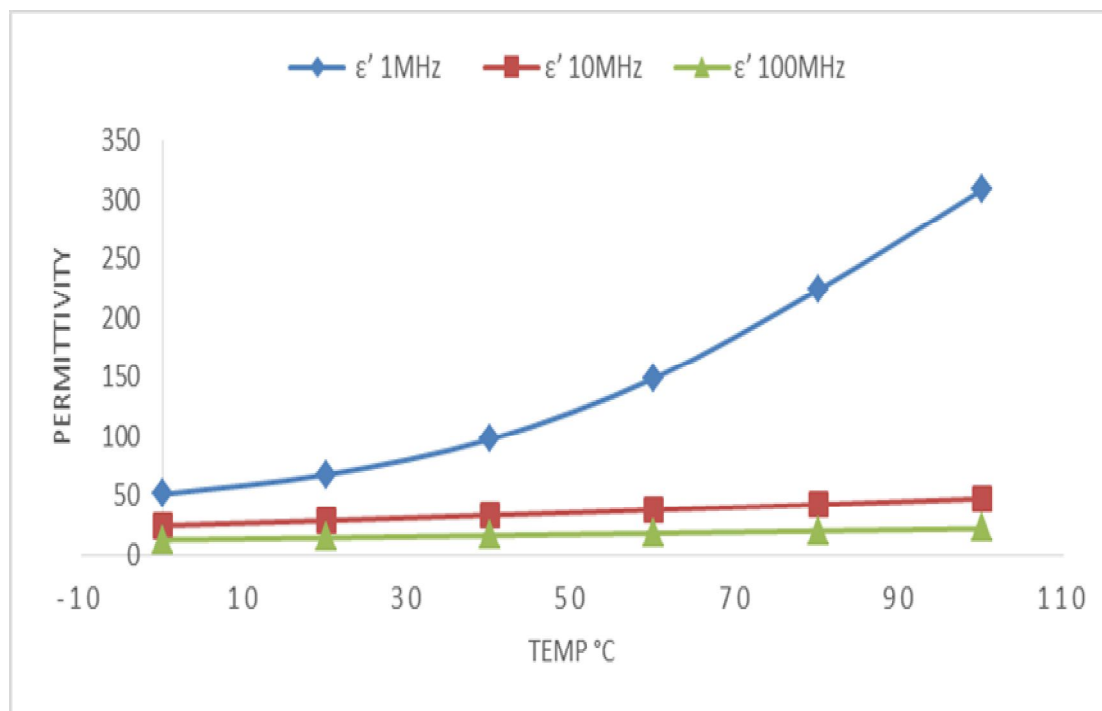


Fig-2: Dielectric permittivity ϵ' versus temperature of CuO/ZnO nanoscale composite junction

The graph of dielectric permittivity against temperature of the sample is shown in figure 2. From graph, at 1MHz (low) frequency, the permittivity ϵ' of sample goes on increasing with temperature. As the frequency is increased to 10MHz, ϵ' value drops down. It is due to the polarization of nanoscale composite junction [14-17]. It remains almost constant over the entire temperature range. As we increased the frequency to 100MHz (high), ϵ' again drops down.

3.3 Loss Tangent δ

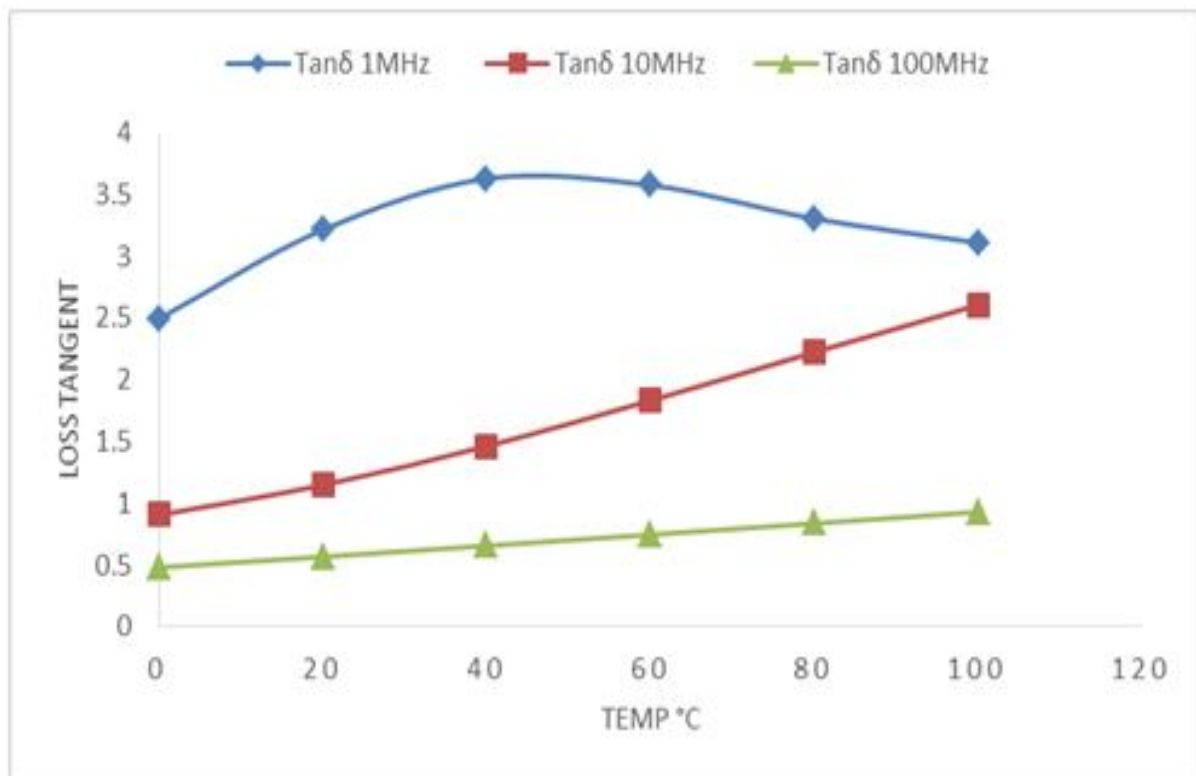


Fig-3: Loss tangent δ versus temperature of CuO/ZnO nanoscale composite junction

Figure 3 shows the loss tangent δ as a function of temperature. Its value increases with increase in temperature and is maximum at low frequency 1MHz. As the frequency is increased, loss tangent δ value is decreased.

3.4 Ac Conductivity σ

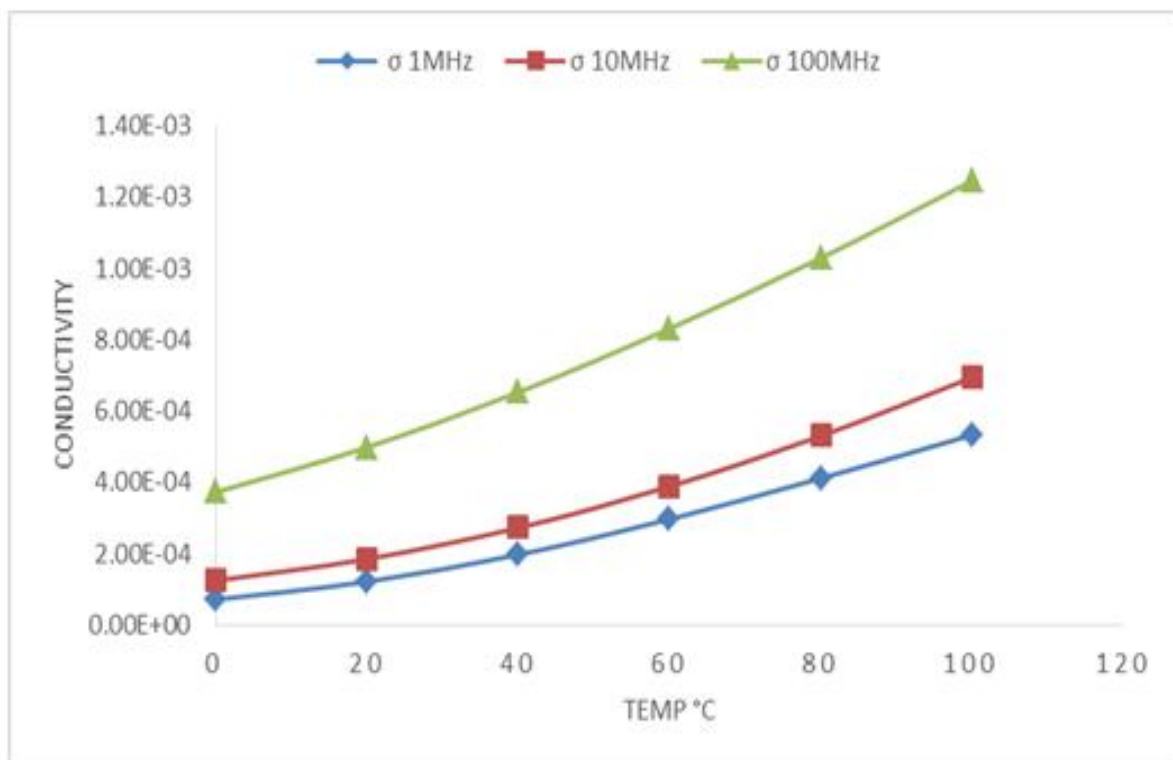


Fig-4: Conductivity σ versus temperature of CuO/ZnO nanoscale composite junction

The AC conductivity of CuO/ZnO nanoscale composite junction with frequency at different temperature is shown in fig.4. From figure it is evident that AC conductivity is frequency dependent and it increases with increase in frequency and temperature. It is in agreement with earlier study.

3.5 Capacitance

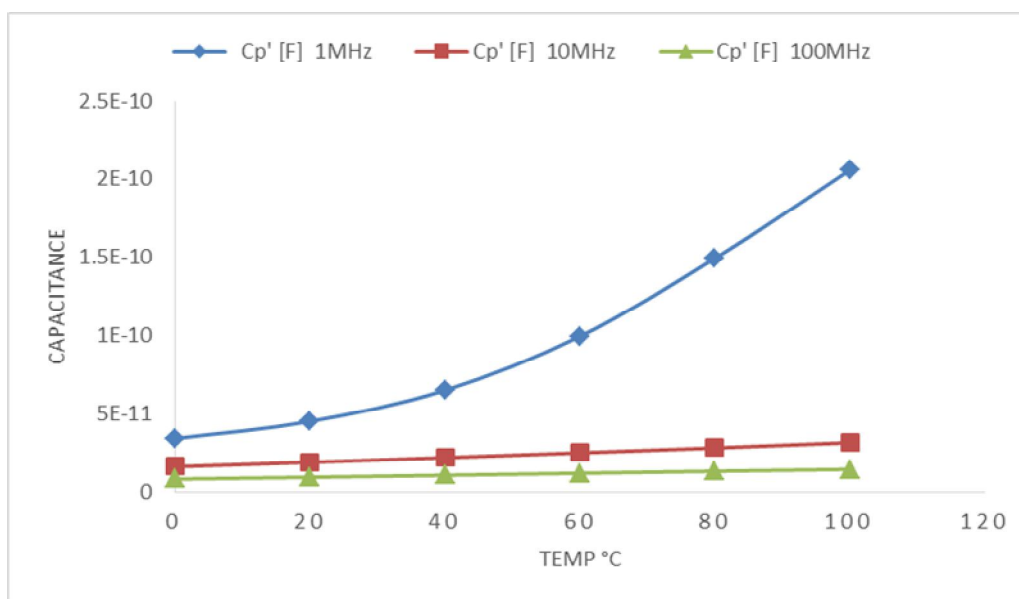


Fig-5: Capacitance C versus temperature of CuO/ZnO nanoscale composite junction

From figure 5, it is observed that capacitance value is high at low frequency 1MHz and it increases with increase in temperature. As we increased the frequency, the capacitance value get reduced. From this it is concluded that capacitance of CuOZnO nanoscale composite junction is temperature dependent at low frequency. At high frequency, it is relatively constant.

4. CONCLUSION

The formation of CuO/ZnO nanoscale composite junction was confirmed from the XRD study. The Dielectric permittivity of sample were investigated with varying temperature and frequency. It is found to be temperature dependent at low frequency. The loss tangent δ of the sample was found to be temperature dependent. AC conductivity is frequency dependent and it increases with increase in temperature and frequency. The capacitance of sample is temperature dependent at low frequency and it increases with temperature. All this study of CuO/ZnO nanoscale composite junction is found to be consistent with past study.

REFERENCES

1. A.A. Farghali, M. Moussa, M.H. Khedr, J. Alloys Compd. 499 (2010) 98–103.
2. N.M. Deraz, J. Alloys Compd. 501 (2010) 317–325.
3. Li-Dong Zhao, Bo-Ping Zhang, Jing-Feng Li, Min Zhou, Wei-Shu Liu, Jing Liu, J. Alloys Compd. 455 (2008) 259–264.
4. P.G. Li, M. Lei, W.H. Tang, X. Guo, X. Wang, J. Alloys Compd. 477 (2009) 515–518.
5. Xiaorui Hou, Shengming Zhou, Yukun Li, Wenjie Li, J. Alloys Compd. 494 (2010) 382–385.
6. A. Kargar, Y. Jing, S.J. Kim, C.T. Riley, X. Pan, D. Wang, ZnO/CuO heterojunction branched nanowires for photoelectrochemical hydrogen generation, ACS Nano 7 (2013) 11112–11120.
7. Z. Liu, H. Bai, S. Xu, D.D. Sun, Hierarchical CuO/ZnO “corn-like” architecture for photocatalytic hydrogen generation, Int. J. Hydrog. Energy 36 (2011) 13473–13480.
8. T. Terasako, T. Murakami, A. Hyodou, S. Shirakata, Structural and electrical properties of CuO films and n-ZnO/p-CuO heterojunctions prepared by chemical bath deposition based technique, Sol. Energy Mater. Sol. Cells 132 (2015) 74–79.
9. J. Yu, S. Zhuang, X. Xu, W. Zhu, B. Feng, J. Hu, Photogenerated electron reservoir in hetero-p-n CuO–ZnO nanocomposite device for visible-light-driven photocatalytic reduction of aqueous Cr(VI), J. Mater. Chem. A 3 (2015) 1199–1207. [http:// dx.doi.org/10.1039/C4TA04526B](http://dx.doi.org/10.1039/C4TA04526B)
10. Eric R. Waclawik et. al., Beilstein J. Nanotechnol. 2012, 3, 368–377.
11. Nanto, Hidehito; Minami, Tadatsugu; Takata, Shinzo, Journal of Applied Physics; 7/15/1986, Vol. 60 Issue 2, p482.

-
12. C. Shifu, C. Lei, G. Shen, and C. Gengyu, *Materials Chemisry andPhysics* 98, 116 (2006).
 13. G. G. Patil, Sayyad S. B., JETIR November 2017, Volume 4, Issue 11 543-546.
 14. A. Liu, L. H. Bac, J.-S. Kim, B.-K. Kim and J.-C. Kim, Synthesis and characterization of conducting polyaniline–copper composites, *J. Nanosci. Nanotechnol.* 13, 7728 (2013)
 15. L. N. Shubha and P. Madhusudana Rao JOURNAL OF ADVANCED DIELECTRICS Vol. 6, No. 3 (2016) 1650018
 16. Y. Ravikiran, M. Lagare, M. Sairam, N. Mallikarjuna, B. Sreedhar, S. Manohar, A. MacDiarmid and T. Aminabhavi, Synthesis, characterization and low frequency fACg conduction of polyaniline/niobium pentoxide composites, *Synth. Met.* 156, 1139 (2006).
 17. N.J. Tharayil, R. Raveendran, A. Varghese Vaidyan, P.G. Chithra, *Indian J. Eng.Mater. Sci.* 15 (2008) 489–496.

DETERMINATION OF RADIOLOGICAL DATA OF LIPIDS USING GAMMA RAY SPECTROMETRY

Prashant S. Kore¹, Ram Bhosale², Dr. Jai Shri Kumar³, Madhav Rode⁴ and Pravina P. Pawar⁵^{1, 2, 4, 5}Department of Physics, Vaidyanath College, Parli Vajinath³Assistant Professor of Physics, Government College Kharkhara, Rewari

ABSTRACT

The absorption effects of gamma radiations on lipids are shown using radiological parameters such as mass attenuation coefficients, total attenuation cross section and molar extinction coefficient. Which will be useful, particularly in the energy region of 122 to 1330keV photon energies, by performing transmission experiments using gamma active sources ⁵⁷Co, ¹³³Ba, ²²Na, ¹³⁷Cs, ⁵⁴Mn, and ⁶⁰Co sources. Accurate values of these physical parameters provide essential data in medical physics have been calculated for some sphingolipids were measured using gamma ray spectrometry with energy resolution 8.2% at 663 keV was used for detection. Gamma ray transmission method with a narrow beam good geometry set up are used in the study. Observed values are decrease initially and then tends to be almost constant at higher energies. Experimental results of radiological parameters were observed in good agreement with WinXCom values.

Keywords: Gamma ray Spectrometry, lipids, Mass attenuation coefficients (μ_m), Molar extinction coefficient (ϵ), Radioactive sources, Total attenuation cross section (σ_{tot}), WinXCom program.

1. INTRODUCTION

A living cell is a dynamic biological system composed primarily of carbohydrates, lipids, nucleic acids, and proteins that structurally and functionally interact with many other molecules to carry out normal cell metabolism. The present research work is about effect of radiation on such types of lipids and it is rather well documented that plasma membrane of mammalian tissues are rich in sphingolipids and especially sphingoglycolipids. Sphingolipids were first described by [1] in A Treatise on the Chemical Constitution of Brain. Sphingoglycolipids are a family of complex lipids with structures representing a large variety of carbohydrate compositions which are characteristics for a mammalian organ and can vary depending on the species of origin [2]. The study of sphingoglycolipid composition in various, radiosensitive and non-radiosensitive tissues, might indicate whether damages induced by the ionizing radiation on the plasma membrane matrix are involved in the process of cell death [3]. So in this research work we focus the effect of radiation on lipids at medical, radiological, biological research point of view.

Biological significance of sphingolipids; Sphingolipids are found in essentially all animals, plants, and fungi, as well as some prokaryotic organisms and viruses. They are mostly in membranes, but are also major constituents of lipoproteins. The functions of sphingolipids are still being discovered, but there are at least three, i.e., structure, recognition and signal transduction [4]. Later studies fulfilled Thudichum's faith in the value of basic research when several genetic diseases were found to have elevated amounts of sphingolipids (such as sphingomyelin in Niemann-Pick's disease and cerebroside in Gaucher's disease) arising from defects in enzymes responsible for sphingolipid turnover, activator proteins for such enzymes, or lipid trafficking [5,6]. This knowledge allowed development of methods for diagnosis of such sphingolipid storage diseases, screening of families at risk, and, for at least Gaucher's disease, some degree of correction of the disorder by enzyme replacement. There are also indications that sphingolipids and sphingolipid analogs may be useful for prevention and treatment of disease, e.g., gangliosides [7] and alpha-galactosylceramide have potent effects as modulators of the immune system, ceramide-coated balloon catheters limit neointimal hyperplasia after stretch injury in carotid arteries [8] and dietary sphingolipids protect against colon tumorigenesis [9]. So, the relation between radiation and sphingolipids is very much important in medical and research context. Because the research area of absorption, penetration, attenuation and photon interactions with biological material such as amino acids, fatty acids, lipids, vitamins, and carbohydrates is essential in radiation medicine and biology, nuclear technology and space research[10]. The study of photon interactions with matter is important and the data on the transmission and absorption of X-rays and gamma rays in biological shielding and dosimetric materials assumed great significance by virtue of the diverse application in the field of medical physics and medical biology [11,12]. [13] reported μ_{en}/ρ data for elements, compound and mixtures as a function of energy of photons[14]. Selection of material for radiation shielding and protection needs an accurate assessment of interaction parameters [15].

There have been recent experimental and theoretical investigations [16,17] to determine Absorption coefficient, mass attenuation coefficients, total attenuation cross section and such type of radiological parameters for

complex biological molecules such as lipids, carbohydrates, proteins, fats and oils composed of H, C, N and O elements in varying proportions.

2. THEORY

In this section, some theoretical relations are summarized that have been used for the determination of mass absorption and related parameters in the present work. When a monochromatic beam of gamma ray photons is incident on a target, some photons are emitted due to the dominant interaction processes and therefore, the transmitted beam is attenuated. The extent of attenuation depends on given elemental target. This attenuation of the beam is expressed by the following equation:

$$I = I_0 e^{-\mu t} \quad (1)$$

where I_0 and I are the incident and transmitted photon intensities, respectively, μ (cm^{-1}) is the linear attenuation coefficient of the material and t (cm) is the sample thickness. Rearrangement of Eq. (1) yields the following equation for the linear attenuation coefficient:

$$\mu = \frac{1}{t} \ln \left(\frac{I_0}{I} \right) \quad (2)$$

In Eq. (2), the mass attenuation coefficients μ_m ($\text{cm}^2 \text{g}^{-1}$) for the samples were obtained from Eq. (3) by using the density of the corresponding samples:

$$\mu_m = \frac{\mu}{\rho} (\text{cm}^2 \text{g}^{-1}) = \frac{1}{\rho t} \ln \left(\frac{I_0}{I} \right) \quad (3)$$

where ρ (g/cm^3) is a measured density of the corresponding sample. The values of mass attenuation coefficients were then used to determine the total attenuation cross section (σ_{tot}) by the following relation

$$(\sigma_{\text{tot}}) = \mu_m (M / N_A) \quad (4)$$

where $M = \sum_i n_i A_i$ is the molecular weight of the compound, N_A is the Avogadro's number.

And the values of molar extinction coefficients were determined using the following relation:

$$\varepsilon = 0.4343 N_A \sigma_{\text{tot}} \quad (5)$$

All these radiological parameters are convenient parameters used to characterize the radiation response of a multi-element material in many technical and medical applications. Accurate values of these physical parameters provide essential data in medical physics.

3. EXPERIMENTAL SET UP AND MEASUREMENTS

The gamma active radioactive sources ^{57}Co , ^{133}Ba , ^{22}Na , ^{137}Cs , ^{54}Mn , and ^{60}Co were used in the present investigation having energies 122, 356, 511, 662, 835, 1173, 1275 and 1332 keV emitted by the above radioactive sources were collimated and detected by the NaI (TI) based gamma ray spectrometry. The signals from the detector were amplified and analyzed with 13-bit multichannel analyzer. In the present study, samples of lipids (sphingolipids) are in powder form which are 99.9% pure and by using KBr press machine it converted into pellet forms (0.13 g/cm^2 of uniform thicknesses) shaped and confined in a cylindrical plastic container having the same diameter as that of sample pellets. The diameters of the samples were determined with the help of a traveling microscope. These pellets are placed on an empty plastic container which play a role of substrate. It was observed that the attenuation of photons of the empty containers were negligible. The sample thickness was selected in order to satisfy the following ideal condition as far as possible [4]: $2 \leq \ln(I_0/I) \leq 4$.

The schematic view of the experimental set up is displayed in Fig.1. From the measured values of unattenuated photon intensity I_0 (with empty plastic container) and attenuated photon intensity I (with sample), the mass attenuation coefficients (μ_m) for all the samples of sphingolipids were calculated using Eq.(3). The experimental values of mass attenuation coefficients were compare against the Win-Xcom program by [2] at all photon energies of current interest which, can give the theoretical numerical data of all compounds, mixture, metal, alloys for references. The contribution of coherent as well as incoherent scattering at such angles in the measured cross-sections at intermediate energies is negligible. Hence, no small angle scattering corrections were applied to the measured data. The error due to the sample impurities can be high only when large percentage of high Z impurities is present in the sample. The samples sphingolipids are used in the present study

were of high pure and sample impurity corrections were not applied to the measured data. Here all the radiological quantities; mass attenuation coefficients, total attenuation cross section and molar extinction coefficient are determined by using equations 1 to 5.

4. FIGURES AND TABLES

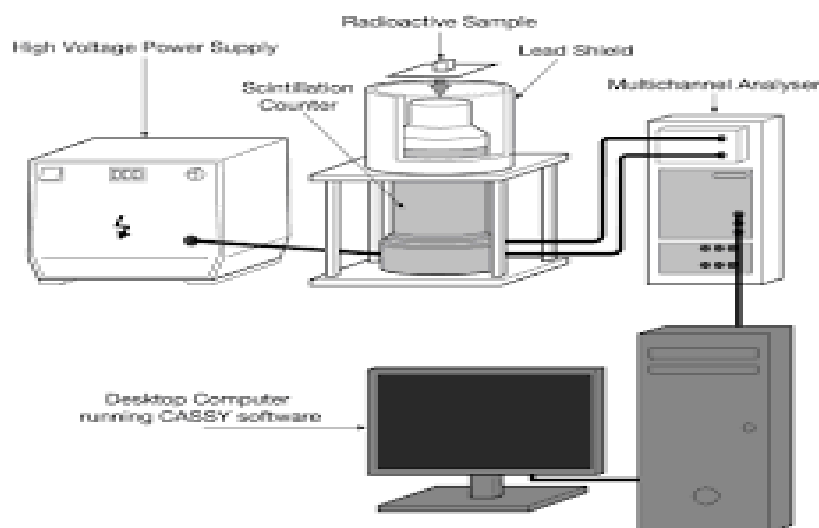


Fig-1: The schematic view of Scintillation counter.

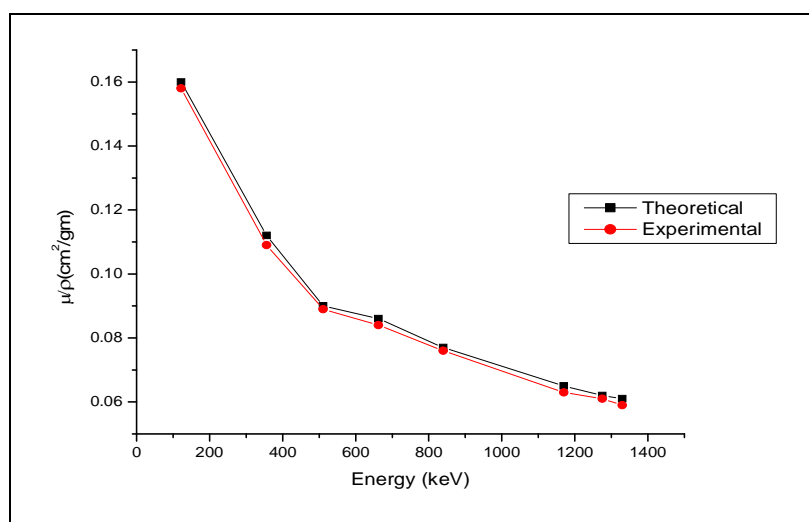


Fig-2: Plot of μ_m versus photon energy for Dehydrophytosphingosine ($C_{18}H_{37}NO_3$).

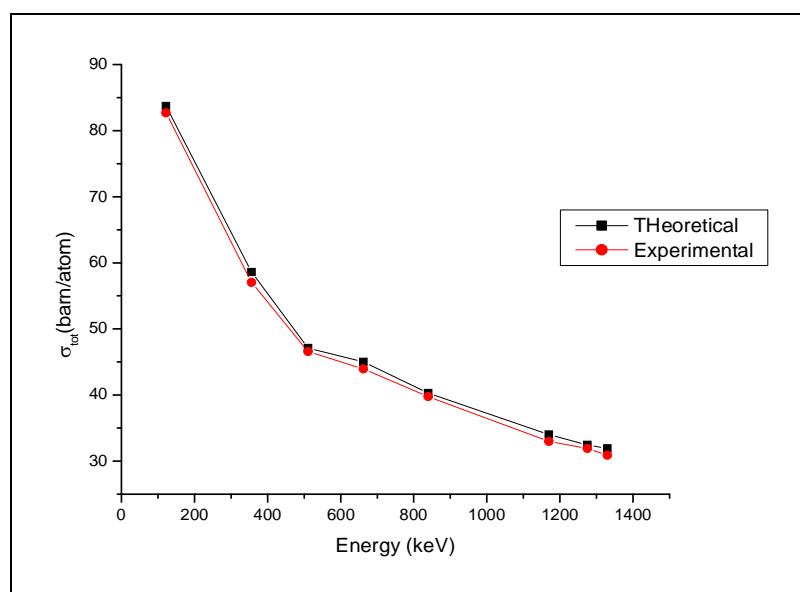


Fig-3: Plots of σ_{tot} versus photon energy for Dehydrophytosphingosine ($C_{18}H_{37}NO_3$).

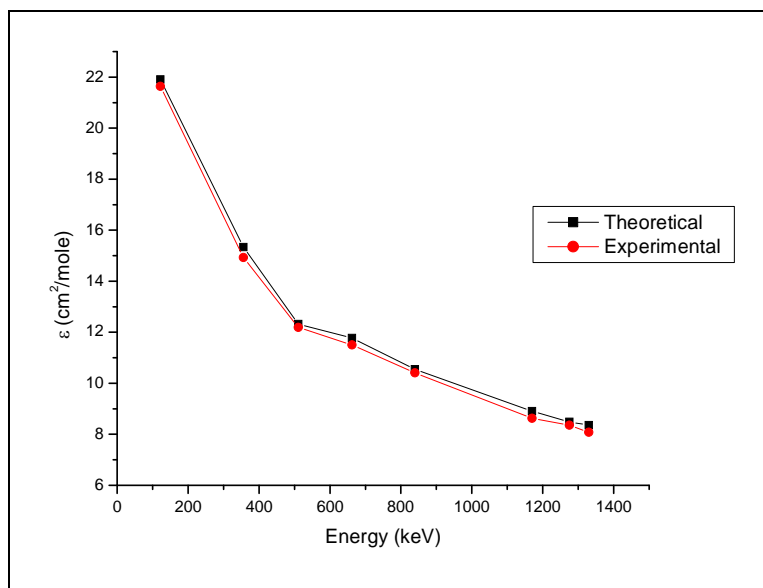


Fig-4: Plots of ϵ versus photon energy for Dehydrophytosphingosine ($C_{18}H_{37}NO_3$).

Table-1: Mean atomic numbers (Z) calculated from the chemical formula for sphingolipids.

Sphingolipids	Molar mass (g/mol)	Chemical Formula	Mean atomic number, Z
Dehydrophytosphingosine	315.28	$(C_{18}H_{37}NO_3)$	3.11
Myriocin	401.28	$(C_{21}H_{39}NO_6)$	3.31
Hemsleyin imine A	605.57	$(C_{39}H_{75}NO_3)$	2.89

Table-2: Comparison of measured and calculated values of mass attenuation coefficient (μ_m cm²/g) of sphingolipids at different photon energies. The calculated values are based on Win-XCOM program.

Sr.	Sphingolipids	122keV	356keV	511keV	662keV	835keV	1173keV	1275keV	1332 keV
No.		Exp. Theo.	Exp. Theo.	Exp. Theo.	Exp. Theo.	Exp. Theo.	Exp. Theo.	Exp. Theo.	Exp. Theo.
1.	Dehydrophytosphingosine	0.158 0.160	0.109 0.112	0.089 0.090	0.084 0.086	0.076 0.077	0.063 0.065	0.061 0.062	0.059 0.061
2.	Myriocin	0.156 0.158	0.107 0.110	0.092 0.094	0.086 0.085	0.075 0.076	0.066 0.064	0.060 0.061	0.058 0.060
3.	Hemsleyin imine A	0.163 0.161	0.110 0.112	0.098 0.096	0.085 0.087	0.076 0.077	0.067 0.066	0.064 0.063	0.060 0.062

Table-3: Comparison of measured and calculated values of total attenuation cross section (σ_{tot} barn/atom) of sphingolipids at different photon energies. The calculated values are based on Win-XCOM program.

Sr.	Sphingolipids	122keV	356keV	511keV	662keV	835keV	1173keV	1275keV	1332 keV
No.		Exp. Theo.	Exp. Theo.	Exp. Theo.	Exp. Theo.	Exp. Theo.	Exp. Theo.	Exp. Theo.	Exp. Theo.
1.	Dehydrophytosphingosine	0.158 0.160	0.109 0.112	0.089 0.090	0.084 0.086	0.076 0.077	0.063 0.065	0.061 0.062	0.059 0.061
2.	Myriocin	0.156 0.158	0.107 0.110	0.092 0.094	0.086 0.085	0.075 0.076	0.066 0.064	0.060 0.061	0.058 0.060
3.	Hemsleyin imine A	0.163 0.161	0.110 0.112	0.098 0.096	0.085 0.087	0.076 0.077	0.067 0.066	0.064 0.063	0.060 0.062

Table-4: Comparison of measured and calculated values of molar extinction coefficient (ϵ cm²/mol) of sphingolipids at different photon energies. The calculated values are based on Win-XCOM program.

Sr.	Sphingolipids	122keV		356keV		511keV		662keV		835keV		1173keV		1275keV		1332 keV	
No.		Exp.	Theo.	Exp.	Theo.	Exp.	Theo.	Exp.	Theo.	Exp.	Theo.	Exp.	Theo.	Exp.	Theo.	Exp.	Theo.
1.	Dehydrophytosphingosine	21.6343	21.9081	14.9249	15.3357	12.1864	12.3233	11.5017	11.7756	10.4063	10.5433	8.6263	8.9001	8.3524	8.4894	8.0786	8.3524
2.	Myriocin	27.1870	27.5355	18.6475	19.1703	16.0333	16.3819	14.9877	14.8134	13.0706	13.2449	11.5022	11.1536	10.4565	10.6308	10.1080	10.4565
3.	Hemsleyin imine A	41.5538	42.0798	28.6668	29.4558	23.4069	23.6699	22.0919	22.6179	19.9879	20.2509	16.5689	17.0949	16.0429	16.3059	15.5169	16.0429

5. RESULTS AND DISCUSSION

The values of mean atomic numbers calculated from the chemical formulae of sphingolipids studied in the present work are displayed in Table 1. The experimentally measured values of μ_m (cm²/g) for some sphingolipids such as Dehydrophytosphingosine, Myriocin, Hemsleyin imine A at 122, 356, 511, 662, 835, 1173, 1275 and 1332 keV photon energies tabulated in Table 2. The typical plot of μ_m versus energy E for Dehydrophytosphingosine (C₁₈H₃₇NO₃) is displayed in Fig.(2). The Fig.(2) also includes the variation of theoretically determined μ_m values versus energy. It is clearly seen that the μ_m depends on photon energy and decreases with increasing photon energy. The experimental (μ_m) values agree with theoretical values calculated using the Win-XCom program. The total experimental uncertainty of the (μ_m) values depend on the uncertainties of I_0 (without attenuation), I (after attenuation), mass thickness measurements and counting statistics. Typical total uncertainty in the measured experimental (μ_m) values is estimated to be 2-3%. Measured total atomic cross section (σ_{tot}) and molar extinction coefficient (ϵ) values for the presently studied sphingolipids have been displayed in Table 3 and Table 4, respectively. The typical plots of σ_{tot} versus E and ϵ versus E are displayed in Figs.(3) and Fig.(4) respectively. The behavior of σ_{tot} and ϵ with photon energies shows almost similar behavior to (μ_m) plots. All calculations of molar extinction are done according to XCOM program and our calculations are based on Win-XCom which is updated version of XCOM also arrange narrow beam good geometry setup for performing experiment.

The present experimental study has been undertaken to get information on mass attenuation coefficient μ_m values and related parameters σ_{tot} , ϵ for bio-molecules samples which are convenient parameters used to characterize the radiation response of a multi-element material in many technical and medical applications. Accurate values of these physical parameters provide essential data in medical physics and mainly in dosimetry. The μ_m and related quantities were found to decrease with increasing photon energies. The measured data were compared against Win-XCom program.

6. CONCLUSIONS

- ❖ The biological effect of ionizing radiation on human being depends on absorber dose, types of radiation alpha, beta, gamma and organs irradiated. Photon entering the bodies not only lose but also they give rise energy and are finally absorbed, but also they give rise to new photons by multiple scattering. Gamma and X-rays are used for diagnostic in nuclear medicine, computed tomography scanning, radiography, radiotherapy, gamma knife radio surgery etc for treatment of many diseases.
- ❖ The results on μ_m , ϵ , Z_{eff} , and N_{eff} of biological C,H,N,O based compounds, reported in the present work, would be useful, particularly in the energy region of interest, in many medical and biological applications (e.g. for the interpretation of absorbed dose), and in radiation shielding and protection.
- ❖ With proper knowledge of the attenuation parameters and buildup of photons in human organs and tissues, energy-absorption in the human body can be carefully controlled. The experimental data will also help in estimating safe dose levels for radiotherapy patients. For people working with gamma radiation and X-rays, especially at reactors and nuclear power plants, the present studies on the energy-absorption factor of human organs and tissues will help them to take proper precautions.

7. REFERENCES

1. Thudichum, J.L.W., (1884). A Treatise on the Chemical Constitution of Brain. Bailliere, Tindall, and Cox, London.
2. Miras C., (1972). The effect of gamma irradiation, on the lipid metabolism of radiosensitive tissues. IAEA-R-625-F.
3. Kurudirek Murat,(2014). Effective atomic numbers and electron densities of some human tissues and dosimetric materials for mean energies of various radiation sources relevant to radiotherapy and medical a... Radiation Physics and Chemistry 102,139–146.
4. Alfred H., et al., (2002). Sphingolipids: metabolism and cell signaling, Vance D.E. and Vance J.E. (Eds.) Biochemistry of Lipids, Lipoproteins and Membranes (4th Edn).
5. Hakomori S. (1983). Chemistry of glycosphingolipids. In: J.N. Kanfer and S. Hakomori (Eds.), Sphingolipid Biochemistry. Plenum, New York, NY, pp. 1-164.
6. Schuette C.G., Doering T., Kolter T. & Sandhoff K., (1999). The glycosphingolipidoses – from disease to basic principles of metabolism. Biol. Chem. 380, 759-766.
7. McKallip R., et al.,(1999). Tumor Gangliosides Inhibitthe Tumor-Specific Immune, Response; J Immunol,163:3718-3726;
8. Charles R. et al.,(2000). Ceramide-Coated Balloon Catheters Limit Neointimal Hyperplasia After Stretch Injury in Carotid Arteries, Circ Res. 2000;87:282-288.
9. Schmelz E.M., et al., (2001). Modulation of Intracellular-Catenin Localization and Intestinal Tumorigenesis in Vivo and in Vitro by Sphingolipids, Cancer research 61, 6723–6729.
10. Jackson, D.F. & Hawkes,D.J. (1981). X-ray attenuation coefficients of elements and mixtures Phys. Rep.70, 169-233.
11. Kaewkhao J.,Laopaiboon J. & Chewpraditkul.(2008). Determination of effective atomic numbers and effective electron densities for Cu/Zn alloy.Journal of Quantitative Spectroscopy and Radiative Transfer 109 1260-1265.
12. Han I. and Demir L.(2010). Studies on effective atomic numbers, electron densities and mass attenuation coefficients in Au alloys. Journal of X-Ray Science and Technology 18, 39–46.
13. Seltzer S.M. (1993). Calculation of photon mass energy-transfer and mass energy-absorption coefficients. Radiation research 136, 147-170.
14. Hubbell, J. H., (1999). Review of photon interaction cross section data in the medical and biological context Phys.Med.Biol.44:R1-R22.
15. Teli, M. T., Mahajan C.S., Nathuram R., (2001). Measurement of mass and linear attenuation coefficient of gamma rays for varies elements through aqueous solution of salts Indian J Pure Appl. Phys. 39,816-824.
16. Kore, P.S. & Pawar P.P, (2014). Measurement of mass attenuation coefficient, effective atomic number and electron density of some amino acids. Radiat. Phys. Chem.92, 22-27.
17. Kore, P.S., Pawar P.P. & Palani T S (2016). Evaluation of radiological data of some saturated fatty acids using gamma ray spectrometry. Radiat. Phys.Chem. 119,74-79.

STUDY THE MASS ATTENUATION COEFFICIENT OF ALCOHOL SOLUBLE COMPOUND AT ENERGY 511eV**Mitkari S R and Deshmukh V P**

Shri Siddheshwar Mahavidyalaya, Majalgaon, Dist. Beed

ABSTRACT

Linear and mass attenuation of 511eV gamma radiations from alcohol ethanol by dilute solution of Para-nitro aniline ($C_6H_5O_2N_2$) studied for different concentrations. Mixture rule for theoretical calculation of attenuation coefficient is developed for the solution; our study explores the validity of the expected exponential absorption law for gamma-ray radiations in solution and also provides an alternative method for direct determination of linear and mass attenuation coefficients of soluble compound in alcohol.

Keywords: Mass and linear attenuation coefficients, Gamma-rays, HP (Ge) photon detector, Para-nitro aniline and ethanol.

INTRODUCTION

Linear and mass attenuation coefficient for gamma rays for different materials and solutions plays an important role in RSID units. There are different measurement techniques to measure them. As the technology developed day by day, the gamma rays are used in many fields, like medicine, food preservation and with their measurement techniques are developed but we find these measurements can be made with still simpler method. Recently Teli et al has developed the mixture rule and we have modified the rule with simpler approach and are considered for our research work.

This method is developed from single element mass attenuation coefficient of gamma rays to mixtures (solute and solvent) Dongarge S.M. (2010) extended the mixture of liquid and solid materials also. There are various reports on the measurement of these quantities (1-6). Hubbell (3) has developed the rule for calculation of gamma absorption coefficient for mixtures and gave tables of theoretical values for various elements and their mixtures. Teli et al (1994) have measured the attenuation coefficient of 123 Kev gamma radiations by dilute solution of sodium chloride. Dongarge et al (2010) reported the linear attenuation coefficient for measurement of linear attenuation coefficients of gamma ray for ammonium sulfate by aqueous solution method. 1.28 MeV gamma energy.

So for the study of both types of absorption coefficient for gamma rays has been done for materials in solid and crystal forms by using various techniques as reported above and the observations are compared with the theoretical values as calculated from Hubbell's mixture rule and his table

We give here the measurement of mass attenuation of ethanol soluble compound Para-nitro aniline at energy level 511eV for different concentrations.

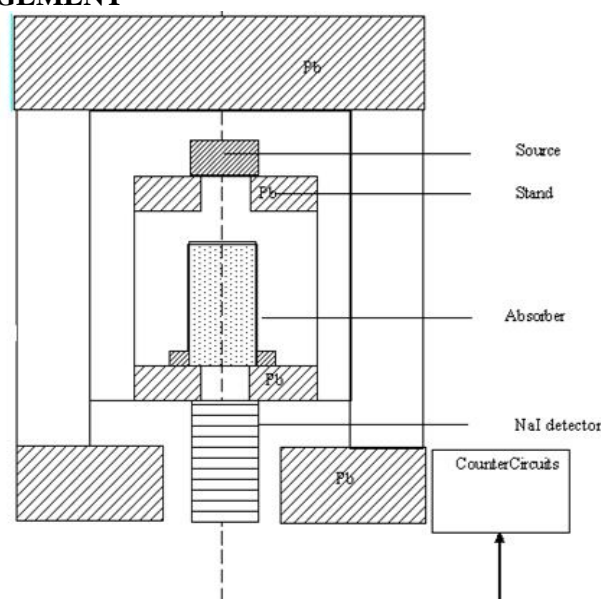
EXPERIMENTAL ARRANGEMENT

Fig-1: Experimental arrangement

The experimental arrangement is as shown in fig. (1) Cylindrical prefix container of internal diameter 2.46 cm was placed below the source at a distance 1.2 cm and above the detector at 2.2 cm by using efficient geometrical arrangement. The NaI (T1) crystal is used as the detector connected to multichannel analyzer. The stand is made up of prefix sheet with suitable size the source and absorber are placed along the axis of the stand the whole system is enclosed in a lead castle.

METHOD OF OBSERVATIONS

First the gamma rays are passed through empty container reaching the detector. The spectrum is obtained for 1800 sec. using MCA which gives plot of channel number Vs counts, we select the interested peak which is smoothed for avoiding the random nature and obtain the peak gross area A_0 (The sum of the spread counts which are coming under the peak) this is obtained because in MCA the counts get spread over some energy range around the photo peak. This increases the accuracy of measured solution kept in the container and gamma rays are passed through it. The concentration varied by p-nitro-aniline compound adding to it. The gamma rays are passed through such solutions and interested peak gross area measured as A_1, A_2, \dots, A_{10} the other quantities measured in the experiment are the volume of para-nitro aniline (V_a) and ethanol V_e added together to give total volume (V).

The actual volume V of the solution is calculated by measuring its height in the container and by multiplying it by the cross-sectional inner area of the container (πr^2). This procedure is repeated for all the concentrations we prepared for gamma energy 511eV.

THEORETICAL DEVELOPMENT FOR THE EXPERIMENT

The graph of $\ln(A_0/A)$ versus height of liquid column h (cm) is measured as shown in graph-1. The observed points are seen to be closely distributed around the line having positive slopes. These lines are obtained by fitting the experimental data by the least square method. Their slope gives the linear coefficient and thus the linearity of the curves with positive slopes suggests the relation.

$$\frac{A}{A_0} = e^{-\mu h} \quad \text{-----} \quad (1)$$

This indicates the validity of the standard exponential absorption law of gamma rays when they pass through liquid substances.

$$A = A_0 e^{-\mu h} \quad \text{-----} \quad (2)$$

We know Hubbell's mixture rule (1982). The mass attenuation coefficient of gamma rays in chemical or any other mixtures of compound is assumed to depend upon the sum of the cross section presented by all the atoms in the mixture because the bonds are only of the order of few electron volts, there have no significant effects on the Compton, photo or pair interaction.

Where, A_0 and A are the initial and final intensities of interacting photons respectively. The μ (cm^{-1}) is linear attenuation coefficient of the sample and h (cm) is the thickness of a material. The linear attenuation coefficient (μ) of the materials from equation (2) is expressed as

$$\mu = \frac{1}{h} \ln \left(\frac{A_0}{A} \right)$$

We have Hubbell's mixture rule the mass attenuation coefficient of gamma rays in chemical or any other mixtures of compound is assumed to be depending upon the sum of the cross sections presented by all the atoms in the mixture because the bends are only of the order of few electron volts; there is no significant effect on the Compton, photo or pair interaction. Mass attenuation coefficient for solution is given by.

$$\frac{\mu}{\rho} = \sum_i W_i \left(\frac{\mu}{\rho} \right)_i \quad \text{-----} \quad (3)$$

Where ρ is the density and which is made up on solution of elements. W_i is the fraction by weight.

The effect of shrinkage on the linear attenuation coefficient of a solution is given by Bragg mixture rule which we assume without approximation for alcohol namely,

$$\left(\frac{\mu}{\rho} \right)_{\text{sol}} = \left(\frac{\mu}{\rho} \right)_a W_a + \left(\frac{\mu}{\rho} \right)_c W_c \quad \text{-----} \quad (4)$$

When the Phenol is dissolved in ethanol then the homogeneous solution is forms. If the solution is homogeneous then one can neglect the density from both sides. If we use this formula for the proposed work in the following way then it will be

$$\mu_{\text{solution}} = \mu_{\text{ethanol}} W_{\text{ethanol}} + \mu_{\text{aniline}} W_{\text{aniline}} \quad \text{-----} \quad (5)$$

Table 1 gives the values using equation (5) for various concentration and theoretical values of (μ_{ethanol}) and (μ_{aniline}) are calculated by multiplying their densities to (μ/ρ) which is calculated by Hubble mixture rule.

$$\frac{\mu}{\rho} = \sum_i W_i \left(\frac{\mu}{\rho} \right)_i \quad \text{-----} \quad (6)$$

SOLUTION TECHNIQUE FOR CALCULATION OF MASS ATTENUATION COEFFICIENT OF PHENOL

The mass (m_p) of the phenol is already weighted using four digit digital balance. Mass of ethanol (m_e) is obtained (at room temp.) by multiplying density of ethanol to volume of ethanol. The cross sectional area of the container is measured, and then the experimental mass-attenuation coefficient for phenol solution is calculated by the formula as

$$\frac{\mu}{\rho} = \frac{A}{m} \ln \left(\frac{A_0}{A} \right) \quad \text{-----} \quad (7)$$

Where - $m = m_p + m_e$ mass of solution

A = gross area obtained for the different concentrations of the solution after passing gamma rays through them.

A_0 = is the initial gross area of the interested peak of the observed spectrum when gamma rays are passed through the empty container.

The Braggs mixture rule for mass attenuation coefficient is given by

$$m \left(\frac{\mu}{\rho} \right) = m_p \left(\frac{\mu}{\rho} \right)_p + m_e \left(\frac{\mu}{\rho} \right)_e$$

The graph of $m \left(\frac{\mu}{\rho} \right) = A \ln \left(\frac{A_0}{A} \right)$ against mass of ethanol gives a straight line whose intercept gives

$m_p \left(\frac{\mu}{\rho} \right)_p$ and slope gives $\left(\frac{\mu}{\rho} \right)_e$. The $\left(\frac{\mu}{\rho} \right)_p$ and $\left(\frac{\mu}{\rho} \right)_e$ values are calculated for phenol and ethanol at 0.84 MeV

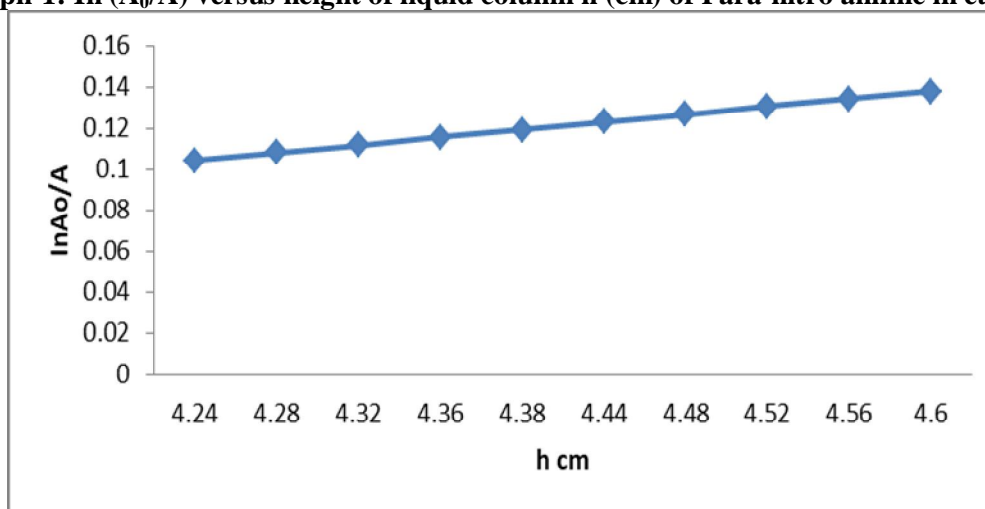
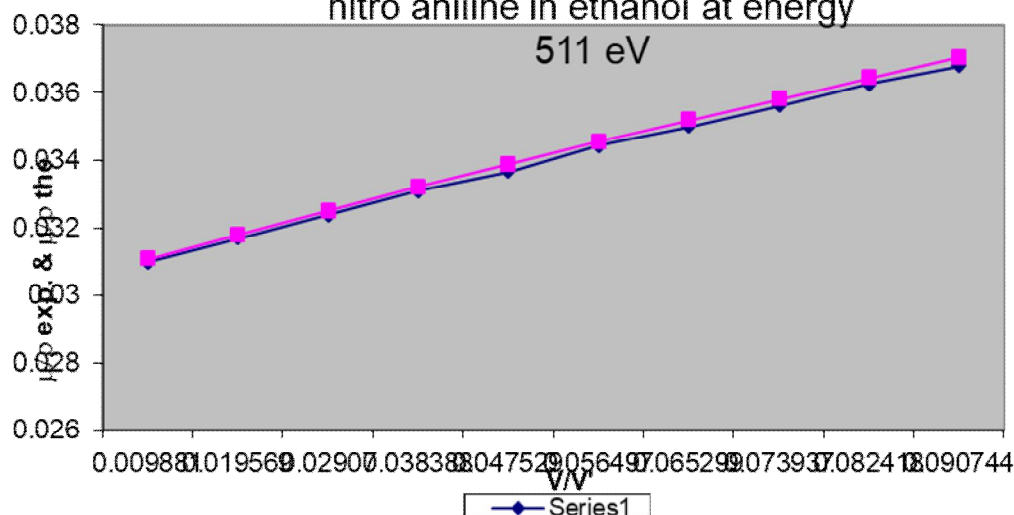
gamma ray energies. The measured values are found to be agreeing well with the theoretical values. The percentage error with respect to theoretical values of mass absorption coefficient of phenol the formula as follows.

$$\% \text{ error} = \frac{\left(\frac{\mu}{\rho} \right)_{\text{the}} - \left(\frac{\mu}{\rho} \right)_{\text{exp}}}{\left(\frac{\mu}{\rho} \right)_{\text{the}}} \times 100 \quad \text{-----} \quad (8)$$

μ/ρ for alcohol and Para-nitro aniline is obtained from Hubbell Table by multiplying its density we get theoretical μ_{the} for alcohol and Para-nitro aniline then by using eq.(5) μ_{the} is obtained, the calculated results are tabulated in table 1 for Para-nitro aniline solution. Eqⁿ (5) is the eqⁿ of straight line between μ_{exp} and concentration in which alcohol volume is fixed. The intercept is the attenuation coefficient for the alcohol and its slop the attenuation coefficient for Para-nitro aniline. We observe from these tables that the experimental values μ_{exp} are within the acceptable limit showing very good agreement. The graph -1 shows the $\ln(A_0/A)$ versus height of liquid column h (cm) of Para-nitro aniline in ethanol. The μ_{exp} (cm^{-1}) and μ_{the} (cm^{-1}) versus concentration v/v' at 511eV gamma ray energy for Para-nitro aniline are shown in graph 2.

Table no-1: Mass attenuation coefficient for Para-nitro aniline solution in ethanol for $A_0=32.7$ and for energy 511 eV

v/v'	A/m	A	$\ln(A_0/A)$	$(\mu/\rho)_{\text{exp}}$	$(\mu/\rho)_{\text{the}}$	%error
0.009881	0.29691	29.46	0.104341667	0.030979693	0.031072088	0.297355211
0.019569	0.29324	29.35	0.108082532	0.031694202	0.031800667	0.334788675
0.02907	0.28966	29.24	0.111837443	0.032395352	0.032511476	0.357177245
0.038388	0.28617	29.13	0.115606507	0.033083657	0.033205157	0.365904994
0.047529	0.28277	29.03	0.1190453	0.033662184	0.033882321	0.649710743
0.056497	0.27944	28.91	0.123187522	0.034423666	0.034543553	0.347060136
0.065299	0.27619	28.81	0.126652529	0.034980398	0.035189407	0.593955485
0.073937	0.27302	28.70	0.130477955	0.035622731	0.035820414	0.551870846
0.082418	0.26991	28.59	0.134318072	0.036254432	0.03643708	0.501269001
0.090744	0.26688	28.49	0.137821929	0.036782195	0.037039888	0.695715887

Graph-1: $\ln(A_0/A)$ versus height of liquid column h (cm) of Para-nitro aniline in ethanol**Graph-2 Mass attenuation coefficient for Para-nitro aniline in ethanol at energy 511 eV**

CONCLUSIONS

Our experimental measurement of mass attenuation coefficient of alcohol soluble Para-nitro aniline for different concentrations and estimated from them the attenuation coefficient for pure compound by using the mixture rule developed by Teli (1998) established the validity and utility of the solution technique. This method is simple and avoids the need of preparation of pure crystalline compound for experiment there by saving time and expenditure. The use of multichannel analyzer has also improved the results as we could replace the counts at the photo peak by the area under it. Further the variation of concentration of solution is made easy by adding alcohol to solution without changing the compound amount in it. This saves the compound quantity and thus further economizes the experiment. The results are in good agreement (Mitkar S R et al 2012).

ACKNOWLEDGMENT

The author is very much thankful to Dr. S.M.Dongarge for his fruitful discussion.

REFERENCES

1. Dongarge S M et al, *Intl J of Phys & Appl ISSN Volume 2, Number 1 (2010)*, pp. 1--8
2. Teli M T Chaudharin L M and Malode S S (**1994a**), *Appli.Rasiat Isot* 45,987
3. Teli M T Chaudharin L M and Malode S S (**1994b**), *Ind.J. of Pure and Appl.Phys.*32, 410
4. Teli M T Chaudharin L M and Malode S S (**1994c**), *Nucl.Instrum.Meths A346*, 220-224
5. Teli M T (**1996**), *Rad. Phy. chem* 47,531.
6. Gerward L: *Rad Phys And Chem* (**1996**) 48,679
7. Hubbell J H *Int J Appl Radiat Isot* (**1982**) 33, 1269
8. Pravina P. Pawar *J. Chem. Pharm.Res.* (**2011**), 3(5); 267-273
9. Midgley S M *Phys. Med. Biol.* 49, (**2004**), 307–25.
10. Mitkar S R and Dongarge S M (**2012**), *J. Chem. Pharm. Res.* 4(8):3944-3949
11. Mitkar S R and Dongarge S M (**2012**), *Arc of Appl Sci Res*, 4 (4):1748-1752

SYNTHESIS OF NANO-COMPOSITE CERIUM-ALUMINA: ADVANCED MATERIAL FOR CATALYTIC SUPPORT

R. M. Belekar¹ and B. A. Shingade²¹Department of Physics, Government Vidarbha Institute of Science and Humanities, Amravati²Department of Physics, Bhavbhuti Mahavidyalaya, Amgaon, Dist.Gondia

ABSTRACT

The catalysts supported on ceria-alumina show higher conversions compared to the one supported on alumina at a temperature range of 800-900°C, which can be attributed to the redox properties of ceria. In the present study, Al₂O₃-CeO₂ mixed nano-composites (1:1) were successfully prepared by using self-sustaining solution combustion synthesis process using aluminium nitrate and cerium nitrate as precursors whereas urea as fuel. The synthesized powders were characterized using X-ray diffraction technique for their phase analysis, BET surface area analyzer for specific average surface area, and transmission electron microscope for particle size. XRD revealed presence of both alumina and ceria phases in Al₂O₃-CeO₂ nano-composite with crystallite size in nanometer scale. TEM images showed that the material was composed of nano-particles with an average size of 35 nm, whereas surface area calculated from BET analysis was found to be 261.0539 m²/g which included an external surface area of 132.2495 m²/g, and a micropore area of 128.8044 m²/g.

Keywords: Al₂O₃-CeO₂, Nanocomposite, BET, surface area, micropore area.

1. INTRODUCTION

Alumina is a porous material and widely used as a catalyst. Its properties differ substantially those of other porous material. Alumina is extensively used in chemical applications due to its high specific surface and its much cleared pore structure. [1] Ceria (CeO₂) is one of the oxides which are mostly used to progress the performance of alumina. [2] CeO₂ is a multifunctional rare earth oxide with various physics and chemical properties. [3] Ceria can affect the structural stability and thermal stability of alumina, the degree of dispersion of a metal catalyst supported on an alumina catalyst carrier. [4] Thus CeO₂-Al₂O₃ is used in many ways of catalytic process. [5-7]

Doping of CeO₂ into Al₂O₃ matrix was found to improve dry reforming activity for H₂ and CO production at the operating temperatures (800–900°C). The catalyst provides significantly higher reforming reactivity and resistance toward carbon deposition compared to the conventional Ni/Al₂O₃. These enhancements are mainly due to the influence of the redox property of ceria [8-13]. This material (ceria) is an important material for a variety of catalytic reactions involving oxidation of hydrocarbons (e.g. automobile exhaust catalysts). It contains a high concentration of highly mobile oxygen vacancies, which act as local sources or sinks for oxygen involved in reactions taking place on its surface [12]. According to the literature [12], during dry reforming process, the gas-solid reaction on ceria surface takes place, which reduces the degree of carbon deposition on catalyst surface from methane decomposition and Boudard reactions. In this study, Al₂O₃-CeO₂ nano composite in ratio 1:1 have been prepared by solution combustion synthesis using urea as fuel and their properties have been studied using various characterization techniques.

2. EXPERIMENTAL

Alumina-Ceria (Al₂O₃-CeO₂) nano-composite were prepared by single step solution combustion synthesis. The precursors involved in this synthesis are aluminium nitrate (Al(NO₃)₃·9H₂O) and cerium nitrate Ce(NO₃)₃·6H₂O, both from Merck (AR Grade). Urea CO(NH₂)₂ is used as fuel because of its relatively low price, availability, commercially grade and safety. The stoichiometric quantities of the oxidizers [Al(NO₃)₃·9H₂O and Ce(NO₃)₃·6H₂O] and fuel [Urea] were mixed in 50 ml deionized water with constant stirring. Aluminum nitrate to Cerium nitrate ratio was maintained 1:1. The solution was then kept on hot plate in order to evaporate more than half of water content. This solution moved to microwave with power of 900 W. After some minutes, first a gel-like structure was obtained and then swelled, followed by the evolution of a large volume of gases. In other word self propagating solution combustion occurred. This reaction product was treated at temperature of 800°C to obtain desired phase of Al₂O₃-CeO₂. The identification and phase determination of the compound were done by powder XRD.

3. RESULT AND DISCUSSION

It can be seen from the figure 1, both alumina and ceria phases exist together. The peaks are relatively broader indicating smaller particle size. The average grain size calculated from Scherrer equation was found to be 30 nm. As mentioned in literature the cerium is present as Ce³⁺ and replaces Al³⁺ in Al₂O₃ lattice. [13]. The alumina and

ceria powders with ratio 1:1 show only the cubic CeO_2 phase because of the relative high peak intensity of ceria peaks over alumina. However, both cubic ceria and γ -alumina phases co-exist.

The TEM images and selected area electron diffraction pattern (SAED) of the Al_2O_3 - CeO_2 nano composite prepared in a ratio (1:1) are shown in **figure 2**. It can be seen from the figure that there are many irregular particle with shape close to spherical. The average particle size can be seen from the TEM images was found to be 35 nm which is close agreement with value calculated from XRD by Scherer formula. The SAED pattern reveals the formation of crystalline phase highlighting various diffraction planes which can be conformed from XRD analysis.

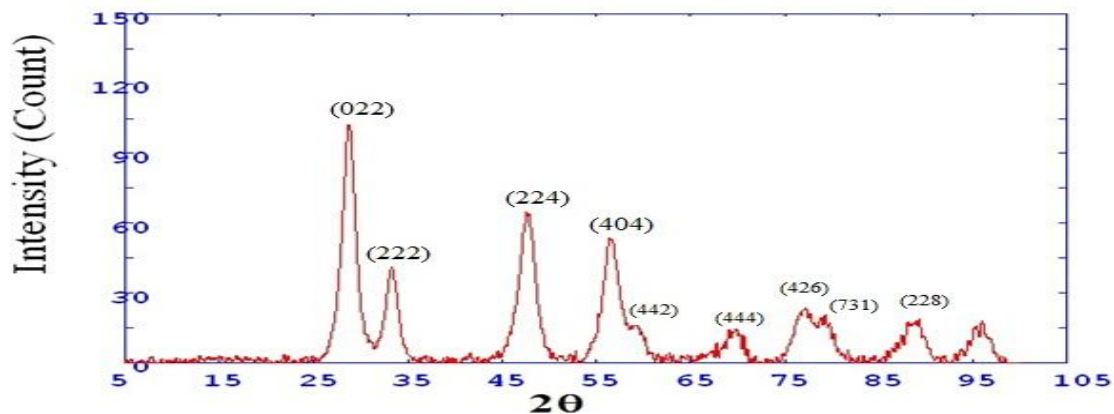


Figure-1: XRD pattern of Al_2O_3 - CeO_2 identified a mixture of a gamma alumina phase (JCPDS file no. 10-0425) and a cubic ceria phase (JCPDS file no. 34-394).

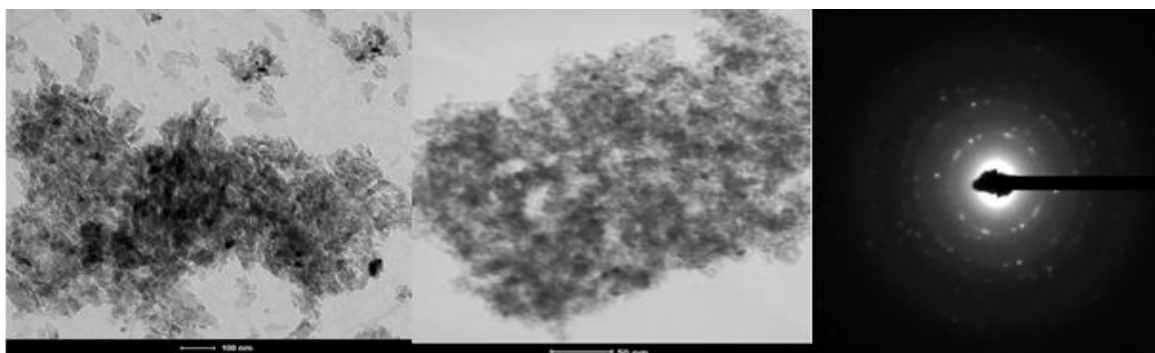


Figure-2: TEM images and SAED pattern of Al_2O_3 - CeO_2 nano composite prepared in a ratio (1:1) sintered at 800°C .

In this study, surface area and micropore volumes of the samples were determined using Micromeritics 2020 (Accelerated Surface and Porosimetry System) BET Surface analyzer. Prior to analysis, 0.6g of sample was first degassed under vacuum at 90°C for 1 hour. Then the temperature was increased to 300°C and degassed overnight. The typical N_2 adsorption isotherms for the Al_2O_3 - CeO_2 nano-composite are shown in **figure 3**. To obtain detailed information about the pore size, the specific surface area, the mesopore volume and the pore size distribution, a N_2 adsorption and desorption isotherm were performed on the Al_2O_3 - CeO_2 nano-composite.

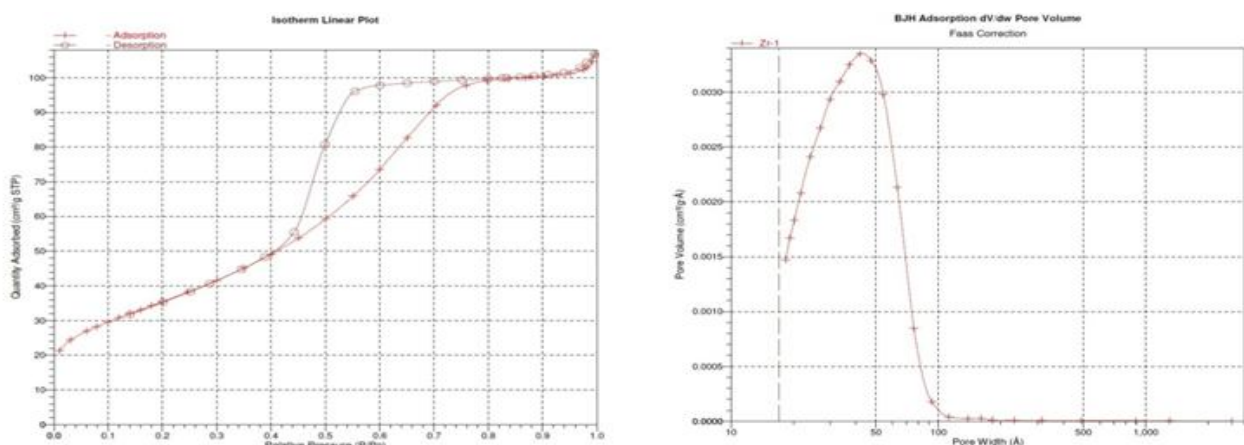


Figure-3: N_2 adsorption/desorption isotherm and pore volume distribution of Al_2O_3 - CeO_2 nano-composite

Using the BET method, a large total surface area of 261.0539 m²/g was obtained which included an external surface area of 132.2495 m²/g, and a micropore area of 128.8044 m²/g which is very high as compared with pure CeO₂ (85 m²/g as reported by *P. Periyat et al*) [15]. Therefore Al₂O₃-CeO₂ system can act as excellent support system for acid catalysis [16], in which Al₂O₃ serves as a support material. A BJH adsorption pore distribution reported an accumulative pore volume 0.172464 cm³/g at cumulative pore surface area of 157.314 m²/g, whereas for desorption BJH method gave a cumulative pore volume of 0.171159 cm³/g at cumulative pore surface area 185.0207 m²/g. Noteworthy, the pores are filled with liquid adsorptive, especially in the case of mesoporous filling. Due to this assumption, the micropore volume was determined using t-plot method; generating a value of -0.002891 cm³/g. The existence of such high surface area and pore volume is due to the evolution of large amount of gases during combustion process. The BJH method for calculating pore size distribution using Kelvin equation generated an adsorption pore diameter of 49.1522 Å, with BJH desorption average pore diameter of 43.852 Å (figure 4). These values are within the acceptable range as compared with the average pore diameter of 37.003 Å obtained using the BET method. However the BET method is used most importantly to investigate surface areas. These values are within the range 20-100 Å which shows the Al₂O₃-CeO₂ nanocomposite falls within the diameter range expected for mesoporous material as per the literature survey conducted by Blasto et al (1965).

4. CONCLUSION

Al₂O₃-CeO₂ nano-composite has been successfully prepared via solution combustion synthesis method. Both the alumina and ceria phases were found in the composite as seen in XRD and SEM. The samples were obtained in nanoscale with average particle size 35 nm. The BET surface area was found to be 157.314 m²/g, with average pore diameter 49.1522 Å showing mesoporous nature of the material which finds many applications in catalytic support. In nano-scale form, the amount of lattice defects such as oxygen vacancy and grain boundary increases as the particle size decreases which results in increase in surface area. Moreover, ceria is expected to play a key role as it can supply oxygen coming from its lattice and replace it through the dissociation of carbon dioxide on its surface. These oxygen vacancies are the active sites for the dissociative adsorption of CO₂, where carbon dioxide adsorbs through the oxygen atom. Charge transfer from the support to the adsorbate is weakening the C-O bond, facilitating the dissociation of CO₂. As a consequence higher CO₂ conversion and lower amounts of carbonaceous deposits are expected.

REFERENCES

1. B. Huang, C.H. Bartholomew, S.J. Smith, B.F. Woodfield, *Microporous Mesoporous Mater.* 165 (2013) 70–78.
2. S.A. Hassanzadeh-Tabrizi, E. Taheri-Nassaj, *J. Alloys Compd.* 494 (2010) 289–294.
3. Y. Huang, Y. Cai, D. Qiao, H. Liu, *Particuology* 9 (2011) 170–173.
4. D.N. Nhiem, L.M. Dai, N.D. Van, D.T. Lim, *Ceram. Int.* 39 (2013) 3381–3385.
5. A. Trovarelli, *Catalytic Science Series*, Imperial College Press., London, 2002.
6. J. Kašpar, P. Fornasiero, M. Graziani, *Catal. Today* 50 (1999) 285.
7. J. Kašpar, M. Graziani, P. Fornasiero, in: K.A. Gschneidner Jr., L. Eyring (Eds.), *Handbook on the Physics and Chemistry of Rare Earths: The Role of Rare Earths in Catalysis*, Vol. 29, Springer, Berlin, 2000, pp. 159–267 (Chapter 184).
8. N. Laosiripojana, S. Assabumrungrat, *Applied Catal. B: Environmental* 60 (2005) 107–116.
9. Belekar, R. M. & Dhoble, S. J., *Nano-Structures & Nano-Objects*. 16. (2018) 322–328.
10. Seung-Chan Baek, Jong-Wook Bae, JooYeong Cheon, Ki-Won Jun, Kwan-Young Lee, *Catal Lett* (2011) 141:224–234.
11. Belekar R. M., *Journal of Physical Sciences*, Vol. 23, 2018, 189–199.
12. N. Laosiripojana, W. Sutthisripok b, S. Assabumrungrat, *Chemical Engineering Journal* 112 (2005) 13–22.
13. R.M. Laine, S. C. Rand, T. R. Hinklin, G. R. Williams, “Ultrafine powders and their use as lasing media,” U.S. Patent 6, December 2, 2003, 656,588.
14. P. Pichestapong, U. Injarean, *Journal of Metals, Materials and Minerals* 20 (2010) 51–54.
15. P. Periyat, F. Laffir, S. A. M. Tofail and E. Magner, **RSC Adv.**, 1, (2011), 1794–1798.
16. A.M. Arias, M.F. Garcia, L.N. Salamanca, R.X. Valenzuela, J.C. Conesa, J. Soria, *J. Phys. Chem. B* 104 (2000) 4038.

EFFECT OF Zn⁺⁺ ION SUBSTITUTION ON DIELECTRIC BEHAVIOUR OF MAGNESIUM FERRITE WITH VARYING FREQUENCY**C. T. Birajdar**

S. M. P. M. Murum, Dist. Osmanabad

ABSTRACT

The samples of zinc substituted magnesium ferrite with formula $MgZn_{1-x}Cr_xO_4$ spinel ferrite systems varying x [$x=0.0-1.0$] were synthesized via standard wet-chemical co-precipitation technique using AR grade sulphate. The formation of single phase cubic spinel structure of all the samples under investigation have been carried out using X-ray diffraction technique at room temperature. The dielectric constant (ϵ'), dielectric loss (ϵ''), dielectric loss tangent ($\tan\delta$) was measured as a function of frequency by using LCR-Q meter. The frequency dependence of dielectric measurements was carried out within the range 100 Hz to 1 MHz. The Knowledge of dielectric loss in ferrite is considered to be originated from two mechanisms namely electron hopping and charge defect dipoles. Electron hopping contributes to the dielectric loss mainly in the low frequency region. In the high frequency region the dielectric loss mainly results from the response of defect dipole to the field. These dipoles in ferrites are found due to the change of cation valance state such as Fe^{3+}/Fe^{2+} , Mg^{2+}/Mg^{3+} during sintering process. It is observed that the dielectric constant (ϵ'), dielectric loss (ϵ''), dielectric loss tangent ($\tan\delta$) appreciable increases with zinc concentration x but decrease with increase in frequency.

Keywords-Mg-Zn spinel Ferrite, XRD, dielectric properties.

INTRODUCTION

Ferrites are ferromagnetic materials with good magnetic, dielectric properties and a large number of technical applications in satellite communication. In recent time processing of ferrites by non-conventional solution technique has gained importance with a view to obtain good quality and high performance materials for various applications [1]. Wet chemical co-precipitation is one of the techniques for synthesis of nano size ferrites.

Ferrites, ferromagnetic cubic spinel possesses the combined properties of magnetic materials and electrical insulators. They have been extensively investigated and being the subject of great interest because of their importance in many technological application [2]. The important, structural, electrical and magnetic properties of nano size ferrites are responsible for their application in various fields[3,4].The spinel ferrites belong to an important class of magnetic materials, because of their remarkable magnetic properties particularly in radio frequency region, physical flexibility high electrical resistivity, mechanical hardness and chemical stability.

Among the different spinel type ferrites the Mg-Zn spinel ferrite system is one of the most versatile, from the point of view of their large number of potential applications[5,6].In the present study, zinc substituted magnesium ferrite ($Mg_{1-x}Zn_xFe_2O_4$) system is prepared by wet chemical co-precipitation technique. The results obtained on structural, electrical and dielectric properties are presented in this work. Magnesium ferrite, $MgFe_2O_4$ is a soft magnetic n-type semi-conducting material [7,8], which finds applications in absorption, sensor and in magnetic technologies. According to crystal structure $MgFe_2O_4$ is inverse spinel ferrites whose degree of inversion depends on the heat treatment. In the present study, zinc substituted magnesium ferrite ($Mg_{1-x}Zn_xFe_2O_4$) system is prepared by wet chemical co-precipitation technique. The aim of present work is to study dielectric loss in ($Mg_{1-x}Zn_xFe_2O_4$) ferrite prepared by wet chemical co-precipitation method.

Experimental details The samples of $Mg_{1-x}Zn_xFe_2O_4$ spinel ferrite systems with varying x [$x = 0.0, 0.2, 0.4, 0.6, 0.8$ and 1.0] were synthesized via wet chemical co-precipitation technique. AR grade sulphates of magnesium, zinc and ferrous were used for the preparation of Mg-Zn ferrites[9,10]. The aqueous solutions of sulphate were prepared using stoichiometric molar proportion. The solutions were mixed together and allowed to settle for 24 hours. The initial pH of the solution was measured. A two molar NaOH solution was prepared and slowly added to the mixed solution. H_2O_2 was also added simultaneously in the mixed solution to increase the oxidation reaction[11,12]. The solution was constantly stirred and heated at low temperature i.e. 600C during the addition of NaOH and H_2O_2 . The NaOH was added in the solution until the precipitate becomes dark brownish in colour and pH of the precipitation become 11. The precipitation is washed several times by acetone and then by double distilled water and then filtered to get fine particles of Mg-Zn ferrites. The fine powders were then heated at 1500C to remove water molecules. The powders were then sintered at 8000C for 10 hours[13,14].

All the synthesis powders were characterized using X-ray diffraction (Philips X-ray diffractometer, model PW3710) technique at room temperature. The XRD patterns were recorded in the 2θ range of 20-80 using Cu-K α radiation. Microstructure and particle size of all the samples were studied using scanning electron microscopy (SEM)[15,16]. IR spectra were recorded using Perkin Elmer spectrometer by the KBr pellet. Each of the sintered disc shaped pellets were polished before electrical measurement for ensuring a good electrical contact. The d.c. / a.c. electrical measurement were carried out in the temperature range 300-850K using two probe method. The dielectric properties were measured as a function of composition and frequency using LCR-Q meter (Model HP 4284A). The dielectric measurements were performed in the frequency range 100 Hz – 1 MHz.

RESULT AND DISCUSSION

XRD (X-ray diffraction):The XRD pattern shows that all the samples possess single-phase cubic spinel structure. The XRD pattern shows the presence of (220), (311), (222), (400), (422), (333) and (440) planes. All these planes belong to face centered cubic structure. The figure shows typical XRD pattern for $x=0.2$. The Bragg's peak are sharp and intense it gives the values of inter-planer spacing and corresponding Miller indices along with the Bragg's angle[10,11]. It is observed that the lattice constant increases slowly by increasing concentration of zinc. Figure shows the X-ray diffraction patterns recorded at room temperature anner spacing 'd' values changes with the composition x .

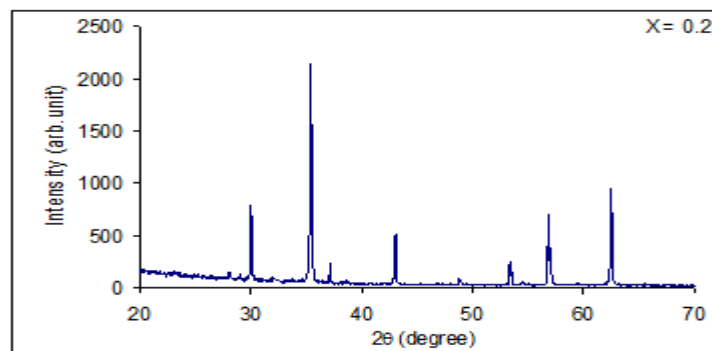
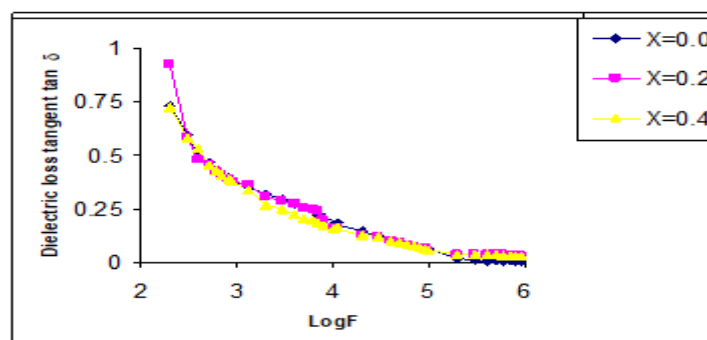


Fig-1: Typical X-ray diffraction pattern of the system ($Mg_{1-x}ZnXFe_2O_4$)for $X = (0.0, 0.2)$

DIELECTRIC PROPERTIES

Frequency dependent dielectric properties of all the samples of Mg-Zn ferrite system are investigated using LCR-Q meter in the frequency range 100 Hz to 1 MHz. The dielectric constant (ϵ') and dielectric loss tangent ($\tan\delta$) are calculated using the relation. Figure shows the variation of dielectric constant ϵ' with $\log F$. It can be observed that the dielectric constant decreases with increasing frequency. The similar behaviour of dielectric constant with frequency was observed in bulk samples of Mg-Zn spinel ferrite [17,18]. The decrease in dielectric constant is of expontional nature. At low frequency the dielectric constant decreases fast for all composition. At high frequency the dielectric constant decreases very slowly.

The behaviour of dielectric loss tangent with frequency is shown in Figure. It is evident from figure that the dielectric loss tangent decreases with increasing frequency. The dielectric behaviour and dispersion phenomenon in spinel ferrite can be explained on the basis of polarization process[19]. The dielectric constant is a function of degree of polarization. As frequency increases beyond the certain frequency, the electronic exchange $Fe^{2+} \leftrightarrow Fe^{3+}$ does not follows the applied alternating field resulting in reduction of dielectric behaviour. All the samples of Mg-Zn spinel ferrite system revealed dispersion due to Maxwell-Wagner interfacial polarization in agreement with Koops phenomenological theory .



Figures: The variation of Dielectric loss tangent ($\tan \delta$) with Log F

CONCLUSION

1. Synthesis of spinel ($Mg_{1-x}Zn_xFe_2O_4$) ferrite was successful carried by wet- chemical co precipitation technique.
2. Single phase cubic spinel structured of various sample obtained successfully by this technique.
3. The dielectric constant ϵ' , dielectric loss ϵ'' and dielectric loss tangent $\tan\delta$ decreases with increase in frequency.

REFERENCES

1. A. Dyal, K. Loss, M.Nato, S.W. Chang, C. Spagnoil, K.V.P.M. Shafi, A. Ulman, M. Cowman, R.A. Gross, J.A.M. Chem. Soc. 125 (2003) 1684.
2. E.J. Choi, Y.Ahn, S.Kim, D.H.An. K.V. Kang, B.G.Lee, K.S. Back, H.N. Oak. J. Magn. Magn. Meter. 263 (2003) L198.
3. C. N.R. Rao, A. K. Cheetam, J. Mater. Chem. 11 (2001) 2887.
4. G.A. Ozin, Adv. Meter. 4 (1992) 612.
5. M. Tsuji, T. Kodama, Yoshida, V. Kitayama, Y. Tamaura J. Catalysis 164 (1996) 315. Li., Mater. Sci. Eng. B34 (1995) I.
6. R.Skmoski J. Phys: Condens, Matter 15 (2003) R841.
7. M.R.J. Gibbs, Curr. Opin. Solid State Material Sci. 7 (2003) 83.
8. R. J. Willey, P. Noirclerc, G. Busca, Chem. Eng. Commun. 123 (1993) 1.
9. E.J. M. Vrewey, E.L. Helimann J. Chemi. Phys. 15 (1947) 174.
10. D. J. Kim. J. Am. Ceram. Soc. 72 (1989) 1415.
11. P. Ingel and D. Lewis J. Am. Ceram. Soc. 69 (1986) 325.
12. H. Klug and L. Alexander, "X-ray diffraction procedure" Wiley, New York (1962) 491.
13. 2C.Prakash. J.Mater. Sci. lett.6(1987)
14. Yu. P. Irkhin, E. Turov. JEPT 33 (1957)
15. Van Uitert L.G, J. Chem. Phys. 24 (1956) 1294
16. C. Prakash, J. S. Basal, J. Less-Common Met. 107 (1985) 51.
17. J.C. Maxwell, Electricity and magnetism, Oxford Univ. Press London 1973
18. K.W. Wagner, Ann phy. 40 (1993) 81
19. C.G. Koops Phy.6 (1997) 108

ENERGY DISPERSIVE X-RAY [EDAX] SEM AND INFRARED SPECTROSCOPY STUDY OF Cd^{2+} SUBSTITUTED TO NICKEL FERRITE NANO PARTICAL

M. B. Solunke and B. H. Devmunde

Department of Physics, Vivekanand Art's Sardar Dallipsing Commerce & Science College, Aurangabad

ABSTRACT

Various method have developed to synthesis Nano-Crystalline Spinal ferrites with superior properties the synthesis of solid can be achieved by number of methods these method include co-precipitation sol-gel, hydrothermal among these synthesis method sol-gel auto combustion is most commonly used the method has advantage like homogeneity good crystallinity and economy the synthesis of nano material is an important orientation for good quality and desired application A series of nano-crystalline sample $\text{Ni}_{1-x}\text{Cd}_x\text{FeO}_4$ ($x=0.0, 0.1, 0.2, 0.3, 0.4$) Were prepared by auto combustion method XRD studies confirm the prepared sample are nano size E-DAX are good agreement with its nominal composition. Infrared spectra showed two distinct absorption band near 400cm^{-1} and 600cm^{-1} at octahedral and tetrahedral sites, indicating spinal ferrites SEM micrograph shows grain growth is uniform

Keywords: Ftir, E-DAX, Spinal Ferrites, SEM

1. INTRODUCTION

Chemically ferrites are very inert substance oxides and many metals are basic and so are soluble in dilute acid oxides of metal are atmospheric and dissolved readily in aqueous solutions of basic oxides the ferrites are very stable even though they one ionic [1] because of their insolubility in ionizing solvents the electrical conductivity of soft ferrite law as compared to magnetic material [2]

The presence of Fe^{2+} ions is sometimes desirable as it reduces magnetostriction and resistivity and conduction mechanism in spinal can explained on basis of small polaron hopping mechanism [3,4] ferrites have vast application to radio frequencies [5] the low conductivity of ferrites cause them for its use in microwave application they exhibit high resistivity and dielectric properties and dielectric properties depend upon method of preparations chemical composition and grain size. The substitution of Cd^{2+} in ferrites is well known to enhance the magnetic and electrical properties like saturation magnetization [6,7]

2. SAMPLE PREPARATION

Nanocrystalline powders of $\text{Ni}_{1-x}\text{Cd}_x\text{Fe}_2\text{O}_4$ ($0.0 < x < 0.4$) were synthesized by using sol gel auto combustion method In this procedure, nickel nitrate hexahydrate ($\text{Ni}(\text{NO}_3)_2 \cdot 6\text{H}_2\text{O}$), cadmium nitrate hexahydrate, ferric nitrate monohydrate, citric acid ($\text{C}_6\text{H}_8\text{O}_7 \cdot \text{H}_2\text{O}$) were used as starting material double distilled water was used as solvent according to the stoichiometric proportion of $\text{Ni}_{1-x}\text{Cd}_x\text{Fe}_2\text{O}_4$, (Where $X=0.0, 0.1, 0.2, 0.3, 0.4$)

All the nitrates were separately dissolved in distilled water and stirred on magnetic stirred for 20 minutes. All the solutions were mixed together and stirred on a magnetic stirrer until the nitrates were completely dissolved. The metal nitrate to citric acid ratio was taken as 1:3 The solution were stirred the continuous stirring on magnetic stirrer; drop by drop ammonia solution was added to adjust the pH value to 7. Then the solution was heated on hot plate at 900°C with constant stirring until gel was formed. Instantaneously gel ignites with the formation of large amount of gas, resulting in to light weight voluminous powder. The resulting precursor powder was annealed at 700°C for 6 h to obtain $\text{Ni}_{1-x}\text{Cd}_x\text{FeO}_4$ nano crystalline material.

3. ENERGY DISPERSIVE X-RAY ANALYSIS [EDAX]

The EDAX measurement was done in order to determine the chemical composition on the surface of the sample to support our observation on the structure of the ferrites the typical EDAX pattern $\text{Ni}_{1-x}\text{Cd}_x\text{Fe}_2\text{O}_4$ are shown in fig. a

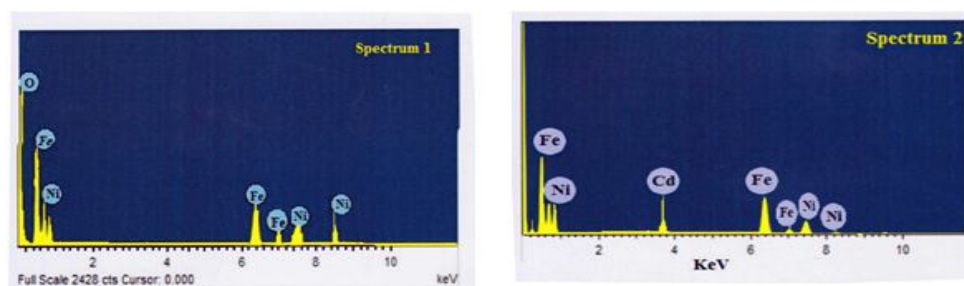


Fig-a

4. INFRARED SPECTROSCOPY (IR)

The IR spectra of $\text{Ni}_{1-x}\text{Cd}_x\text{FeO}_4$ samples are shown in fig. b.

Indicating the two absorption bands in wave number range $350\text{--}800\text{ cm}^{-1}$ it has been reported that the occurrence of 600 cm^{-1} and 400 cm^{-1} band are attributed to the intrinsic vibrations of tetrahedral and octahedral groups respectively [8,9]

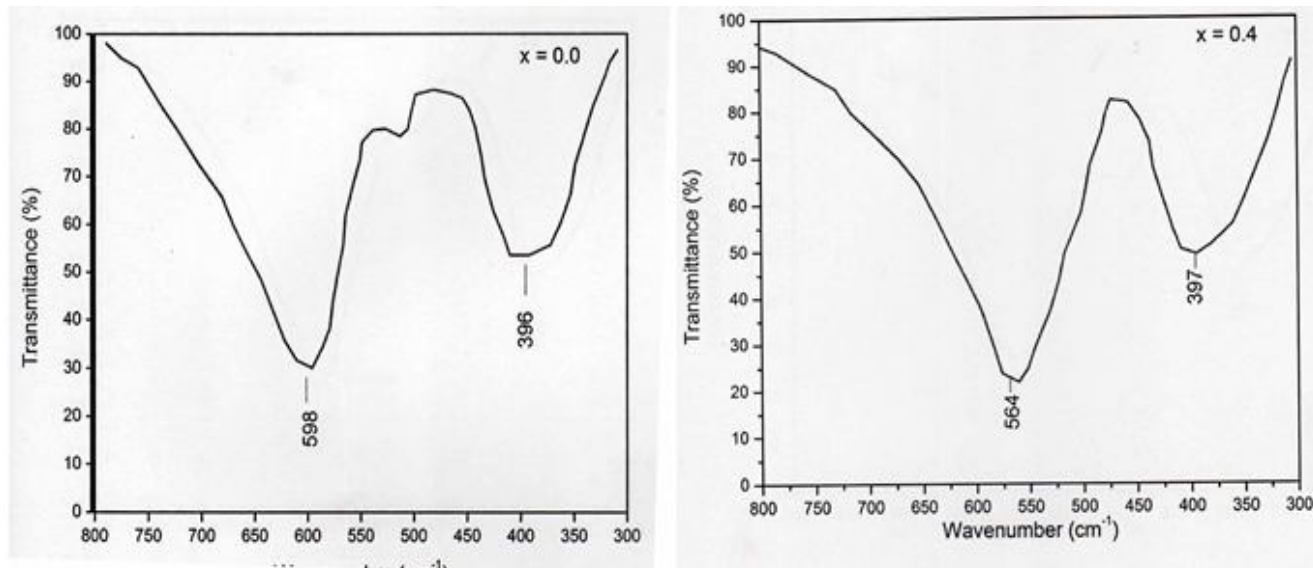


Fig-b

5. SCANNING ELECTRON MICROSCOPY (SEM)

Average grain size and surface morphology of Cd^{2+} substituted $\text{Ni}_{1-x}\text{Cd}_x\text{FeO}_4$ nano particles were determined by using scanning electron microscope technique by selecting 35000 magnification range. SEM images for $x=0.0$ & 0.1 and shown in fig. c micrograph shows the grain growth is uniform and porous and uniform microstructure with spherical morphology of ferrite sample

The effect of Cd substitution on microstructure NiFe_2O_4 can be explained in terms of the increase pore mobility due to erection or excess caution vacancies [10]

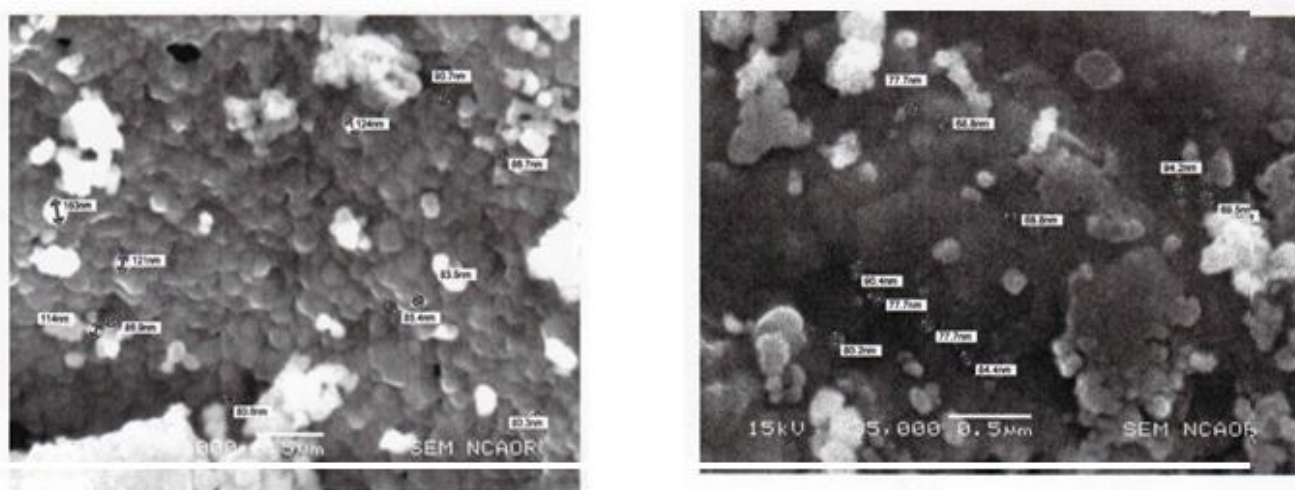


Fig-c

CONCLUSION

- Cd^{2+} substituted nickel ferrites, with nominal compositions $\text{Ni}_{1-x}\text{Cd}_x\text{FeO}_4$ ($0.0 \leq x \leq 0.4$) nanoparticles were successfully synthesized by a sol-gel auto combustion method.
- The average grain size obtained from scanning electron microscopy was found in the range of 80-102nm.
- Energy dispersive spectroscopy analysis confirmed that the synthesized sample were near stoichiometric.
- Infrared spectra exhibit two distinct absorption bands near about 400 cm^{-1} and 600 cm^{-1} at octahedral and tetrahedral sites, respectively indicating the characteristic features of spinel ferrites.

REFERENCES

- [1]. Sefanita, C.-G from Bulk to nano: the many sides of magnetism,. springer Science & Business Media: **2008**; Vol.117.
- [2]. Stoppels, D., Joural of Magnetism and Magnetic Materials 1996 160, 323-328.
- [3]. Kambale R; Shaikh P; Bhosale C.; Rajpure K; Kolekar Y, Smart Materials and structures 2009 18(8) 085014.
- [4]. Austin I; Mott, N.F., Advances in Physics **1969**, 18(71), 41-102.
- [5]. Pardavi-Horvath, M., Journal of Magnetism and Magnetic Materials 2000. 215, 171-183.
- [6]. Batoo, K.M.; Kumar, S; Lee, C.G., Current Applied Physics 2009, 9(4), 826-832.
- [7]. Farea, A; Kumar, S; Batoo,K.M; Yousef,A; Lee, C.G.,Journal of alloys and compounds 2008, 464(1), 361-369.
- [8]. Pradeep,A.; Priyadharsini,P; Chandrasekaran, G., Journal of Magnetism and Magnetic Materials 2008, 320(21), 2774-2779.
- [9]. Pradeep,A.; Chandrasekaran, G., Materials Letters 2006m 60(3), 371-374.
- [10]. Shokrollahi,H.; Janghorban, K., Materials Sciences and engineering: B 2007, 141 (3),91-107.

INVESTIGATION OF PHYSICOCHEMICAL PROPERTIES USING LCR METER TECHNIQUE

P. T. Sonwane and S. R. Gaur

Sants Ramdas Arts, Science & Commerce College, Ghansawangi, Dist. Jalna

ABSTRACT

Study of Physicochemical Properties like Viscosity, Density and Refractive Index for Binary Mixture of 1-Propanal+2-butoxyethanol. Concentration range are measured at 308 K, the experimental data further use to determine the excess properties Viz. Excess molar Volume, Excess viscosity and excess molar refraction. The values of excess Properties further Fitted with Redlich-Kister equation to calculate the binary Coefficients. The resulting Excess Parameters are used to indicate the presence of intermolecular interactions and strength of Intermolecular interactions between the molecules in the binary mixtures.

Keywords: Dielectric Constant, Density, Viscosity, Refractive Index, LCR meter.

INTRODUCTION

The study of binary liquid mixtures provides sensitive tool for detecting molecular interactions. In order to study the effect of increase of molecular size on solute solvent interaction the series of alcohols and alkoxyalkanols are selected because no attempts have been made to study this

binary system. Alcohols play an important role in many chemical reactions [1-4] due to their ability to undergo self-association with manifold internal structure and are in wide use in industry and science as reagent, solvent and fuels. Monoalkylethers of [5] ethylene glycol may exist in dynamic equilibrium existing in Gauche as well as open chain form. In this case monoalkyl ethers of dimethylene glycol intermolecular hydrogen bonding decreases with the increase in the size of the alkyl group. These molecules are also found to exist in both intermolecular hydrogen bonded form in equilibrium with open chain form in dilute solutions. The intermolecular association is found to be absent in dilute solutions, whereas in pure liquid state the molecule existing in open chain may form multimers [6]. Because of such interesting facts it is decided to carry out dielectric relaxation study of Alcohols with Alkoxyalkanols.

EXPERIMENTAL DETAILS

The setup consists of Digitizing oscilloscope Auto compute LCR QMETER et Model 4910

Density Measurement: The Density measurement were Carried out by Portable Digital Density Meter (Anton Paar-35) for pure liquids and binary mixture.

Viscosity Measurements: Viscosity of the sample in the present study were measured by using Brookfield Viscometer Model LV DV-II+Pro, Cone plate Model with CPE-40 Spindle.

Refractive Index: Measurement: Refractive Index Measurement are Studied using Abbeys Refractometer. LCR Meter Technique: Dielectric Constant were measured in the Present Study By using Auto compute LCR Q-METER et Model 4910

RESULTS AND DISCUSSIONS

Table-1: Excess Molar Volume of 1 Propanol+2-butoxyethanol Ethanol at 308 K.

Volume of fractional 1-Propanal+2-butoxyethanol	Density	Viscosity	Refractive Index	Dielectric Constant
0	0.7935	0.541	1.332	6.8
0.163	0.7932	0.549	1.336	7.64
0.305	0.793	0.587	1.339	8.40
0.429	0.7928	0.610	1.411	9.30
0.539	0.7925	0.665	1.414	10.30
0.637	0.7922	0.692	1.416	11.50
0.724	0.792	0.768	1.418	12.80
0.803	0.7917	0.835	1.422	14.30
0.875	0.7914	0.892	1.425	15.95
0.940	0.791	0.9850	1.427	17.30
1	0.7907	1.014	1.432	19.10

The existence of an intermolecular interaction through hydrogen bounded structures between Binary Mixtures. Dielectric relaxation study of liquids generally carried out on dilute solution of polar and non-polar liquids or binary mixture in dilute solutions of non-polar liquids and on mixtures of polar liquids or simply binary mixtures. A large amount of work has been done on dilute solutions. Difficulty arises in measuring the dielectric absorption data in pure liquids

because of its viscosity, bipolar interactions and internal field. Therefore, dielectric properties are usually carried out in dilute solutions of non-polar solvents. In these cases polar molecules will be quasi isolated state.

CONCLUSION

If a dielectric medium consists of polar molecules (permanent dipole) then the dipoles are oriented at random in the absence of an external electric field when an electric field is applied then the forces acting on a dipole give rise to a couple whose effect is to orient the dipole along the direction of electric field. Thus the polar molecules become induced dipoles when they are oriented by the field and therefore their dipole moments get increased. This phenomenon is known as orientation polarization.

ACKNOWLEDGEMENT

The Authors wish to thank Dr S. R. Gaur this work and UGC for providing fund to do this Work also Department of Physics Sant Ramdas ACS College Ghansanwani Dist. Jalna

REFERENCES

1. Pradeep Gaikwad P T Sonwane S R Gaur International Journal of Universal Print Vol. 4 Issue 1 (2018), 57-59.
2. P. Sivagurunathan, K. Dharmalingam, K. Ramachandran, B. Prabhakar Undre, P.W. Khirade, S.C. Mehrotra Physica B., 387 (2007), 203-207.
3. K. Dharmalingam, K. Ramachandran, P. Sivagurunathan, B. Prabhakar Undre, P.W. Khirade and S.C. Mehrotra J. Molecular Physics, 104, 18, (2006), 2835-2840.
4. P. Sivagurunathan K. Dharmalingam K. Ramachandran B. Prabhakar Undre, P.W. Khirade and S.C. Mehrotra. J. Mol. Liq. 133 (2007) 139-145.
5. H.D. Purohit and R.J. Sengwa J. of molecular Liquids, 47 (1990) 53-62.
6. Pradeep Gaikwad. Prashant Sonowane Journal of medical chemistry and Drug Delivery, 2(2017), 502-504.

SYNTHESIS AND CHARACTERISATION OF POLYCRYSTALLINE Mn^{4+} DOPED Cu-Zn FERRITEPadampalle A. S.¹, Labde B. K.², Suryawanshi A. D.³ and Suryawanshi D. D.⁴Assistant Professor¹ and Associate Professor², Department of Physics, S. C. S. College, OmergaAssistant Professor³, Department of Physics, B. J. College, PuneDepartment of Chemistry⁴, S. C. S. College, Omerga

ABSTRACT

Polycrystalline spinel ferrites are prepared by using double sintering ceramic method. In this, ferrite material shows single phase cubic spinel structure verified by X-ray diffractometer techniques. Lattice constant changes with changing Mn ion concentration. Generally, lattice constant is affected by the surface reconstruction that results in a deviation from its mean value. Theoretical values of lattice constant are good agreed with experimental values. The ionic radii of tetrahedral (A) site goes on increases and that of octahedral [B] site goes on decreases linearly. X-ray density increases with Mn ion concentration, bulk density reflect same behavior as X-ray density where as porosity decreases with increasing Mn ion concentration. Particle size increases with increasing Mn ion Concentration. IR spectra of system Mn-Cu-Zn ferrites have been analyze in the frequency range 200-800 cm^{-1} . Two absorption bands are observed in the frequency range 585-593 cm^{-1} and 410- 413 cm^{-1} . The force constant K_t abruptly changes with composition x and K_o increases linearly with increasing composition x .

Keywords: Spinel ferrites, X-ray diffraction, particle size, porosity, IR.

1. INTRODUCTION

Now days, a wide variety of ferrite cores are available, resulting in a great expansion in the field of its application both in consumer equipment such as radio, tape recorders and T. V. receivers as well as professional equipment such as computers, control equipment, telephone exchanges, transmission equipment, etc.

Copper ferrite and copper containing ferrites have been focus of continuous interest in many years. The application of Mn-Zn ferrites in power electronics is constantly increasing. Particularly the growth of commercial market for switch mode power supplies demands on ferrite industry to produce high performance ferrite cores capable of operating at increasingly higher frequencies [1]. Recently, many efforts have been made to develop low power loss Mn-Zn ferrites for application at high frequencies [2, 3]. Mn containing ferrites have various applications such as electromagnetic interference [4], transformers [5], asymmetric digital subscriber line [6] etc. Otherwise, the processing techniques have been a sensitive factor for the magnetic properties. The magnetic properties of Mn-Zn ferrite depend upon their chemical composition, grain size etc. [7]. In this paper, the attempt has been made to investigate the effect of Mn^{4+} ion on copper-zinc ferrite to study structural and infrared properties.

2. EXPERIMENTAL DETAILS

The standard double sintering ceramic technique is used to prepare polycrystalline spinel ferrites having compositional formula $Cu_{0.7+x}Zn_{0.3}Mn_xFe_{2-2x}O_4$ where $x=0.0, 0.1$, and 0.2 . The analytical reagent oxides such as CuO, ZnO, MnO_2 and Fe_2O_3 (all are 99.9% pure) are used. They are weighed and mixed in their proper proportions and ground in agate mortar for minimum two hours. For pre-sintering, the samples are heated at 700°C for 12 hours in muffle furnace and then slowly cooled to room temperature. Then again samples were ground for minimum two hours. The pellets were made by applying a pressure of 5 ton/inch² for 10 minutes. Finally, these pellets and remaining samples are sintered at 980°C for 24 hours and slowly cooled to room temperature.

To study structural behavior, X-ray diffraction pattern were recorded at our Department, Shri Chhatrapati Shivaji College, Omerga on Regaku Miniflux II, Desktop X-ray diffractometer using $CuK\alpha$ radiation ($\lambda=1.54056$ Å). To study the absorption bands, IR spectra in the range 200 to 800 cm^{-1} were recorded at room temperature on infrared spectrometer (model 783 Perkin –Elmer).

3. RESULTS AND DISCUSSION

3.1 X-ray diffraction

Fig. 1 shows X-ray diffraction pattern of polycrystalline spinel ferrites having chemical formula $Cu_{0.7+x}Zn_{0.3}Mn_xFe_{2-2x}O_4$ where $x=0.0, 0.1$ and 0.2 . X-ray diffraction pattern shows a sharp diffraction line which confirms the single phase spinel structure.

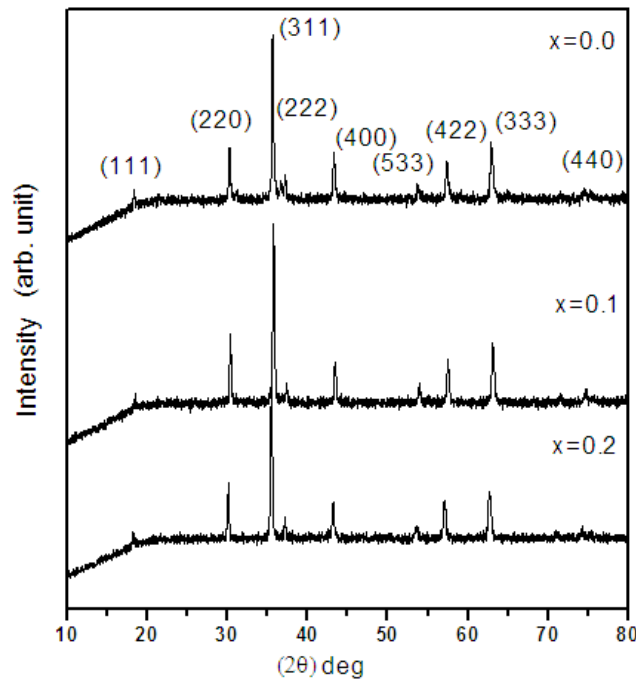
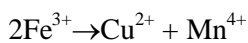


Figure-1: XRD Pattern of polycrystalline spinel ferrite $\text{Cu}_{0.7+x}\text{Zn}_{0.3}\text{Mn}_x\text{Fe}_{2-2x}\text{O}_4$ system where $x= 0.0, 0.1$ and 0.2 . The planes observed are (111), (220), (311), (222), (400), (422), (333), (440) and (533) which corresponds to the allowed values for cubic spinel structure. Bragg's peak (311) observed at an angle $2\theta \approx 35.33^\circ$ which indicate formation of ferrite material.

Lattice constant ' a ' is determined by knowing the values of interplanar distance ' d ' and miller indices h, k , and l using relation $a = d\sqrt{h^2 + k^2 + l^2}$. The Values of lattice constant ' a ' decreases linearly from 8.4190 to 8.4102 Å° with increasing composition ' x ' is as shown in table 1.

The decrease in lattice constant ' a ' with composition ' x ' is due to replacement of 2Fe^{3+} (0.64Å°) ion by Cu^{2+} (0.72 Å°) and Mn^{4+} (0.52 Å°) ions i.e.



Regarding that ionic radius of 2Fe^{3+} ions are larger than that of Cu^{2+} and Mn^{4+} ions. So that increase of Mn^{4+} ion concentration leads to decrease of lattice constant which obeys Vegard's laws [8]. Similar behavior of lattice constant also reported in study of Ge^{4+} [9].

Theoretical value of lattice constant can be calculated using the values of tetrahedral and octahedral radii (r_A and r_B) and is given by the relation [10],

$$a_{th} = \frac{8}{3\sqrt{3}}[(r_A + r_O) + \sqrt{3}(r_B + r_O)]$$

where R_o is radius of oxygen ions (1.32Å°).

The cations distribution of given samples should be known to calculate r_A and r_B . According to cations distribution of given series, the value of r_A and r_B can be calculated as,

$$r_A = [t r_{\text{Cu}^{2+}} + x r_{\text{Zn}^{2+}} + (1 - x - t) r_{\text{Fe}^{3+}}]$$

and

$$r_B = \frac{1}{2}[(1 - x - t + y) r_{\text{Cu}^{2+}} + y r_{\text{Mn}^{4+}} + (1 + x + t - 2y) r_{\text{Fe}^{3+}}]$$

where $r_{\text{Cu}^{2+}}$, $r_{\text{Mn}^{4+}}$, $r_{\text{Zn}^{2+}}$ and $r_{\text{Fe}^{3+}}$ is the ionic radius of copper (0.72 Å°), manganese (0.52 Å°), zinc (0.83 Å°) and iron (0.64 Å°) respectively.

Theoretical value of lattice constant (a_{th}), experimental values (a), ionic radii (r_A and r_B) are tabulated in table 1. It is observed that theoretical values of lattice constant are good agreed with experimental values. The ionic radii of (A) site goes on increasing linearly by values $\approx 0.0248 \text{ \AA}$ and [B] site goes on decreasing linearly by values $\approx 0.032 \text{ \AA}$. This increase or decrease in ionic radii on tetrahedral and octahedral site depends upon the site preference of cations.

The X- ray density ' d_x ' is calculated using the relation, $d_x = \frac{ZM}{NV}$

where Z is number of molecules per unit cell ($Z=8$), M is molecular weight, N is Avogadro's number (6.023×10^{23}) and $V (= a^3)$ is volume of unit cell. The values of X-ray density are increases and bulk density decreases with increasing composition 'x' as shown in table 1. This increasing X-ray density is attributed to decrease in lattice constant and increase in molecular weight of compositions.

The percentage porosity was calculated using the relation, $P = (1 - \frac{d}{d_x}) \times 100\%$ where d is bulk density and d_x is X-ray density. Porosity decreases as Mn content increases which reflects the opposite behavior of density.

The particle size of each composition is calculated by using Scherrer's formula, $t = \frac{0.9\lambda}{B \cos \theta}$ where λ is

wavelength (1.54056 \AA) of Cu target, B is full width at half maximum diffracted line in radian. The values of particle size is as shown in table 1. Particle size increases with increasing Mn ion concentration which is consistent with particle size prepared by ceramic techniques.

Table-1: Compositional variation of theoretical and experimental values of lattice constant, ionic radii of (A) and [B] site, X-ray density, bulk density, porosity and particle size of the $\text{Cu}_{0.7+x}\text{Zn}_{0.3}\text{Mn}_x\text{Fe}_{2-2x}\text{O}_4$ system.

(x)	Theo. value of lattice Constant (a_{th}) in \AA	Expt. value of lattice Constant (a_{th}) in \AA	Ionic Radii of A-site and B-site		X-ray density d_x in (gm/cm^3)	Bulk density d in (gm/cm^3)	Porosity P in(%)	Particle size t in (\AA)
			r_A (\AA)	r_B (\AA)				
0.0	8.4068	8.4190	0.6986	0.6671	4.819	4.9707	6.84	187.6
0.1	8.4022	8.4140	0.7010	0.6640	5.376	4.7492	11.40	268.0
0.2	8.3973	8.4102	0.7034	0.6608	5.408	4.7852	11.10	277.9

3.2 IR studies

Fig. 2 shows IR spectra of polycrystalline spinel ferrites having chemical formula $\text{Cu}_{0.7+x}\text{Zn}_{0.3}\text{Mn}_x\text{Fe}_{2-2x}\text{O}_4$ where $x=0.0, 0.1$ and 0.2 . There are two absorption bands are observed in expected region of IR.

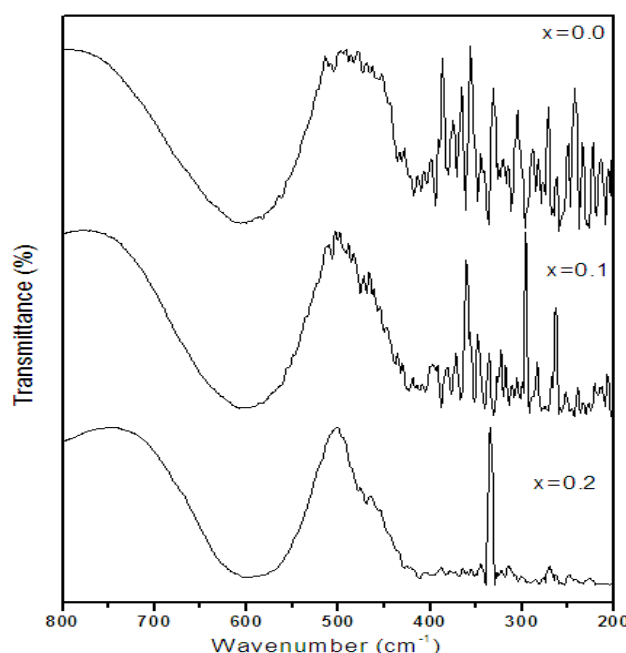


Figure-2: IR absorption band positions of polycrystalline spinel ferrite $\text{Cu}_{0.7+x}\text{Zn}_{0.3}\text{Mn}_x\text{Fe}_{2-2x}\text{O}_4$ system where $x=0.0, 0.1$ and 0.2

The band position, force constant and bond length are summarized in table 2. According to Waldron [11], the Band ν_1 is arises due to the stretching vibration of tetrahedral complexes and ν_2 to that of octahedral complexes. The high frequency band ν_1 is obtained in the range of 585-593 cm^{-1} and is related to the intrinsic vibrations of tetrahedral group and second band ν_2 is in the range of 410- 413 cm^{-1} and is due to octahedral metal complexes. An absorption band positions increases with increasing composition x . This difference in position of bands for the various compositions was expected because of difference in the distances for the octahedral and tetrahedral ions [12]. The difference in position of two strong bands ν_1 and ν_2 could be related to the difference in $\text{Fe}^{3+} - \text{O}^{2-}$ distance for A- sites and B-sites [13]. The similar observations have been made by Srinivasan et al. [14]. Most of the workers [15-16] have also observed the IR bands in the ferrites and their conclusions are in agreement with result of Waldron.

The force constant at tetrahedral site K_t and octahedral site K_o have been obtained from the infrared absorption data. The values of K_t abruptly changes with composition x and K_o increases linearly with increasing composition x as shown in table 2.

Table-2: Compositional Variation of band position, force constants and bond lengths of the $\text{Cu}_{0.7+x}\text{Zn}_{0.3}\text{Mn}_x\text{Fe}_{2-2x}\text{O}_4$ system.

(x)	Band position		Force constant		Bond length	
	$\nu_1 \text{ cm}^{-1}$	$\nu_2 \text{ cm}^{-1}$	K_t dyne/cm	K_o dyne/cm	R_A (\AA°)	R_B (\AA°)
0.0	585	410	15349.9	10437.0	0.5028	0.7847
0.1	590	412	14887.8	10534.0	0.5017	0.7835
0.2	593	413	14946.02	10717.0	0.5009	0.7826

The molecular weight of tetrahedral and octahedral site has been calculated by assuming the cations distribution formula. The bond length R_A and R_B values are obtained by using relation,

$$R_A = (u - \frac{1}{4})a\sqrt{3} - r(\text{O}^{2-})$$

$$R_B = (\frac{5}{8} - u)a - r(\text{O}^{2-})$$

$$\text{where } u = \frac{3}{8} \text{ and } r(\text{O}^{2-}) = 1.32 \text{ \AA}.$$

The values of bond length R_A and R_B both decreases with increasing content of Mn^{4+} . This decrease of bond length should be normally leads to increase in force constant.

4. CONCLUSION

From X-ray diffraction pattern, it is observed that the Mn^{4+} doped Cu-Zn ferrites confirm cubic spinel structure. Lattice constant decreases with increasing composition x . Theoretical values of lattice constant are good agreed with experimental values. The ionic radii of (A) site goes on increases and that of [B] site goes on decreases linearly. Porosity decreases as composition x increases which reflects the opposite behavior of density. Particle size increases with increasing composition x . Two main IR absorption bands are observed, the high frequency band ν_1 is obtained in the range of 585-593 cm^{-1} and low frequency band ν_2 is observed in the range of 410-413 cm^{-1} . The force constant K_t and K_o changes with composition x and it is attributed to decrease in bond length.

ACKNOWLEDGEMENT

The authors are thankful to our Bharat Shikshan Sanstha, Omerga for providing XRD facility in our institute.

REFERENCES

1. Jianhu Nie, Haihua Li, Zekun Feng and Huanhui He, (2003), Journal of magnetism and magnetic materials, 265, 172-175.
2. Otsuki E, Yamada S., Otsuka T., Shoji K. and Sato T. (1991), journal of applied physics, 69, 5942.
3. Takadate K., Yamamoto Y., Makino A., Yamaguchi T. and Sasada I. (1998), journal of applied physics, 83, 6861.
4. Arshak K. I., Ajina A. and Egan D., (2001), Microelectron Journal, 32, 113.

-
5. Lee J. H., Martin M. and Yoo H. I. (2000), Journal of Physics and chemistry of solids 61, 1597.
 6. Ott G., Wrba J. and Lucke R. (2003), Journal of magnetism and magnetic materials, 254-255, 535.
 7. Costa A. C. F. M., Tortella E., Morelli M. R. and Kiminami R. H. G. A (2003), Journal of magnetism and magnetic materials, 256, 174.
 8. Winfrey C. G., Eckort D. W. and Tauber A., (1960), Journal of American Chemical Society, 82, 2695.
 9. Padampalle A. S. and Birajdar D. S. (2012), International journal of basic and applied research, Vol. 02, 93-100.
 10. Hemeda O. M. and El-Saadawy M. (2003) Journal of magnetism and magnetic materials, 256, 67.
 11. Waldron R. D., (1955), Physics review, 99, 1727.
 12. Amer M. A. and Hemeda O. M. (1995), Hyperfine Interaction, 96, 99-109.
 13. Evans B. J. and Hafner, (1968), Journal of Physics and chemistry of solids, 29, 1573.
 14. Srinivasan T. T., Srivastava C. M., Venkataramani N. and Patni M. J. (1984), Bulletin of material science, 6, 1063.
 15. Bellad S. S., Pujar R. B. and Chougule B. K. (1998), Indian Journal of pure and applied physics 36, 598.
 16. Patil S.A., Mahajan V.C., Ghatage A.K., Lotke S.D. (1998), Materials chemistry and physics, 57, 88.

STUDY OF MAGNETIC PROPERTIES OF $\text{MgZn}_x\text{Mn}_x\text{Fe}_{2-2x}\text{O}_4$ SPINEL FERRITE SYSTEMSS. V. Kshirsagar¹, S. S. Raut², P. R. Maheshmalkar³, S. J. Shukla⁴ and K. M. Jadhav⁵^{1, 2, 3}Department of Physics, Mrs. K. S. K. College, Beed⁴Department of Physics, Deogiri College, Aurangabad⁵Department of Physics, Dr. B. A. M. University, Aurangabad

ABSTRACT

The samples of $\text{MgZn}_x\text{Mn}_x\text{Fe}_{2-2x}\text{O}_4$ spinel ferrite systems with varying x [$x = 0.0, 0.1, 0.2, 0.3, 0.4, 0.5$ and 0.6] were synthesized by double sintering ceramic method. A. R. grade oxides of magnesium, zinc, manganese and ferric were used for the preparation of $\text{MgZn}_x\text{Mn}_x\text{Fe}_{2-2x}\text{O}_4$ ferrite.

All the synthesis powders were characterized by using X-ray diffraction (Philips X-ray diffractometer, Model PW3710) technique at room temperature. The X-ray diffraction patterns were recorded in the 2θ range of 20° - 80° using $\text{Cu-K}\alpha$ radiation. The magnetic properties were measured using pulse field technique provided by Magneta company.

INTRODUCTION

The spinel ferrite represented by the formula MFe_2O_4 (where, $\text{M} = \text{Ni}, \text{Cu}, \text{Mn}, \text{Co}, \text{Fe}$, etc.) have a value for many technological applications due to their insulating property, high permeability, and moderate magnetization. The spinel ferrites are used in high frequency transformers, filters, isolators, automobiles, communication equipments, radio, television, and microwave and satellite communication [1].

Magnesium ferrites have been the subject of study for a long time [2, 3]. A number of researchers have studied the electrical and magnetic properties of magnesium ferrite substituted by divalent [4], trivalent [5] and tetravalent [6] ions. The simultaneous substitutions of divalent non magnetic and tetravalent magnetic cations like Zn, Mn ions in magnesium ferrites may give rise to an interesting result.

EXPERIMENTAL DETAILS

The samples of $\text{MgZn}_x\text{Mn}_x\text{Fe}_{2-2x}\text{O}_4$ spinel ferrite systems with varying x [$x = 0.0, 0.1, 0.2, 0.3, 0.4, 0.5$ and 0.6] were synthesized by double sintering ceramic method. A. R. grade oxides of magnesium, zinc, manganese and ferric were used for the preparation of $\text{MgZn}_x\text{Mn}_x\text{Fe}_{2-2x}\text{O}_4$ ferrite. [7]

The magnetic properties were measured using pulse field technique provided by Magneta company. A.C. susceptibility measurements were carried out using double coil setup in the temperature range 300-800K. [8]

RESULTS AND DISCUSSION

The magnetic properties like saturation magnetization (M_s), remanant magnetization (M_r), coercivity (H_c) and others are investigated using pulse field hysteresis loop technique. Fig 1 (a and b) represents the M-H plots for all the compositions ($x=0.0$ to 0.6). All the samples of the series $\text{MgZn}_x\text{Mn}_x\text{Fe}_{2-2x}\text{O}_4$ exhibit typical hysteresis curve showing ferrimagnetic behavior of the samples. These M-H plots are used to obtain the values of coercivity, remanant magnetizations etc. and the values of these magnetic parameter are presented in Table 1.

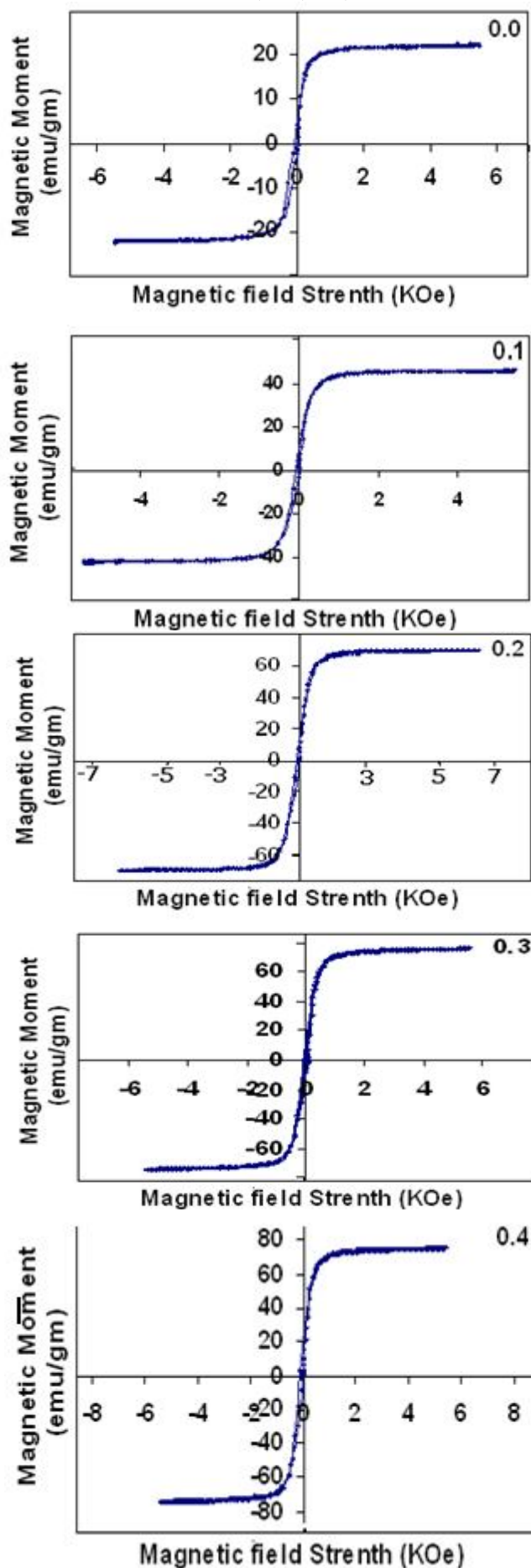
The values of saturation magnetization are used to determine the magneton number (n_B)(the saturation magnetization per formula unit in μ_B). [9]

The decrease in Curie temperature with increase in zinc ion concentration 'x' is related to decrease in magnetic linkages associated with tetrahedral (A) and octahedral [B] site. [10]

Table-1: Magnetization parameters of the system $\text{MgZn}_x\text{Mn}_x\text{Fe}_{2-2x}\text{O}_4$.

Comp. x	Magnetization parameter		
	Mr (emu/gm)	Ms (emu/gm)	Hc (Oe)
0.0	4.24	22.50	58.48
0.1	1.62	45.93	2.34
0.2	0.19	70.01	11.18
0.3	27.31	76.12	42.83
0.4	0.75	75.29	6.93
0.5	12.76	52.90	33.23

Figure 1. a) Variation magnetic field strength with magnetic moments for the system $\text{MgZn}_x\text{Mn}_x\text{Fe}_{2-2x}\text{O}_4$ for $X = 0.0, 0.1, 0.2, 0.3$



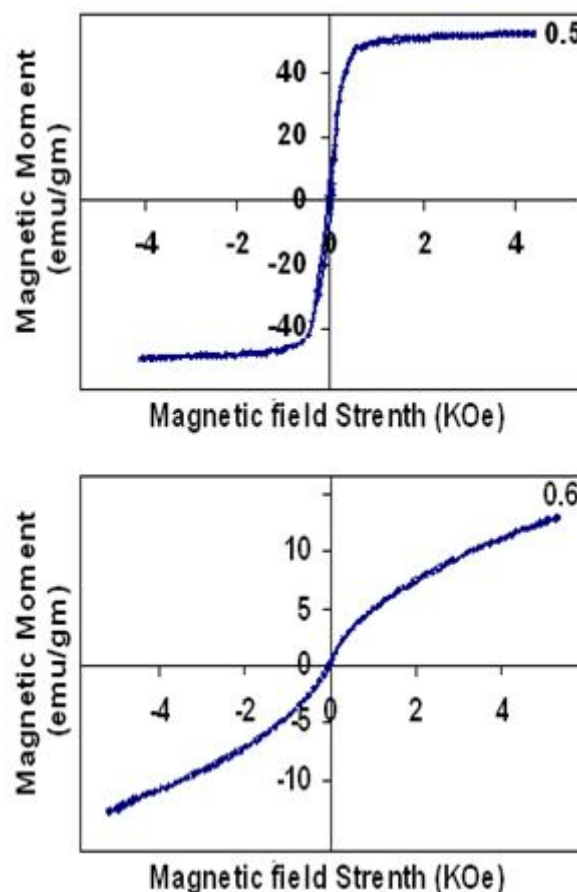


Fig-1.b): Variation magnetic field strength with magnetic moments for the system $\text{MgZn}_x\text{Mn}_x\text{Fe}_{2-2x}\text{O}_4$ for $X = 0.4, 0.5, 0.6$,

CONCLUSIONS

The saturation magnetization M_s initially increases and then decreases with Zn, Mn concentration 'x'.

REFERENCES

1. T. Abraham.A.M.Ceram.Soc. Butt.73 (1994)62.
2. V.R.K. Murthy, J. Vishvanathan.Science and technology of ferrite materials.
3. Z. Cvejic, S.Rakic, A. Kremenovic. B.Antic, C.Jovaletic P.Colomban.Solid State Sci. 8(2006) 908.
4. S. Hallynck, G. Pourroy, S. Vilminot, D. Autissier, H. Pascard, Solid State Sci. 8(2006)24.
5. S. A. Morrison, C. L. Cahill, E.E. Carpenter S. Calvin, V. Harris, J. Appl. Phys. 95(2004)6392.
6. X. Huang,Z.Chen,Solid State. Sci. 8(2006)24
7. N. Rezlescu, N. Iftimie, E.Rezlescu, C.Dorofte, P.D. Popa,Sens. Actuators B 114(2006)427.
8. E.C Sousa, M. H. Sousa, G.F. Goya, H. R. Rechenberg, J.Deperyrot, F.A.Tourinho,J. Magn. Magn. Mater 272(2004)1215.
9. L. John Berchmans, R. KalaiSelvan. C. O. Augustin,Mater. Lett. 58(2004)1928.
10. G.Srinivasana, V.M.Laletsinb, R.Hayesa, N.Puddubnayab,E.T.Rasmussena,D.J.Fekela, Solid state commun.124(2002)373.

GREEN SYNTHESIS OF GOLD AND COPPER NANOPARTICLES USING CINNAMOMUM TAMALA STEAM EXTRACTS

Zuber H. Mapkar¹, Surbhi Benjamin² and Manohar V Lokhande³^{1,2}Department of Chemistry, PAHER University, Udaipur³Department of Chemistry, Sathaye College, Mumbai

ABSTRACT

The Cost effective and eco-friendly technique for green synthesis of Gold and Copper nanoparticles using Cinnamomum tamala (tejpatta) steam aqueous extract was carried out in this study. The formation of Gold nanoparticles (AuNPs) and Copper Nanoparticles (CuNPs) were confirmed by different techniques such as UV-Visible spectroscopy, X-ray diffraction, Energy dispersive X-ray spectroscopy (EDX) and scanning electron microscopy (SEM). Gold and Copper nanoparticles of different sizes were synthesised by optimizing method parameters. The average particle size of AuNPs and CuNPs were found to be 15 and 52 nm calculated using sherrer equation. The synthesized Copper and gold nanoparticles show size dependent catalytic activity. The effect of particle size on catalytic reduction was studied using UV-Vis spectrophotometry. These nanoparticles were used for synthesis various organic molecules. The Biomedical application of Gold nanoparticles can be rendered more effective by using biologically synthesized nanoparticles that are found to be exceptionally stable, minimize toxicity and cost.

Keywords: AuNPs, CuNPs, Cinnamomum tamala, Green synthesis, SEM and EDX.

INTRODUCTION

Synthesis of metal nanoparticles (MNP) has been a prime area of interest for the researcher's community in the recent times [1, 2]. This is mainly because of the their astonishing optical, electrical as well as biological properties, due to which they are extensively employed in medicinal [3], Catalytic [4], Pharmaceuticals [5], Sensors [6] and so on [7]. metal nanoparticles can now be routinely synthesized by adopting various chemical and physical methods. Their acts and applications mainly depend upon shape, size and composition of nanoparticles [8].

Gold Nanoparticles and Silver nanoparticles (AuNPs) were studied by considering their exceptional applications in optical receptors [9], filters [10], electrical batteries [11], bio-sensing [12], antimicrobial agents [13]. Metal nanoparticles also find potential applications in medicines, especially in ointments to cure the burns, open wounds [14]. There are copious methods reported in literature for synthesis of AuNPs. On the other hand, biological methods are suitable methods as they are not only inexpensive, but also are environmentally benign. This is because they don't incorporate any hazardous chemicals and also don't form any harmful bi-products, thereby abiding the principles of green chemistry [15,16]. Also by incorporating biomaterials, synthesis of nanoparticles become inexpensive, rapid, eco-friendly and generally consists of a single step [17]. Bio-synthesis of metal nanoparticles has been achieved in two ways: i) by using microorganisms ii) by using plant materials. Many recent reports show synthesis of nanomaterials by means of microorganisms such as E. coli [18], Fusarium oxysporum [19]; and by using plants such as basil [20] and Corundum Sativum [20]. These bio-organisms are advantageous for synthesis because they use natural reducing agents present in plants and are generally needless of any capping agents as phytochemicals are readily available to serve that purpose.

Cinnamomum tamala, Indian bay leaf, also known as , tejpat, tejapatta, Malabar leaf, Indian bark, Indian cassia, or malabathrum, is a tree in the Lauraceae family that is native to India, Bangladesh, Nepal, Bhutan, and China. It can grow up to 20 m (66 ft) tall. Its leaves have a clove-like aroma with a hint of peppery taste, they are used for culinary and medicinal purposes. It is thought to have been one of the major sources of the medicinal plant leaves known in classic and medieval times as malabathrum (or malobathrum). The bark is sometimes used for cooking, although it is regarded as inferior to true cinnamon or cassia. Methanolic extract of C. tamala leaves fed at 10 mg/kg to alloxan-induced diabetic rats for 15 days resulted in significant reduction in blood glucose level, blood glycosylated haemoglobin, LPO, serum AST and ALT, and significant increase in the antioxidant enzymes such as CAT, GSH and SOD. C. tamala could be used as an adjunct therapy in diabetes.[21]

In this paper, the eco-friendly, solvothermal synthesis of Gold and Copper nanoparticles involving Cinnamomum tamala leave extract is reported. The lustrous black coloured Copper nanoparticles are obtained when copper nitrate is treated with extract in certain proportion and no other capping agent was required to stabilize CuNPs. The characterization was done by UV-visible spectroscopy and X-ray diffraction (XRD). Surface morphology in terms of shape was determined by employing scanning electron microscopy (SEM),

energy dispersive X-rays analysis (EDX) and transmission electron microscopy (TEM). The above synthesized Ag nanoparticles find potential applications in catalysis. To the best of our knowledge, it is a first instance where AuNPs were synthesized using Cinnamomum tamala extract.

MATERIAL AND EXPERIMENTAL METHODS

Chemicals: Gold Chloride (AuCl_3), cupric nitrate ($\text{Cu}(\text{NO}_3)_2$), and nitro phenols were obtained from Merck Chemicals. All glassware has been properly washed with distilled water and dried in oven before use.

Preparation of Cinnamomum tamala leaf extract : Leaf of Cinnamomum tamala were collected from local area, Mumbai. The voucher specimen was numbered and kept in our lab for further reference. Following procedure was followed for the preparation of leaf extract: The leaves were cleaned by washing twice with tap water and finally with distilled water. They were gently dried using a soft cotton cloth. The clean leaves were finely cut and then were crushed using mortar-pestle by adding water occasionally. The paste prepared above was taken in a beaker and equal amount of water was added. The resultant mixture was sonicated using ultrasonic bath for 25-30 min with frequent stirring in order to have aqueous extract containing plant components. The mixture was filtered using Whatmann filter paper and filtrate was collected in a beaker. This aqueous Cinnamomum tamala leaf extract was used for synthesis of Silver nanoparticles.

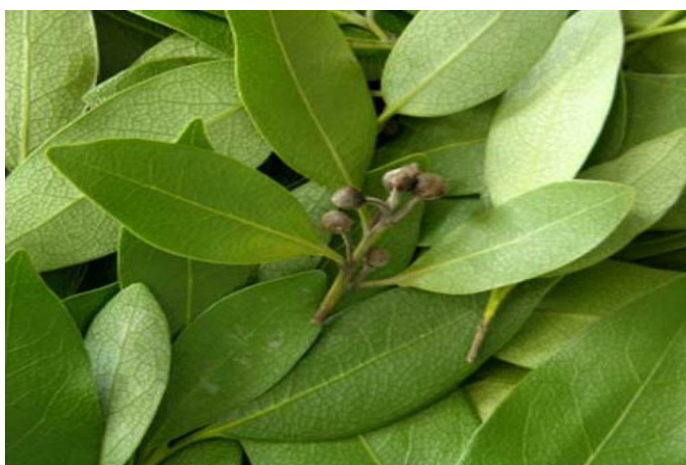


Figure -1: Cinnamomum tamala leaf

Synthesis of Gold nanoparticles using Cinnamomum tamala leaf extract: AuNPs were synthesized by following method: 50 cm³ of fresh aqueous leaf extract was taken in a 150 cm³ beaker. To this, 25 cm³ of 1000 ppm gold chloride solution was slowly added. The colour of the solution readily changed when gold chloride was added and silvery colloidal suspension was formed. The suspension was then stirred for eight hours at 500 rpm using magnetic stirrer bar. The stirring was stopped and precipitate was allowed to settle down. The solution was then centrifuged several times at 3500 rpm to get AuNPs which were dried at 70° C for two days and were stored in a bottle kept in dark place. The ratio of plant extract: gold chloride was also varied and it was observed that 50 cm³ of leaf extract along with 25 cm³ of 1000 ppm AuNO_3 gave best results and thus were chosen to be final proportion.

The AuNPs synthesized in this manner involved direct interaction between AuCl_3 and phytochemicals present in leaf extract which resulted in dexterous reduction of gold to produce AuNPs without making use of any chemicals. As a result, reaction followed green chemistry principles and could definitely be called cent percent green method. In addition, Cinnamomum tamala linn leaf extract mediated synthesis of AuNPs didn't require any stabilizers or capping agents as secondary metabolites in the plant were mainly causing a formation of robust coating on gold nanoparticles and thus preventing the self-agglomeration.

Synthesis of Copper nanoparticles using Cinnamomum tamala leaf extract: The 25 gm of leafs was boiled with 100 ml deionized water for 120 minutes. The extract was cooled down and filtered with Whatman filter paper and extract was stored in a refrigerator. The CuNPs were prepared by adding 20 cm³ of aqueous extract of plant material to 100 cm³ of 0.01M aqueous solution of cupric nitrate. The mixture was irradiated in microwave oven for 5 hours and allowed to cool at room temperature. Finally, the reaction mixture was centrifuged at 3500 rpm for 25-30 minutes and residue was dried at room temperature.

Instrumental Techniques: Remi (1 MLH) magnetic stirrer with magnetic was bar used for solvothermal synthesis of AuNPs and CuNPs. UV-Visible spectra was recorded on UV-Visible spectrophotometer (UV-2450), Shimadzu having Version 2.32 software. Scanning electron microscopy (SEM) images were obtained

from S-4800 field emission SEM system (FEI Quanta 200) operating at 20.0 kV equipped to perform elemental chemical analysis by energy dispersive X-ray spectroscopy (EDX). Transmission electron microscopy (TEM) micrographs were performed using a field emission transmission electron microscope (TEM) (JEOL JEM-2100F TEM/STEM, Oxford Instruments, USA) operated at 200 kV. XRD studies were carried out using Maxima 7000S XRD (Shimadzu, Japan). FTIR analysis was performed using Fourier transform infrared spectrophotometer from Perkin Elmer (Frontier Sr. No. 91579).

RESULTS AND DISCUSSIONS

UV- Visible spectroscopic analysis: UV-Visible spectroscopy is a handy technique to acquire information about formation of nanoparticles. AuNP were characterized by UV-Visible spectroscopy within a range of 200 -700 nm. For this, minimum amount of AuNP were added in 5 cm³ water and suspension was sonicated for 30 min to have better dispersivity of nanoparticles. As it can be seen from Figure-2A, a distinct surface Plasmon resonance (SPR) band at 530.4 nm was observed which is a prominent characteristic of gold nanoparticles is. At longer wavelengths, SPR band showed tailing giving a broad peak which may be attributed to distribution of particles. There was a little self-aggregation and AuNPs were found to be stable in aqueous medium.

The UV-Visible spectra of CuNPs prepared from leaves extract are shown in Figure -2B. The absorption band of CuNPs occurs at 540.1 nm. The CuNPs exhibit a yellowish-brown color in aqueous solution due to the excitation in UV-visible spectrum depending upon the particle size. The absorption bands for CuNPs have been reported to be in the range of 450-800 nm [22]. The absorption peak ascribed to the SPR of Cu particles formed here [23]. The intensity of peak increases as a function of time for four hours the peak at 540.1nm but for one hour no value in spectra.

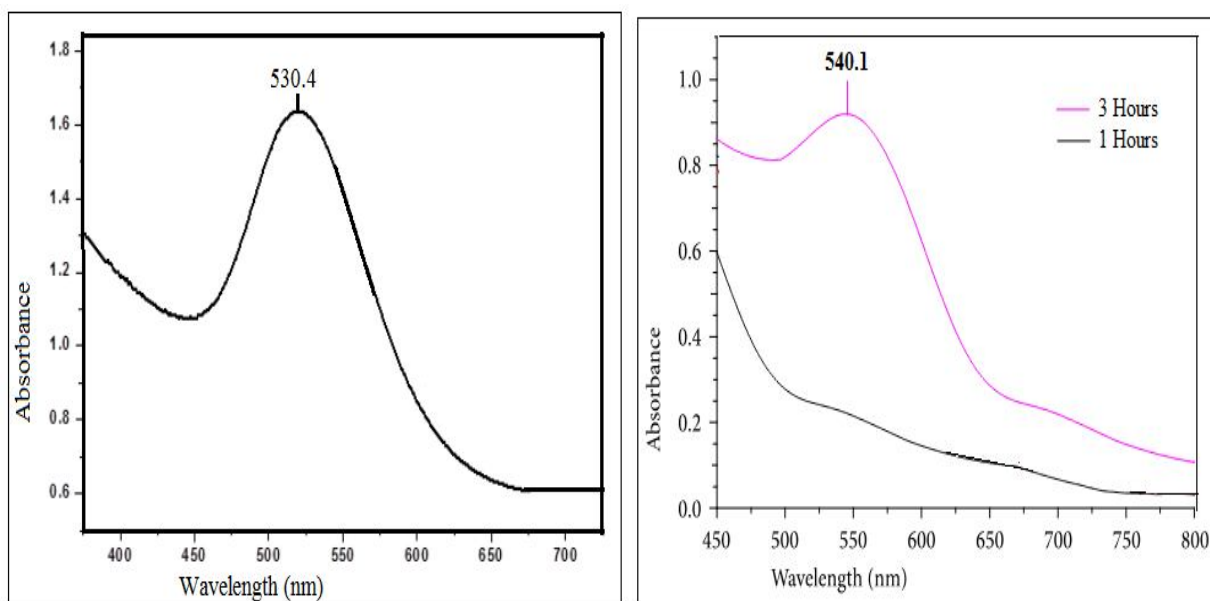


Figure-2: UV-visible spectra of AuNPs (A) & CuNPs (B) of Cinnamomum tamala leaf extract

X-ray diffraction (XRD) analysis : The formation of nanoparticles and its composition was analyzed using XRD technique by spreading the AuNPs on glass substrate with wide range of Bragg angles 2θ at a scanning rate of $2\theta \text{ min}^{-1}$. The five distinct diffraction peaks were obtained at $2\theta = 39.1^\circ, 44.8^\circ, 65.0^\circ, 78.7^\circ$ and 82.3° (Figure-3A), when 2θ range $30^\circ - 90^\circ$ was kept for analysis. These peaks were accredited for (111), (200), (220), (311) and (211) planes of a face center cubic (fcc) lattice. XRD analysis is also used for calculation of particle size by making use of Debye Scherrer equation given below:

$$t = 0.89 \times \lambda / \beta \cos \theta. \quad \text{----- (I)}$$

Where t is particle size of nanomaterials, λ is X-ray wavelength, β is Line broadening half maximum intensity and θ = Bragg's angle of diffraction. By incorporating all these values in equation (I), the particle size of AuNPs using Cinnamomum tamala linn extract was found to be 15 nm.

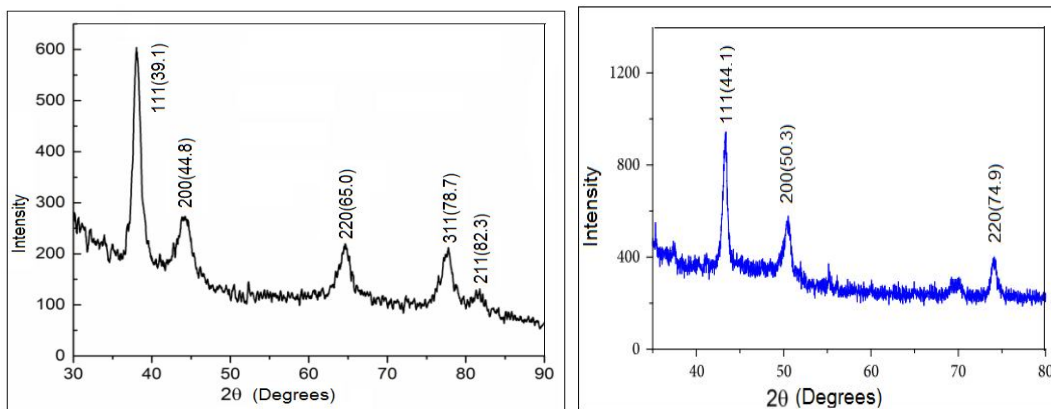


Figure-3: X-ray Diffraction AuNPs (A) & CuNPs(B) of Cinnamomum tamala leaf extract

The powder XRD of the CuNPs was recorded between 2θ values 40° to 80° exhibits crystalline nature showing possible peaks of copper metal in Figure -3 B. Bragg's diffraction peaks for Copper nanoparticles are observed at 44.1° , 50.3° , 74.9° , corresponding to 111, 200 and 220 respectively, representing face centered cubic structure of Copper. The average crystallite size of CuNPs was calculated to be about 52 nm, respectively, using Scherrer formula, where λ is incident X-ray wavelength ($\text{Cu K}\alpha = 1.542 \text{ \AA}$), β is full width half maximum in radians of the prominent line that is, (111), and θ is position of that line in the pattern.

Table 1: Peak Intensity from d-spacing Value for AuNPs

Sr. No	2θ	d-spacing	$1000/d^2$	hkl
1	39.1	2.30	168.91	111
2	44.8	1.98	255.10	200
3	65.0	1.52	432.90	220
4	78.7	1.24	740.74	311
5	82.3	1.12	800.0	211

Table 2: Peak Intensity from d-spacing Value for CuNPs

Sr. No	2θ	d-spacing	$1000/d^2$	hkl
1	44.1	1.95	263.15	111
2	50.3	1.72	338.98	200
3	74.9	1.22	972.04	220

Scanning electron microscopic analysis (SEM) and Transmission electron microscopic (TEM) analysis: Scanning electron microscope employed for surface characterization of the nanoparticles was FEI Quanta-200, with an operating voltage of 20 kV. SEM analysis shows the surface morphology of nanomaterials including its size and shape. SEM and TEM analysis shows the presence of well distributed spherical gold nanoparticles as shown in Figure -4. This was followed by EDAX analysis (as depicted in Figure -5) in which peak of gold can be seen, proves that nanoparticles formed by green synthesis are gold nanoparticles only.

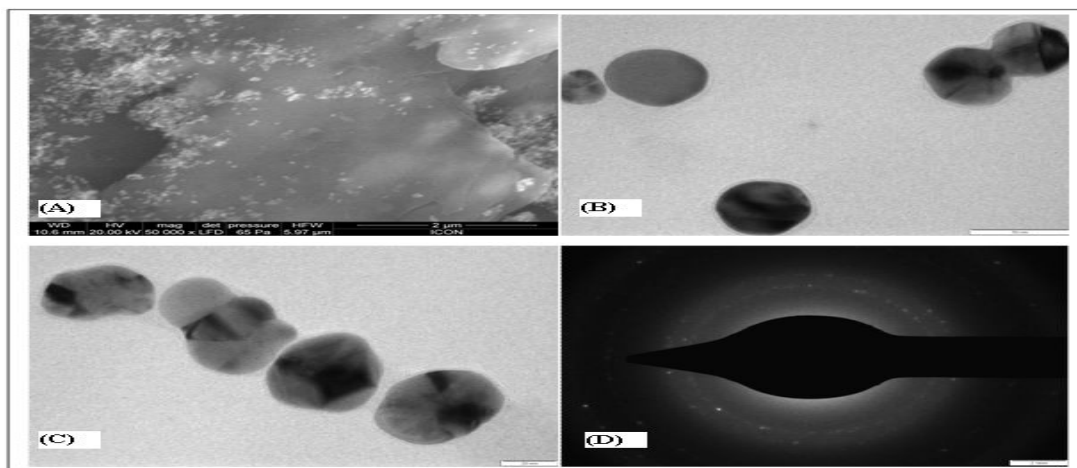


Figure-4: (A) SEM image of Gold nanoparticles, (B) and (C) TEM images of AuNPs, (D) SAED pattern for AuNPs

APPLICATIONS OF GOLD NANOPARTICLES FOR DETERMINING THEIR CATALYTIC ACTIVITY

The AuNPs synthesized by green method were employed to investigate catalytic activity, using reduction of 4-nitrophenol to 4-aminophenol by sodium borohydride as a standard/ model reaction. To a 1 cm³ cuvette, freshly prepared sodium borohydride (0.35 cm³, 0.5 M) along with 4-nitrophenol (0.70 cm³, 0.5 mM) were added. The UV-visible absorption spectra was recorded for the reduction of 4-nitrophenol catalyzed by AuNPs. 4-aminophenol in aqueous form shows λ_{max} at 297 nm when scanned in the range of 200-800 nm, whereas 4-nitrophenol shows its characteristic spectra having absorption maxima at 317 nm. After addition of sodium borohydride, the peak for 4-nitrophenol (317 nm) shifts to 400 nm which is attributed to the formation of 4-nitrophenolate ion as observed in the literature. After addition of AuNPs to the previous solution, the cuvette was shaken vigorously for some time and was then placed in the spectrophotometer. The disappearance of peak at 400 nm was observed and new peak was formed at 297 nm which was because of the absorption of 4-aminophenol.

CONCLUSION

Green synthesis of spherical shaped AuNPs and CuNPs of Cinnamomum tamala leaf extract was achieved. The mode of synthesis was simple, safe, eco-friendly which did not produce any harmful bi-products. The phytochemicals present in the plant acted as reducing agent for formation of AuNPs. The nanoparticles were stable and were characterized by means of UV-visible spectroscopy, XRD, SEM, TEM and EDX which provided evidences for their successful synthesis.

The present method is advantageous as compared to chemical synthesis due to absence of hazardous chemicals. The method is also superior to microbial method as it is free from microbial agents which can cause diseases to human beings. Above all, a low cost route of metal nanoparticles synthesis has been found which is economically viable. These Gold nanoparticles proved to be an excellent catalyst for facile reduction of 4-nitrophenol to 4-aminophenol. These nanoparticles could be applied in the fields of drug delivery, biodiagnostics, and filters as well as in optical imaging. Green synthesized MNPs have various relevance's in biochemical-pharmacological investigations such as anti-microbial, anti-oxidant, anti-diabetic and wound healing activities. In addition, this green synthetic practice would be a better alternative to the accessible methods.

ACKNOWLEDGEMENTS

The authors are thankful to the Supriya Life sciences, Mumbai. The authors thanks to TIFR and Department of Chemistry, University of Mumbai for Instrumental Facilities .

REFERENCES

1. Pradeep,T. Anshup,S. (2009). Noble metal nanoparticles for water purification: A critical review, *Thin Solid Films*, 517, 6441–6478.
2. Li,W. Jia,X. Hsing-Lin,Q. Wang, Q. (2006). Facile synthesis of metal nanoparticles using conducting polymer colloids, *Polymer*, 47, 23–26.
3. Rao, C.N.R. Muller,A. Cheetham,K.(2011). The chemistry of nanomaterials: Synthesis, properties and applications, Publisher Wiley VCH
4. Wu,B. Kuang,Y. Zhang,X. Chen,J.(2011). Noble metal nanoparticles/carbon nanotubes nanohybrids: Synthesis and applications, *Nano Today* ,6, 75—90.
5. Prow,T.W. Grice,J.E. Lin,L.L. Faye, R. (2011). Nanoparticles and micro particles for skin drug delivery, *Advanced Drug Delivery Review*, 63, 470–491.
6. Davila , D. Tarancon ,A. Calaza , C. Salleras , M. Fernandez-Regulez , M. Paulo , A.S. Fonseca, L.(2012). Monolithically integrated thermoelectric energy harvester based on silicon nanowire arrays for powering micro/nanodevice, *Nano Energy* 1, 812–819.
7. Prakash,S. Chakrabarty,T. Singh,A.K. Shahi,V.K.(2002). Polymer thin films embedded with metal nanoparticles for electrochemical biosensors applications, *Biosensor & Bioelectron*, 41, 43–53.
8. Rao,C.N.R. Kulkarni,K.U. John Thomas,P. (2002). Size-Dependent Chemistry: Properties of Nanocrystals, *Chemistry European Journal*, 8(1), 253-262.

9. Jaworska,a. Malek, k. (2014). A comparison between adsorption mechanism of tricyclic antidepressants on Goldnanoparticles and binding modes on receptors. Surface-enhanced Raman spectroscopy studies, *Journal of . Colloid Interface Science*, 431, 117–124.
10. Jain,P. Pradeep,T. (2005). Potential of silver Nanoparticle-Coated Polyurethane Foam As an Antibacterial Water Filter, *Biotechnology and Bioengineering*, 90, 59-63.
11. Kwon,K. Lim,H.S. Sun,Y.K. Suh,K.D.(2013). Improved rate capability of lithium-ion batteries with Ag nanoparticles deposited onto silicon/carbon composite microspheres as an anode material, *Solid State Ion*, 237, 28–33.
12. Farkhari ,N. Abbasian,S. Moshaii , A. Nikkhah,K.(2016). Mechanism of adsorption of single and double stranded DNA on gold and Silver nanoparticles: Investigating some important parameters in bio-sensing applications, *Colloids Surface-B*, 148, 657–664.
13. Musarrat, S. Dwivedi,J. Singh,B.R. Al-Khedhairi, A.A. Azam, A. Naqvi,A,(2010). Production of antimicrobial Goldnanoparticles in water extracts of the fungus *Amylomyces rouxii* strain KSU-09, *Bioresource Technology*, 101, 8772–8776.
14. . Ip, M. Lui,S.L. Poon,K.V.M. Lung,I Burd,A.(2006). Antimicrobial activities of Silver dressings: an in vitro comparison, *Journal of Medicinal Microbiology*, 55, 59–63.
15. Kharissova,O.V. Dias,H.V.R. Kharisov, B.I. Perez, I.O. Jimenez P.I. (2013). The greener synthesis of nanoparticles, *Trends Biotechnology*, 4 , 240-248.
16. Thakkar,K.N. Mhatre, S.S. Parikh,R.Y.(2010). Biological synthesis of metallic nanoparticles, *Nanomedicine* , 6 , 257–262.
17. Mishra,A. Tripathy,S.K. (2012). Fungus mediated synthesis of gold nanoparticles and their conjugation with genomic DNA isolated from *Escherichia coli* and *Staphylococcus aureus*, *Process Biochemistry* . 47,701–711.
18. Dar,M.A Ingle,A. Rai,M.(2013). Enhanced antimicrobial activity of AgNPs synthesized by *Cryptonectria* sp. evaluated singly and in combination with antibiotics, *Nanomedicine* 9, 105–110.
19. Ahmad,A. Mukherjee,P. Senapati,S. Mandal,D. Khan,M.I. Kumar,R. Sastry,M. (2003). Extracellular biosynthesis of AgNPs using the fungus *Fusarium oxysporum*, *Colloids Surface-B*, 28 , 313-318.
20. Ahmad,N. Sharma,S.Alam,M.K. Singh,V.N. Shamsi,V.R. Mehta,B.R. Fatma,A. Rapid synthesis of Goldnanoparticles using dried medicinal plant of basil, *Colloids Surf. B* 81 (2010) 81–86.
21. Philip,D.(2010). Rapid green synthesis of spherical gold nanoparticles using *Mangifera indica* leaf, *Spectrochim Acta A molecular . Biomolecular Spectroscopy*, 77, 807–810.
22. Sathyavathi,R. Krishna,M.B. Rao,S.V. Saritha,R. Narayana Rao,D.(2010). Biosynthesis of AuNPs using *Corundum Sativum* leaf extract and their application in nonlinear optics, *Advanced Science Letters*, 3(2), 138–143.
23. Syed, S.H. Singh,S. R. Parikh,R.S. (2008). Bacterial synthesis of copper/copper oxide nanoparticles, *Journal of Nanoscience and Nanotechnology*, 8(6), 3191–3196.

SYNTHESIS, STRUCTURAL AND DIELECTRIC PROPERTIES OF $\text{Ni}_{0.3}\text{Zn}_{0.7-x}\text{Co}_x\text{FeCrO}_4$ FERRITED. L. Navgare¹, U. B. Tumberphale², Shyam K. Gore³, V. B. Kawade⁴¹ShriMadhavraoBhosale Jr. College Mortala, Tq. Ausa, Dist. Latur²Late. Laximibai Deshmukh Mahila Mahavidyalaya, Parli Vaijanath, Dist. Beed³Microwave Research Laboratory N. E. S. Science College Nanded⁴Dnyanopasak Shikshan Mandal's Arts, Commerce and Science College, Jintur

ABSTRACT

Cobalt doped zinc nickel ferrite $\text{Ni}_{0.3}\text{Zn}_{0.7-x}\text{Co}_x\text{FeCrO}_4$ ($0 \leq x \leq 0.5$) nanostructures was synthesized by sol-gel combustion route. The structural parameter derived from XRD data. The XRD spectra revealed that the all ferrite samples were cubic spinel structure with 23-35 nm average crystallite size. The lattice parameter was decreased and crystallite size decreased with Co^{2+} substitution caused increase in porosity which resulted decrease in the bulk density of the sample. The different properties like dielectric constant (ϵ'), dielectric loss (ϵ''), loss tangent (δ) and AC conductivity have been studied by LCR-Q meter with increasing frequency for all samples. Low loss at high frequency was supported high feasibility of synthesized doped ferrites for microwave and absorbing materials application.

Keywords: Lattice parameter, Dielectric constant, Loss tangent, A. C. Conductivity

1. INTRODUCTION

Ferrite was known from ancient as lodestone (i.e. Fe_3O_4) as navigation compasses used by sea travellers. Modern ferrite has been studied after 1930s for their structural, magnetic and electrical properties [1]. Basically ferrite is insulating magnetic oxide materials, they possess very high permeability from low to high frequency. The low eddy current losses made the material unique for various electronic applications [2].

The ferrite structure, be it spinel, garnet or magnetoplumbite, the crystal structure arrangement has closed packed structure of oxygen. The metallic cations reside on the interstices of the closed-packed oxygen lattice. The spinel structures have tetrahedral (A) and octahedral (B) sub-lattice forms closed pack arrangement. The magnetism in ferrite arises from super-exchange mechanism. This is the reason that magnetization in ferrite is lower than the magnetism of 3d metallic alloys in which spins are parallel aligned. Spin arrangement of B-site and A-site in ferrite are antiparallel, the magnetization (M) can be increases by imbalance between A and B sub-lattice. This can be done by substituting nonmagnetic cations like Bi^{3+} or Zn^{2+} for A-site.

To develop new generation microwave devices technology ferrite materials must be made to have special properties. The intrinsic property of ferrite depends upon chemical composition, type of substitution and preparation method. The small amount of non- magnetic ions can change structural, magnetic and electrical properties. In order to increase the applicability of ferrite materials, in present work magnetic Co^{2+} substituted zinc ferrite has been undertaken. We have reported sol-gel auto-combustion method for the preparation of cobalt doped Zinc ferrite. We also present the effect of Co^{2+} on structural and dielectric properties of cobalt ferrite.

2. EXPERIMENTAL DETAILS

2.1 Synthesis

Cobalt-bismuth ferrite $\text{Ni}_{0.3}\text{Zn}_{0.7-x}\text{Co}_x\text{FeCrO}_4$ (where $x = 0.0, 0.1, 0.2, 0.3, 0.4, 0.5$) samples were prepared by sol-gel routes. The high purity AR grade (99.99%) starting materials used were nickel nitrate $\text{Ni}(\text{NO}_3)_2 \cdot 9\text{H}_2\text{O}$, ferric nitrate $\text{Fe}(\text{NO}_3)_3 \cdot 9\text{H}_2\text{O}$, cobalt nitrate $\text{Co}(\text{NO}_3)_2 \cdot 6\text{H}_2\text{O}$, zinc nitrate $\text{Zn}(\text{NO}_3)_2 \cdot 5\text{H}_2\text{O}$, chromium nitrate $\text{Cr}(\text{NO}_3)_3 \cdot 9\text{H}_2\text{O}$ and citric acid ($\text{C}_6\text{H}_8\text{O}_7 \cdot \text{H}_2\text{O}$) (99.9% sd-fine). All reagents were weighed in stoichiometric proportions; the products of the system were produced by keeping metal nitrate to citrate ratio 1:3. All the metal nitrates are dissolved into certain amount deionized water and mixed together to get clear solution ($\text{pH} \approx 3$). An aqueous solution of citric acid was mixed with metal nitrate as chelating agent and the pH of solution was kept constant and equal to 7 during the reaction adding ammonia solution. The reaction was carried out in natural medium. The solution was kept on hot plate with continuous stirring at 100 °C during evaporation; the solution becomes viscous and finally formed very viscous gel. When finally all water molecules were removed from the mixture, after few minutes the gel automatically ignited and burnt with glowing flints. The auto-ignition was completed within one minute, yielding the brown color ashes termed as precursor. The as prepared powders of all samples were heated separately at 500 °C for 4h to get the final product. These heat treated powders were used for further characterization.

2.2 Characterization tools

The X-ray powder diffraction patterns were recorded on Rigaku –denki (Japan) X-ray diffractometer (D/MAX2500) using Cu-K α radiation ($\lambda=1.5418$ Å). The XRD patterns were in the 2θ range from 20° to 70° with scanning rate $10^\circ/\text{min}$. The measurements were taken at room temperature. The dielectric constant (ϵ'), dielectric loss (ϵ''), and dielectric loss tangent ($\tan\delta$) were measured as a function of frequency by using (LCR Hi Tester 3520-50) LCR-Q meter.

3. RESULT AND DISCUSSION

3.1 Structural analysis

Figure 1 depicts the XRD spectra of all $\text{Ni}_{0.3}\text{Zn}_{0.7-x}\text{Co}_x\text{FeCrO}_4$ ferrite samples at various x values. The XRD data is in good agreement with powder data of JCPDS card number 22-1012 which concludes the formation of zinc ferrite of the investigated samples [3]. Analysis of the diffraction patterns of all samples reveals the formation of single phase cubic spinel structure. The XRD data shows considerable line broadening, indicating that the particles were nanosized with average particle sizes and lattice parameter as listed in table 1. All the diffraction peaks were indexed as (111), (220), (311), (400), (422), (511), (440) and (533). The inter-planer spacing “ d ” was calculated using Bragg’s law. The lattice parameter “ a ” was calculated using the relation [4].

$$\left(\frac{1}{d^2}\right) = \frac{h^2 + k^2 + l^2}{a^2}$$

1

Where a is the lattice constant, $(h\ k\ l)$ are miller indices and d is the inter-planar distance.

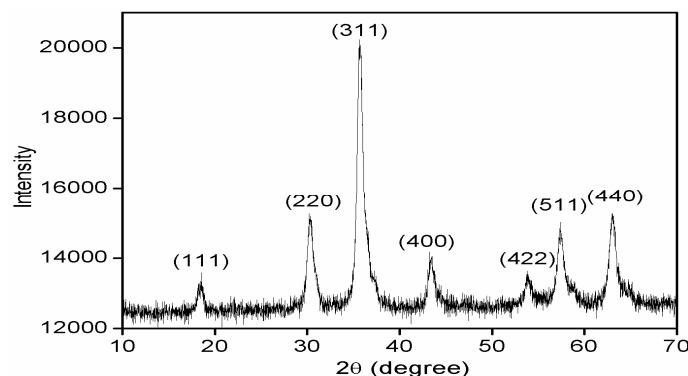


Figure-1: XRD pattern of $\text{Ni}_{0.3}\text{Zn}_{0.7-x}\text{Co}_x\text{FeCrO}_4$ sintered at 500°C for 4h.

The values of lattice parameters were calculated using Bragg’s equation. The calculated lattice parameter indicated the samples to be cubic spinel. The crystalline size for each composition was calculated from XRD line width of the (311) peak using Scherrer formula [5]. The crystallite size, lattice constant and X-ray density were deduced from X-ray data and presented in table 1 along with bulk density of the samples. The variation of lattice parameter of investigated samples as a function of Co-concentration is shown in figure 2(a). The lattice parameter exhibited a continuous decreases with increase in Co substitution which can be explained on the basis of the relative ionic radius of $\text{Co}^{2+}=0.78$ Å and $\text{Fe}^{3+}=0.67$ Å. As varying components were cobalt and zinc, replacement of smaller Fe^{3+} ions for larger Zn^{2+} ions in $\text{Ni}_{0.3}\text{Zn}_{0.7-x}\text{Co}_x\text{FeCrO}_4$ ferrite causes increase in decreases constant. In short decrease in lattice parameter may logically be attributed to the difference in ionic radius where a partial replacement of Fe^{3+} ion by Co^{2+} causes the decrease of the unit cell dimensions there by decrease the lattice parameter.

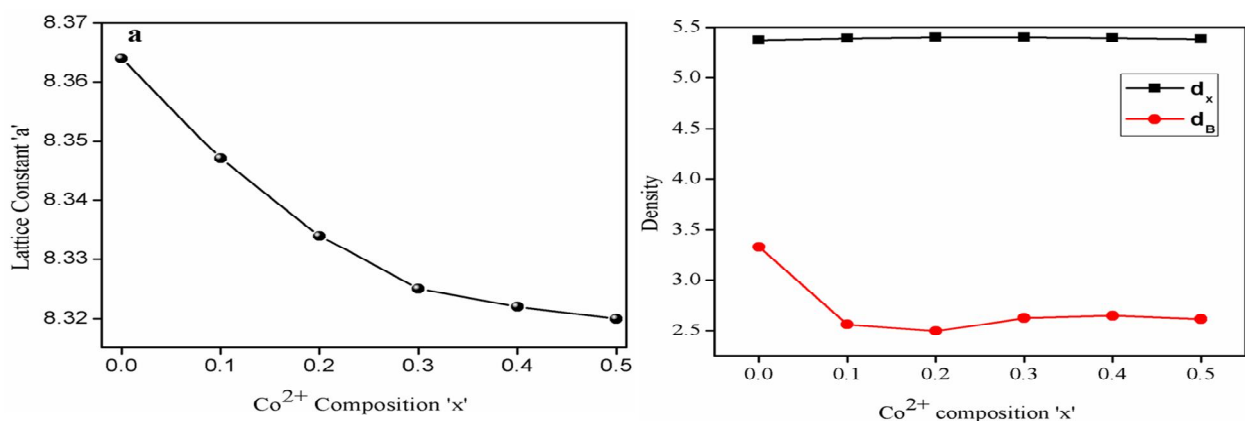


Figure-2: (a) Variation of lattice constant, (b) x-ray and bulk density with bismuth content ‘ x ’.

Table-1: Lattice constant (a), X-ray density (d_x), bulk density (d_b), porosity (P) and crystallite size (D) of Ni_{0.3}Zn_{0.7-x}Co_xFeCrO₄ samples.

Composition 'x'	'a' (Å)	'd _x ' (gm/cm ³)	'd _b ' (gm/cm ³)	'P' (%)	'D' (nm)
0	8.364	5.375	3.326	46	34
0.1	8.347	5.393	2.564	48	26
0.2	8.334	5.404	2.497	49	32
0.3	8.325	5.407	2.628	48	25
0.4	8.322	5.398	2.652	53	23
0.5	8.320	5.386	2.618	48	22

The X-ray density (d_x) of cobalt substituted zinc ferrites was calculated using following formula.

$$d_x = \frac{8M}{Na^3} \quad \text{gm/cm}^3 \quad 2$$

where, M is molecular weight, N the Avogadro's constant, a is the lattice constant and 8 is the number of molecules per unit cell for cubic structure.

The density plays important role in structural properties of ferrite. The values of bulk density and X-ray density are presented in table 1. The X-ray densities (true density) of prepared samples calculated from X-ray diffraction pattern. The X-ray density increases linearly with the increase of Co concentration [figure 2(b)]. The X-ray densities were higher in magnitudes than the corresponding bulk densities in ferrites which could be due to the existence of pores which were formed and developed during the preparation of samples or the sintering process [6]. The bulk density was found to decrease with increasing Co²⁺ substitution. In the present series, both the molecular weight and volume of the unit cell was decrease with increasing Co²⁺ substitution [7]. But the decrease in volume overtakes the increase in molecular weight which results in decrease of bulk density, which led to a increase in porosity (P). The average crystallite size was determined from the full width at half maxima (FWHM) using Debye Scherrer equation [8]

$$D = \frac{0.9\lambda}{\beta \cos \theta} \quad 4.3$$

where D is the crystalline size (nm), λ is wavelength (1.54 Å for Cu K_α) of the X-ray radiation, θ is Bragg's angle, β is the full width of the diffraction line at half maximum intensity measured in radians for (311) peak. Using this relation the particle sizes of all samples have been calculated and are listed in table 1. It is clear that samples of nanometer particle size can be prepared by sol gel auto combustion method.

4. DIELECTRIC STUDIES

The pellets of the samples were prepared using KBr press for the dielectric measurement. The dielectric constant (ε') measurements were carried out in frequency range from 100Hz to 5 MHz. The dielectric constant was calculated using the formula [9].

$$\epsilon' = \frac{Cd}{\epsilon_0 A} \quad 3$$

where C is the capacitance of pallet in farad, d is the thickness of the pallet in meter, A is the cross-sectional area in m² of the flat surface of the pallet and ε₀ is the constant of permittivity of free space.

The dielectric loss tangent can be calculated using the relation [10],

$$\tan \delta = \frac{1}{2\pi f R_p C_p} \quad 4$$

where δ is loss angle, f is the frequency, R_p is the equivalent parallel resistance and C_p is the equivalent parallel capacitance. The dielectric loss (ε'') was also measured in terms of tangent loss factor (tanδ) defined by the relation [11],

$$\epsilon'' = \epsilon' \tan \delta \quad 5$$

The AC conductivity was calculated using the values of frequency, dielectric constant and dielectric loss tangent [11].

$$\sigma_{AC} = 2\pi f \epsilon_0 \epsilon' \tan \delta \quad 6$$

where ε₀, ε' and tanδ are defined above.

The variations dielectric constant (ϵ') and dielectric loss (ϵ'') with frequency are shown in figures 3 for all samples. From figures 3 (a) and (b) that both dielectric constant and loss were decreased with increase of frequency. Such behavior is common in ferrites for example Mn-Zn ferrite [12], Cr- Co ferrite [11], Co-Zn and Co-Mg ferrite [13] etc. The dielectric constant (ϵ') and dielectric loss (ϵ'') decreased with increasing frequency due to the fact that the polarization was decreased with increasing frequency and then remains constant at high frequencies. The variation in ϵ' and ϵ'' can be explained on the basis of space charge polarization, which was due to an inhomogeneous structure governed by number of space charge carriers and the resistivity of the samples [11, 14]. The space-charge polarization resulting from electron displacement on the application of electric field and subsequent charge build up at the insulating grain boundary could be major contribution to dielectric properties in ferrites [15]. The values of ϵ' and ϵ'' were decreased from 98 to 18 and 66 to 24 at 1KHz ,13.57 to 6.09 and 59.29 to 36.30 at 1MHz and 7.69 to 4.0 and 37.17 to 24.98 at 5MHz, respectively, with addition of bismuth in cobalt ferrite. The decrease in dielectric constant (ϵ') and dielectric loss (ϵ'') rapidly at low frequencies and slowly at high frequencies were confirmed.

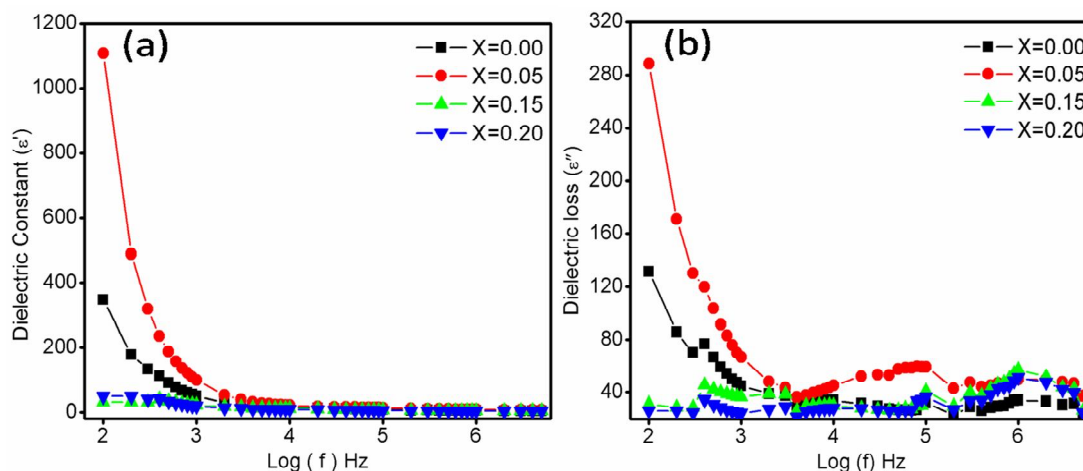


Figure-3: (a) Variation of dielectric constant (ϵ'), (b) dielectric loss (ϵ'') with log (f) in Hz at room temperature.

This could be explained as at low frequency AC electric field was smaller than the movements of electrons from Fe^{2+} to Fe^{3+} ions, electrons were responding to low AC field and loss is high [15]. When frequency of applied AC electric field was much larger than the hopping frequency of electron, then the electron could not jump from ion to ion and dielectric loss was decreased [15]. Therefore, the decrease in both ϵ' and ϵ'' on increasing the frequency took place when hopping frequency of electrons exchange between Fe^{2+} and Fe^{3+} ions were not following the alternating frequency [16]. Figure 4(a) shows variation of dielectric loss tangent ($\tan\delta$) with frequency at room temperature for all samples. The values of dielectric loss tangent were decreased from 1.4 to 0.76 at 1 KHz, 0.22 to 0.16 at 1MHz and 0.20 to 0.16 at 5MHz with addition of bismuth. Dielectric loss tangent in ferrites was considered to originate from two mechanisms; electron hopping and charged defect dipoles. Former contributed to dielectric loss tangent in the low frequency region, while in the high frequency range; dielectric loss tangent mainly was caused from the response of the defect dipoles to the AC applied field. These dipoles in ferrites were formed due to change in cation sites, such as $\text{Fe}^{2+}/\text{Fe}^{3+}$, during the sintering process. Figure 4(b) shows the dependence of AC conductivity on the frequency and composition at room temperature.

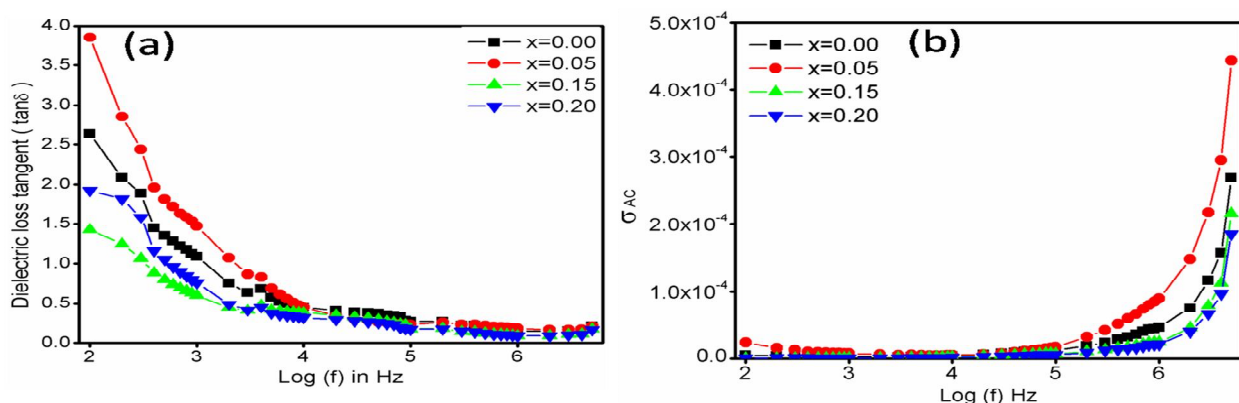


Figure-4: (a) Variation of dielectric loss tangent ($\tan\delta$), (b) AC conductivity (σ_{AC}) with log (f) in Hz.

To understand the conduction mechanism and the type of ions responsible for conduction, the variation of AC conductivity of nano-sized bismuth substituted cobalt ferrites was studied as a function of frequency from 100 Hz to 5 MHz. The AC conductivity was increased with frequency of the applied AC field. As the frequency of the AC increased, hopping of charge carriers also was increased, thereby increasing the AC conductivity. The variation of AC conductivity with applied frequency could be explained on the basis of Koops model [17]. According to this model, the AC conductivity at low frequency is due to the conducting grain boundaries while; the conductivity at high frequencies is due to conducting grains.

CONCLUSION

Bi^{3+} substituted cobalt ferrite $\text{Ni}_{0.3}\text{Zn}_{0.7-x}\text{Co}_x\text{FeCrO}_4$ ($0 \leq x \leq 0.5$) nanostructures were successfully synthesized by sol-gel auto combustion method. The XRD spectra revealed that the all ferrite samples were cubic spinel structure with 23-35 nm average crystallite size. The lattice parameter was decreased and crystallite size decreased with Co^{2+} substitution caused increase in porosity which resulted decrease in the bulk density of the sample. The dielectric constant (ϵ'), dielectric loss (ϵ'') and loss tangent were decreased with increasing Co^{2+} doping for increasing frequency. AC conductivity was increased with increasing frequency for all samples. Low loss at high frequency was supported high feasibility of synthesized doped ferrites for microwave and absorbing materials application.

REFERENCES

1. V. G. Harris, A. Geiler, Y. Chen, S. D. Yoon, M. Wu, A. Yang, Z. Chen, P. He, P. V. Parimi, X. Zuo, C. E. Patton, M. Abe, O. Acher, C. Vittoria, J. Mag. Magn. Mater., 2009, 321, 2035-2047.
2. H. Shokrollahi, K. Janghorban, J. Mater. Process. Tech., 2007, 189, 1-12.
3. M. Wang, Z. Ali, L. Zhang, J. Phys. C. 2008, 112, 13163-13170.
4. A. B. Gadkari, T. J. Shinde, P. N. Vasambekar, Mater. Chem. Phys., 2009, 114, 505-510.
5. A. Alarifia, N.M. Deraza, B. S. Shaban. J. Alloy. Comp 2009, 486, 501-506.
6. A. K. M. AktherHossaina, T. S. Biswasa, T. Yanagidab, H. Tanakab, H. Tabatac, T. Kawaib. Mater Chem. Phys 2010, 120, 461-467.
7. M. Penchal Reddy, I. G. Kim, D. S. Yoo, W. Madhuri, M. VenkataRamana, A. Shaaban, N. R. Reddy, K. V. S. Kumar, R. R. Reddy. Superlattice. Microstr. 2013, 56, 99-106.
8. U. Holzwarth, N. Gibson, Nature Nanotech. 2011, 6, 534.
9. A. Faraz, N. M. Ahmad. Adv. Appl. Ceram. 2012, 111, 381.
10. U.B. Shinde, S. E. Shirsath, S. M. Patange, S. P. Jadhav, K. M. Jadhav, V. L. Patil. Ceram. Int., 2013, 39, 5227-5234.
11. E. Pervaiz, I. H. Gul. J. Magnet. Mag. Mater., 2012, 324, 3695-3703.
12. M. A. Iqbal, M. Islamn, I. Ali, H. M. Khan, G. Mustafa, I. Ali. Ceram. Int., 2013, 39, 1539-1545.
13. K. Verma, A. Kumar, D. Varshney. J. Alloy. Comp., 2012, 526, 91-97.
14. I. H. Gul, E. Pervaiz. Mater. Res. Bul., 2012, 47, 1353-1361.
15. A. Thakur, P. Thakur, J. H. Hsu. J. Alloy. Comp., 2011, 509, 5315-5319.
16. N. Sivakumar, A. Narayanasamy, N. Ponpandian, G. Govindaraj. J. Appl. Phys., 2007, 101, 084116.
17. C. G. Koops. Phys. Rev., 1951, 83, 1.

POLYANILINE MATRIX FOR BIOELECTRONICS DEVICES

P. D. Gaikwad

Department of Physics, Sunderrao Solanke Mahavidyalaya Majalgaon, Beed

ABSTRACT

The polyaniline matrix is synthesized using potentiostatic method. The synthesized matrix was characterized by using electrochemical technique. The enzyme was immobilized by cross-linking via glutaraldehyde on the Polyaniline matrix. The characterization of resulting has been determined. The stability and life time of the Polyaniline matrix have been studied. In the present work biochemical signal through Boolean logic networks composed to bioelectronics devices.

Keywords: Polyaniline, glucose oxidase, cross-linking, Boolean logic Network.

INTRODUCTION

The synthesis and characterization of electro active polymers have become two of the most important areas of research in polymer and materials science [1]. polyaniline (PANI) receives greater attention as a conducting organic material due to its good environmental stability [2-3]. The ability to be formed in aqueous electrolytic solutions [4]. PANI is recognized to be an air-stable organic conducting polymer with interesting electrochemical properties. In particular, glucose is of special importance because of its involvement in human metabolic process [5]. The amperometric biosensors are reliable, relatively cheap and highly sensitive for clinical, industrial and environment purposes [6-7].

Enzymatic logic gates allowed information processing mimicking various Boolean logic operations: AND, OR, XOR, NAND, NOR, etc. [8-9], the system consisted of AND/OR logic gates based on the concerted operation of, glucose oxidase, [10]. AND/OR, as progress in networking these gates and coupling of the resulting system to responsive electrode for output readout, have opened new biosensing opportunities.

Synthesis of PANI-HCl Matrix: The electro polymerization of aniline was carried out by potentiostatic technique,. The Polyaniline Matrix was synthesized from an aqueous solution of distilled water containing 0.2 M aniline and 1 M of Hydrochloric acid (HCl) . After synthesis, polymer coated electrodes were rinsed thoroughly in distilled water and dried in cold air and then used for subsequent characterization.

Immobilization of GODx on Polyaniline matrix:The stock solution of GODx (1 mg/ml) prepared in 0.1 M phosphate buffer was adsorbed onto the surface of Polyaniline matrix. The enzyme GOD (SISCO) was immobilized by cross-linking via glutaraldehyde (Loba Chemie) on Polyaniline matrix. This kind of immobilization results in greater physical and chemical stability due to the cross-linking of enzyme.

RESULT AND DISCUSSION

The chronoamperogram of synthesized Polyaniline matrix is shown in Fig. 1.

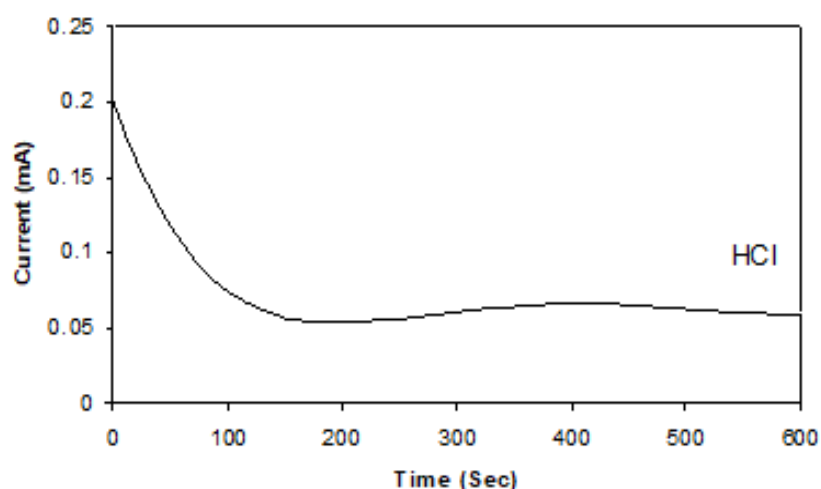


Fig-1: Chronoamperogram of PANI-HCl Matrix

Figure.1 has resulted in conducting Polyaniline matrix with uniform and porous surface morphology. The behavior of the amperometric synthesis overshoot during first few second probably indicates difficult formation of dimmers and oligomers. After this, current remain constant suggesting that building up of the matrix proceeds according to the same reaction along the full thickness of the polymer.

Current response of Polyaniline matrixl-GODx electrodes: The GODx was immobilized on electrochemically synthesized Polyaniline matrix by cross-linking via glutaraldehyde. The current -time relationship of Polyaniline-GODx electrode when the applied current set at 0.6 mV in phosphate as shown in Fig.2 .

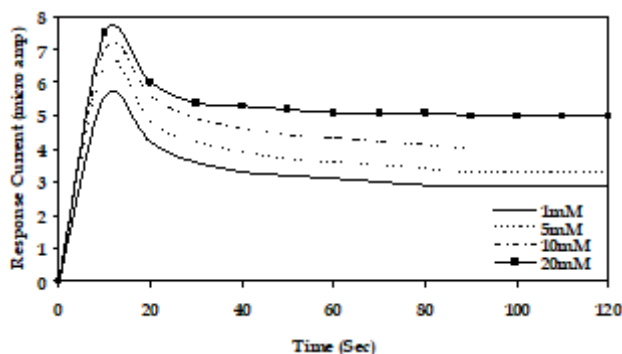


Fig-2: Current-time curves for the PANI-GODx electrode for various glucose concentrations in 0.1M phosphate buffer with pH 5.

The apparent Michaelis-Menten constant (K_m) was calculated for the immobilized enzyme by amperometric method . The values of response current (I_{max}) and K_m for phosphate buffer are $7.5\mu A$ and 5.3 mM respectively. Table 1. The value of the K_m depends on the immobilization of enzyme lesser K_m gives faster response to glucose .

Table-1: The analytical performance of PANI-HCl-GODx electrode for sphate at pH 5.

Arameters	Phosphate Buffer
I_{max} (μA)	7.5
K_m (mM)	5.3
Linearity (mM)	0-2
Sensitivity($\mu A/mM$)	1.1
Lifetime(days)	25

Stability of the PANI-GODx electrodes:It was found that the PANI-HCl-GODx electrode exhibited excellent stability for 25 days in phosphate buffer. The amount of glucose can be determined by measuring the Current of oxidation of hydrogen peroxide, produced in the reaction given below

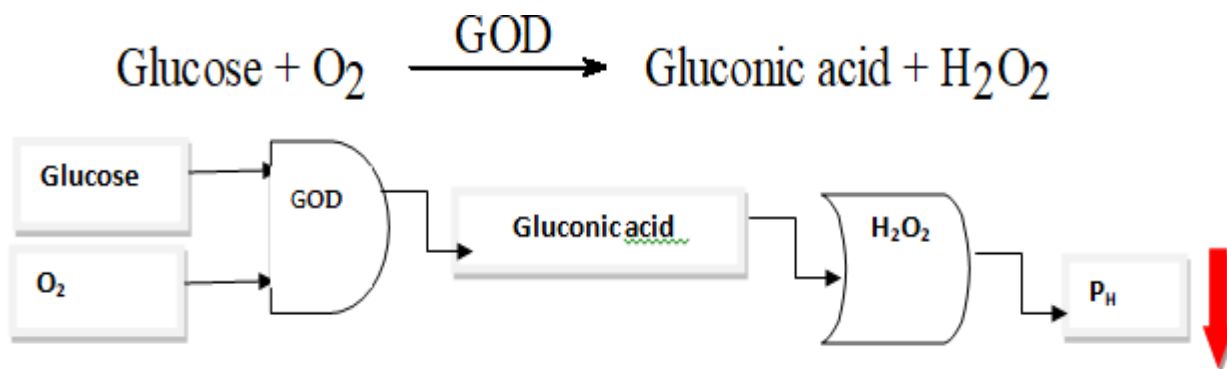


Fig-3: Enzymatic Boolean AND/OR logic gate

CONCLUSIONS

The PANI-GODx Matrix have been successfully synthesized and by crosslinking via glutaraldehyde has been successfully carried out. The sensitivity of PANI-GODx electrode was found to be higher excellent response in phosphate buffer (5.0 pH) and also excellent stability for 25 days. Biochemical signal applied in Combination of logic process for Bioelectronics devices.

ACKNOWLEDGEMENTS

Author is thankful to the UGC Pune for the project.

REFERENCES

1. Kang E T, Neoha K G and Tanh K L, 1998 Prog. Polym. Sci 23 211
2. Lacroin J C and Diaz A F 1988 J. Electrochem. Soc. E135 1457
3. Camalet C, J Lacroix C, Aciyach S, Chaneching K, Lacaze P C, 1998 Synth. Met. 93 133

-
4. Roth S and Graupher W 1993 *Synth. Met.* 57 3623
 5. Diaz A F and Logan J A, *J Electroanal. Chem.* 111 (1980) 111.
 6. Akundy G S, Rajagopalan R and Iroh J O, *J Applied Polymer Science* 83 (2002) 1970.
 7. Fabiano S, Tran-Minch C, Piro B, Dang L A, Pharm M C and Vittori O. *Mat. Sci. Eng.* 21 (2002) 61.
 8. Strack, G.; Pita, M.; Ornatska, M.; Katz, E. Boolean logic gates using enzymes as input signals, *ChemBioChem* 2008, 9, 1260-1266.
 9. Baron, R.; Lioubashevski, O.; Katz, E.; Niazov, T.; Willner, I. Logic gates and elementary computing by enzymes, *J. Phys. Chem. A* 2006, 110, 8548-8553.
 10. Pita, M.; Zhou, J.; Manesh, K.M.; Halámek, J.; Katz, E.; Wang, J. Enzyme logic gates for assessing physiological conditions during an injury: Towards digital sensors and actuators, *Sens. Actuat. B* 2009, 139, 631-636

MEASUREMENT OF ATTENUATION DATA OF VITAMINS USING Na(I) DETECTOR

Amol Mandle¹, Anil Gachhe², Prashant S. Kore³, Madhav Rode⁴ and Pravina P. Pawar⁵^{1,3,4,5}Department of Physics, Vaidyanath College, Parli Vajinath²Vasantrao Naik College, Nanded

ABSTRACT

In the present work, the electronic cross-section is evaluated experimentally and theoretically for Vitamins using the obtained of mass attenuation coefficients and total attenuation cross section at photon energies of radioisotopes Co57 (122 keV), 22Na (511 and 1275 keV), Cs137 (662 keV), and Co60 (1330 keV). The attenuation effect of gamma radiations against vitamins are shown using related parameters such as mass attenuation coefficient, total attenuation cross section and electronic cross-section. Observed values provide essential data in medical health physics have been calculated for some vitamins were measured using Na(I) with energy resolution 8.2% at 0.663 MeV was used for detection. Observed values are decrease initially and then tends to be almost constant at higher energies. Experimental results of radiological parameters were observed in good agreement with actual theoretical XCom values.

Keywords: *Electronic cross-section(σ_{ele}), Mass attenuation coefficients (μ_m), Na(I) Detector, Radioactive sources, Total attenuation cross section (σ_{tot}), XCom program.*

1. INTRODUCTION

Complex molecules such as carbohydrates, proteins, lipids, enzymes, vitamins and hormones perform a variety of physiological functions in biological systems. These complex molecules have as their basic building blocks, sugars, amino acids and fatty acids etc., which are essentially H, C, N and O based compounds. Thus, in several applications of medical physics and radiation biology such as radiotherapy with photons, μ/ρ values of such samples are a prerequisite for radiation dosimetry. However, it is worth noting that the mass absorption coefficients (μ/ρ) cannot be measured directly, but are instead derived from the linear attenuation coefficients (μ) in terms of the theoretical f -factors provided by Seltzer [1]. The study of photon interactions with matter is important and the data on the transmission and absorption of X-rays and gamma-rays in biological shielding and dosimetric materials assumed great significance by virtue of their diverse applications in the field of medical physics and medical biology [2]. The photon interaction cross-section can be expressed as a function of the photon energies and the atomic number Z . At a given photon energies, the interaction cross section is proportional to Z^n . n is expected to be between 4 and 5 for the photoelectric effect, 1 for the Compton Effect and 2 for pair production[3]. Experimental results were compared with theoretical values. A variety of physiological functions inside living systems are performed by complex molecules such as Lipids, Carbohydrates, Proteins, Fats and Oils composed of H, C, N and O based compounds. Photon energies from 1500 keV down to about 5 keV are widely used in medical and biological applications [4] especially during diagnosis and therapy. A thorough knowledge of the nature of interaction of these biologically important complex molecules such as Vitamins is desirable over this energy region. Theoretical values for the mass attenuation coefficients can be found in the tabulation by Hubbell and Seltzer [5]. A convenient alternative to manual calculations using tabulated data is to generate attenuation data as needed using a computer. For this purpose Berger and Hubbell [6] developed WIN-XCOM software for calculating mass attenuation coefficients or photon interaction cross-sections for any element compound for a wide range of energies.

There have been a great number of experimental and theoretical investigations to determine mass attenuation coefficients for complex biological molecules such as Lipids, Carbohydrates, Proteins, Fats and Oils composed of H, C, N and O elements in varying proportions Sandhu et al. [7] have investigated fatty acids in the energy region 81-1330 keV. Gowda et al. (2004, 2005) [8,9] have reported total attenuation cross-sections for sugar and amino acids. Measurements on the sample containing H, C and O in the energy range 54-1333 keV have been reported by El-Kateeb and Abdul Hamid [10]. There have been recent experimental and theoretical investigations [11,12] to determine Absorption coefficient, mass attenuation coefficients, total attenuation cross section and such type of radiological parameters for complex biological molecules such as lipids, fatty acids, amino acids composed of H, C, N and O elements in varying proportions. In this work we measured the mass attenuation coefficients, the atomic cross-sections, the electronic cross section and the for H, C, N and O based Vitamins in the energy range 122 keV to 1330 keV and then compared these experimentally evaluated parameters with theory using WIN-XCOM program.

2. THEORETICAL CALCULATIONS

In this section, some theoretical relations are described which have been used for the determination of mass absorption and related parameters in the present work. The mass attenuation coefficients μ_m ($\text{cm}^2 \text{g}^{-1}$) for the samples were obtained from Eq. (3) by using the density of the corresponding samples:

$$\mu_m = \frac{\mu}{\rho} (\text{cm}^2 \text{g}^{-1}) = \frac{1}{\rho t} \ln \left(\frac{I_0}{I} \right) \quad (1)$$

where ρ (g/cm^3) is a measured density of the corresponding sample. The values of mass attenuation coefficients were then used to determine the total attenuation cross section (σ_{tot}) by the following relation

$$(\sigma_{\text{tot}}) = \mu_m (M / N_A) \quad (2)$$

where $M = \sum_i n_i A_i$ is the molecular weight of the compound, N_A is the Avogadro's number.

Similarly, electronic cross-section (σ_{ele}) for the individual element is given by :

$$(\sigma_{\text{ele}}) = \frac{1}{N_A} \sum_i \frac{f_i A_i}{Z_i} (\mu_m)_i \quad (3)$$

All these radiological parameters are convenient parameters used to characterize the radiation response of a multi-element material in many technical and medical applications. Accurate values of these physical parameters provide essential data in medical physics.

3. EXPERIMENTAL SET UP AND MEASUREMENTS

The measurement of incident and transmitted photon energies were done with the help of narrow beam good geometry set up. Fig.1 gives the schematic view of the experimental set up. The signal from the detector (2"X2") NaI(Tl) crystal having energy resolution of 8.2% at 662keV gamma ray from the decay of Cs^{137} after suitable amplification was recorded in EG&G ORTEC 8K plug-in-card coupled to a PC/AT. The radioactive sources of strengths Co^{57} , Na^{22} , Cs^{137} and Co^{60} (134kBq) were obtained from Bhabha Atomic Research Centre, Mumbai, India. The stability and reproducibility of the arrangement was tested before and after each set of runs in the usual manner. The experiments were performed in an air-conditioned room to avoid possible shifts of the photopeaks. To minimize the contribution of small angle scattering and multiple scattering events to the measured intensity; the transmitted intensity was measured by getting the channels at the full-width at half-maximum position of photo peak.

The diameters of the samples were determined with the help of a traveling microscope. Cylindrical pellets by pressing the weighed quantity of the finely ground powder in a hand operated hydraulic press at a pressure of 10 ton. The attenuation of photon for empty container was found to be negligible. The sample thicknesses were selected in order to satisfy the following ideal condition as far as possible.

$$2 \leq \ln (I_0 / I) \leq 4$$

The room temperature was $23 \pm 1^\circ\text{C}$ throughout the experimental period. In the transmission experiments a rigid good geometry was maintained, placing the sample normal to the beam and midway between source and detector. The transmitted intensity of gamma-rays for various combinations of specimen thickness was recorded and corrected for background intensity.

4. FIGURES AND TABLES

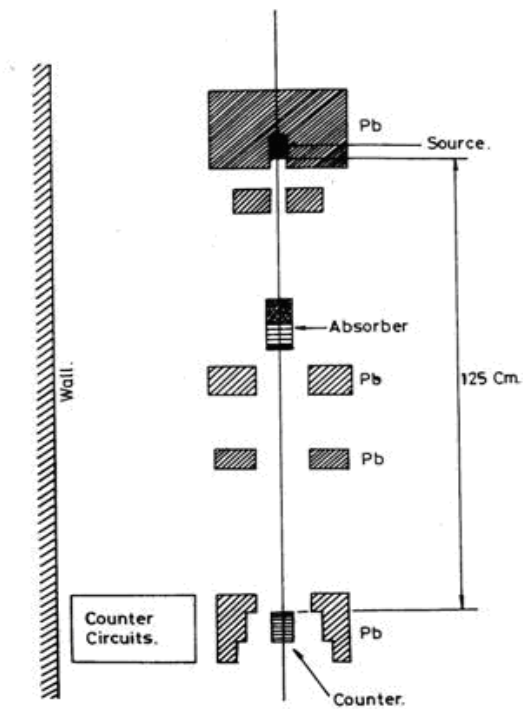


Fig-1: The schematic view of the experimental set up.

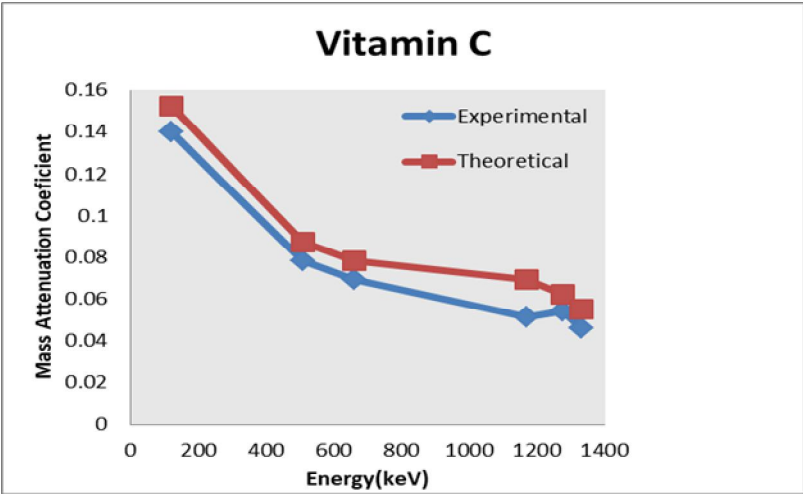


Fig-2: Plot of μ_m versus photon energy for Vitamin C.

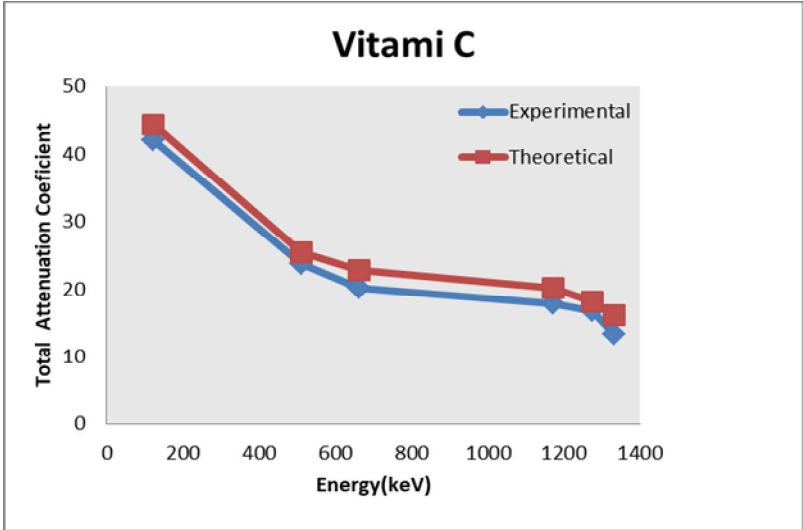
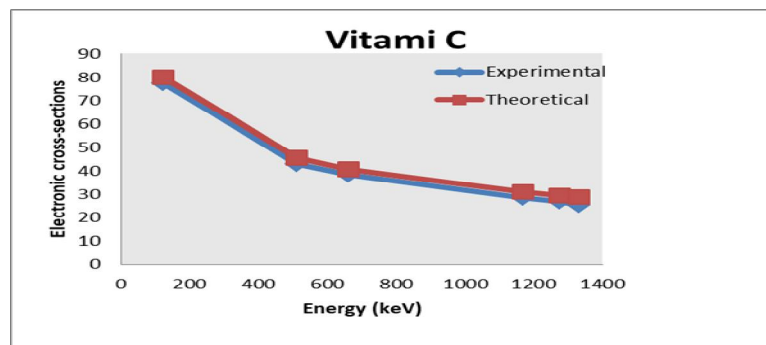


Fig-3: Plots of σ_{tot} versus photon energy for Vitamin C

Fig-4: Plots of versus σ_{ele} photon energy for Vitamin C**Table – 2: Mass attenuation coefficient μ_m (cm^2/g) of Vitamins**

Sr. No.	Vitamins	122keV		511keV		662keV		1170keV		1275keV		1330 keV	
		Exp.	Theo.	Exp.	Theo.	Exp.	Theo.	Exp.	Theo.	Exp.	Theo.	Exp.	Theo.
1.	Vitamin C	0.154	0.152	0.088	0.087	0.079	0.078	0.071	0.069	0.064	0.062	0.056	0.055
2.	Vitamin B ₁	0.161	0.160	0.090	0.091	0.083	0.081	0.061	0.062	0.060	0.059	0.057	0.058

Table – 3: Atomic cross-sections, σ_t (barn/molecule) of Vitamins

Sr. No.	Vitamins	122keV		511keV		662keV		1170keV		1275keV		1330 keV	
		Exp.	Theo.	Exp.	Theo.	Exp.	Theo.	Exp.	Theo.	Exp.	Theo.	Exp.	Theo.
1.	Vitamin C	45.01	44.43	25.72	25.43	23.09	22.80	20.75	20.17	18.70	18.12	16.37	16.07
2.	Vitamin B ₁	80.34	79.88	44.93	45.63	41.44	40.84	30.45	31.05	29.95	29.40	28.45	28.90

Table – 4: Electronic cross-sections, σ_{ele} (barn/molecule) of Vitamins

Sr. No.	Vitamins	122keV		511keV		662keV		1170keV		1275keV		1330 keV	
		Exp.	Theo.	Exp.	Theo.	Exp.	Theo.	Exp.	Theo.	Exp.	Theo.	Exp.	Theo.
1.	Vitamin C	2.560	2.527	1.463	1.446	1.313	1.296	1.180	1.147	1.064	1.030	0.931	0.914
2.	Vitamin B ₁	4.791	4.759	2.678	2.718	2.470	2.433	1.185	1.850	1.785	1.752	1.696	1.722

5. RESULTS AND DISCUSSION

The experimentally measured mass attenuation coefficient μ_m (cm^2/g) for the Vitamins C and B₁ at 122, 360, 511, 662, 1170, 1275 and 1330 keV. The schematic view of the experimental set up is shown in Fig.(1). The typical plot of μ_m versus energy E for Vitamin C is displayed in Fig.(2). The Fig.(2) also includes the variation of theoretical and experimental values of μ_m values versus energy. It is clearly seen that the mass attenuation coefficient (μ_m) depends on photon energy and decreases with increasing photon energy. As can be seen in Table 1 and the typical plot displayed in Fig.(2). The experimental (μ_m) values agree with theoretical values calculated using the XCOM program based on the mixture rule. The total experimental uncertainty of the (μ_m) values depend on the uncertainties of I_0 (without attenuation), I (after attenuation), mass thickness measurements and counting statistics. Typical total uncertainty in the measured experimental (μ_m) values is estimated to be 2-3%. Measured total cross-sections (σ_{tot}) and Electronic cross-sections (σ_{ele}) values for the Vitamins have been displayed in Table 2 and Table 3, respectively. The typical plots of σ_{tot} versus E and σ_{ele} versus E are displayed in Figs.(3) and Fig.(4) respectively. The behavior of both quantities with photon energies shows almost similar behavior to (μ_m) plots. The present experimental study has been undertaken to get information on mass attenuation coefficient μ_m values and related parameters for bio-molecules samples which are convenient parameters used to characterize the radiation response of a multi-element material in many technical and medical applications. Accurate values of these physical parameters provide essential data in medical physics and mainly in dosimetry. The μ_m and related quantities were found to decrease with increasing photon energies. The measured data were compared against XCom program.

6. CONCLUSIONS

- ✓ The results on μ_m , σ_{tot} and σ_{ele} of Vitamins, reported in the present work, would be useful, particularly in the energy region of interest, in many medical and biological applications (e.g. for the interpretation of absorbed dose). With proper knowledge of the attenuation parameters and buildup of photons in human organs and tissues, energy-absorption in the human body can be carefully controlled. The experimental data will also help in estimating safe dose levels for radiotherapy patients. For people working with gamma radiation and X-rays, especially at reactors and nuclear power plants, the present studies on the energy-absorption factor of human organs and tissues will help them to take proper precautions.

7. REFERENCES

1. Seltzer M. (1993). "Calculation of photon mass energy transfer and mass energy absorption coefficients", Radiation Research 136, 147.
2. Kaewkhao,(2008). "Determination of effective atomic numbers and effective electron densities for Cu/Zn alloy." Journal of Quantitative Spectroscopy and Radiative Transfer 109,1260-1265.
3. Henriksen T. and Baarli J. (1957) "The effective atomic number".Radiation Research,6(4), 415-423.
4. Hubbell J. H., (1999). Review of photon interaction cross section data in the medical and biological context Phys.Med.Biol.44:R1-R22.
5. Hubbell J.H., Seltzer S.M. (1995) "Tables of X-Ray of Mass attenuation coefficient and mass energy absorption coefficient 1 KeV to 20 MeV for elements. Z = 1 to 92 and 48 additional substances of dosimetric interest"
6. Hubbell J. H. and Berger M.J.,(1987). "Photon attenuation in : Engineering compendium on radiation shielding." edited by R G Jaerger 9IAEA,Vienna, Austria,1968) vol.1,ch.4,p.198.
7. Sandhu G K., Kulwant Singh,Lark B. S. and Gerward, 2002 "Molar extinction coefficients of some fatty acids." Radiat.Phys.Chem.65, 211-215.
8. Gowda S. et al., 2004. "Photon mass attenuation coefficients ,effective atomic numbers and electron densities of some thermoluminescent dosimetric compounds." Pramana –J. Phys. 63, 529-541.
9. Gowda S. Krishnaveni S. and Gowda R.2005. "Studies on effective atomic numbers and electron densities in amino acids and sugars in the energy range 30-1333keV."Nucl. Instrum. Methods Phys.Res.B 239, 361-369.
10. El-Kateb A. H., Abdul-hamid A. S., (1991). "Photon attenuation coefficients study of some materials containing hydrogen, carbon and oxygen." Appl.Radiat.Isot.42 303-307.
11. Kore, P.S. & Pawar P.P, (2014). Measurement of mass attenuation coefficient, effective atomic number and electron density of some amino acids. Radiat. Phys. Chem.92, 22-27.
12. Kore, P.S., Pawar P.P. & Palani T S (2016). Evaluation of radiological data of some saturated fatty acids using gamma ray spectrometry. Radiat. Phys.Chem. 119,74-79.

DEVELOPMENT OF NANO-TiO₂/Al ELECTRODE FOR NON-ENZYMATIC GLUCOSE BIO-SENSING APPLICATION

Kiran D. More¹, Nilesh S. Shinde², Jagdish W. Dadge³, Megha P. Mahabole⁴, Rajendra S. Khairnar⁵ and Kashinath A. Bogle⁶

^{1,2,4,5,6}Thin Films and Devices Laboratory, School of Physical Sciences, Swami Ramanand Teerth Marathwada University, Nanded

³Department of Physics, College of Engineering, Pune

ABSTRACT

This work reports development of a nano-TiO₂ coated aluminum tip electrode for non-enzymatic amperometric glucose sensor, working at very low applied potential of 0.2 V. A highly fractured TiO₂ film with porous structures is synthesized on aluminum substrate via dip coating method followed by annealing at 350 °C. Glucose sensing properties were determined via amperometric measurement and showed high sensitivity of 0.766 mA/mM-cm² over a linear range of 0.55 to 55 mM with a lower detection limit of 0.55 mM of glucose. With such good analytical performance of the slack porous nano-TiO₂ prepared from a simple process, it is believed that nano material coated metal tips become smart tips for its use in the biosensors, particularly non-enzymatic sensors.

Keywords: Nano-materials; TiO₂; dip-coating; non-enzymatic biosensors; glucose; amperometric sensors

1. INTRODUCTION

Looking at current scenario of death and disability of human across the World, diabetes mellitus happens to be one of the principal cause, which is highly responsible for heart disease, kidney failure and effective blindness. International Diabetes Federation (IDF) report reveals that about 8.8 % of the adult population worldwide is suffering from diabetes and this share is predicted to reach ~ 10 % by the year 2045¹. Now a day, frequent testing of physiological blood glucose level, to avoid diabetic emergencies, turn out to be crucial for making a decision of effective treatment. Currently available glucose sensors in market are basically enzyme based electrochemical sensors, which utilizes glucose oxidase as bio-recognition material²⁻⁴. Even though enzymatic sensors have several merits, like high sensitivity and selectivity, the catalytic activity of glucose oxidase may easily reduce by variations in pH, temperature, humidity and interference offered by other substances⁵. Therefore, to overcome with these issues, there is a need to develop non-enzymatic glucose sensor.

Currently researchers are focusing on non-enzymatic glucose sensors based on metal oxide and became popular due to their acceptable reproducibility, stability, low costs and simplicity. Metals oxides, such as NiO, TiO₂, CuO, ZnO, etc. are very often recognized in their native or modified forms for the oxidation of glucose and reported (in various geometries) for non-enzymatic glucose sensors⁶⁻⁹. Still more work is required in the fabrication of non-enzymatic glucose sensor electrodes for improving their sensitivity and selectivity via modifying the bare electrode surface with metal oxide nanoparticles. Modified electrodes provide a greater surface area, improving the electron transfer between the sensing reaction and the electrode.

Titanium oxide (TiO₂) in homogenous nano size and well defined dispersion receive high demand for the numerous applications including electrical, optical and catalysis. Looking for it's application in bio-sensing, electrical and catalytic properties plays important role in enhancing the sensing signal via improving interaction between biomolecules and the surfaces of electrode. Various routes are available so far for the fabrication of TiO₂ nano-material including sol-gel, surfactant mediated synthesis, thermal decomposition, polymer matrix assisted preparation, etc.

In this work, nano-TiO₂ coated aluminium (Al) tip/electrodes were synthesized by a simple dip coating method. The electrodes successfully utilized for enzyme free glucose sensor through amperometric measurements. The sensor tip is very stable, reproducible, repeatable and sensitive.

2. EXPERIMENTAL

2.1. Fabrication of nano-crystalline TiO₂/Al tip/electrode: For fabrication of the nano-TiO₂/Al tip using dip coating method, Ti(OH)_x solution was prepared using Titanium Tetra iso-propoxide (TTIP). In a typical synthesis, appropriate amount of TTIP was added into 20 ml of ethanol containing few drops of acetic acid and stirred for 2 hrs at room temperature. A transparent solution was obtained upon evaporation of the excess ethanol. Film of Ti(OH)_x was fabricated on highly polished Al sheet (99.99 % pure Al substrate of thickness 0.14 mm procured from Alfa Aesar). A tip shaped strip (as shown in Figure 1(a)) was cut from the Al sheet and manually dipped (up to ~ 1 cm from tip side) into this solution for 5 seconds. The tip was dried using hot air

blower for few seconds. Similar procedure was repeated three times to get good coating on the tip (as shown in Figure 1(a)). Al tip coated with $\text{Ti}(\text{OH})_x$ show a white color film on the electrode. After coating, the film was annealed at 350 oC for 2 hours to get pure TiO_2 phase on the tip.

2.2. Preparation of glucose and buffer solution: For glucose detection, liquid glucose sample (similar to normal blood glucose level of 5.5 mM/L) was prepared by dissolving using Dextrose (99 %, procured from Merck Chemicals) in distilled water. Dextrose is basically glucose. Four solutions of concentration 0.55, 2.1, 5.5 and 55 mM/L were prepared. Along with this, NaCl buffer solution (which is also present in blood at 140 mM/L) was also prepared by dissolving NaCl (99 %, procured from SD Fine Chemicals) in distilled water to get solution of 14, 70, 140 and 280 mM/L. As the blood also contains both NaCl and glucose, solutions of various glucose concentrations in 140 mM/L NaCl buffer were prepared; namely Mix-A (0.55 mM/L Glucose + 140 mM/L NaCl), Mix-B (2.1 mM/L Glucose + 140 mM/L NaCl), Mix-C (5.5 mM/L Glucose + 140 mM/L NaCl) and Mix-D (55 mM/L Glucose + 140 mM/L NaCl) for glucose level detection using nano- TiO_2/Al tips.

2.3. Device Fabrication: Glucose detection test was performed using nano- TiO_2/Al electrodes in the geometry shown in Figure 1(b). Two coated electrodes were mounted (facing each other) across a small circular open area on a non-conductive double sided tape pasted on a clean glass slide. For amperometric measurement, electrodes were connected in series with a DC power supply and Keithley 6514 current meter. A drop of 30 μL of distilled water or glucose solution or NaCl solution or mix solution was used for amperometric measurement and current was recorded at an interval of 10 seconds.

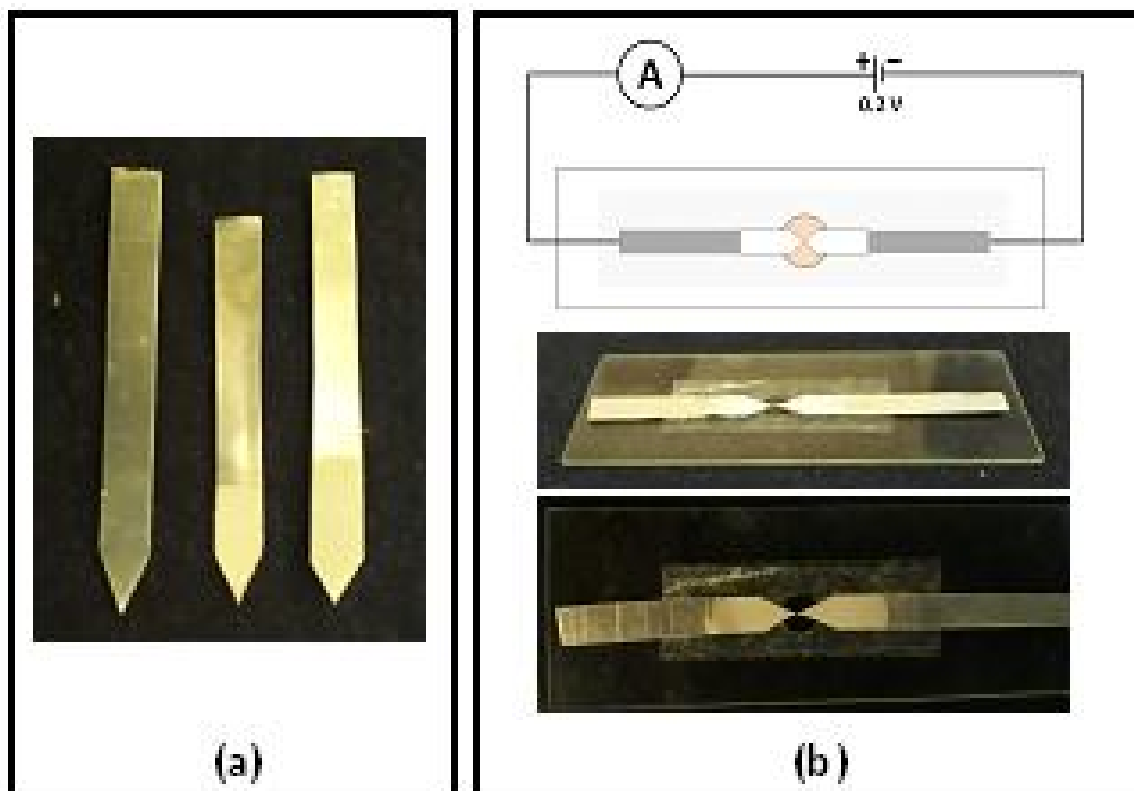


Figure-1: (a) From left to right is pure Al tip, $\text{Ti}(\text{OH})_x$ coated Al tip and TiO_2 coated Al tip and (b) Schematic of the test setup and actual setup with TiO_2 coated Al tip on glass substrate.

2.4. Characterization: The structural, morphological and elemental analysis of nano- TiO_2 coated Al electrode was carried out using x-ray diffraction (XRD), scanning electron microscopy (SEM) and energy dispersive x-ray spectroscopy (EDS) techniques, respectively.

3. RESULTS AND DISCUSSION

3.1. Structural, morphological and elemental analysis of TiO_2/Al tip

The structural, morphological and elemental analysis of the TiO_2 coated Al tip are shown in Figure 2. XRD pattern of TiO_2 film deposited on Al tip, Figure 2(a), exhibits peak corresponding to (101), (004), (200), (105), (211), (204) and (215) crystal planes of anatase phase of TiO_2 (JCPDF#84-1286)10. Along with TiO_2 peaks, * marked peak represents Al. Particle size calculated from the full width half maxima (FWHM) of (101) peak signify nano sized TiO_2 crystallites with size $\sim 60 \pm 10$ nm. These results indicate polycrystalline-nano-anatase TiO_2 particles on Al tip.

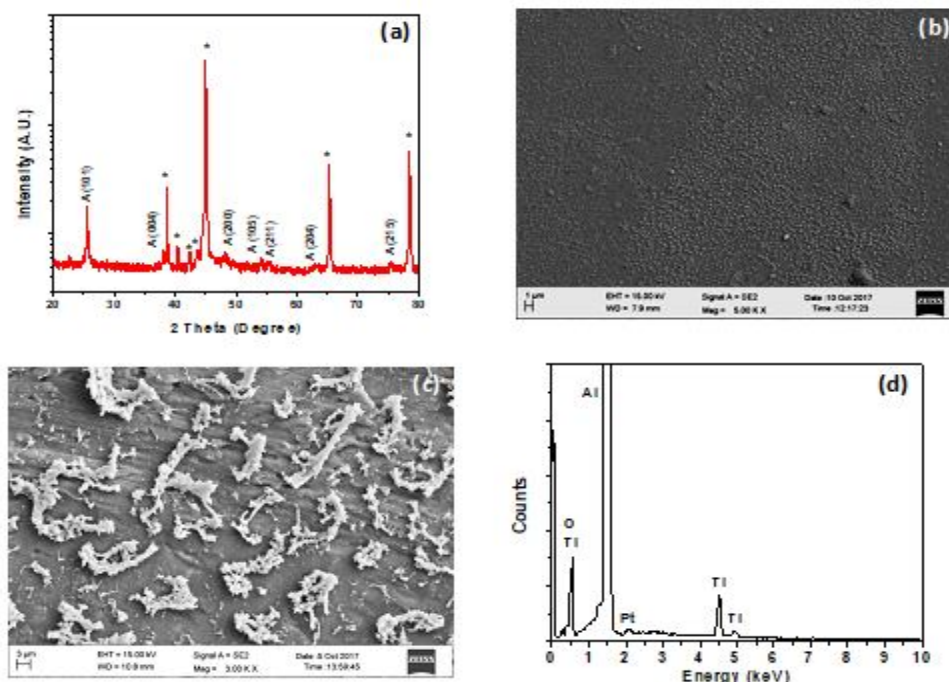


Figure-2: (a) XRD pattern, (b) and (c) are SEM images of Ti(OH)_x film and nano-TiO₂ on Al tip and (d) EDS spectra of TiO₂ coated Al tip.

Figure 2(b) and 2(c) show surface morphological SEM images of as deposited Ti(OH)_x and nano-TiO₂ (after annealing at 350 °C) film on Al tip. As deposited Ti(OH)_x film have nearly 100 % coverage of Al tip surface with formation of small particulates. Whereas, annealing of the film at 350 °C converts Ti(OH)_x into TiO₂ and SEM image (Figure 2(c)) represents fractured film with small and porous algi like nano-structures on the tip. The EDS data captured on nano-TiO₂ coated Al tip, shown in Figure 2(d), confirms the presence of Ti and O elements in the film along with Al. A peak for Pt is because of the conducting coating made on the film to capture clear SEM images.

3.2. Glucose sensing measurement

The glucose sensing performance of nano-TiO₂/Al tip was carefully investigated via amperometric measurement utilizing the setup shown in Figure 1(b) and results are shown in Figure 3 for glucose, buffer and glucose with buffer. During measurement, one nano-TiO₂/Al tip was connected to the positive terminal and another nano-TiO₂/Al tip to the negative terminal of the digital power supply. This allow to use both the tips for oxidation or reduction reaction while glucose interaction with the nano-TiO₂. Operating voltage of 0.5 V was applied and the transient current across the tips in the presence of respective solution was recorded. Before starting glucose sensing measuring, a drop of distilled water was placed between the tip and the background current (observed to be stable at 0.1 μA) was recorded for 10 min. For 0.55 mM glucose, Figure 3(a), the current was observed to jump suddenly to higher value of 1.1 μA from 0.1 μA and later on starts decaying slowly with increasing measurement time. During amperometric measurement the current decays by 37 % in 100 sec. As the glucose concentration increases, an increase in the current was observed. The current was found to be 2.3 μA for 5.5 mM glucose, which decays almost by 10 % after 100 sec. Further increase in the glucose concentration to 55 mM results with more increase in the current. No saturation effect was observed till 55 mM glucose concentration. This observed current after glucose addition is due to the glucose oxidation process using nano-TiO₂. The highest sensitivity of glucose for the nano-TiO₂/Al tip was about 0.157 mA/mM-cm².

As NaCl is vital content in physiological fluids (blood, at normal concentration of 140 mM/L) and have an electro-active nature, which may interfere with the detection of glucose in blood. Therefore, amperometric sensing activity of the nano-TiO₂/Al electrode with nascent NaCl at concentration in the range from 14 to 280 mM was carried out. The amperometric measurement performed at lower operating voltage (0.2 V) due to electro-active nature of NaCl, which may degrade the electrode. The measurement, Figure 3(b), show relative higher current (3.2 μA) at lower NaCl concentration (1.4 mM, which is 100 times lower than normal level found in human blood) as compared with the solvent (0.1 μA), which decay slowly (by 22 %) in 100 sec. It is well known that the NaCl concentration in blood for a normal person is around 140 mM and at this concentration the recorded current was 7 μA, which decays by 25 % after 100 seconds. At very higher NaCl concentration (280 mM) the current was found to increase linearly and reaches to 10 μA.

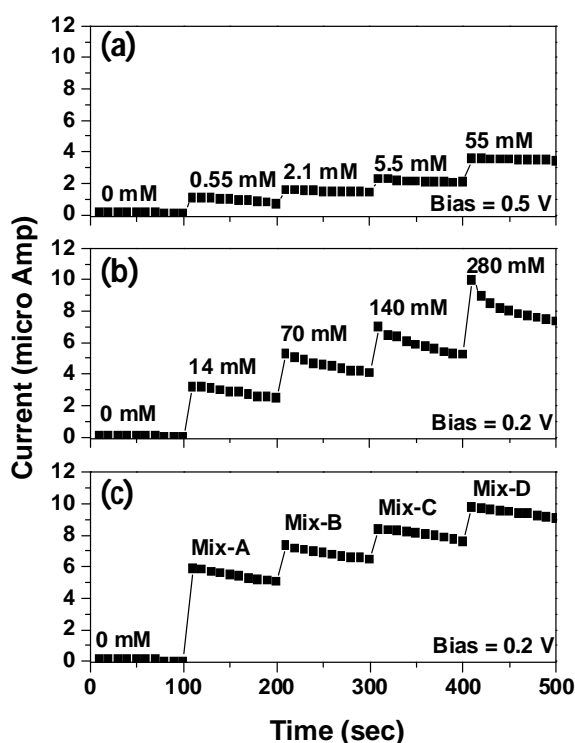


Figure-3: The sensing performance of nano-TiO₂/Al tip (a) only glucose, (b) only buffer and (c) glucose with buffer (140 mM NaCl) measured at operating voltage of 0.5 and 0.2 V respectively.

Based on the above results, a NaCl concentration of 140 mM was chosen as a buffer solution for glucose sensing, which mimics the human blood. For amperometric measurement, mixed solutions were prepared as discussed in methods by mixing glucose (at various concentrations) in 140 mM NaCl solution under vigorous stirring. Amperometric sensing recorded at 0.2 V for nano-TiO₂/Al electrode is shown in Figure 3(c). A fast and stable increase in current was observed when glucose was added in buffer solution. For Mix-A, the current was observed to jump to 5.9 μ A, which decays slowly by 15 % after 100 sec. The sensor shows a good linear trend response in the range 0 to 55 mM with no saturation effect up to 55 mM of glucose. The sensitivity of the sensor is in the linear range and estimated to be 0.766 mA/mM-cm², which is almost \sim 5 times higher than recorded for pure glucose. As comparing with the pure glucose case (Figure 3(a)), the current signal intensified with increase of concentration due to accumulation of more and more intermediate species on electrode surface.

The stability of the developed sensor tip was investigated by measuring its current response for glucose over 4 months and shown in Figure 4. The prepared nano-TiO₂/Al tip was used to record the amperometric response for mixture A, B, C and D with a frequency of 30 day/ 1 month.

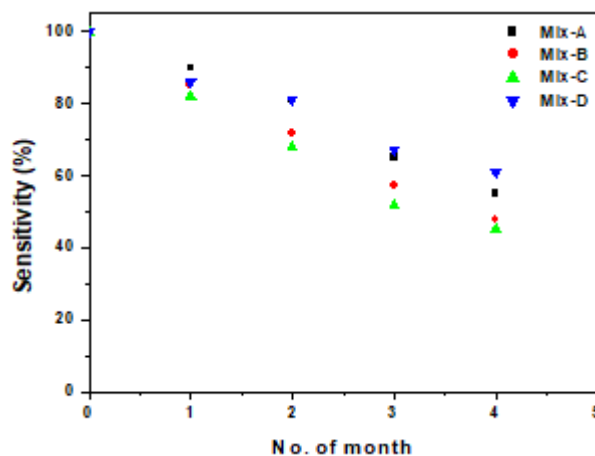


Figure-4: Stability of the nano-TiO₂/Al tip glucose sensor over 4 months for mixture A, B, C and D at 0.2 V.

The sensor shows almost 100 % sensitivity for all mixture solution at start, however, at the end of 1st month the sensitivity drops down by 10 % and further drops down linearly and at the end of 4th months it still remained above 50 % of its initial response, revealing a good stability of the non-enzymatic glucose sensor electrodes. Interestingly, for lower and higher concentration of glucose in mixture solutions, the sensitivity remains above

60 % suggesting a good capability of the electrodes. Thus nano-TiO₂/Al tip acts as a good glucose sensor due to the glucose oxidation ability of the nano-TiO₂. As these tips are kept under normal environmental conditions for long time, few of the active sites available on the surface of nano-TiO₂ gets blocked by the adsorbed species and the oxidization of glucose restricts, resulting in sensitivity decay.

To understand the mechanism of oxidation of glucose, one needs to understand the oxidation of glucose. Nano-TiO₂ modified tip mediates the heterogeneous redox reactions resulting Ti(IV) species¹¹⁻¹⁷, which provides charges to flow across the applied bias. As the concentration of glucose increases, the concentration of charges increases resulting in higher current. The obtained results show typical steady-state amperometric response of nano-TiO₂/Al tip with a successively increasing glucose concentration. It is well known that the glucose and NaCl concentration for a normal person ranges from 4.4 to 6.6 mM and 135 to 145 mM. The current response of nano-TiO₂/Al tip toward mix solution increase linearly, while that for pure glucose is much lower and only realized a slight increase with the addition of glucose into the test cell. The present nano-TiO₂/Al based glucose sensors show a linear dependence on the glucose concentration with a dynamic range of 0.55 to 55 mM, with a sensitivity of 0.766 mA/mM-cm² and a low detection limit of 0.55 mM. The response of the glucose biosensor based on nano-TiO₂/Al tip was found to be larger than those of the biosensors based on TiO₂ thin films or nanostructures. This novel nano-TiO₂/Al electrode glucose sensor exhibits good sensitivity, a low detection limit and a fast response time in less than 2 seconds. This indicates that the as-prepared nano-TiO₂/Al tip glucose biosensor is suitable for detecting the human blood sugar concentration for the diagnosis of diabetes mellitus.

4. CONCLUSION

In summary, we demonstrate a simple and effective method for development of highly sensitive glucose biosensor based on a nano-TiO₂ coated on Al tip fabricated using a simple dip coating technique. The obtained results reveal that the nano-TiO₂ improved the electro-activity in the solution, which in turn enhanced the sensitivity of the biosensor for glucose detection. Furthermore, the performance of the biosensor showed high and reproducible sensitivity of 0.766 mA/mM-cm² over a linear range from 0.55 to 55 mM with a response time of less than 2 s and good stability over relatively long-term storage (more than 4 months). The large surface area, together with the good electrical properties, made the nano-TiO₂/Al tip promising electrode for sensing applications. This study would probably provide an economic way to meet the industrial requirements of a low cost processing technique for large-scale production.

ACKNOWLEDGEMENTS

The author KAB would like to acknowledge the funding provided by Swami Ramanand Teerth Marathwada University, Nanded under UGC-XII plan. The authors acknowledge Dr. P. B. Vidyasagar (Vice-Chancellor, SRTMUN) for constant support and discussions

REFERENCES

1. <https://www.idf.org/our-activities/advocacy-awareness/resources-and-tools/53-global-diabetes-scorecard.html> (accessed on 20/01/2018)
2. L. Wang, X. Gao, L. Jin, Q. Wu, Z. Chen, X. Lin, Amperometric glucose biosensor based on silver nanowires and glucose oxidase. *Sens. Actuator B Chem.* 176 (2013) 9–14.
3. A. Ramanavicius, A. Kausaite, A. Ramanaviciene, J. Acaite, A. Malinauskas, Redox enzyme–glucose oxidase–initiated synthesis of polypyrrole. *Synth. Met.*, 156 (2006) 409–413.
4. C. M. Welch, R. G. Compton, The use of nanoparticles in electroanalysis: A review. *Anal. Bioanal. Chem.*, 384 (2006) 601–619.[5] S. Park, H. Boo, T. D. Chung, Electrochemical non-enzymatic glucose sensors, *Analytica Chimica Acta*, 556 (2006) 46–57.
5. Z. H. Ibupoto, K. Khun, V. Beni, M. Willander, Non-Enzymatic Glucose Sensor Based on the Novel Flower Like Morphology of Nickel Oxide, *Soft Nanoscience Letters*, 3 (2013) 46-50.
6. Y. Wanga, J. Chena, C. Zhoua, L. Zhoua, Y. Konga, H. Longa, S. Zhonga, A novel self-cleaning, non-enzymatic glucose sensor working under a very low applied potential based on a Pt nanoparticle-decorated TiO₂ nanotube array electrode, *Electrochimica Acta*, 115 (2014) 269– 276.
7. C. Espro, N. Donato, S. Galvagno, D. Aloisio, S. G. Leonardi, G. Neri, CuO Nanowires-based Electrodes for Glucose Sensors, *Chemical Engineering Transactions*, 41 (2014) 415-419.
8. M. Ahmad, C. Pan, Z. Luo, J. Zhu, A Single ZnO Nanofiber-Based Highly Sensitive Amperometric Glucose Biosensor, *J. Phys. Chem. C*, 114 (2010) 9308–9313.

9. K. A. Bogle, K. D. More, J. W. Dadge, M. P. Mahabole, R. S. Khairnar, Nano-crystalline TiO₂ thin film: Synthesis and investigation of its optical switching characteristics, *Thin Solid Films*, 653 (2018) 62-66.
10. Ali M. A. Abdul Amir AL-Mokaram, R. Yahya, M. M. Abdi, Habibun Nabi Muhammad Ekramul Mahmud, *Nanomaterials*, 7 (2017) 129-132.
11. C. Di Valentin, E. Finazzi, G. Pacchioni, A. Selloni, S. Livraghi, M. C. Paganini, E. Giamello, N-Doped TiO₂: Theory and Experiment. *Met. Oxides*, 339 (2007) 44–56.
12. G. Colón, M. Maicu, M. C. Hidalgo, J. A. Navío, Cu-Doped TiO₂ Systems with Improved Photocatalytic Activity. *Appl. Catal. B Environ.*, 67 (2006) 41–51.
13. K. Morita, T. Shibuya, K. Yasuoka, Stability of Excess Electrons Introduced by Ti Interstitial in Rutile TiO₂(110) Surface. *J. Phys. Chem. C*, 121 (2017) 1602–1607.
14. K. E. Toghill, R. G. Compton, Electrochemical non-enzymatic glucose sensors: A perspective and an evaluation. *Int. J. Electrochem. Sci.*, 5 (2010) 1246–1301.
15. P. Si, Y. Huang, T. Wang, J. Ma, Nanomaterials for electrochemical non-enzymatic glucose biosensors. *RSC Adv.*, 3 (2013) 3487–3502.

STRUCTURAL PROPERTIES OF RARE EARTH DOPED COBALT FERRITE

P. K. Gaikwad

Department of Physics, Shri Chhatrapati Shivaji College, Omerga

ABSTRACT

Rare earth doped cobalt ferrite materials with chemical formula $\text{CoFe}_{2-x}\text{R}_x\text{O}_4$ ($x = 0.00$ and 0.02 where $\text{R}^{3+} = \text{Sm}^{3+}, \text{Nd}^{3+}, \text{Dy}^{3+}$) have been synthesized by standard ceramic technique using AR grade CoO , Sm_2O_3 , Nd_2O_3 , Dy_2O_3 and Fe_2O_3 . The X-ray diffraction (XRD) measurements confirmed the formation of a single phase cubic spinel structure. The unit cell volume, particle size, Hopping length and lattice constant decreases, while the X-ray density, bulk density, porosity increases with rare earth doped CoFe_2O_4 .

Keywords: Cobalt ferrite, rare earths and Structural properties.

1. INTRODUCTION

Spinel ferrites with general formula MFe_2O_4 (M is a divalent metal ion) are very important materials because of their high electrical resistivity, moderate saturation magnetization and low eddy current and dielectric losses, which makes them useful in many applications. The important electrical and magnetic properties of ferrite depend on chemical compositions, method of preparation and cation distribution in the two sub-lattices i.e. tetrahedral (A) and octahedral [B] site. The study of cation distribution in spinel ferrites is essential to understand structural and magnetic properties of spinel ferrites [1, 2].

In the family of spinel ferrites CoFe_2O_4 is a unique ferrite having inverse spinel structure. CoFe_2O_4 is a hard magnetic material possessing high magneto crystalline anisotropy, high Curie temperature, high coercivity and moderate saturation magnetization along with the chemical stability and mechanical hardness [3, 4]. Several researchers have studied pure and substituted cobalt ferrite with a view to understand their basic properties [5-7].

Spinel with rare earth ions has attracted great attention in the material science field because of their interesting properties such as infrared emission, catalytic, photoelectric and magnetic properties [8, 9]. Many investigations have been carried out to make further improvements on the structural and magnetic properties of substituted ferrites. It is known that the rare earth (RE) ions have unpaired 4f electrons which have the role of originating magnetic anisotropy because of their orbital shape. Doping of rare earth ions into spinel ferrites, the occurrence of 4f-3d coupling which determine the magneto crystalline anisotropy in ferrites can also improve the electrical and magnetic properties of spinel ferrites.

Recent research shows by introducing rare earth ions into the spinel lattice, can lead to small changes in the structural, magnetization and Curie temperature of the spinel ferrite [10-12]. In the present work, we report our result on the structural properties of rare earth doped CoFe_2O_4 .

2. EXPERIMENTAL DETAILS:

Samples with chemical formula $\text{CoFe}_{2-x}\text{R}_x\text{O}_4$ ($x = 0.00$ and 0.02 where $\text{R}^{3+} = \text{Sm}^{3+}, \text{Nd}^{3+}, \text{Dy}^{3+}$) were prepared by standard ceramic technique [13] using analytical reagent grade oxides. Compounds were accurately weighted in molecular weight percentage with single pan microbalance. The mixed powders were wet ground and pre-sintered at 950°C for 24 hours. The sintered powder is again re-ground and pelletized. Polyvinyl alcohol was used as a binder in making circular pellets of 10mm diameter and 2–3mm thickness. The pellets were finally sintered in muffle furnace for 1180°C for 24 hours and then slowly cooled to the room temperature.

X-Ray diffraction patterns were taken at room temperature to confirm the crystal structure of the prepared samples. The XRD patterns were recorded in the 2θ range from 20° to 80° using $\text{Cu-K}\alpha$ radiation ($\lambda = 1.5406 \text{ \AA}$) with scanning rate 2° per/m.

3. RESULTS AND DISCUSSION

3.1 Structural analysis

Room temperature X-ray powder diffraction patterns (XRD) for series having molecular formula $\text{CoFe}_{2-x}\text{R}_x\text{O}_4$ were ($x=0.00$ and $x=0.02$ where $\text{R}^{3+} = \text{Sm}^{3+}, \text{Nd}^{3+}, \text{Dy}^{3+}$) prepared by standard ceramic technique shown in Fig 1.

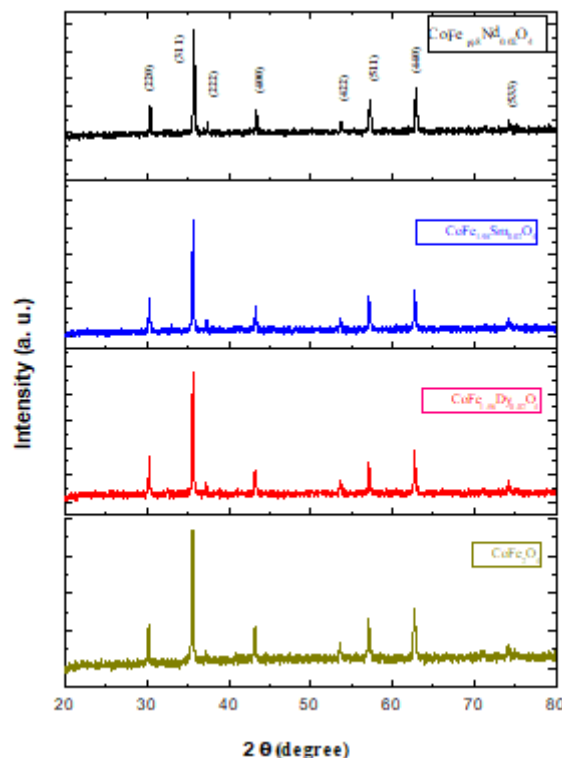


Fig-1: XRD patterns of $\text{CoFe}_{2-x}\text{R}_x\text{O}_4$ ($x = 0.00$ & 0.02 where $\text{R}^{3+} = \text{Dy}^{3+}, \text{Sm}^{3+}, \text{Nd}^{3+}$)

The Braggs reflections (hkl) belonging to the plane (220), (311), (222), (400), (422), (511), (440) and (533) confirms the formation of single phase cubic spinel structures. No extra peak of rare earth doped CoFe_2O_4 materials is observed for $x = 0.02$. Similar reports of XRD pattern are available in the literature [14-16].

Table-1: Lattice constant (a), X- ray density (d_x), bulk density (d_B), Porosity (P) and Particle size (t) of $\text{CoFe}_{2-x}\text{R}_x\text{O}_4$ system.

$\text{CoFe}_{2-x}\text{R}_x\text{O}_4$	'a' (Å)	'a' ³ (Å) ³	d_x (gm/cm ³)	d_B (gm/cm ³)	P (%)	t (Å)
CoFe_2O_4	8.376	587.64	5.305	3.864	27.16	396.71
$\text{CoFe}_{1.98}\text{Sm}_{0.02}\text{O}_4$	8.362	584.70	5.373	3.866	28.05	395.47
$\text{CoFe}_{1.98}\text{Nd}_{0.02}\text{O}_4$	8.343	580.72	5.407	3.877	28.30	395.59
$\text{CoFe}_{1.98}\text{Dy}_{0.02}\text{O}_4$	8.369	586.16	5.305	3.864	27.16	417.40

Using XRD data the lattice constant (a) was calculated using standard relation for cubic spinel structure. The values of lattice constant are given in Table 1 that the lattice constant of rare earth doped CoFe_2O_4 is less than pure CoFe_2O_4 . A minor decreases in lattice parameter, a_0 of CoFe_2O_4 with rare earth doped, which may be due to the compressive pressure exerted on the ferrite lattice by $\text{R}^{3+}\text{FeO}_3$ [17]. The X-ray density (d_x) was calculated using the equation

$$d_x = \frac{ZM}{N_a a^3} \quad \dots(1)$$

Where 'Z' is number of molecules per unit cell. (For spinel system $Z = 8$), 'M' is the molar mass of the ferrite, ' N_a ' is the Avogadro's number and ' a^3 ' is the unit cell volume computed from the values of lattice constant. X-ray density (d_x) increases almost linearly with the doped of R^{3+} because the Fe^{3+} ions on the octahedral sites are being replaced by the larger mass R^{3+} ions.

The bulk density of the samples was measured by using Archimedes principle [18] and values are presented in Table 1. The porosity of the samples was calculated by using the following relation and values are tabulated in Table 1.

$$P = \left(1 - \frac{d_B}{d_x} \right) \times 100\% \quad \dots(2)$$

where d_B is the bulk density and d_x is X-ray density.

The particle size ‘t’ of sample was determined by most intense peak (311) by using the relation

$$t = \frac{0.9\lambda}{\beta \cos \theta} \quad \dots(3)$$

Where β the full width at half maximum (FWHM) and λ is wavelength of the target material. The particle size values are given in Table 1. It is observed from table 1 that the particle size of rare earth doped is smaller than the pure CoFe_2O_4 .

The values of the tetrahedral and octahedral bondlength (d_{AX} and d_{BX}), the tetrahedral edge (d_{AXE}), and the shared and unshared octahedral edge (d_{BEX} and d_{BXE}) can be calculated according Eqs (4) ~ (8). Using the value of the lattice parameter ‘a’ (Å) and the oxygen position parameter ‘u’ ($u=0.381$ Å). The value of the bondlength of the tetrahedral and octahedral sites are shown in Table 2, It is seen that the all values are depend on the lattice parameter so, the lattice parameter decrease, then the edge and the bondlength of the tetrahedral and octahedral sites are decreases.

$$d_{AX} = a\sqrt{3}\left(u - \frac{1}{4}\right) \quad \dots(4)$$

$$d_{BX} = a\left[3u^2 - \left(\frac{11}{4}\right)u + \left(\frac{43}{64}\right)\right]^{\frac{1}{2}} \quad \dots(5)$$

$$d_{AXE} = a\sqrt{2}\left(2u - \frac{1}{2}\right) \quad \dots(6)$$

$$d_{BAX} = a\sqrt{2}(1 - 2u) \quad \dots(7)$$

$$d_{BXE} = a\left[4u^2 - 3u + \left(\frac{11}{16}\right)\right]^{\frac{1}{2}} \quad \dots(8)$$

The distance between magnetic ions (hopping length) in the tetrahedral sites is given by Eqs (9) ~(10).

$$L_A = \frac{a\sqrt{3}}{4} \quad \dots(9)$$

$$L_B = \frac{a\sqrt{2}}{4} \quad \dots(10)$$

where ‘a’ is the lattice constant, the value Hopping length (L_A , L_B) are shown in Table 2, Hopping length (L_A , L_B) values are depend on the lattice parameter so that the lattice parameter are decrease so the Hopping length (L_A , L_B) also decreases.

Table-2: Hopping length (L_A , L_B), Tetrahedral bond (d_{AX}), Octahedral bond (d_{BX}), tetra edge (d_{AXE}) and octaedge (d_{BXE}) (Shared and non-shared) of $\text{CoFe}_{2-x}\text{R}_x\text{O}_4$ system.

$\text{CoFe}_{2-x}\text{R}_x\text{O}_4$	L_A (Å)	L_B (Å)	d_{AX} (Å)	d_{BX} (Å)	d_{AXE} (Å)	d_{AXE} (Å)	
						(Shared)	(Unshared)
CoFe_2O_4	3.629	2.961	1.901	2.045	3.103	2.819	2.963
$\text{CoFe}_{1.98}\text{Sm}_{0.02}\text{O}_4$	3.621	2.956	1.897	2.042	3.098	2.815	2.958
$\text{CoFe}_{1.98}\text{Nd}_{0.02}\text{O}_4$	3.613	2.950	1.893	2.037	3.091	2.808	2.952
$\text{CoFe}_{1.98}\text{Dy}_{0.02}\text{O}_4$	3.629	2.959	1.899	2.043	3.101	2.817	2.961

4. CONCLUSIONS

The $\text{CoFe}_{2-x}\text{R}_x\text{O}_4$ ($x = 0.00$ and 0.02 where $\text{R}^{3+}=\text{Sm}^{3+}$, Nd^{3+} , Dy^{3+}) spinel ferrite system was successfully prepared by standard ceramic technique. The X-ray powder diffraction analysis of the samples revealed that the prepared sample possesses single phase cubic spinel structure. The lattice constant, particle size decreases but X-ray density, bulk density and porosity increases with rare earth doped CoFe_2O_4 . Hopping length, tetrahedral bond, Octahedral bond, tetra edge and octa edge are decreases with rare earth doped CoFe_2O_4 .

REFERENCES

1. M. Ishaqu, M. U. Islam, M. A. Khan I. Z. Rahman A. Genson, S. Hampshire Physica B 405(2010) 1532.
2. L. Gama, A.P. Diniz, A.C.F.M. Costa, S.M. Rezende, A. Azevedo, D.R. Cornejo Physica B 384 (2006) 97.
3. J. Peng, M. Hojamberdiev, Y. Xu, B. Cao, J. Wang, H. Wu. J. Magn. Magn. Mater. 323(2011) 133.
4. P. S. Aghav, V. N. Dhage, M. L. Mane, D. R. Shengule, R. G. Dorik, K. M. Jadhav. Physica B 406(2011) 4350.
5. I. P. Muthuselvam, R.N. Bhowmik J. Magn. Magn. Mater. 322 (2010) 767.
6. C. Yan, F. Cheng, Z. Peng, Z. Xu, and C. Liao J. Appl. Phys. 84 (1998) 10.
7. M Maisnam, S Phanjoubam, H.N.K. Sarma, C Prakash, L. R Devi, O.P. Thakur Physica B 370 (2005) 1.
8. Y. M. Al Angari J. Magn. Magn. Mater. 323 (2011) 1835.
9. M. A. Ahmed, E. Ateia, F. M. Salem. Physica B 381 (2006) 144.
10. K. K. Bharathi, R. S. Vemuri, C. V. Ramana. Chem. Phys. Lett. 504 (2011) 202.
11. K. K. Bharathi, J. A. Chelvane, G. Markandeyulu. J. Magn. Magn. Mater. 321 (2009) 3677.
12. E. E. Sileo, S. E. Jacobo. Physica B 354 (2004) 241.
13. D. R. Patil, B. K. Chougule. Mater. Chem. Phys. 117 (2009) 35.
14. Mansor Al-Haj. J. Magn. Magn. Mater 299(2006) 435.
15. S. Jie, W. Lixi, X. Naicen, Z. Qitu. J. Rare Earths 28(2010) 451.
16. J. Jiang, Y. Yang, L. Li. Physica B. 399 (2007) 105.
17. P. K. Roy, J. Bera. J. Magn. Magn. Mater 321 (2009) 247.
18. M. L. Mane, R. Sundar, K. Ranganathan, S. M. Oak, K. M. Jadhav. Nucl. Instrum. Methods B 269 (2011) 466.

TEMPERATURE DEPENDENT GAS DETECTION OF SPRAY DEPOSITED ZNO THIN FILMS

E. U. Masumdar¹ and M. A. Barote²¹Thin Film Physics Laboratory, Department of Physics, Rajarshi Shahu Mahavidyalaya, Latur²Department of Physics, Azad College, Ausa

ABSTRACT

ZnO semiconductor thin films were prepared by cost effective chemical spray pyrolysis technique. The effect of temperature on different gases detection properties has been studied. The ZnO film showed more selectivity for LPG over Ethanol and Acetone at an operating temperature of 300 °C. The effective surface area for LPG to react increased and so the response increased, which offered more efficient surface area for interaction with LPG molecules on the surface as well as inside porous structure, compared to other films.

Keywords: Spray pyrolysis; ZnO films; sensing properties; dynamic response.

INTRODUCTION

There has been a great deal of interest in zinc oxide (ZnO) semiconductor materials lately, as seen from a surge of a relevant number of publications. The interest in ZnO is fueled and fanned by its prospects in optoelectronics applications owing to its direct wide band gap ($E_g \sim 3.3$ eV at 300 K). Some optoelectronic applications of ZnO overlap with that of GaN, another wide-gap semiconductor ($E_g \sim 3.4$ eV at 300 K) that is widely used for production of green, blue-ultraviolet, and white light-emitting devices (LED). However, ZnO has some advantages over GaN among which are availability of fairly high quality ZnO bulk crystals and a large exciton binding energy (60 meV). ZnO also has much simpler crystal-growth technology, resulting in a potentially lower cost for ZnO-based devices [1-8]. As a direct wide-band-gap material, ZnO is attracting a lot of attention for a variety of electronic and optoelectronic applications. Advantages associated with a large band gap include higher breakdown voltages, ability to sustain large electric fields, lower noise generation, and high temperature and high-power operation. Among the tetrahedrally bonded semiconductors, ZnO has the highest piezoelectric tensor or at least one comparable to that of GaN and AlN. This property makes it a technologically important material for many applications, which require a large electromechanical coupling [9-15].

EXPERIMENTAL DETAILS

Zinc oxide films were deposited by spray pyrolysis method using an aqueous zinc nitrate solution. The Zinc oxide thin films were deposited

- By varying the concentration of sprayed solution from 0.10 to 0.75 M by changing the amount of zinc nitrate dissolved in an aqueous solution. The deposited thin films were termed as ZM1, ZM2, ZM3 and ZM4.
- By varying the spray rate as 2 ml/min, 2.5 ml/min, 3 ml/min and 4 ml/min and the deposited films were denoted as ZS1, ZS2, ZS3 and ZS4.
- By varying the substrate to nozzle distance as 30 cm, 28 cm and 2 cm and films were termed as ZD1, ZD2 and ZD3.
- By varying the substrate temperature from 425 °C to 475 °C at an interval of 25 °C and deposited films were labeled as ZT1, ZT2 and ZT3

The solution was sprayed through a glass nozzle onto the ultrasonically cleaned glass substrates kept at various temperatures. The substrate temperature was optimized to 450 °C. The spray rate was maintained using air as a carrier gas and the spray rate of 3 ml/min was optimized. The temperature was controlled using electronic temperature controller. Hazardous fumes that evolved during the thermal decomposition of initial ingredient were expelled out. The nozzle to substrate distance was optimized as 28 cm. Here, after the deposition process completed, the films were kept on the heater at deposition temperature for 30 min in order to provide sufficient time and temperature for recrystallization.

RESULTS AND DISCUSSIONS

Temperature dependent gas detection

Fig. 1 and Fig. 2 shows the histogram of gas response to different gases with operating temperature for the optimized sample for (a) 0.5 M molar concentration (ZM3), (b) spray rate of 3 ml/min (ZS3), (c) substrate to nozzle distance of 28 cm (ZD2), (d) substrate temperature at 400 °C (ZT2). The histogram revealed that the sensor offered maximum response to Ethanol (16%) at 300 °C, Acetone (27%) at 300 °C and LPG (47%) at 300 °C. The sensor selects a particular gas at a particular temperature. Thus, by setting the temperature, one can use

the sensor for particular gas detection. The same sensor could be used for the detection of different gases by operating it at particular temperature for a typical gas. Different gases have different energies for adsorption, desorption and reaction on the metal oxide surface, and therefore, the response of the sensor at different temperatures would depend on the gas being sensed. The ZnO film showed more selectivity for LPG over Ethanol and Acetone at an operating temperature of 300 °C.

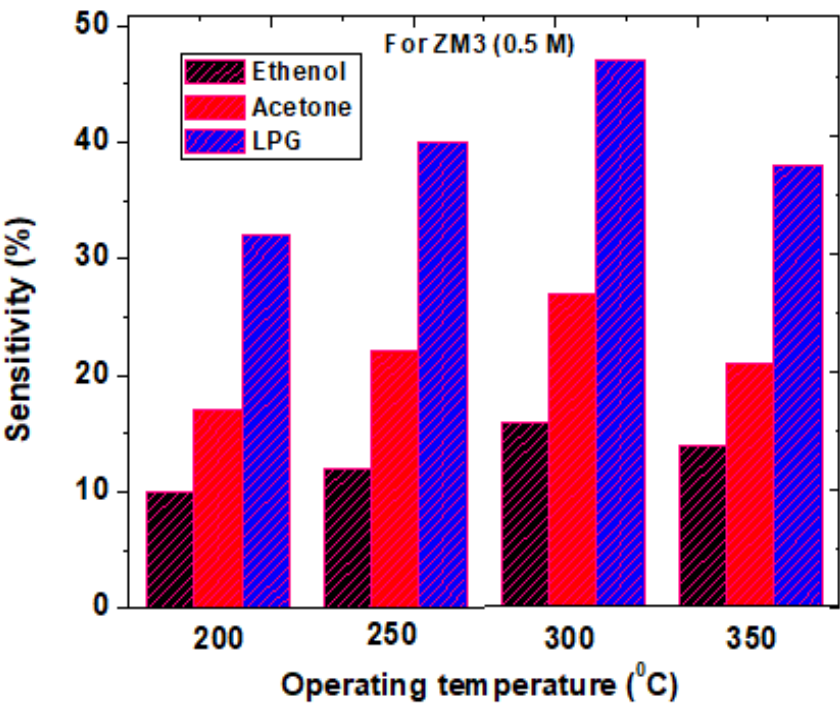


Figure-1: Gas response of ZnO film (0.5M) with operating temperature for different gases at a fixed gas concentration 1000 ppm.

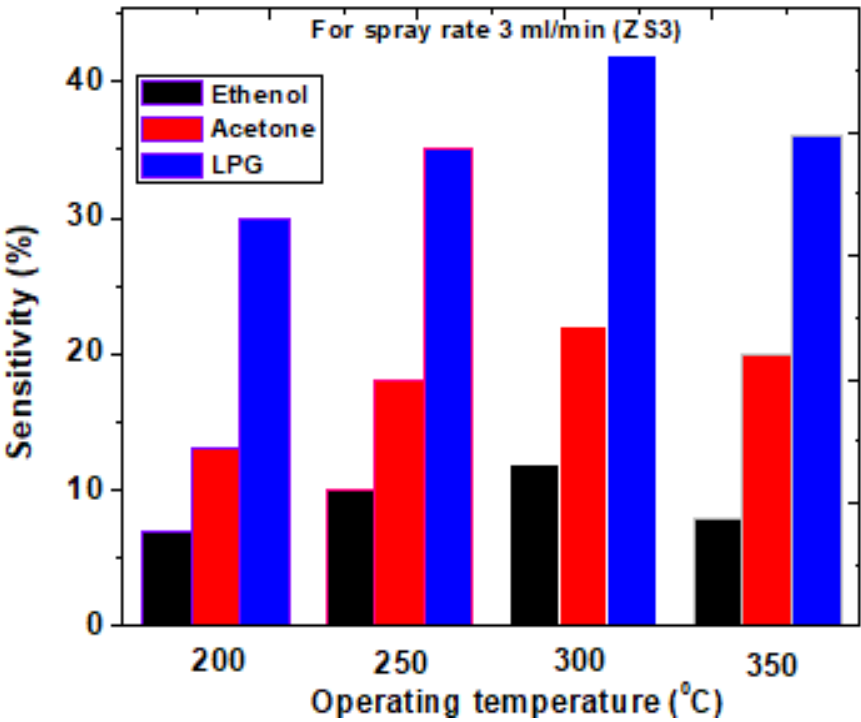


Figure-2: Gas response of ZnO film (spray rate 3ml/min) with operating temperature for different gases at a fixed gas concentration 1000 ppm.

It revealed that LPG is the more selective against other two. The response of all the films does not exhibit any significant difference at lower temperatures. At a low operation temperature, the low response can be expected because the gas molecules do not have enough thermal energy to react with the surface adsorbed oxygen species. As the electrons are drawn from the conduction band of the ZnO by the adsorbed oxygen, and a

potential barrier to charge transport is developed. At higher temperatures the thermal energy obtained was high enough to overcome the potential barrier, and a significant increase in electron concentration resulted from the sensing reaction. The response of a semiconductor oxide gas sensor to the presence of a given gas depends on the speed of the chemical reaction on the surface of the grains and the speed of diffusion of the gas molecules to that surface which are activation processes, and the activation energy of the chemical reaction is higher. In this case, at low temperatures the sensor response is restricted by the speed of the chemical reaction, and at higher temperatures it is restricted by the speed of diffusion of gas molecules. At some intermediate temperature, the speed values of the two processes become equal, and at that point the sensor response reaches its maximum [16].

DYNAMIC GAS RESPONSE

Fig. 3 shows the dynamic gas response transients of ZnO films of different molar concentrations, spray rate, nozzle to substrate distances and substrate temperatures for LPG at 300 °C. The maximum response was obtained with film 0.5 M (ZM3), spray rate 3 ml/min (ZS3), substrate to nozzle distance 28 cm (ZD2) and substrate temperature at 400 °C (ZT2). In the gas sensitivity, the grain size and porosity of the film played an important role [17]. For film ZS3, ZM3, ZT2 and ZD2 have the porous and non-spherical grains were observed. As exposure area of these films increased, the sensitivity was gradually increased. One can observe from SEM image the spherical grains with more porosity. Such kind of morphology helped for providing larger surface area to expose and react on the outer surface as well as inside porous surface more efficiently. Thus, the effective surface area for LPG to react increased and so the response increased, which offered more efficient surface area for interaction with LPG molecules on the surface as well as inside porous structure, compared to other films. When LPG was introduced in the gas chamber, the gas response initially increased with time and then remained stable.

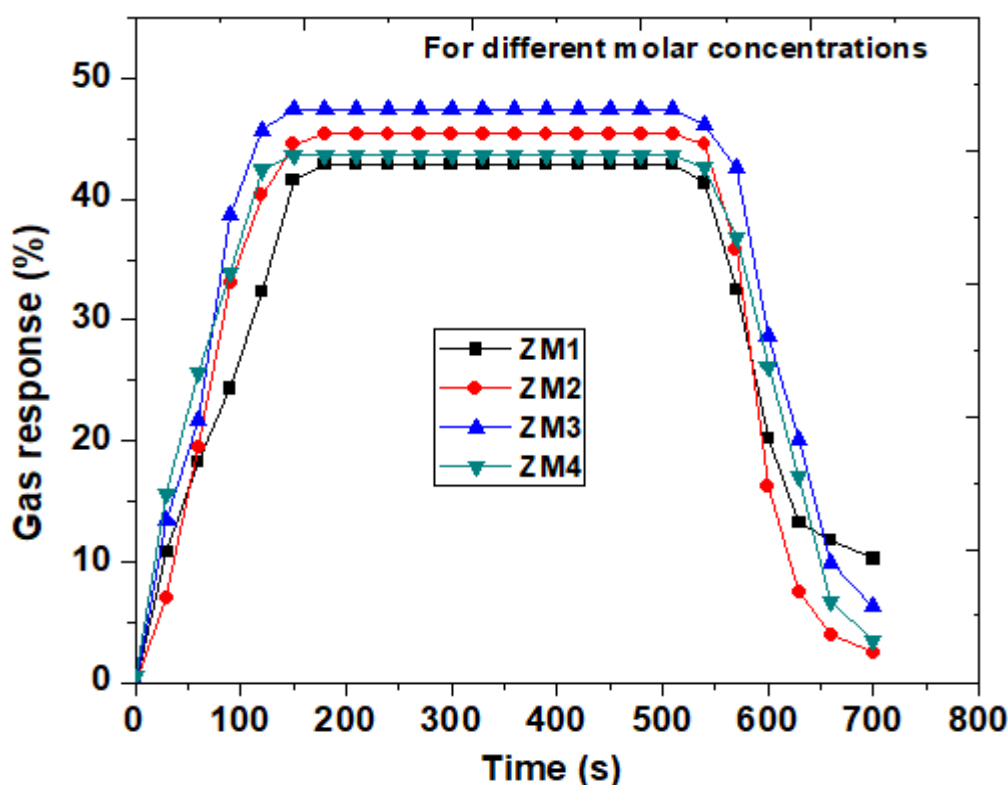


Figure-3: The dynamic response transients of ZnO films of various molar concentrations

CONCLUSION

- Zinc oxide films were deposited by spray pyrolysis method using an aqueous zinc nitrate solution.
- The sensor offered maximum response to Ethanol (16%) at 300 °C, Acetone (27%) at 300 °C and LPG (47%) at 300 °C.
- The ZnO film showed more selectivity for LPG
- The maximum dynamic response was obtained with film 0.5 M (ZM3), spray rate 3 ml/min (ZS3), substrate to nozzle distance 28 cm (ZD2) and substrate temperature at 400 °C (ZT2).
- The effective surface area for LPG to react increased and so the response increased.

REFERENCES

1. Ü. Özgür, Ya. I. Alivov, C. Liu, A. Teke, M. A. Reshchikov, S. Doğan, V. Avrutin, S.-J. Cho, and H. Morkoç J. App. Phys. 98 (2005) 041301.
2. A. Dal Corso, M. Posternak, R. Resta, and A. Baldereschi, Phys. Rev. B 50 (1994) 10715.
3. M. Losurdo, D. Barreca, P. Capezzuto, G. Bruno, E. Tondello, Surf. Coat. Technol. 151–152 (2002) 2.
4. T. S. Moss, Optical Properties of Semiconductors, Chap. 3 Butter-Worth, London, 1961.
5. G. H. Jeffery, J. Bassett, J. Mendham, R. C. Denney, Vogels Textbook of Quantitative Chemical Analysis, Longman Scientific Technical, U. K. 1989.
6. L. P. Deshmukh, S. G. Holikatti, R.P. Rane, M. I. Belle, P. P. Hankare, Bull. Electrochem. 9 (1993) 237.
7. S. Gover, C. Hodes, J. Phys. Chem. 98 (1995) 5338.
8. G. Hodes, Isr. J. Chem. 33 (1993) 95.
9. M.A. Barote, A.A. Yadav, E.U. Masumdar, Physica B, 406 (2011) 1865.
10. T. V. Vimalkumar, N. Poornima, C.Sudha Kartha, K. P. Vijaykumar, Appl. Surf. Sci. 256 (2010) 6025-6028.
11. N. N. Jandow, F. K. Yam, S. M. Thahab, K. Ibrahim, H. Abu Hassan, Materials Letters 64 (2010) 2366.
12. T. Minami, S. Ida, T. Miyata, Y. Minamino, Thin Solid Films 445 (2003) 268–273.
13. G. H. Jeffery, J. Bassett, J. Mendham, R. C. Denney, Vogels Textbook of Quantitative Chemical Analysis, Longman Scientific Technical, U. K. 1989.
14. L. P. Deshmukh, S. G. Holikatti, R.P. Rane, M. I. Belle, P. P. Hankare, Bull. Electrochem. 9 (1993) 237.
15. S. Gover, C. Hodes, J. Phys. Chem. 98 (1995) 5338.
16. T.G. Nenov, S.P. Yordanov, Ceramic Sensors, Technology and Applications, Technomic Publishers, Lancaster, 1996, p. 138.
17. K. Arshak, I. Gaiden, Mater. Sci. Eng. B 118 (2005) 44–49.

SURFACE WATER LEVEL ESTIMATION FROM MICROWAVE SIR-C SAR IMAGE: A HYDROLOGICAL STUDY USING CLASSIFICATION TECHNIQUES

Shaikh M. A.¹, Sonawane D K², Karle S. C.³, Momin R. K⁴, Sayyad S. B⁵^{1,2,3}Department of Elect. Sci., New Arts, Commerce and Science College, Ahmednagar^{4,5}Milliya Arts, Science & Management Science College, Beed

ABSTRACT

Surface water plays an essential role in determining the economic and social health of the areas on the Earth. The estimation of Earth surface water level using the microwave Synthetic Aperture Radar (SAR) is an interesting task. The SAR is an active remote sensing system. It allows the observation during the day as well as on night and independent from weather conditions. In the present work surface level assessed using classification techniques. It includes unsupervised and supervised classifiers. Here L-band quad polarized SIR-C satellite SAR image of Kolkata, West Bengal, India is used. The hydrological study includes, the water distribution, and its amount of area covered on the Earth. The classification results are compared and analysed. It is concluded that the unsupervised classification is better compare to supervised classification for water level estimation.

Keywords: SAR, SIR-C, unsupervised and supervised classification, hydrological study.

INTRODUCTION

The SAR is an active remote sensing system, which acquired very high resolution images of the Earth [1]. It has the capacity to penetrate through clouds, smoke, fog, etc., though there is change in environmental condition. The classification is one of the important tasks in image analysis, which is the process of assigning a set of is given data elements to a given set of classes. In remote sensing classifying data is very challenging because of many factors, such as the selected study area, the complexity of the scene in the study area, accuracy assessment and the types of classification techniques used in image processing.

In the Earth, the total area covered by Water is more than 70%. Hence, many researcher works towards the various ocean applications. It includes sea surface pollution studied by Shaikh et. al. (2015), Sea ice type mapping by Scheuchl et. al. (2004), oil slicks finding by Maurizio et. al. (2007) and Zhang et. al. (2011) etc. Cedric et. al. (2006) and Chi et. al. (2008) classified microwave L band SAR dataset using the supervised classification. They reported that the accuracy of the L band dataset for both Wishart and SVM supervised classification is nearly same [2-7].

In the present study, we have been using SIR-C satellite L-Band MLC (multi-look complex) format Kolkata city, India data. The MLC data is based on an averaging of multiple looks, and consists of one file for each scene per frequency which have been multilook and usually resampled to a ground range projection. The data also had speckle noise and was not geocoded [8-9]. Therefore, the azimuth and the range direction were different, hence slant range to ground range conversion was performed to equalize these resolutions. This resulted in the creation of an image with square pixels due to equalization of the azimuth and range resolution using multilooking process. This process was carried out to improve the radiometric accuracy of the measurements. Then further processing is carried out using speckle filtering and decomposition techniques. Hence, in the present work we have been H-alpha, Wishart H-alpha and Wishart H-A-alpha decomposition techniques used for unsupervised classification and supervised classification of SAR image.

The objective of these works is to separate the polarimetry measurements from a random media into independent elements and estimate the water surface area present on the Earth using classification techniques. This paper will provide comparative simulation model results of classification SIR-C PolSAR image analysis as per above mentioned decomposition techniques for classification by using PolSARPro Ver. 5.0 and NEST Ver. 5.0.16 software. The both software's are freely available on the internet developed by ESA.

CLASSIFICATION

The classification is one of the important tasks in image analysis, which is the process of assigning a set of is given data elements to a given set of classes. The unsupervised classification technique used is based upon polarimetric H-A-alpha decomposition classification parameters such as Entropy (H), Anisotropy (A) and Alpha (α) and this classification procedure is carried out using decomposition theorem and the H/A/ α set of the coherency matrix. The entropy (H) provides information on the scattering degree of randomness. The anisotropy (A) gives information on the relative importance of secondary mechanisms whereas the alpha (α) parameter indicates the nature of the scattering single or double bounce reflection or scattering over anisotropic

media. The both H and A parameter cannot be interpreted separately from the entropy. Another type of classification is supervised classification which approach to pixel labelling requires the user to select representative training data for each predefined number of classes [10].

Unsupervised Classification

The classification of SAR image is to identify the different spectral classes present in it and their relation to some specific ground cover type. The result of classification done here is based on H-alpha parameters and the Wishart classification based on the Wishart statistics of multilook coherency matrix. In the present work result from the H-alpha and Wishart H-alpha and Wishart H-A-alpha decomposition can be initialising as training sets of the unsupervised classifier is studied [11-12].

Supervised Classification

The supervised classification involved three basic steps, in the training stage, the analyst identifies the training areas and developed numerical description of the spectral attributes of each object on the Earth of interest in the scene. Then in the classification stage each pixel in the dataset is categorized into the specific class. The accuracy of creating class depends upon selecting the training area and identifying the same pixel from the dataset. Then in the final stage classified output image is used for further analysis [13-14].

STUDY AREA

The study area is located in the capital of West Bengal, Kolkata city with longitude $87^{\circ}51'57.60''\text{E}$ to $88^{\circ}35'06.00''\text{E}$ and latitude of $21^{\circ}52'58.80''\text{N}$ to $22^{\circ}45'07.20''\text{N}$ [15]. The data is in MLC (multi-look complex) format and incident angle is 32.878° . The SIR-C image with the quad polarization obtained on 05/10/1994 is used in this study. The figure 1 shows the location of study area with map of India and selected study area in Kolkata, West Bengal, India and figure 2 shows original quad dataset of SIR-C SAR satellite dataset with HH, HV, VH, VV polarization.

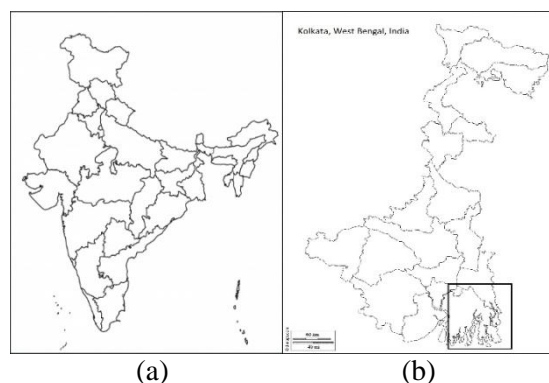


Figure-1: Location of study area (a) map of India (b) selected area in Kolkata, West Bengal, India

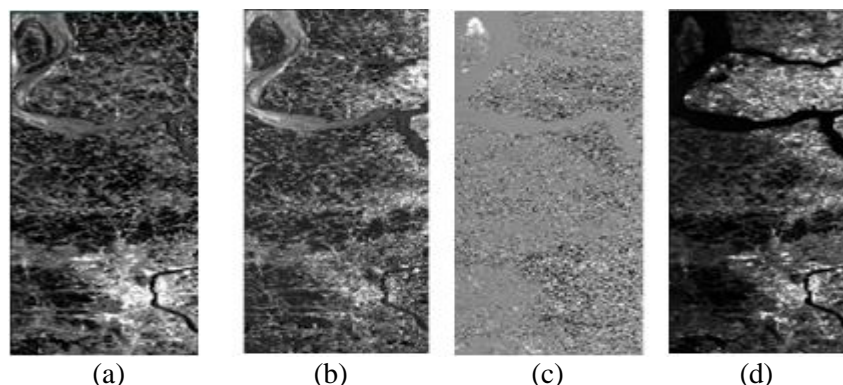


Figure-2: Original Quad PolSAR SIR-C image of Kolkata, India (a) HH (b) HV (c) VH (d) VV

RESULT AND DISCUSSION

The SIR-C SAR image was in MLC format, hence initially it is converted into the ground range using a multilook processing after importing the data in PolSARPro 5.0 software. The figure 3 (a) shows the Pauli RGB image, the Pauli decomposition image also called Pauli image which shows the in red, blue and green colours respectively representing all the polarimetric information of the matrix. Next the data filtered with 5×5 window size by using Lee Refined speckle filter, because speckle noise degrades the quality of SAR image. Then decomposition parameters the Entropy (H), Anisotropy (A) and Alpha (α) are generated images shown in figure 3 (b), (c), (d).

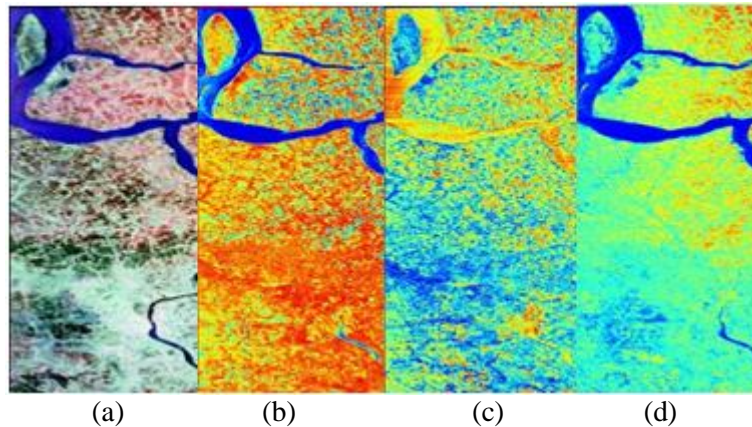
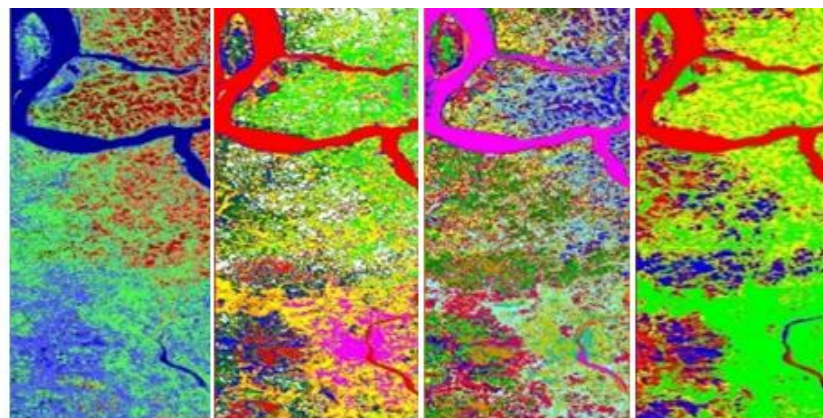


Figure-3: (a) Pauli RGB; Decomposition Parameter (b) Entropy (c) Anisotropy (d) Alpha Image

Later, the images are classified using H-alpha, Wishart H-alpha and Wishart H-A-alpha unsupervised classifier and supervised classifier. The results of classified images are shown in the figure 4 (a), (b), (c), and (d) respectively.



1. Water 2. Open Land 3. Vegetation 4. Settlement

Figure-4: Unsupervised Classification (a) H Alpha (b) Wishart H Alpha (c) Wishart H A Alpha (d)

SUPERVISED CLASSIFICATION

These classified images results are further analysed by using NEST software. By comparing the H-alpha and Wishart H-alpha classification images, it is observed that though H-alpha and Wishart H-alpha having 8 number of classes but Wishart H-alpha shows more accurate results. Similarly, by comparing results of Wishart H-A-alpha classified image having 16 classes and the results are much better than H-alpha and Wishart H-alpha classified image.

In supervised classification 4 major classes are made and it is compare with the all unsupervised classification. From the comparison it is observed that the all four classes in supervised classifier having much larger value than the unsupervised classifier. The Table. 1 shows comparison for major 4 classes like water, open land, vegetation and settlement area of the above mentioned unsupervised and supervised classes.

Table-1: Unsupervised Classification of SIR-C SAR Image

Class	Types of Unsupervised Classification			Supervised Classification (%)
	H Alpha (%)	Wishart H Alpha (%)	Wishart H A Alpha (%)	
Water	11.001	12.956	8.861	24.741
Open Land	25.939	8.853	9.358	9.850
Vegetation	9.586	12.291	4.069	26.626
Settlement	38.553	22.284	14.554	38.782

The present study is more focus on Water class for surface water estimation. Hence from the above all classification results the water class is separate out. The figure 5 shows all unsupervised and supervised classification results for water class only. It is further compared and its comparison is shown in figure 6.

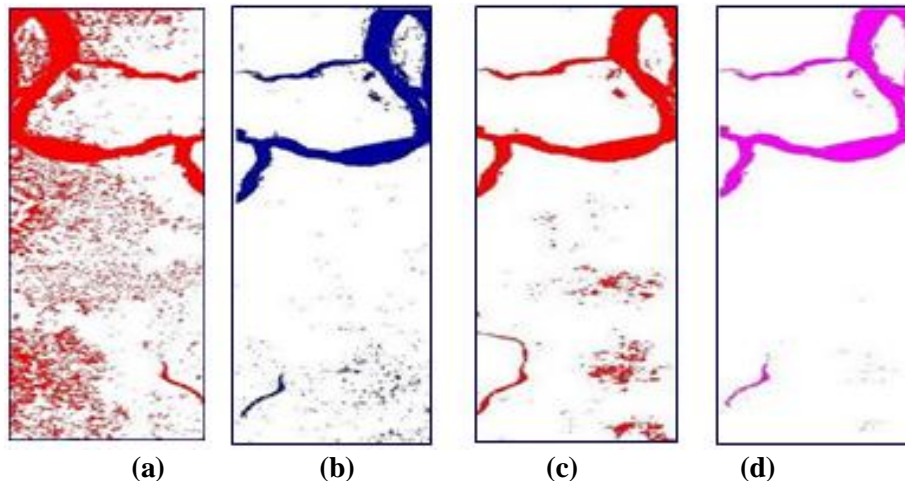


Figure-5: Water class for Unsupervised Classification (a) H Alpha (b) Wishart H Alpha (c) Wishart H A

Alpha (d) Supervised classification

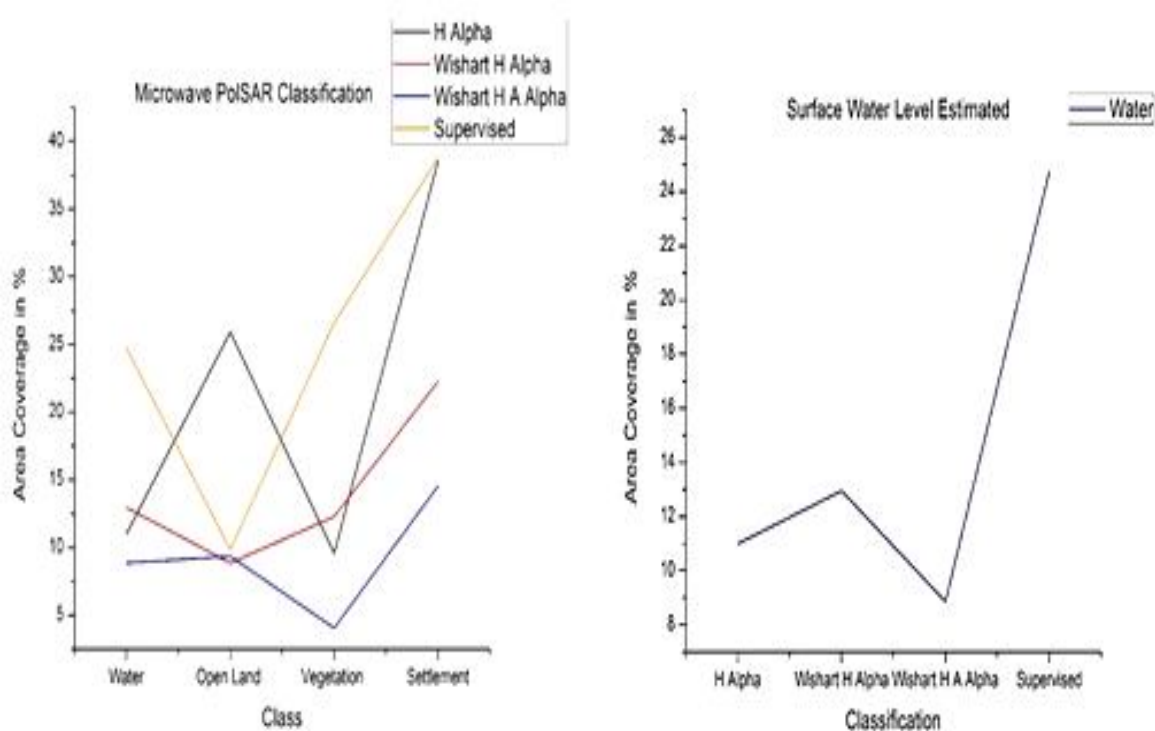


Figure-6: Graph of 4 Class for H Alpha, Wishart H-alpha & Wishart H-A-alpha Classification

In comparison between three types of unsupervised and supervised classification. It is observed that Wishart H-A-alpha shows lower area coverage as compared to other classification. Because a number of classes in Wishart H-A-alpha is more. The supervised classification results show the highest value for water class, but practically the study area does not have that much water surface. Hence, in comparison, Wishart H Alpha shows better results for water surface area estimation. This result is very important for hydrological planning.

CONCLUSION

We have classified SAR SIR-C quad polarized MLC data using PolSARpro software for water surface area estimation. The decomposition techniques were used for generating the entropy, anisotropy, and alpha images. Then by combining these parameters, the H-alpha, Wishart H-alpha, and Wishart H-A-alpha techniques are used for unsupervised classification. The supervised classification is made by manually selected class. The classification results are compared and analyzed by using NEST software. The more accuracy and large number of classes were found in Wishart H Alpha unsupervised classified image as compared to supervised classification. The reason for that is due to the less number of classes and low resolution of the dataset in selecting a training area while creating the classes. Hence, from all these studies, it is concluded that the classification accuracy is better in Wishart H Alpha than other H Alpha and Wishart H A Alpha unsupervised, and supervised classification.

REFERENCES

1. Jensen R. J. (2014). *Remote Sensing of the Environment an Earth Resource Perspective*. (2nd ed.) Pearson.
2. Shaikh, M. A., Gadkar, V. B., Sayyad, S. B. (2015). SAR image analysis for microwave C-band fine quad polarised RADARSAT-2 using decomposition and speckle filter technique. *International Journal of Innovations in Engineering, Research and Technology (IJIERT)*, Issue ICITDCEME'15, Novateur Publication's.
3. Scheuchl, Bernd., Flett, Dean., Caves, Ron., Cumming, Ian. (2004). Potential of RADARSAT-2 data for operational sea ice monitoring. *Canadian Journal of Remote Sensing*, 30(3), 448–461.
4. Maurizio, Migliaccio., Attilio, Gambardella., Massimo, Tranfaglia. (2007). SAR polarimetry to observe oil spills. *IEEE Transactions on Geoscience and Remote Sensing*, 45(2), 506-511.
5. Zhang, Biao., Perrie, William., Li, Xiaofeng., Pichel, William G. (2011). Mapping sea surface oil slicks using RADARSAT-2 quad-polarization SAR image. *Geophysical Research Letters*, 38, L10602, 1-5.
6. Cedric, Lardeux., Pierre-Louis, Frison., Jean-Paul, Rudant., Jean-Claude, Souyris., Celine, Tison., Benoit, Stol. (2006). Use of the SVM classification with polarimetric SAR data for land use cartography. *Proceeding of IEEE*, 497-500.
7. Chi, M., Feng, R., Bruzzone, L. (2008). Classification of hyperspectral remote sensing data with primal SVM for small-sized training dataset problem. *Advances in Space Research*, 41(11), 1793–1799.
8. Domenico S., Paolo F., Giovanni S., Paolo D. M., Marco C. (1996). Analysis of SIR-C/X-SAR data on montespertoli test site. *Department di Informatics, Sistemi e Produzione University Tor Vergata, Roma, Italy*.
9. Sayyad S. B., Khirade P. W., Shaikh M. A. (2015). Speckle filtering of microwave c-band fine quad polarized RADARSAT-2 SAR image using mean and median filter. *Bionano Frontier*. 8, (3), 294-297.
10. Cloude S. and Pottier E. (1996). A review of target decomposition theorems in radar polarimetry. *IEEE Transactions of Geoscience and Remote Sensing*. 34, (2), 498-518.
11. Lee J. S., Grunes M. R., Ainsworth T. L., Du L. J., Schuler D. L., Cloude S. R. (1999). Unsupervised classification using polarimetric decomposition and complex wishart distribution. *IEEE Transactions Geoscience and Remote Sensing*. 37/1, (5), 2249-2259.
12. Ouarzeddine M., and Souissi B. Unsupervised classification using wishart classifier. *USTHB, F.E.I, BP No 32 El Alia Bab Ezzouar, Alger*.
13. Lillesand T. M., Kiefer R.W. (1999). *Remote Sensing and Image Interpretation*. (4th ed.). John Wiley & Sons, Inc.
14. Cloude S. R. and Pottier E. (1997). An entropy based classification scheme for land applications of polarimetric SAR. *IEEE IGRS*. 35, (1), 68-78.
15. L- Band SIR-C Dataset download from <http://earthexplorer.usgs.gov/>

STRUCTURAL, MORPHOLOGICAL AND OPTICAL PROPERTIES OF Zn_{1-x}Fe_xS NANOPARTICLES PREPARED BY CO-PRECIIPITATION METHOD**V. V. Jadhavar¹, V. D. Mote^{1,2} and B. S. Munde³**^{1,2}Thin films and Materials Research Laboratory, Dayanand Science College, Latur³K. K. M. College, Manwat**ABSTRACT**

Structural, morphological and optical properties of Zn_{1-x}Fe_xS nanoparticles have been prepared by Co-precipitation method at room temperature. The crystal structure, size and lattice strain have been estimated by X-ray diffraction techniques. The pure and Fe doped ZnS nanoparticles exhibit cubic crystal structure. The small decrease in lattice constant has been observed of Fe doped ZnS samples which can be attributed to the small distortion of Zn tetrahedron. The lattice strain increased with increasing Fe doping. The SEM images of all samples show that nanocrystalline nature. The UV-Vis measurement has been used to study the effect of Fe doping on absorption spectra and optical band gap.

Keywords: ZnS; nanocrystals; x-ray diffraction; strain; optical study.

1. INTRODUCTION

Nanocrystals are in huge expansion worldwide due to its unique functional properties. In recent years, a great effect has been made to the design and controls the development of nanocrystals such as Zinc sulfide [1-2].

ZnS is an efficient luminescent material that belongs to the II-IV semi-conducting material with wide band gap energy of 3.7 eV and a large exciton binding energy (40 meV) [3-4]. Due to its excellent properties ZnS has versatile potential applications electro luminescent device, optical coatings, photoconductor, field effect transistor, optical sensors, photovoltaic cells and LEDs [5-9]. In addition ZnS is a most promising material in biological application [10]. Interesting, the properties of ZnS has been change when doped with transition metals (TM) such as Ni, Fe, Mn, Cr, Co and Cu [11-17]. Among them, the doping of Fe into ZnS matrix become wide versatile owing their solubility in the ZnS lattice.

In this work we report an investigation of structural, morphological and optical properties of ZnS particles doped with Fe. TM ions doped ZnS nanocrystals can be obtained in many ways such as spray-based method, Gamma irradiation method, chemical precipitation method, polymerization and sol-gel method [18-22]. We preferred co-precipitation method for the synthesis of ZnS as this method is simple, low-cost and availability of the equipments. Crystal structure and average grain size were measured using XRD. SEM is used to study the morphology. Optical energy band gap of pure and Fe doped ZnS nanocrystals were study using UV-Visible absorption spectroscopy.

2. EXPERIMENTAL DETAILS

Samples with compositional formula Zn_{1-x}Fe_xS with x = 0.00, 0.02, and 0.06 were prepared by co-precipitation route. In this procedure, Zinc acetate dehydrate of 1M is diluted in distilled water (50 ml) and sodium sulfide 1M is diluted in distilled water (50 ml) were prepared and added by under vigorous stirring to obtain pH 13.5 for 2 h. A white precipitate was obtained which was separated by centrifugation. The precipitate which is separated is washed several times with distilled water and ethanol then dried under vacuum at 60 °C to get the powder samples of ZnS nanocrystals. For the synthesis of Fe doped ZnS nanocrystals were prepared at room temperature by mixing calculated

amounts of zinc acetate solution and Fe acetate solution followed by drop wise addition of saturated solution of sodium sulfide up to pH 13.5. The mixture was vigorously stirred for 2 h. The precipitate was filtered from the reaction mixture and washed several times with ethanol to remove all sodium particles. The wet precipitate was then dried. Similarly prepared for samples of 2%, 6% Fe doped ZnS samples.

XRD measurements were employed to investigate the structural properties and average crystallite size of the Fe-doped ZnS nanocrystals (Model: PW-3710). The structural analysis of the synthesized samples was carried out using a powder X-ray diffractometer (XPERT-PRO) with a Cu-K α radiation source of wavelength 1.5406 Å. The surface morphology and particle size of prepared samples were characterized using by Scanning electron microscopy (SEM). The optical properties of pure and Fe doped ZnS samples were study using by Ultra-visible spectroscopy.

3. RESULTS AND DISCUSSIONS

3.1 Structural properties

Figure 1 shows x-ray diffraction patterns of the pure and Fe doped ZnS nanoparticles prepared by co-precipitation method. The pure and Fe doped ZnS nanoparticles exhibit cubic crystal structure. No extra impurity phases were observed which means that Fe^{3+} ions would be uniform substitute into the Zn^{2+} ions in the ZnS lattice. In addition, compared with ZnS increasing Fe content caused the position of the diffraction peaks shift of the Fe doped ZnS nanoparticles to higher diffraction angle. The lattice constant of prepared samples was estimated from XRD pattern. From XRD analysis found that the lattice constant of the samples decreased with increasing Fe doping in the ZnS lattice. It may be due to the small difference between the Zn^{2+} ions and Fe^{3+} ions. The volume of unit cell of pure ZnS samples was higher than that of Fe doped ZnS nanocrystals.

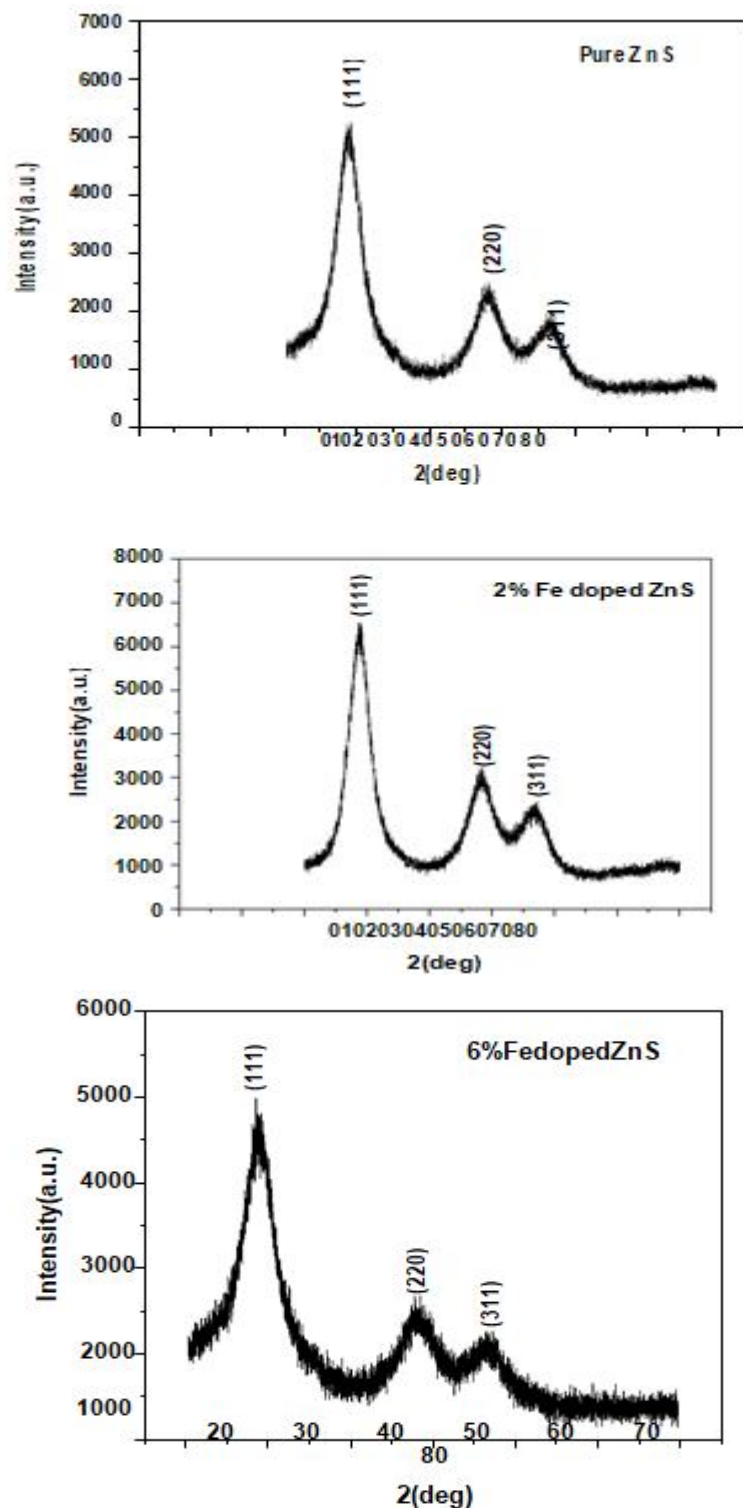


Figure-1: XRD pattern pure and Fe doped ZnS samples

The average crystallite size was calculated using Scherrer's formula. It was found that the average crystallite size is in the range of 1-2 nm. The average crystallite size decreased with increasing Fe doped ZnSnanocrystals. It may be due to the small grain growth of pure ZnS sample as compared to the Fe doped ZnS samples. The lattice strain of samples increased with increasing Fe doping, this was attributive due to the decreased size of thenanocrystals.

Sr. no.	Lattice Constant (Å)	Volume (Å) ³	D (nm)	Strain (ε) ×10 ⁻³	Energy band (eV)
1.	5.3814	155.84	1.709	57.62	3.33
2.	5.3694	154.80	1.6488	59.05	2.92
3.	5.3640	154.33	1.6267	59.68	2.85

3.2 Morphological study

Figure 2 shows the SEM images of pure and Fe doped ZnSnanocrystals. The pure ZnS image is found that the Fe doping content has been significant influences of the surface morphology. The pure ZnS sample is composed of spherical like nature with distribution the grain size. For the Fe doped ZnSnanoparticles observed the agglomerated grain size and porous like structure. This may be due to the formation of structure by the difference in the size of Zn and Fe ions.

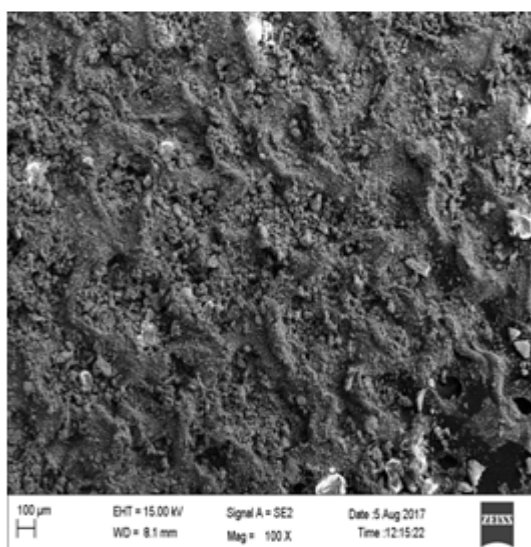


Fig-2 (a). SEM image of ZnS sample

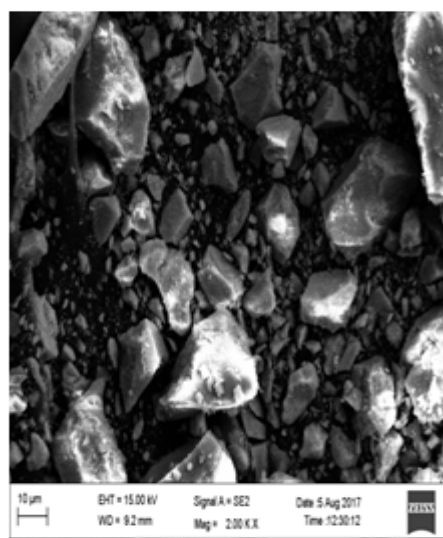


Fig.2(b). SEM image of 2% Fe doped ZnS sample

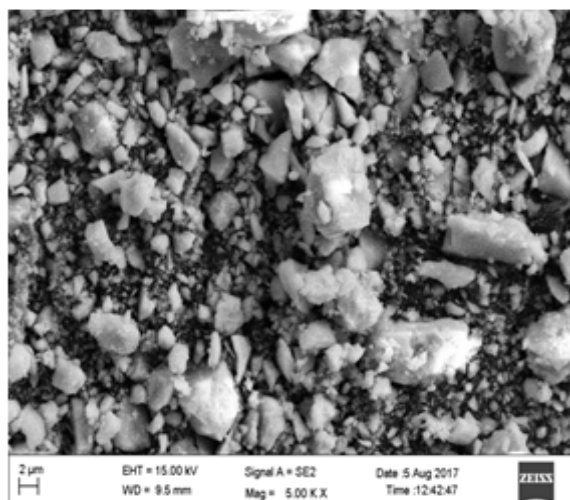


Fig-2(c). SEM image of 6% Fe doped ZnS sample

3.3 Optical properties

The optical absorption spectra of pure and Fe doped ZnS nanocrystals are shown in figure 3. From figure 3, it is shown that a region of the absorption is located in the range of 300 to 400 nm. The figure 4 shows the plots of $(\alpha h\nu)^2$ versus photon energy ($h\nu$) for pure and Fe doped ZnS samples. Optical band gap were found to be vary from 3.33 to 2.85 eV as shown in table 1. It was shown that the optical band gap decreases with increasing Fe doping. This may due to the sp-d exchange interaction between the Fe ions and Zn ions.

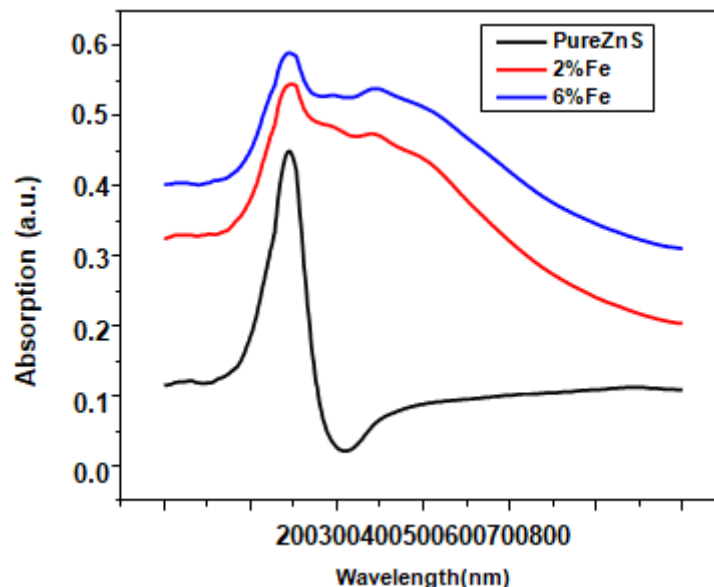


Figure-3: Absorption spectra of pure and Fe doped ZnS nanocrystals.

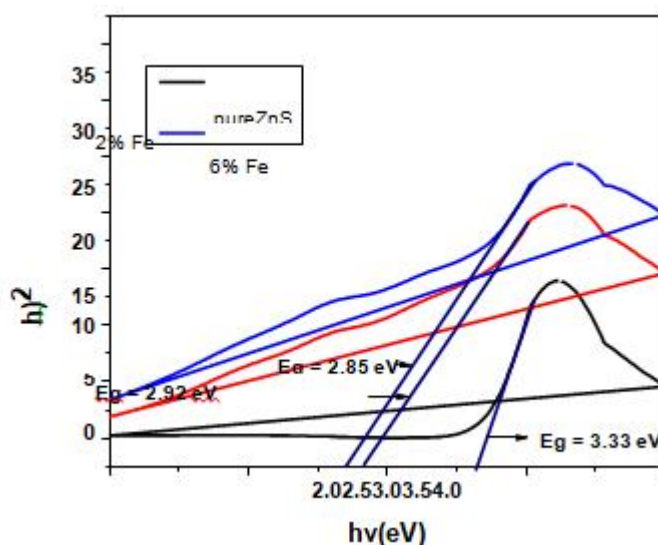


Figure-4: $(\alpha h\nu)^2$ vs $h\nu$ for pure and Fe doped ZnS samples

4. CONCLUSIONS

Fe doped ZnS nanocrystals were successfully prepared by co-precipitation method at room temperature. All prepared samples show cubic crystal structure without any extra phases. The lattice constant of samples found to decrease with increasing Fe doping into the ZnS lattice. The volume of unit cell was also decreased with increasing Fe content. The strain of pure ZnS nanocrystals increased with increasing Fe doping, it may be due to the decreasing average crystallite size. The surface morphology of prepared samples was studied using scanning electron microscopy. The SEM results shown that all samples have nanocrystalline structure. The optical band gap decreased with increasing Fe content into the ZnS lattice.

5. REFERENCES

1. X. Fang, L. Wu, L. Hu, Adv. Mater., 23 (2011) 585-598.
2. X. Wang, H. Hunag, B. Liang, Z. Liu, D. Chen, G. Shen, Solid state and materials Sciences, 38 (2013) 57-90.
3. Deng H, Russell JJ, Lamb RN, Jiang B (2004) Thin Solid Films 458:43-46.

4. Goktas A, Aslan F, Yasar E, Mutlu IH (2012) J. Mater.Sci.Mater.Electron 23:1361–1366
5. S. Lindroos, T. Kanninen, M. Leskelä, E. Rauhala, Thin Solid Films. 263 (1995) 79–84.
6. H.J. Lee, S. Il Lee, Curr. Appl. Phys. 7 (2007) 193–197.
7. F. Göde, C.Ş. Gümü, M. Zor, Journal of Optoelectronics and Advanced Materials, 9 (2007) 2186–2191.
8. G. Sharma, S.D. Han, J.D. Kim, S.P. Khatkar, Y. Woo Rhee, Mater. Sci. Eng. B Solid- State Mater. Adv. Technol. 131 (2006) 271–276.
9. A. Goudarzi, G.M. Aval, S.S. Park, M.-C.Choi, R. Sahraei, M.H. Ullah, A. Avane, C.-S. Ha, Chem. Mater. 21 (2009) 2375–2385.
10. M. Wadhwani, S. Jain, Res. J. Recent. Sci., 4 (2015) 36-39.
11. S. Darafarin, R. Sahraei, A. Daneshfar, Alloys Compd. 658 (2016) 780–787.
12. R. Sahraei, S. Darafarin, J. Lumin. 149 (2014) 170–175.
13. R. Sahraei, S. Darafarin, Spectrochim. Acta - Part A Mol. Biomol. Spectrosc. 149 (2015) 941–948.
14. M.S. Akhtar, M.A. Malik, Y.G. Alghamdi, K.S. Ahmad, S. Riaz, S. Naseem, Mater. Sci. Semicond.Process. 39 (2015) 283–291.
15. D.A. Reddy, D.H. Kim, S.J. Rhee, B.W. Lee, C. Liu, Nanoscale Res. Lett. 9 (2014) 20.
16. J.K. Salem, T.M. Hammad, S. Kuhn, M.A. Draaz, N.K. Hejazy, R. Hempelmann, J. Mater. Sci. Mater. Electron. 25 (2014) 2177–2182.
17. W.-S. Ni, Y.-J. Lin, J. Alloys Compd. 649 (2015) 968–972.
18. H. Yang, P. Hollway, J. Appl. Phys. 93 (2003) 586-593.
19. J. H. Chung, C. S. Ah, D. J. Jang, J. Phys. Chem. B 105 (2001) 4128-4132.
20. I. Yu, I. Tetsukio, M. Seena, J. Phys. Chem. Solids 57 (1996) 373-79.
21. K. Manzoor, S. R. Vadera, N. Kumar, T. R. N. Kutty, Mater. Chem. Phys. 82 (2003) 718-725.
22. N. Karan, R. Suchitra, F. Singh, J. Cryst. Growth 268 (2004) 585-89.

ELECTROCHEMICAL IMPEDANCE SPECTROSCOPIC STUDY OF DYE SENSITIZED SOLAR CELL WITH AL DOPED TiO₂ NANOPARTICLES PHOTO ANODE SENSITIZED BY EOSIN Y DYE**Swati S. Kulkarni¹, Gajanan A. Bodkhe², Nikesh Ingle³, S. S. Hussaini⁴, N. N. Shejwal⁵ and Mahendra D. Shirsat⁶**^{1,2,3,6}RUSA Centre for Advanced Sensor Technology, Department of Physics, Dr. Babasaheb Ambedkar Marathwada University, Aurangabad⁴Crystal Growth Laboratory, Department of Physics, Milliia Arts, Science & Management Science College, Beed⁵All India Shri Shivaji Memorial Society's College of Engineering, Pune**ABSTRACT**

In the present investigation the electrochemical impedance spectroscopy has been applied to analyse the dye sensitized solar cells (DSSCs). The characteristics of the dye sensitized photo anode has been investigated using various techniques like Atomic force Microscopy, UV visible spectroscopy. Consequently, the measurement of photovoltaic characteristics has been discussed and lastly, the EIS study of fabricated DSSCs have been done in order to analyse the DSSCs using Al doped TiO₂ nanoparticles photo anode sensitized by eosin Y dye which reveals that the DSSC with 0.07M Al doped TiO₂ nanoparticles photo anode has the charge transfer resistance of 138 ohm at the TiO₂/dye/electrolyte interface

Al doped TiO₂, DSSCs, Eosin Y dye, EIS, photo anode

1. INTRODUCTION

Being mimicry of photosynthesis, dye sensitized solar cell has ever accepted as the best solar cell from last few decades [1]. DSSC is an electrochemical device, converting light energy into electrical energy, consist of three active layers namely, dye sensitized nano-crystalline semiconductor layer (known as photo anode), counter electrode and an organic electrolyte containing redox couple sandwiched between prior two layers. Both the semiconductor layer and counter electrode has synthesized usually on the Fluorine doped transparent conducting oxide layer on glass [2]. The highest efficiency ever achieved has been found to be 13% using porphyrin dye [3]. Charge generation and transfer process depends on the nature and compatibility of each layer with another and more particularly on the photo anode [4]. TiO₂ nanoparticles has been proved to be most viable member to synthesize the photo anode owing to its properties like wide band gap, large exciton binding energy, low cost, non-toxic and environmental benign. The absorption in TiO₂ layer can be increased by either doping or adsorbing the dye molecules on its surface [5]. Nanostructure of TiO₂ photo anode provides the sufficiently large surface area for dye adsorption [4]. Further, doping the TiO₂ will form the new valance state, decreases the Band gap, enhances the surface area and creates the charge carrier trapping sites which helps to increase the photo current [6]. Various metals and non-metals and other elements have been tried for doping the TiO₂ in the thrust of enhancing the photo-catalytic activity of TiO₂ photo anode [7]. Aluminium, the transitional metal having good optical quality, low resistivity, high conductance and high crystal qualities, when doped in TiO₂ shifts onset of absorption from UV region to visible region [8-9]. According to the previous optimization it has been observed that the aluminium doping concentration of 0.07M exhibits superior results [10]. Hence, in the current study 0.07M aluminium doped TiO₂ nanoparticles have been synthesized and used to create the photo anode of DSSC.

The basic purpose behind the development of DSSC has been found to investigate a low cost, environmental friendly solar cell through the use of eco-friendly materials and methods [11]. Hence, while designing the DSSC, high efficiency along with the least environmental hazard must be the agenda. Sensitizer used to harvest the photo energy is the crucial parameter on this basis, deciding the response of DSSC. Inorganic metal complex dyes and organic dyes have been intensively investigated by researchers since from last two decades. Inorganic metal complex dyes has been studied, involves lengthy, tedious and expensive manufacturing steps [12-13]. Moreover, inorganic dyes contain heavy metals which are rarely found and hence become costly. Also, their toxic nature becomes hazardous for environment. On the contrary, organic dyes which are abundantly available in nature and found to be ideal for eco-friendly DSSCs being non-toxic, having affordable cost, renewable, biodegradable and easily available, not producing any hazardous by products. Particularly, Eosin Y dye has been shown to be one of the best synthetic dyes having high molar extinction coefficient ($60803\text{M}^{-1}\text{cm}^{-1}$), upon excitation becomes more reducing and oxidizing and found to be applied in cell staining, as pH indicator and as a dye pigment in cosmetics also [14]. Eosin Y is having single carboxyl group which is suitable to anchor with TiO₂ molecules in photo anode [15].

In the previous studies it has been found that though the eosin Y dye sensitized Al doped TiO₂ photo anode showing the potential candidate for natural DSSC, it's overall efficiency obtained was trivial [16-17]. Prominent factors limiting the efficiency of DSSC are the recombination of photo generated electrons, insufficient catalytic activity of counter electrode to reduce the electrolyte and overall series resistance of the interfaces [2]. Physico-chemical dynamic processes at the photo anode and the cathode have been successfully studied using electrochemical impedance spectroscopy (EIS) [18-20]. Subsequently, in the present study, EIS has been employed to investigate the reason behind the low efficiency of DSSC synthesized using Al doped TiO₂ photo anode adsorbed with Eosin Y dye and platinum cathode accompanied by iodine/triiodide electrolyte.

2. MATERIALS AND METHODS

2.1 Materials

Titanium Tetra iso-propoxide (TTIP) (Otto Chemicals, Germany), Eosin Y dye and Chloroplatinic acid (H₂PtCl₆) (Ward Hill, U.S.A.), Aluminium Nitrate (Al(NO₃)₃) and Poly-ethylene Glycol (Otto Chemicals, India), Lithium iodide and iodine all reagents were used without further purification.

2.2 Preparation of dye sensitized solar cell

0.07M Aluminium doped TiO₂ nanoparticles has been synthesized using TTIP, Aluminium nitrate, Polyethylene glycol, Triton X-100, Ethanol and deionised water by sol gel method and characterized by XRD, Raman, SEM-EDAX, FTIR spectroscopic methods and the DSSC has been synthesized as described in our previous work [10,16-17].

2.3 Measurements

I-V characteristics and electrochemical impedance spectroscopic measurements has been taken one after other, immediately after preparation of DSSC, using Keithley 4200 Source Measurement Unit and Chi 660 electrochemical work station respectively. The EIS experiment has been carried out under illumination with frequency range from 0.01 Hz to 1 MHz with ac amplitude set at 10mV. Park Atomic force microscope has been used to study the morphological characteristics of synthesized photo anodes and UV visible absorption spectra of eosin Y dye sensitized photo anodes has been investigated using 2400 UV visible spectrophotometer.

7.3 RESULT AND DISCUSSION

3.1 Morphological study of dye adsorbed photo anodes

The morphological properties of the synthesized Al doped TiO₂ photo anodes have been investigated using Park AFM optical microscope. Figure 1 explains the morphology of Eosin Y dye sensitized TiO₂ photo anodes with aluminium doping concentration 0.07M. From the AFM investigation the values of root mean square roughness, average roughness and angle of contact of TiO₂ with the FTO surface have been noted and listed in table 1

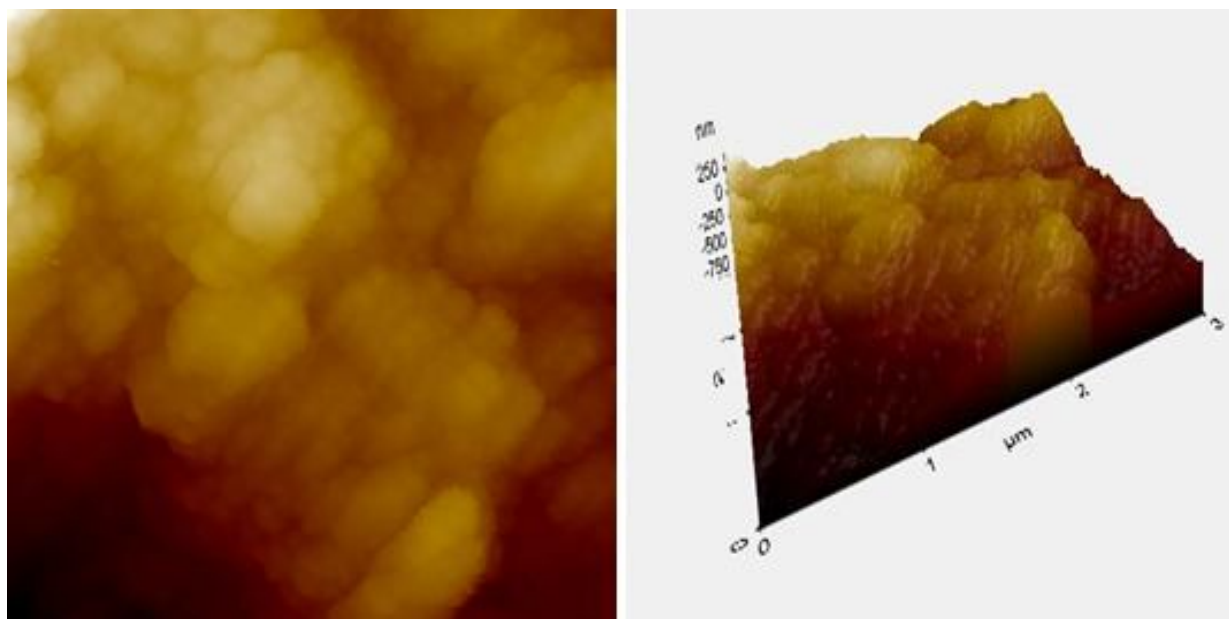


Figure-3: AFM image of 0.07M Al doped TiO₂ photo anode sensitized by Eosin Y dye 3dimentional view

Table-1: AFM surface study parameters of Al doped TiO₂ photo anodes

Al concentration in TiO ₂ photo anode	RMS roughness in μm	Average roughness in μm	Area peak to valley height in μm	Contact angle of contact
0.07M	0.432	0.354	2.88	42.57

From table 7.1 it could be observed that the better rms surface roughness which might have enhanced the dye molecules adsorption on TiO_2 surface to enhance the photo electron generation. Moreover, contact angle has been found to be fairly high for 0.07M Al doping which indicates the better affection of TiO_2 film with the FTO surface [19].

3.2 UV visible absorption of dye adsorbed photo anodes

Figure 2 exhibits the UV visible absorption spectra of Eosin Y dye adsorbed Undoped TiO_2 and Al doped TiO_2 nanoparticles photo anodes. From figure 2 dye sensitized Al doped TiO_2 photo anodes showed the absorption peak near 550nm wavelength which is attributed to better adsorption of Eosin Y dye on doped TiO_2 photo anode [16].

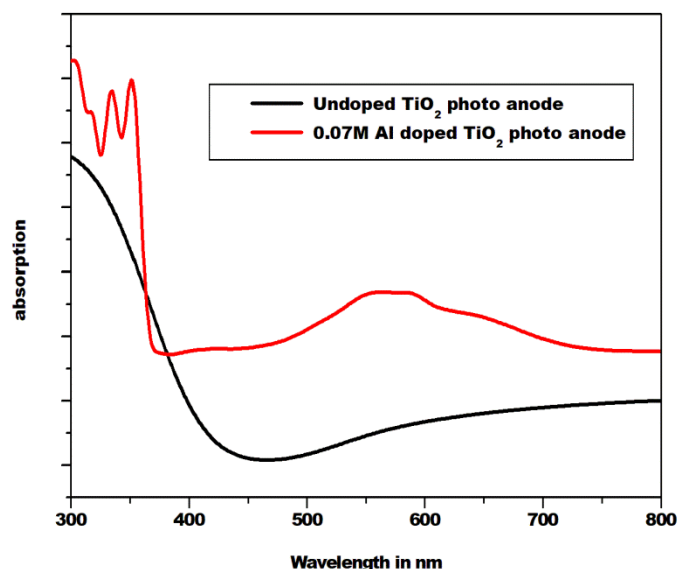


Figure-7.2: UV visible spectro-photograph showing absorption spectra of undoped and Al doped TiO_2 photo anode sensitized by Eosin Y dye

3.3 Photovoltaic characterization of DSSCs

Photovoltaic measurements of DSSCs have been performed by measuring the current-voltage characteristics under irradiation with white light (100mWcm^{-2}) from the indigenous OHP assembly. Performance of DSSCs has been evaluated by short circuit current (J_{sc}), open circuit voltage (V_{oc}), fill factor (FF), and energy conversion efficiency (η). The photovoltaic parameters of the DSSCs sensitized with Eosin Y dye are listed in Table 7.2 and the typical I-V curves of the DSSCs using the 0.07M Al doped photo anode has been shown in Fig. 7.3.

Table-7.2: Photovoltaic Parameters Of DSSCs: Photo Current Density(J_{sc}), Open Circuit Voltage (V_{oc}), Maximum Photo Current(I_{max}), Maximum Photo Voltage(V_{oc}), Fill Factor(ff) And Efficiency(η)

Al doping in photo anode	$P_{max}=I_{max}*V_{max}$ in nw	I_{sc} in μA	V_{oc} in mV	%FF	% η
0.07M	24557.5	249.21	370	26.63	0.0246

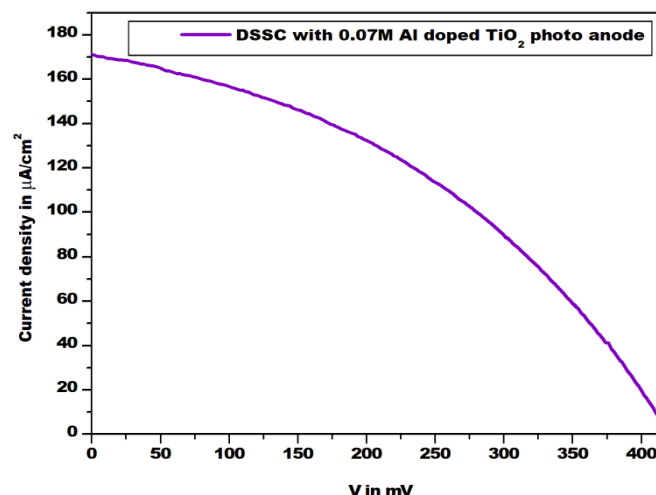


Figure-7.3: Current-voltage characteristics of DSSCs with Eosin Y dye sensitized photo anodes

The fill factor and power conversion efficiency of DSSCs have been calculated using equation (1) and equation. (2)

$$FF = \frac{I_{max} * V_{max}}{I_{sc} * V_{oc}} * 100 \quad (1)$$

$$\eta = \frac{I_{sc} * V_{oc} * ff}{P_{in}} * 100 \quad (2)$$

Where,

Fill factor (ff) is the measure of square shape of the DSSC characteristics curve.

In the present work, though the short circuit current is having better value, the fill factor of the DSSC have found quite small which indicates that series resistance of equivalent circuit of DSSC must be very large and shunt resistance might be very small. Both these factors cause the lower efficiencies of DSSCs. In order to investigate this fact electrochemical impedance spectroscopy has been found to be applied by many researchers [12, 20]

3.4 Electrochemical impedance spectroscopic (EIS) study of DSSCs

EIS has been used as the versatile tool for investigating the dynamics of the bound or mobile charges in the DSSC. Nyquist plot evaluating electrochemical parameters like electrolyte solution resistance R_s , electrode polarization resistance R_p or R_{ct} and double layer capacitance C_{dl} has been illustrated in figure 4. According to Randle's Electrochemical equivalent circuit model, Nyquist plot is always a semicircle due to a RC parallel equivalent circuit and intercept of semicircle to real axis towards the origin denotes the solution resistance R_s whereas, the interpolated intercept on other side gives the sum of R_s and polarization resistance R_p or R_{ct} . Hence, diameter of semicircle is equal to the polarisation resistance [21].

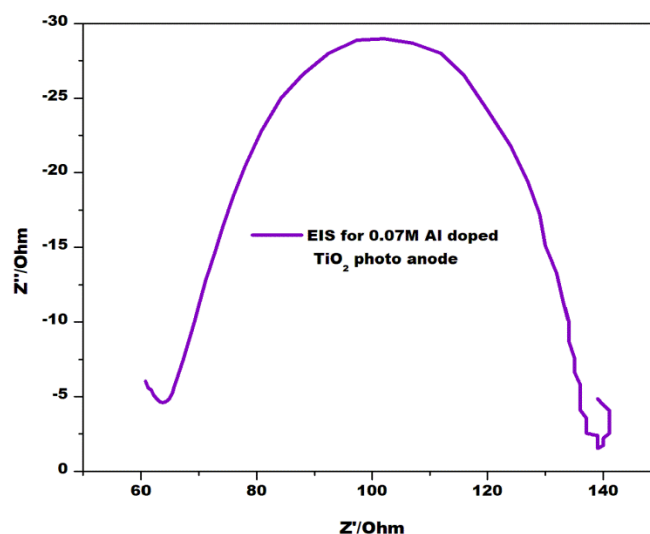


Figure-4: Electrochemical impedance spectra of DSSCs with 0.07M Al doped TiO_2 photo anode sensitized with Eosin Y dye the values of R_s , R_{ct} has been found by interpolation of curves on X axis and Capacitor values is adopted from equivalent circuits directly and listed in table 7.3.

Table-7.3: Fitted impedance parameters of DSSCs with various concentrations Al doped TiO_2 photo anodes sensitized with Eosin Y dye; with active area 1cm^2 and illuminated by Halogen lamp

DSSC with Al concentration in photo anode	R_s Ohm	R_{ct} Ohm	C_{ct}
0.07M (DSSC3)	59	138	7.7×10^{-6}

From table 7.3, it can be observed that the series resistance R_s , indicating the electrolyte resistance, is 59 ohm. Secondly, out of three expected semicircles in nyquist plots, only central semicircle is prominently observed. The diameter of the semicircle has been found to be 138 ohm. This observation reveals that the DSSC with 0.07M Al doped TiO_2 nanoparticles photo anode has low charge transfer resistance at the TiO_2 /dye/electrolyte interface and hence improved photo-electrochemical performance of DSSC for 0.07M Al concentration in photo anode. Al metal ion doping might have reduced the electron hole recombination because the Fermi level of Al is slightly lower than the Fermi level of TiO_2 and hence the conduction band electron might be transferred to this

Fermi level of Al, whereas, holes remains in the valance band of TiO_2 avoiding the recombination of electron holes offering better photo current as compare to DSSC with undoped TiO_2 photo anode [9, 10 & 17]. Thus, EIS study of the photo electrochemical system confirms that charge generation, separation and recombination strongly depend upon the nanostructure of photo anode, amount of dye loading and charge recombination at various interfaces.

4. CONCLUSIONS

Eosin Y dye sensitized Al doped TiO_2 nanoparticles photo anodes of Al 0.07M has been incorporated into DSSCs and cell performance has been evaluated. Investigation of light absorption in dye adsorbed photo anode has proved that the Al doped TiO_2 photo anodes shows the absorption peak near 540 nm wavelength which proves the adsorption of Eosin Y dye on Al doped photo anode. EIS study of DSSC reveals that 0.07M Al doped TiO_2 photo anode DSSC exhibits lower values of R_s and R_{ct} corresponding to Randles equivalent model. However, future of DSSC still depends on increasing the power conversion efficiency by enhancing the light harvesting capacity of solar cell, suggesting development in all components of DSSC particularly photo anode, Dye and electrolyte additives.

REFERENCES

1. http://curusa.ihmc.us/rid=1KLP378FW-2B8F7V5-19NH/Solar_Cell_Inspired_by_Plants.pdf
2. Liberatore, M., Decker, F., Burtone, L., Zardetto, V., Brown, T. M., Reale, A., Di Carlo, A. (2009). Using EIS for diagnosis of dye-sensitized solar cells performance. *J Appl Electrochem*, 39, 2291–2295, DOI 10.1007/s10800-009-9806-5
3. Mathew, S., Yella, A., Gao, P., Humphry-Baker, R., Curchod, B.F., Ashari-Astani N, Tavernelli I, Rothlisberger U, Nazeeruddin, M K, Gratzel, M.(2014). Dye-sensitized solar cells with 13% efficiency achieved through the molecular engineering of porphyrin sensitizers. *Nat. Chem.*, 6, 242–247
4. Ghann, W., Kang, H., Sheikh T., Yadav, S., Chavez-Gil, T., Fred Nesbitt & Jamal Uddin. (2017). Fabrication, Optimization and Characterization of Natural Dye Sensitized Solar Cell, *Scientific Reports*, 7, 41470, 12 pages, DOI: 10.1038/srep41470 Xiaobo Chen and Samuel S. Mao, (2007), *Chem. Rev.*, 107, 2891-2959.
5. Chen, X., and Mao, S. S. (2007). Titanium Dioxide Nanomaterials: Synthesis, Properties, Modifications, and Applications, *Chem. Rev.*, 107, 2891-2959.
6. Hanaor, D.A.H., Assadi, M.H.N., Li, S. Yu, A. and Sorrell, C.C. (2012). Ab Initio Study of Phase Stability in Doped TiO_2 , *Computational Mechanics*, 50,(2) 185-194.
7. Bart Roose, Sandeep Pathak and Ullrich Steiner. (2015), Doping of TiO_2 for sensitized solar cells, *Chem. Soc. Rev.*, 44, 8326-8349; DOI: 10.1039/c5cs00352k.
8. Yun, S., Lee, J., Chung, J., Lim, S. (2010). Improvement of ZnO nanorod-based dye-sensitized solar cell efficiency by Al-doping, 71, 1724–1731
9. Manoharan, K., Venkatachalam, P. (2015). Photoelectrochemical performance of dye sensitized solar cells based on aluminum-doped titanium dioxide structures. *Materials Science in Semiconductor Processing*, 30, 208–217.
10. Kulkarni, S. S., Bodkhe, G. A., Sayyad, P. W., Hussaini, S. S., and Shirsat, M. D. Optimization Of Aluminium Doping Concentration In Titanium Dioxide Nano Particles Photo Anode For Enhancing Efficiency Of Dye sensitized Solar Cell, under press
11. O'Regan B., and Gratzel, M. (1991). Low cost, high efficiency Solar Cells based on Dye Sensitized Colloidal TiO_2 film, *Nature*, 353, 737-739.
12. M. Gratzel. (2014). Light and shade of perovskite Solar cells, *Nat. Mater.*, 13(9), 838–842
13. Zhou, H., Wu, L., Gao, Y., Ma x, T. (2011). Dye-sensitized solar cells using 20 natural dyes as sensitizers, *Journal of Photochemistry and Photobiology A: Chemistry*, 219, 188–194.
14. Hari D. P., and Koinig, B. (2014). Synthetic applications of eosin Y in photo redox catalysis, *Chem. Commun.*, 50, 6688-6699.
15. Zhang, F., Feng Shi, Wei Ma, Fei Gao, Yang Jiao, Hui Li, Wang, J., Shan, X.Y., Lu, X., and Meng, S. (2013). Controlling Adsorption Structure of Eosin Y Dye on Nanocrystalline TiO_2 Films for Improved Photovoltaic Performances, *J. Phys. Chem. C*, 117, 14659–14666. [dx.doi.org/10.1021/jp404439p](https://doi.org/10.1021/jp404439p) |

16. Kulkarni, S. S., Hussaini, S. S., Bodkhe, G. A. and Shirsat, M. D. (2018). Natural Hibiscus Dye and Synthetic Organic Eosin Y Dye Sensitized Solar Cells Using Titanium Dioxide Nanoparticles Photo Anode: Comparative Study, *Surface Review and Letters*, 1850164-1- 1850164-6 DOI: 10.1142/S0218625x18501640
17. Kulkarni, S. S., Bodkhe, G. A., Shirsat, S. M., Hussaini, S. S., shejwal, N. N. and Shirsat, M. D. (2018). Dye Sensitized Solar Cell based on Environmental Friendly Eosin Y Dye and Al doped Titanium Dioxide Nano Particles, *Mater. Res. Express*, 5(3), 036205-036221, doi.org/10.1088/2053-1591/aab2d1
18. Neetu, Maurya, I.C., Gupta, A. K., Srivastava, P., Bahadur, L. (2016). Extensive enhancement in power conversion efficiency of dye-sensitized solar cell by using Al-doped TiO₂ photoanode, *J Solid State Electrochem*, 13 pages, DOI 10.1007/s10008-016-3478-y
19. Wang, J.C., Meng-Yen Tsai, Ming-Kun Lee, Sheng-Fu Horng, T song-Pyng Perng, Chi-Chung Kei, Chih-Chieh Yu and Hsin-Fei Meng. (2010). Highly efficient flexible inverted organic solar cells using atomic layer deposited ZnO as electron selective layer, *J. Mater. Chem.*, 20, 862–866; DOI: 10.1039/b921396a
20. Mali, S. S., Betty C.A., Bhosale, P.N., Patil, P.S. (2012). Eosin-Y and N3-Dye sensitized solar cells (DSSCs) based on novel nanocoral TiO₂: A comparative study, *Electrochimia Acta*, 59, 113; doi:10.1016/j.electacta.2011.10.043
21. Zia, A. I. and Mukhopadhyay, S.C. Electrochemical sensing :Carcinogens in beverages, Chapter 2, Impedance spectroscopy and Experimental setup, 10 May 2016, Chaphttps://link.springer.com/chapter/10.1007/978-3-319-32655-9_2
22. Yang, C.C., Zhang, H. Q., Zheng, Y. R. (2011). DSSC with a novel Pt counter electrodes using pulsed electroplating techniques, *DSSC Current Applied Physics*, 11 (2011), S147eS153d

SYNTHESIS, GROWTH MECHANISM AND PHYSICAL OBSERVATIONS OF In_2Se_3

R. V. Suryawanshi

Azad Mahavidyalaya Ausa, Ta. Ausa, Dist. Latur

ABSTRACT

In_2Se_3 thin films were prepared by spray pyrolysis technique using InCl_3 and SeO_2 as initial chemicals on the amorphous glasses. The deposition conditions were optimized as temperature 400°C , spray rate 5ml/min , air pressure 1.2 kg/m^2 and nozzle to substrate distance kept 30cm . Such deposited films were studied through the compositional, structural and optical properties. The content of In and Se impurities in sprayed In_2Se_3 films were measured by EDS analysis. It is seen that In_2Se_3 sample is In-rich. An excellent quality films were obtained with the spray pyrolysis. The samples were very tightly adhered to the substrate surface, film surface appeared to be smooth and diffusely reflecting with whitish in colour.

Keywords: In_2Se_3 thin films, spray pyrolysis, diffusely reflecting, whitish.

1. INTRODUCTION

Synthesis and Processing Science addresses the fundamental understanding necessary to extend from design and synthesis to the preparation of materials with desired structure, properties, or behavior. This includes the assembly of atoms or molecules to form materials, the manipulation and control of the structure at all levels from the atomic to the macroscopic scale, and the development of processes to produce materials for specific applications. Solution chemistry is used sometimes to prepare the precursor, which is subsequently converted into the nanophase particles by nonliquid phase chemical reactions. Precipitation of a solid from a solution is a common technique for the synthesis of the fine particles. The general procedure involves reactions in aqueous or nonaqueous solution states containing the soluble or suspended salts. Once the solution becomes supersaturated with the product, the precipitate formed is either homogeneous or heterogeneous nucleation. [1-5] for example, to form monodispersed particles. For instance, to prepare unagglomerated particles with a very narrow size distribution, all the nuclei must be formed at nearly the same time and subsequent growth must proceed without further nucleation or agglomeration of the particles [1-5]. In general, for the particle size and particle size distribution, the physical properties such as crystallinity and crystal structure and the degree of dispersion can be affected by the reaction kinetics. In addition, the concentration of reactions, the reaction temperature, and the order of reactants to the solution are also important. In this paper therefore, the growth kinetics and mechanism of In_2Se_3 film formation are presented.

2. EXPERIMENTAL DETAILS**2.1 Deposition of In_2Se_3 thin films**

A modified spray pyrolysis setup as shown in fig.1 is used for deposition of the In_2Se_3 film samples. To deposit the In_2Se_3 films, aqueous solutions of Indium trichloride (InCl_3) and selenium dioxide (SeO_2) were prepared by dissolving appropriate amounts of their salts (all AR grade) in double distilled water. The 0.05 M InCl_3 and 0.33 M SeO_2 solutions were mixed together in appropriate volumes and then sprayed through a nozzle onto the preheated amorphous glass substrates [6,7]. The experiment was carried out in three different steps to optimize the preparative parameters [6]. In the first step, the substrate temperature was varied and kept as 350°C , 375°C , 400°C , 450°C , and 550°C keeping spray rate and deposition time at the arbitrary values. In the second experiment, deposition temperature was kept at its optimum value (400°C) and the spray rate was varied from 3 ml/min to 7 ml/min in a step of 1 ml/min . In the third step, the temperature and spray rate were held at their optimized values and deposition time was varied from 6 to 12 min. The other parameters like quantity of spraying solution (40 ml), gas pressure (1.2 kg/cm^2) and nozzle to substrate distance (30 cm) were selected so as to achieve the required yield [6,7].

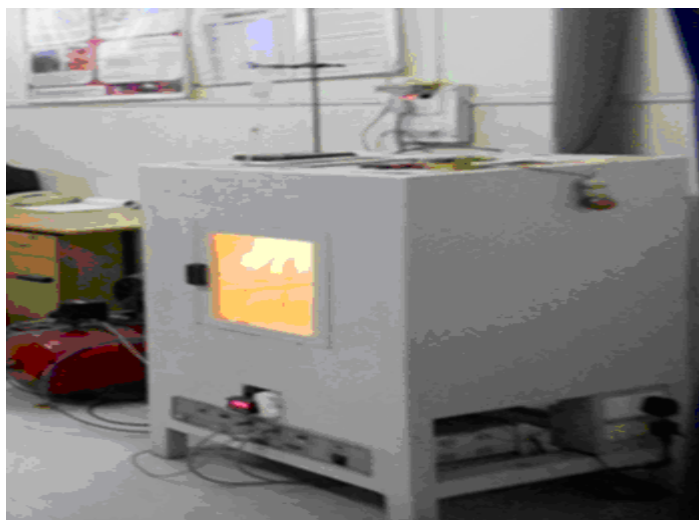


Fig-1: Schematic diagram of a chemical spray pyrolysis(CSP) unit.

3. RESULTS AND DISCUSSION

The spray pyrolysis technique is a chemical deposition process in which fine droplets of the desired materials are sprayed on a heated substrate maintained at elevated temperatures. Continuous films are formed on the hot substrates by thermal decomposition of the materials droplets. The chemical reactants are selected in such a way that products other than the desired compounds will volatile at the deposition temperature. The deposition is favoured by obtaining a mist of the solution conditions are met by spray deposition procedure [6]. Better control over the deposition conditions like spray rate, area of deposition and carrier gas pressure was monitored using a stepper motor controller by means of a PC through serial port [6]. This arrangement is particularly very helpful for large area deposition of thin films with greater uniformity [6,7]. The key parameters in the deposition of In_2Se_3 thin films are the substrate temperature, spray rate and the time for which the deposition process was carried out. The growth rate was measured in terms of a layer thickness and film thickness was measured as a function of the substrate temperature, spray rate and the deposition time, one by one [6]. The substrate temperature was varied (350°C , 375°C , 400°C , 425°C , 450°C , 500°C) with the other parameters (spray rate and the deposition time) kept at their arbitrary values (spray rate = 5 ml / min , deposition time = 10 mins.) and the films were obtained. The layer thickness was measured for each of the deposition temperature. The layer thickness is found to be increased up to 400°C and then decreased for further higher deposition temperatures. It is further seen that, at low temperature, the deposits are non-uniform, flaky and porous and are easily detachable; the reason being incomplete decomposition of the sprayed droplets resulting in precipitation at the film substrate interface leading to easy detachment. Beyond 400°C , fast precipitation and evaporation caused thinner, non-uniform and cracked deposits [6].

The spray rate is another important parameter influencing properties of the films formed. The substrate temperature was kept at its optimized value (400°C), deposition time was chosen as 10 mins and spray rate was varied from 3 ml / min in a step of 1 ml / min . The layer thickness was measured as usual. It is seen that terminal layer thickness increased with increase in ml / min spray solution and is maximum at 5 ml / min spray rate. For further increase in spray rate, the layer thickness decreased. Film quality is also dependent on the deposition time. Hence deposition time was varied from 6 mins to 15 mins with deposition temperature and spray rate kept optimized. The layer thickness was measured for various deposition durations. The variation in layer thickness with the deposition time is quasilinear. Initially, the layer thickness is found to be increased almost linearly up to 8 min deposition time and saturation in layer thickness is observed for further increase in deposition time. A deposition time of 8 min was therefore selected for further deposition of the films[8-11].

In general, tightly adhered, hard and diffused whitish colour with rough surface deposits were obtained as shown in fig.2. We propose the following reaction steps as [6],

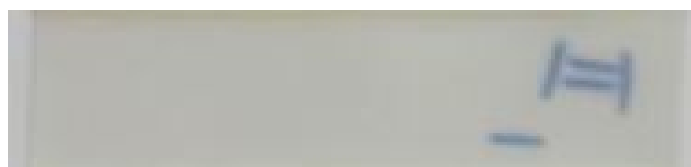
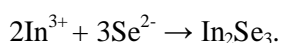


Fig-2: Photo of deposited In_2Se_3 thin film

4. CONCLUSIONS

For the good quality deposition of In_2Se_3 thin films by spray pyrolysis with various preparative parameters like temperature, time of the deposition, spray rate can easily be optimized. The samples were very tightly adhered to the substrate surface, film surface appeared to be smooth and diffusely reflecting with whitish colour.

REFERENCES

1. P. A. Psaras and H. D. Langfor, in "Advancing Materials Research", (eds) U. S. National Academy of Engineering and National Academy of Sciences", National Academy Press, Washington (1987) 203.
2. C. N. R. Rao, Mater. Sci. Eng. B18 (1993) 1.
3. J. T.G. Overbeck, Adv. Colloid Interface Sci. 15 (1982) 38.
4. F. Neilson, Manufacturing Chemist. 53 (1982) 38.
5. K. L. Chopra and S. R. Das, in "Thin Film Solar Cells", (eds) K. L. Chopra and S. R. Das Plenum Press, New York (1983).
6. L. P. Deshmukh, R.V. Suryawanshi, E. U. Masumdar and. M. Sharon, Solar Energy 86 (2012) 1910.
7. A. A. Yadav, M. A. Barote and E. U. Masumdar, J. Alloys Compd. 493 (2010) 179.
8. H. H. Affify, S.A. Nasser and S. E. Demian, J. Mater. Sci. Materials in Electronics. 2 (3) (1994) 700.
9. A. Goswami, in "Thin Film Fundamentals", New Age International (P.) Ltd, India (1996).
10. K. L. Chopra and I. Kaur, in "Thin Film Device Applications, (eds.) Plenum Press, New York (USA) (1983).
11. N. H. J. Stelzer and J. Schoonman, J. Materials Synthesis and Processings. 4(6) (1996) 429.

FLUORESCENCE CHARACTERISTICS OF BREAST CANCER TISSUES

Sanjay Awadhane¹ and D. K. Kendre²¹Department of Physics, Vai. Dhunda Maharaj Degloorkar College, Degloor Dist. Nanded²Department of Physics, Gramin Mahavidyalaya Vasantnagar, Kotgyal, Nanded

ABSTRACT

Fluorescence spectroscopy offers a less invasive approach for the detection of physical and chemical changes occurring in cells and tissue level because it is the most sensitive method for monitoring minor changes in the structure and microenvironment of fluorophores⁽¹⁾. Laser induced fluorescence is a noninvasive technique which is previously used for determination of breast cancer in vitro study involving 11 patients for the valuation of the diagnostic potential of xenon lamp 45 W excited fluorescence spectroscopy of human breast tissue. The eleven (Malignant and non-malignant) samples are collected for the study of fluorescence spectra. The xenon is the source of excited light. The excitation, an emission monochromators are placed at 90° to each other. We recorded the fluorescence spectra of cancer and normal tissue. The significant changes were observed in fluorescence from normal and breast cancer tissue. Our result suggests that a straight forward measurement of the total integrated fluorescence intensity can provide excellent distribution between cancer and normal tissue.

Keywords: Breast cancer, fluorescence.

INTRODUCTION

Cancer incidence and mortality have globally increased in the past decade. It is well known that early diagnosis can increase the survival rate substantially and current method of screening have to be improved. Hence research in the development of noninvasive optical spectroscopic technique. For early diagnosis of malignancies is being carried out extensively all abnormal and malignant tissue. Malignancies of breast are one of the leading cancers in the world and second among Indian woman. Survival rates are shown to heavily depend on the stages of disease. Fluorescence spectroscopy was initially described as an ex vivo technique to differential normal and malignant breast, lung tissue obtained as surgery⁽²⁾.

The number of cancer deaths is increasing every year and among them breast cancer more than 20% of the cancer death, standing second in the cause of death for woman folk. In India the average incident rate of breast cancer is 16 per 1, 00,000 varying from 22-28 in urban area and 6 parts in rural areas. Based on this, the study is aimed to characterize the native fluorescence spectroscopy normal and different cancerous breast tissue by fluorescence emission and excitation spectra in the UV and visible region from the study. It is observed that there is increase in emission of NADH flavin and porphyrin and also increase in hemoglobin reabsorption as the tissues progresses from normal into malignant^(3,4). On the other hand the emission of tryptophan, tyrosine, collagen and elastin decreases as the normal tissues are transferred into malignant.

We have investigated the Fluorescence spectra with respect to variation from site to site over the past decade. The numbers of research ground in the world have more use of medi photonic approach to various medical applications for the diagnosis of various diseases. Intrinsic Fluorescence of the molecule which play role in biological activity might give large amount of information about the help of muscles or organs⁽⁵⁾.

The Fluorescence spectra are recorded for eleven different samples of cancerous and normal tissues. The Fluorescence emitted by the fluorophore in the tissues were detected and analyzed. The Breast cancerous cells exhibits specific changes in the emitted Fluorescence spectra compared to normal cells. In this paper the present study describes light induced Fluorescence spectroscopy for the detection and diagnosis of Cancer tissue of female human breast. We explore the effectiveness of Fluorescence in the study different breast tissue. The goal of this study is to use of these spectral approaches to analyze the state of breast tissue.

MATERIALS AND METHODS

The normal and malignant samples were obtained from different pathologist from Nanded city region in Maharashtra state of India. The normal and malignant tissues were homogenized and resulting homogenate was mixed with equal volume (1:1) of 0.1 normality of perchloric acid, methanol and vortexed. After centrifugation at 3000rpm for 10 min, the clear supernatant was taken for spectral analysis. The steady state Fluorescence measurement in visible region performed with of spox spectrofluorometer (Fluoromax 2 U.S.A.) at an excitation wavelength of 280 nm. by scanning the emission Monochromator and emission spectra was scanned between 300 and 600 nm emission. The signal were detected by using red sensitive photo multiplier tube (R) 928 Instrument has Xenon lamp as source of exciting light. The excitation and emission Monochromator are placed

90° to each other and light is made to fall on the sample through PMT tube. The size of the sample is approximately 10 x 20 x 2 mm³. We have recorded Fluorescence spectra of malignant and normal spectra.

RESULT AND DISCUSSION

We have recorded Fluorescence spectra of muscles of various organs having cancerous growth and normal muscles from the organs in the spectral range 300- 500 nm. Out of the recorded spectra few samples show interesting result. We select 11 samples of human organ and spectra recorded in case of those humans for the details study and analysis. Fig.(A) shows laser induced Fluorescence spectra of cancer of normal breast tissue. Fluorescence spectrum at 280 nm excitation, shows one primary emission peak around 333 nm which may be attributed to aromatic amino acid tryptophan and Fig. (B) shows four additional peaks around 390 nm, 450 nm, 480 nm and 490 nm which may be attributed to the presence of elastic, the coenzyme nicotinamide. Ademine dinucleotide (reduced form of NADH) and coenzyme flavil ademine dinucleotide (FAD). Fig (B) shows laser induced Fluorescence spectra of cancer of normal breast tissue. We also determine the intensity ratio cancer to normal of breast tissue of LIF spectra. We see that muscles in the form of peaks and deepes have exhibited various features. It seems if the spectra are studied and analyzed in details, some part of spectra emitted by cancerous tissues and normal tissues can easily distinguished.

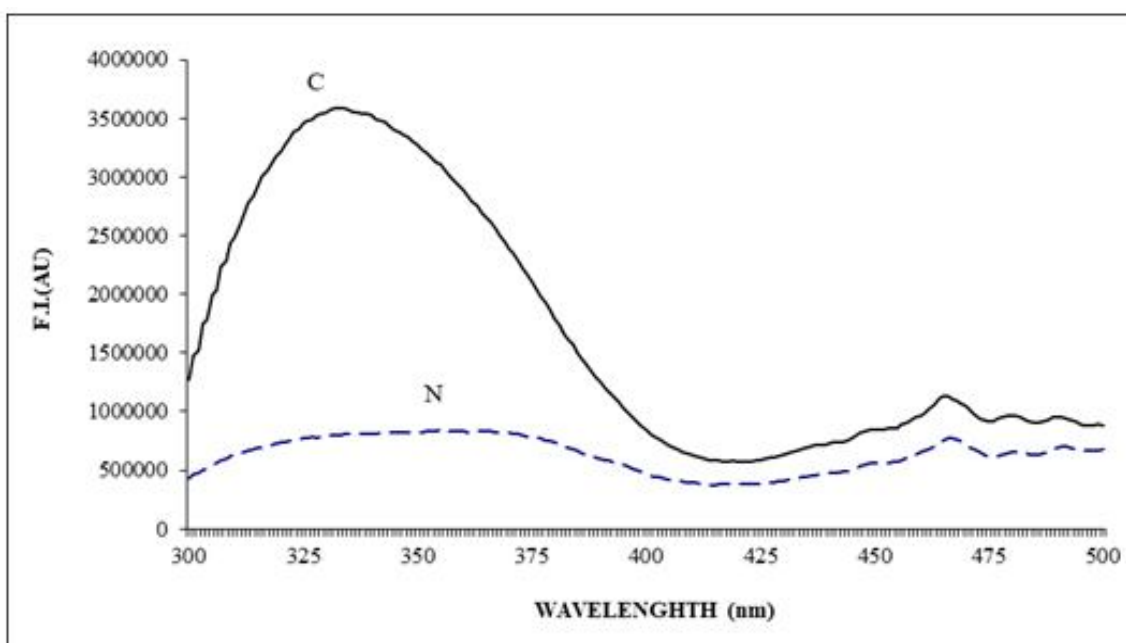


Fig-(A)

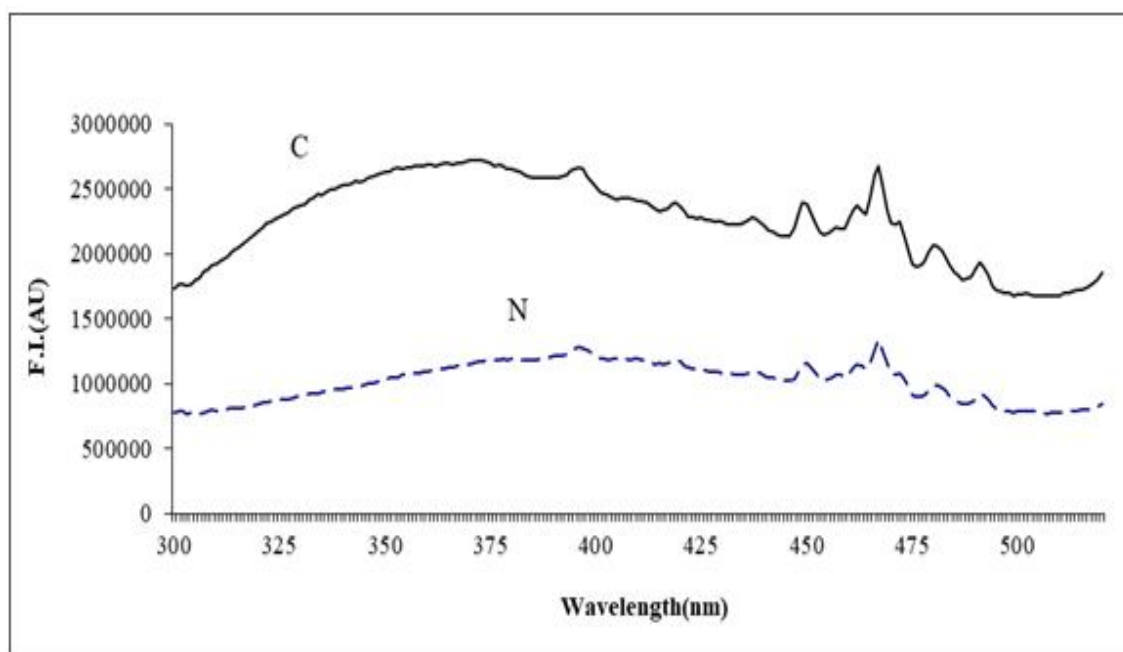


Fig-(B)

CONCLUSIONS

The laser induced Fluorescence spectra of cancerous and normal tissues shows that cancerous tissues can be very easily distinguished from normal tissues. The cancerous tissues in different stages might show different features and therefore we are sure that different stages of cancer can be detected using laser induced Fluorescence spectroscopy.

ACKNOWLEDGEMENT

The author would like to thank Dr. Deshpande, Pathologist Nanded & also Dr. P.A. Kulkarni, Yeshwant College, Nanded for providing the laboratory facility for developing computer software.

REFERENCES

1. Lakoeicez J.R. (1983), Principle & Fluorescence spectroscopy, plenum press , New York.
2. Alfano A.A., Tang G.C. etal. Fluorescence spectra from cancer & normal human breast & lung tissues. QE 23, PP 1806-1819 (1987)
3. Yang Vcelmer E J Szczeparnlak M.Z. and Alfano R.R (1997) excitation spectrum of malignant & benign breast tissue, potential optical biopsy approach, Laser in the life Science 7:249-265.
4. Alexey S. Ladokhin "Fluorescence spectroscopy in peptide and protein analysis", Encyclopedia of analytical chemistry, R.A. Meyers (Ed.), pp.5762-5779.
5. Alfano R.R., Tang G.C. etal. Fluorescence spectra from cancer & normal human breast & lung tissues. QE 23, PP 1806-1819 (1987).

STUDY OF STRUCTURAL PROPERTIES OF Ni-Zn FERRITE AND APPLICATION FOR SYNTHESIS OF PYRANO PYRAZOLE

U. M. Mandle¹, B. L. Shinde², L. A. Dhale³ and K. S. Lohar⁴¹Department of Chemistry, Sangmeshwar College, Solapur²Department of Chemistry, Waghire College, Saswad, Pune^{3,4}Department of Chemistry, ShrikrishnaMahavidyalaya, Gunjoti, Osmanabad

ABSTRACT

Ni_{0.5}Zn_{0.5}Fe₂O₄ ferrite was synthesized by sol-gel auto-combustion method. The precursor sintered at 600 °C for 4 hours. The sintered ferrite characterized by XRD, SEM and I.R Spectroscopic method. The XRD pattern shown the single phase cubic structure. The Infrared spectra were recorded within the range of 300-800 cm⁻¹. The two major bands observed, which are characteristic feature of ferrites. Synthesis of 6-amino-3-methyl-4-phenyl-2, 4-dihydropyrano [2, 3-c] pyrazole-5-carbonitrile from ethyl acetoacetate, hydrazine hydrate, aromatic aldehydes and malononitrile in ethanol was carried using Ni_{0.5}Zn_{0.5}Fe₂O₄ ferrite as a catalyst.

Keywords: Ferrite, XRD, Infrared spectra, PyranoPyrazole.

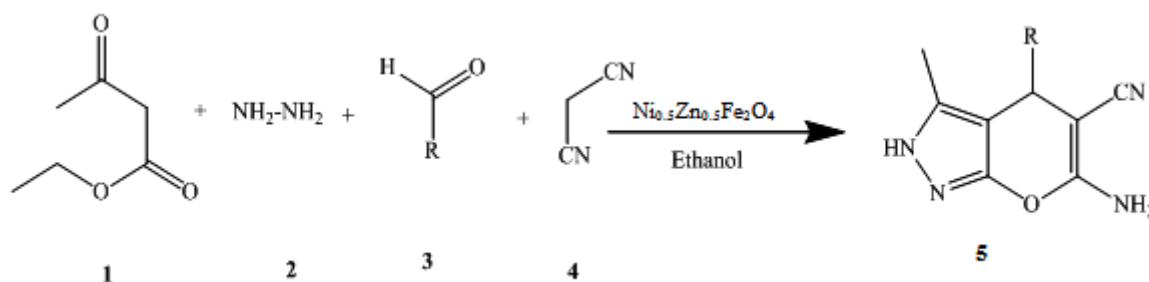
INTRODUCTION

Nano-materials have received prominent attention in recent years due to their remarkable properties and potential applications in diverse field materials at nano scale and it can be easily engineered by controlling shape, crystallinity and composition. These three factors greatly regulate the physico-chemical properties, and consequently play key role for their use in majority of applications (Dhiman, M. et al., 2016). Magnetic nano particles of spinal ferrites (MFe₂O₄) of the great importance for addressing the fundamental relationship between the structure and their physical properties. They have generated diverse technological interests because of their potential applications in magnetic fluids, high frequency magnets, microwave absorbers, high density data storage, sensors, coolants, optical devices, etc. (Singhal, S., et al., 2012). Magnetic ferrite nanoparticles are the topic of current research interest due to their broad applications in technological fields like magnetic fluids, permanent magnets, microwave devices, disk recording, magnetic refrigeration systems and high density information storage (Bhukal, S., et al., 2012).

Soft magnetic ferrites are one of the most used non-metallic magnetic materials, because of their high resistivity and low power loss. They include MnZn, NiZn and MgZn ferrites, in which the NiZn ferrites have much higher operating frequency, Curie temperature and resistivity compared with the other two series of ferrites. Public attention has been aroused to the importance of NiZn ferrites because of their new applications, such as modern communication, internet, electrical appliance, computer circuits (Liu, Z., et al., 2017). The development of nano scale magnetic material has been intensively pursued because of the appearance of some unique physical, chemical and structural properties. These properties allow them available widely for electronic devices, e.g. magnetic recording media and magnetic sensors. Especially, the nano scale spinel ferrite has triggered considerably interesting due to their distinctive properties as well as potential applications in catalysis (Pirouz, M. J., et al., 2015) water purification systems energy storage in super capacitor (Kumbhar, V. S., et al., 2012), antibacterial (Luo, Y., et al., 2014), Biomedical (Sanpo, N., et al., 2013), drug delivery (Wu, H., et al., 2011) and gas sensor (Mukherjee, K., et al., 2012) field. Recently, many efforts have been made to optimize their basic properties by substituting various ions, introducing a coating structure or composite system. Among these modifications on the nano scale spinel ferrite, substituting various ions has been considered as an important way to improve the performance of spinel ferrite nanoparticles (Meng, F., et al., 2017).

Now days, functionalized magnetite nanoparticles used as effective catalyst in different chemical reactions including synthesis of α -amino nitriles (Kassaei, M. Z., et al., 2011), 1,1-diacetates from aldehydes (Esmaeilpour, M., et al., 2012), 1,4-dihydropyridines (Zamani, F., et al., 2013) etc. Many of the pyrano (2, 3-C) pyrazoles are known for their antimicrobial (Sayed, H., et al., 1999), insecticidal (Ismail, Z. H., et al., 2003), anti-inflammatory (Zaki, M. E. A., et al., 2006), activities. Four-component reactions of aldehydes, 1, 3-dicarbonyl compounds, malononitrile, and hydrazine developed for the synthesis of pyranopyrazoles using triethylamine (El-Assaly, S. A., 2011), c-alumina (Mecadon, H., et al., 2011), iodine (Madhusudana Reddy, et al., 2012), alumina (Mecadon, H., et al., 2011), amberlyst A21 (Bihani, M., et al., 2013), etc.

Herein we wish to report an efficient synthesis of pyranopyrazole by one pot four component reaction of ethyl acetoacetate, hydrazine hydrate, aromatic aldehyde and malononitrile using Ni_{0.5}Zn_{0.5}Fe₂O₄ nanoparticles as a magnetically recoverable catalyst (Scheme 1).



Scheme-1: Synthesis of pyranopyrazole using 40 mol % $\text{Ni}_{0.5}\text{Zn}_{0.5}\text{Fe}_2\text{O}_4$ nanoparticles as catalyst.

EXPERIMENTAL

Synthesis of Ferrite

$\text{Ni}_{0.5}\text{Zn}_{0.5}\text{Fe}_2\text{O}_4$ ferrite was synthesized by the sol-gel auto-combustion method. The molar ratio of metal nitrates to citric acid was 1:3. The metal nitrates were dissolved together in the minimum amount of double-distilled water needed to obtain a clear solution. An aqueous solution of citric acid was mixed with the metal-nitrate solution and pH ≈ 7 of solution was adjusted by gradually addition of the ammonia. The mixed solution was kept on a hot plate with constant stirring at 90°C . A viscous brown gel was formed during the evaporation of solution. When all of the water molecules were removed from the mixture, the viscous gel began to froth. After few a minutes, the gel ignited and burnt with glowing flints. The auto-combustion was completed within a minute, yielding brown-coloured ashes referred to as the precursor.

General Procedure for the Synthesis of Pyranopyrazole

A pre-stirred mixture of ethylacetoacetate **1** (1 mmole), hydrazine hydrate **2** (1.5 mmole) in ethanol (15 ml) was added, benzaldehyde **3** (1 mmole) and malononitrile **4** (1mole) and $\text{Ni}_{0.5}\text{Zn}_{0.5}\text{Fe}_2\text{O}_4$ (40 mole %) as a catalyst was added, the reaction mixture then heated under reflux. The completion of reaction was monitored using TLC, [solvent system Ethyl acetate: n-Hexane (2:3)]. The catalyst removed by fixing the catalyst magnetically at the bottom of the flask with a strong magnet, The hot reaction mixture filtered, the residue treated with boiling methanol-ethyl acetate (1:1) and then filtered the orange coloured residue obtained which was then dried, the melting point and, % yield calculated.

Characterization of Catalyst

The crystallographic structure was identified by X-ray powder diffraction with $\text{Cu K}\alpha$ radiation ($\lambda = 1.5405 \text{ \AA}$) by Phillips X-ray diffractometer (Model 3710). Morphology of the powder sample was studied on JEOL-JSM-5600 N Scanning Electron Microscope (SEM). The infrared spectra of the sample were recorded at room temperature in the range 200 to 800 cm^{-1} using Perkin Elmer infrared spectrophotometer.

RESULTS AND DISCUSSION

X-ray diffraction (XRD) patterns of the $\text{Ni}_{0.5}\text{Zn}_{0.5}\text{Fe}_2\text{O}_4$ spinel ferrite system is shown in Figure 1. The XRD patterns confirmed the formation of cubic spinel structure of single phase ferrites without additional peaks corresponding to any other phases. The crystal structures of NiCuZn ferrite are identified as cubic spinel (space group: $\text{Fd}\bar{3}\text{m}$) with the corresponding (220), (311), (222), (400), (422), (333) and (440) planes.

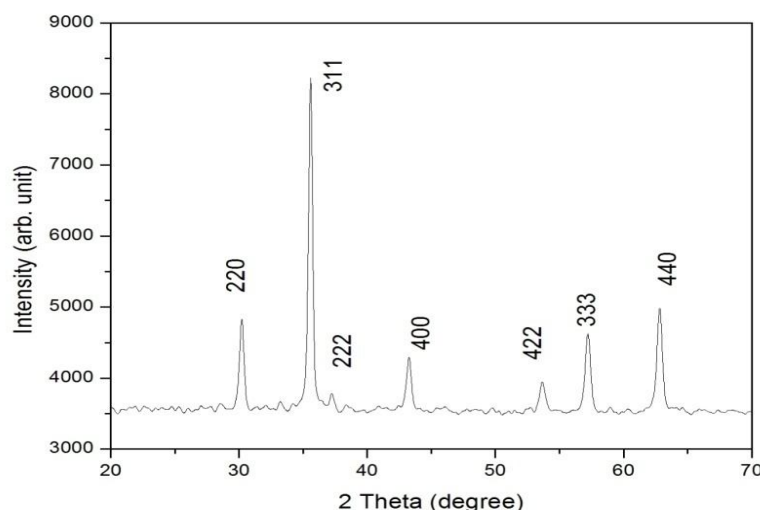


Figure-1: XRD patterns of the sample

The Lattice parameter 'a' was calculated by using XRD data the equation discussed elsewhere (B.D. Culity, 1967) and found 8.394 Å. The average crystalline diameter ' D_{XRD} ' of powder samples estimated from full width at half maxima of the most intense peak (311) of XRD calculated by using Scherer Relation (B.D. Culity, 1967), and found 35.483 nm.

The IR spectra as shown in Fig.2 was recorded at room temperature in the frequency range 200-800 cm^{-1} . The highest band ν_1 observed, at 578.30 cm^{-1} and it corresponds to intrinsic stretching vibrations of the metal at the tetrahedral site (Td), Mtetra- O, whereas the ν_2 lowest band observed at 422.90 cm^{-1} which is assigned to octahedral-metal stretching (Oh), MOcta- O.

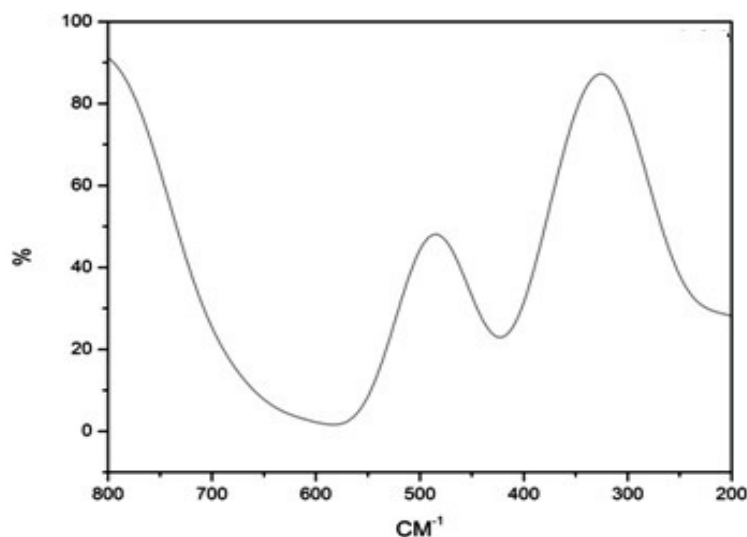


Figure-2: The IR spectra of the sample

Scanning electron micrograph (SEM) of the surfaces of sample is shown in Figure 3. Sample is characterized by a typical porous structure and small rounded grains.

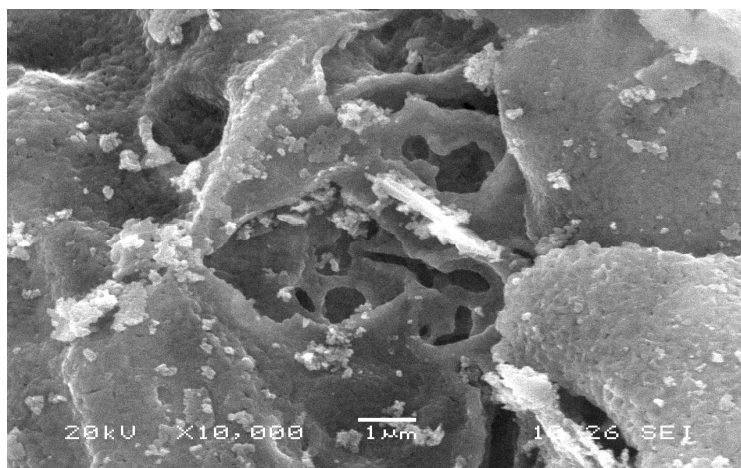


Figure-3: SEM image of the sample

Synthesis of 6-amino-3-methyl-4-phenyl-2, 4-dihydropyrano [2, 3-c] pyrazole-5-carbonitrile (**5**) from ethyl acetoacetate **1**, hydrazine hydrate **2**, aromatic aldehydes **3** and malononitrile **4** in ethanol was carried using $\text{Ni}_{0.5}\text{Zn}_{0.5}\text{Fe}_2\text{O}_4$ ferrite catalyst (Scheme 1). The title compound **5** was isolated with 95% yield in the presence of $\text{Ni}_{0.5}\text{Zn}_{0.5}\text{Fe}_2\text{O}_4$ ferrite (40 mol %) in shorter reaction time (120 min).

CONCLUSION

$\text{Ni}_{0.5}\text{Zn}_{0.5}\text{Fe}_2\text{O}_4$ ferrite successfully synthesized by sol-gel auto-combustion method. The precursor was sintered at 600 $^{\circ}\text{C}$ for 4 hours. The sintered ferrite was characterized by XRD, SEM and I.R Spectroscopic method. The XRD patterns showed the single phase cubic structure and lattice constant (a) observed 8.394 Å. In Infrared spectra two major bands observed, higher frequency band ' ν_1 ' (578.30 cm^{-1}) assigned to tetrahedral sites, while lower frequency band ' ν_2 ' (422.90 cm^{-1}) is assigned to octahedral site. Synthesis of 6-amino-3-methyl-4-phenyl-2, 4-dihydropyrano [2, 3-c] pyrazole-5-carbonitrile from ethyl acetoacetate, hydrazine hydrate, aromatic aldehydes and malononitrile in ethanol was carried using $\text{Ni}_{0.5}\text{Zn}_{0.5}\text{Fe}_2\text{O}_4$ ferrite catalyst.

REFERENCES

- B.D. Culity, Elements of X-Ray Diffraction, 99, Addison-Wesley, Reading, MA, 1967.
- Bhukal, S., Namgyal, T., Mor, S., Bansal, S., &Singhal, S. (2012). Structural, Electrical, Optical And Magnetic Properties Of Chromium Substituted Co–Zn Nanoferrites $\text{Co}_{0.6}\text{Zn}_{0.4}\text{Cr}_x\text{Fe}_{2-x}\text{O}_4$ ($0 \leq x \leq 1.0$) Prepared Via Sol–Gel Auto-Combustion Method. *Journal OfMolecular Structure*, 1012, 162-167.
- Bihani, M., Bora, P. P., Bez, G., &Askari, H. (2013). Amberlyst A21 Catalyzed Chromatography-Free Method For Multicomponent Synthesis Of Dihydropyrano [2, 3-C] Pyrazoles In Ethanol. *Acs Sustainable Chemistry &Engineering*, 1(4), 440-447.
- Dhiman, M., Sharma, R., Kumar, V., &Singhal, S. (2016). Morphology Controlled Hydrothermal Synthesis AndPhotocatalytic Properties Of ZnFe_2O_4 Nanostructures. *Ceramics International*, 42(11), 12594-12605.
- El-Assaly, S. A. (2011). A Simple And Clean Method For Four-Component Synthesis Of Pyrano [2, 3-C] Pyrazole Derivatives. *Der PharmaChem*, 3(5), 81-86.
- Esmaeilpour, M.; Sardarian, A.R.; Javidi, J. (2012). Schiff Base Complex Of Metal Ions Supported On Superparamagnetic $\text{Fe}_3\text{O}_4@\text{SiO}_2$ Nanoparticles: An Efficient, Selective And Recyclable Catalyst For Synthesis Of 1,1-Diacetates From Aldehydes Under Solvent-Free Conditions. *Appl. Catal. A*, 445–446, 359–367.
- Ismail, Z. H., Aly, G. M., El-Degwi, M. S., Heiba, H. I., &Ghorab, M. M. (2003). Synthesis And Insecticidal Activity Of Some New Pyranopyrazoles, Pyrazolopyranopyrimidines, And Pyrazolopyranopyridines. *Egypt. J. Biotechnol*, 13, 73-82.
- Kassaei, M. Z., Masrouri, H., &Movahedi, F. (2011). SulfamicAcid-Functionalized Magnetic Fe_3O_4 Nanoparticles As An Efficient And Reusable Catalyst For One-Pot Synthesis Of α -Amino Nitriles In Water. *Applied Catalysis A: General*, 395(1), 28-33.
- Kumbhar, V. S., Jagadale, A. D., Shinde, N. M., &Lokhande, C. D. (2012). Chemical Synthesis Of Spinel Cobalt Ferrite (CoFe_2O_4) Nano-Flakes For Supercapacitor Application. *Applied Surface Science*, 259, 39-43.
- Liu, Z., Peng, Z., Lv, C., &Fu, X. (2017). Doping Effect Of Sm^{3+} On Magnetic And Dielectric Properties Of Ni-Zn Ferrites. *Ceramics International*, 43(1), 1449-1454.
- Luo, Y., Guo, W., Ngo, H. H., Nghiem, L. D., Hai, F. I., Zhang, J., ... &Wang, X. C. (2014). A Review On The Occurrence Of Micropollutants In The Aquatic Environment And Their Fate And Removal During Wastewater Treatment. *Science Of The Total Environment*, 473, 619-641.
- Madhusudana Reddy, M. B., &Pasha, M. A. (2012). One-Pot, Multicomponent Synthesis Of 4H-Pyrano [2, 3-C] Pyrazoles In Water At 250°C. *Indian Journal OfChemistry. B*, 51, 537-541.
- Mecadon, H., Rohman, M. R., Rajbangshi, M., &Myrboh, B. (2011). γ -Alumina As A Recyclable Catalyst For The Four-Component Synthesis Of 6-Amino-4-Alkyl/Aryl-3-Methyl-2, 4-Dihydropyrano [2, 3-C] Pyrazole-5-Carbonitriles In Aqueous Medium. *Tetrahedron Letters*, 52(19), 2523-2525.
- Meng, F., Shang, X., Zhang, W., &Zhang, Y. (2017). Effect Of In^{3+} Substitution On Structural And Magnetic Properties Of Ni Ferrite Nanoparticles. *Physica B: Condensed Matter*, 504, 69-73.
- Mukherjee, K., &Majumder, S. B. (2012). Synthesis Process Induced Improvement On The Gas Sensing Characteristics Of Nano-Crystalline Magnesium Zinc Ferrite Particles. *Sensors AndActuators B: Chemical*, 162(1), 229-236.
- Pirouz, M. J., Beyki, M. H., &Shemirani, F. (2015). Anhydride Functionalised Calcium Ferrite Nanoparticles: A New Selective Magnetic Material For Enrichment Of Lead Ions From Water And Food Samples. *Food Chemistry*, 170, 131-137.
- Sanpo, N., Berndt, C. C., Wen, C., &Wang, J. (2013). Transition Metal-Substituted Cobalt Ferrite Nanoparticles For Biomedical Applications. *ActaBiomaterialia*, 9(3), 5830-5837.
- Sayed, H., Fakher, A., &BELAL, H. M. (1999). Synthesis And Biological Activity Of Some Pyrazole Derivatives. *Journal Of The Serbian Chemical Society*, 64(1), 9-18.
- Singhal, S., Jauhar, S., Singh, J., Chandra, K., &Bansal, S. (2012). Investigation Of Structural, Magnetic, Electrical And Optical Properties Of Chromium Substituted Cobalt Ferrites ($\text{CoCr}_x\text{Fe}_{2-x}\text{O}_4$, $x=0.0$, $x=1$) Synthesized Using Sol Gel Auto Combustion Method. *Journal Of Molecular Structure*, 1012, 182-188.

-
- Wu, H., Liu, G., Wang, X., Zhang, J., Chen, Y., Shi, J., & Yang, S. (2011). Solvothermal Synthesis Of Cobalt Ferrite Nanoparticles Loaded On Multiwalled Carbon Nanotubes For Magnetic Resonance Imaging And Drug Delivery. *Acta Biomaterialia*, 7(9), 3496-3504.
 - Zaki, M. E. A.; Soliman, H. A.; Hiekal, O. A.; Rashad, A. E. Z. *Naturforsch., C.* 2006, 61, 1.
 - Zamani, F., & Izadi, E. (2013). Synthesis And Characterization Of Sulfonated-Phenylacetic Acid Coated Fe₃O₄ Nanoparticles As A Novel Acid Magnetic Catalyst For Biginelli Reaction. *Catalysis Communications*, 42, 104-108.

STRUCTURAL AND ELASTIC PROPERTIES OF CADMIUM SUBSTITUTED Ni –Cu FERRITES

R. B. Kavade¹, R. G. Vidhate², J. M. Bhandari³, K. H Katke⁵, S. J. Shukla⁵ and K. M. Jadhav⁶¹Bhagawan Mahavidyalaya, Ashti, Dist. Beed,^{2,4}Anandrao Dhonde Mahavidyalaya, Kada, Beed,³Gandhi College, Kada, Dist. Beed⁵P. G. and Research center, Deogiri College, Aurangabad,⁶Department of Physics Dr. B. A. M. U. Aurangabad

ABSTRACT

The samples of cadmium substituted Ni-Cu mixed ferrites having the composition $Ni_{0.5}Cu_{0.5-x}Cd_xFe_2O_4$ ($x = 0.0$ to 0.4 in the step of 0.2) have been synthesized by standard solid state reaction technique using AR grade oxides. The X-ray diffraction and Infrared spectroscopic analysis confirms the formation of single phase cubic spinel structure of ferrite phase. The lattice constant was found to increase with increase in cadmium content and was due to the large ionic radius of cadmium. The structural parameters such as lattice constant, X-ray density, cation distribution, ionic site radii, oxygen positional parameter, theoretical lattice constant, bond length, jump length of tetrahedral (A) site as well as octahedral [B] site, tetrahedral edge length, shared and unshared octahedral edge length was estimated. The estimated cation distribution of ferrite was verified by comparing the observed and theoretical lattice parameters. The elastic parameter of ferrites such as young's modulus, rigidity modulus and bulk modulus was estimated by using IR technique.

Keywords: Elastic properties, Structural Properties, X-ray diffraction.

1. INTRODUCTION

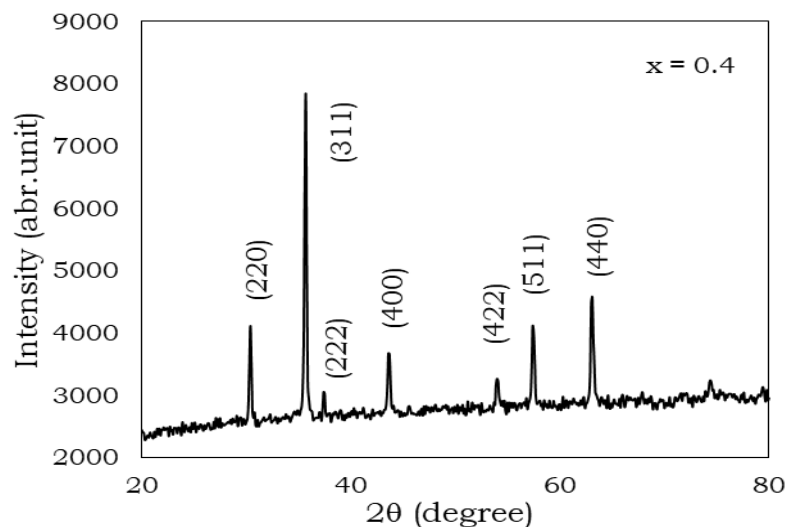
The mixed nickel copper ferrites are technologically important materials as it possess high saturation magnetization, high resistivity, high stability and low loss energy over a wide range of frequency [1, 2]. In fact, cadmium substituted Ni-Cu mixed ferrite are the subject of intensive investigations in the field of fundamental and applied research due to their wide applications in electronic industry. The physical properties of spinel ferrites depend on the type, amount of dopant and distribution of cations over the tetrahedral (A) and octahedral [B] sites [3, 4]. In electronic materials the elastic module are of much importance because they shows the nature of binding force in polycrystalline materials and also helps to understand the thermal properties of these materials.

2. EXPERIMENTAL

The ferrite with composition $Ni_{0.5}Cu_{0.5-x}Cd_xFe_2O_4$ ($x = 0.0, 0.2, 0.4$) were synthesized by standard double sintering ceramic method.[5,6,7] Grinding using agate mortar (4 h) was carried out for each sample. The samples were pre-sintered at 1293 K for 12 h. The sintered powder is again reground and sintered at 1353 K for 14 h. Then the powder of samples compressed into pellets of 10 mm diameter using a hydraulic press with pressure 6 ton/inch² and sintered at 1273K for 12 h. The samples were furnace cooled to room temperature. The prepared samples were characterized by X-ray powder diffractometer in the 2θ range 20° - 80° at room temperature to confirm single phase spinel structure. The infrared spectra of a prepared sample were recorded at room temperature within the range 200 cm^{-1} to 800 cm^{-1} on the infrared spectrometer (Model 783, Perkin-Elmer)

3. RESULTS AND DISCUSSION

The peaks appeared in the XRD pattern (fig.1) of the ferrites are identified. However, the non appearance of extra peaks reveals the formation of single phase cubic spinel structure of ferrite. The increase of observed lattice parameter 'a' and X-ray density 'ρ' with increase of the cadmium content was due to the difference in ionic radii and atomic weight of the component ions in the ferrite system [8]. The distribution of cations in the tetrahedral (A) and octahedral [B] sites can be expressed as [9], $(Cd_xCu_yFe_{1-x-y})^A[Ni_{0.5}Cu_{0.5-x-y}Fe_{1+x+y}]^BO_4$ The theoretical lattice parameter of ferrite samples estimated using the relation [10] were listed in table 1. The good agreement between experimentally estimated and theoretical lattice parameters confirms the assumed cation distribution of the ferrites.


Fig-1: Typical XRD Pattern of $\text{Ni}_{0.5}\text{Cu}_{0.5-x}\text{Cd}_x\text{Fe}_2\text{O}_4$ ($x=0.4$)

The mean ionic radius of the tetrahedral site ' r_A ' found to be increase with Cd ion content where as mean ionic radius of the octahedral site ' r_B ' decreases with cadmium content. The increase of ionic radius ' r_A ' of tetrahedral site with Cd ion content was due to the larger ionic radii of Cd ions. But the values of oxygen positional parameter are almost same in the ferrite systems.

The band positions of IR spectrum are listed in table 1. The shift of band position ν_1 towards lower wavelength side was due to the substituted Cd^{2+} ion, preferably it occupies the tetrahedral (A) site [11]. The octahedral [B] site was occupied by Ni^{2+} ions, where Fe^{3+} , Cu^{2+} ions occupy both tetrahedral and octahedral sites. The force constant for tetrahedral ' k_t ' and octahedral ' k_o ' sites, longitudinal ' V_l ' and transverse ' V_s ' elastic wave velocities, elastic moduli for ferrite samples were estimated using the relations[9] and are listed in table 1. The decreases of octahedral force constant with increase of the Cd ion content, was due to the substitution of Cd ion content, which decreases the amount of Cu^{2+} and increases the amount of Fe ions in the octahedral [B] sites. The increase in rigidity modulus ' G ', bulk modulus ' B ' and young's modulus ' E ' with increase of the cadmium content, may be due to the strengthening of inter atomic bonding between various atoms continuously. The values of poisson's ratio are found to be 0.35 for all the ferrites. The present estimated values of poisson's ratios are lying in the range of -1 to 0.5; which reveals the theory of isotropic elasticity.

Table-1: Structural and elastic parameters of ferrites system $\text{Ni}_{0.5}\text{Cu}_{0.5-x}\text{Cd}_x\text{Fe}_2\text{O}_4$ ($x=0.0, 0.2, 0.4$).

Parameters	$x = 0.0$	$x = 0.2$	$x = 0.4$
a (Å)	8.367	8.423	8.488
$\rho \times 10^3$ (kg/m ³)	5.37	5.479	5.568
$d \times 10^3$ (kg/m ³)	4.003	3.939	3.931
r_A (Å)	0.67	0.73	0.79
r_B (Å)	0.687	0.682	0.677
L_A (Å)	3.623	3.647	3.675
L_B (Å)	2.953	2.978	3.001
R_A (Å)	1.898	1.911	1.925
R_B (Å)	1.990	2.004	2.019
a_{th} (Å)	8.417	8.496	8.575
u	0.386	0.389	0.392
$\nu_1 \times 10^2$ (m ⁻¹)	590	585	581
$\nu_2 \times 10^2$ (m ⁻¹)	389	397	395
k_t (N/m)	1.482	1.751	2.018
$k_o \times 10^2$ (N/m)	0.988	0.965	0.943
V_l (m/s)	5250	5420	5590
V_s (m/s)	3031	3129	3227
$G \times 10^9$ kg m ⁻¹ s ⁻²	49.33	53.64	57.98
$B \times 10^9$ kg m ⁻¹ s ⁻²	148	161	174
$E \times 10^9$ kg m ⁻¹ s ⁻²	133.2	144.8	156.5
σ	0.35	0.35	0.35

4. CONCLUSIONS

The X ray diffraction pattern reveals the formation of cubic spinel structure of ferrite phase. The lattice parameter and X-ray density are found to increase with cadmium content. The estimated cation distribution of ferrites has been verified by comparing the observed and theoretical lattice parameters. The structural parameters estimated through X-ray diffraction were affected with cadmium content. The elastic parameters are found to increase with increase of cadmium content and was explained in terms of inter atomic bonding between various atoms and is being strengthened continuously. The estimated elastic parameters of the present results are in good agreement with the earlier reports.

REFERENCES

1. A. M. Abdeen, (1998) *J. Magn. Magn. Mater.* 185, 199.
2. B. K. Bammannavar, L. R. Naik and R. B. Pujar, (2008) *Mater. Sci. an Ind. J.* 4(3), 160.
3. O. H. Kwon, Y. Fukushima, M. Sugimoto and N Hiratsuka, (1997) *J Phys.* IV, 165.
4. A. Menakshisundaram, N. Gunasekaran and V. Srinivasan, (1982) *Phys. Stat. Solidi. (a)* 69, K15.
5. C.N. Rao, (1994) "Chemical approaches to the synthesis of inorganic materials", Wiley, New York.
6. Zhiyong Xu, Zhong Yu, Ke Sun, Lezhong Li, Haining Ji, Zhongwen Lan, (2009) *J. Magn. Magn. Mater.* 321.
7. S.A. Mazen, S.F. Mansour, T.A. Elmosalami, H. M. Zaki, (2009) *J. Alloys. Compd.* 472 307.
8. P. B. Belavi, G. N. Chavan, L. R. Naik, R. Somasshekar and R. K. Kotnala, (2012). *Mater. Chem. Phys.* 132, 138
9. K. B. Modi, M. K. Rangolia, M. C. Chhantbar and H. H. Joshi, (2006). *J. Mater. Sci.* 41, 7308
10. R. L. Dhiman, S. P. Taneja and V. R. Reddy, (2008). *Adv. Condens. Mat. Phys.* 703479, 7
11. S. A. Patil, V. C. Mahajan, A. K. Gatge and S. D. Lotake, (1998) *Mater. Chem. Phys.* 57, 86.

INVESTIGATION OF CRYSTAL STRUCTURE AND D.C. ELECTRICAL RESISTIVITY OF In^{3+} SUBSTITUTED YTTRIUM IRON GARNET

Vidhate R. G.¹, Kavade R. B.², Bhandari J. M.³, Katke K. H.⁴, and Jadhav K. M.⁵Head¹ and Assistant Professor², Anandrao Dhonde Alias Babaji Mahavidyalaya, Kada, Beed³Head Department of Physics, Bhagwan Mahavidyalaya, Ashti, Beed⁴Bhandari J.M.³, Head Dept. of Physics, Gandhi College Kada, Beed⁵Senior Prof. Department of physics, Dr. Babasaheb Ambedkar Marathwada University, Aurangabad

ABSTRACT

In^{3+} substituted yttrium iron garnet (YIG) samples, with a nominal composition of $\text{Y}_3\text{In}_x\text{Fe}_{5-x}\text{O}_{12}$ with $x = 0.0, 0.2$ and 0.4 were prepared by a solid-state reaction method. The samples were characterized by X-ray diffraction technique. The X-ray diffraction studies of compositions revealed the formation of single phase cubic structure with lattice constant ranging from 12.37 to 12.43 Å.

The FTIR spectra of typical samples are taken in the range of $500\text{-}4000\text{cm}^{-1}$. IR spectra show typical absorption bands indicating the garnet nature of samples. The D.C. electrical resistivity $\rho_{\text{d.c.}}$ was measured in the temperature range 300-725 K. The electrical measurements were carried out by means of two probe method; it is found that resistivity decreases with increase in temperature.

Keyword: Electrical study, Indium, IR Spectra, XRD, Yttrium iron garnet.

INTRODUCTION

Mixed metal oxides with iron (III) oxides as their main component are known as ferrites. Historically ferrites represent an important category of materials, which are in great demands due to their numerous applications in many fields. The electrical and magnetic properties of ferrites are strongly dependent on their chemical composition and their method of preparation [8, 10]. It is important to optimize the electrical and magnetic properties of ferrites, for desired applications. Due to their interesting properties scientists, researchers and engineers are still interested in designing the various types of ferrites material substituted with different cations with different valencies and prepared by different techniques.

In the various types of ferrites rare earth garnet especially yttrium iron garnet (YIG) is of great importance for scientist and technologist because of their applications in microwave communication devices such as circulators, oscillators, gyrators and phase shifters because of its small ferromagnetic resonance line-width, high electrical resistivity and low dielectric loss in microwave regions in many fields [10]. Yttrium iron garnet (YIG) is microwave ferrite, which in polycrystalline form has specific characteristics. The magnetic and crystallographic properties of the magnetic iron garnet have been studied by many workers [1-5]. Substituted iron garnets have found extensive use in wide band non reciprocal microwave devices [11].

EXPERIMENTAL

The samples of In^{3+} substituted $\text{Y}_3\text{In}_x\text{Fe}_{5-x}\text{O}_{12}$ garnets with $x = 0.0, 0.2$ and 0.4 were prepared by well known double sintering ceramic method in which a molar ratio of analytical Y_2O_3 , Fe_2O_3 and In_2O_3 (all 99.99% pure AR grade chemicals, Mumbai) were mixed thoroughly in stoichiometric proportions and then ground to very fine powder by using agate mortar for about 3 hr. These mixtures in powder form were pre-sintered in a Indfur Programmable muffle furnace at 1200°C for 24 hr and cooled to room temperature slowly at the rate of $2^\circ\text{C}/\text{min}$. The samples were reground and re-fired at 1350°C for 30 hr and slowly cooled to room temperature at the rate of $2^\circ\text{C}/\text{min}$., and then reground for 1 hr. The fine powdered sample was pelletized under the pressure 5 ton/inch².

The electrical measurements were carried out by means of two probe method. The samples in the form of discs were polished well to have smooth parallel surfaces, and then these surfaces were coated with silver paste as a contact material for the electrical measurements. The temperature was measured by using chromel-alumel thermocouple in contact with the surface of the samples. The d.c. electrical resistivity $\rho_{\text{d.c.}}$ was measured in the temperature range 300-725 K.

RESULT AND DISCUSSION

Mixed garnet ferrites system under investigation has been structurally investigated by X-ray diffraction technique. The typical XRD pattern shows the reflections namely (321), (400), (420), (422), (431), (521), (611), (444), (640), (642), (800), (842). No extra peaks other than cubic structure have been observed in the XRD pattern. The Bragg peaks are sharp and intense. The lattice parameters are calculated using XRD data and are

given in table-1. It is observed from table-1 that lattice constant increases with increase in indium content 'x'. The ionic radii of yttrium (0.89\AA) Fe^{3+} is (0.67\AA) and indium (0.81\AA) hence we observe variation in the lattice parameter with indium substitution. The bulk density of all samples was measured using Archimedes principle and values are tabulated in table-1. Bulk density increases with increase in indium content 'x'. Using the values of molecular weight and volume of the sample X-ray density was calculated. The values of X-ray density are also listed in Table-1. X-ray density increase with composition 'x'. The observed variation in X-ray density is attributed to increase in volume of the samples. The crystallographic parameters (lattice constant, X-ray density) are in good agreement with reported values [15]. The most intense peak (420) of XRD pattern was used to evaluate particle size of the samples. The particle size was calculated by using Scherer's formula, the values of particle size for all the composition is listed in Table-1.

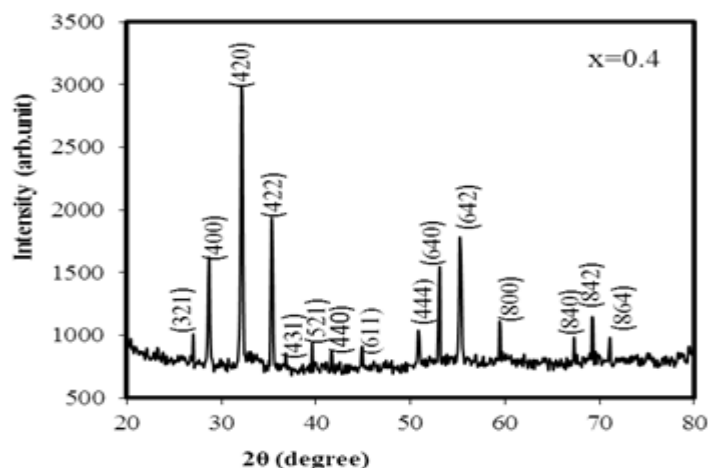


Fig-1: Typical XRD patterns of $\text{Y}_3\text{In}_x\text{Fe}_{5-x}\text{O}_{12}$. ($x = 0.4$)

Table-1: Lattice constant (a), X-ray density (d_x), bulk density (d_b) porosity (P) and particle size (t) of $\text{Y}_3\text{In}_x\text{Fe}_{5-x}\text{O}_{12}$.

x	a (\AA)	d_x (gm/cm^3)	d_b (gm/cm^3)	P (%)	t (μm)
0.0	12.370	5.179	4.13	20.25	3.42
0.2	12.401	5.224	4.19	19.97	3.25
0.4	12.43	5.264	4.26	19.07	3.17

IR spectra show typical absorption bands indicating the garnet nature of the samples. The band positions obtained from IR spectra are given in Table-2 the vibrational frequency depends upon the cation mass, cation oxygen bonding force, distance etc. From IR spectra, it is revealed that, a broad band appears at around 611 cm^{-1} , 547 cm^{-1} and 670 cm^{-1} assignable to the stretching mode of the tetrahedral in the YIG and this indicates that the crystallization of samples is more complete [7,14,17]. The values of absorption bands are given in Table 4.3. Our results on IR studies are in good agreement with the literature reports. [11]

Table-2: Vibrational band frequencies (ν_1 , ν_2 , ν_3 , ν_4) of $\text{Y}_3\text{In}_x\text{Fe}_{5-x}\text{O}_{12}$, for $x = 0.0, 0.2$ and 0.4 .

x	ν_1 (cm^{-1})	ν_2 (cm^{-1})	ν_3 (cm^{-1})	ν_4 (cm^{-1})
0.0	547.1	611.9	670.1	---
0.2	547.1	605.5	861.0	914.0

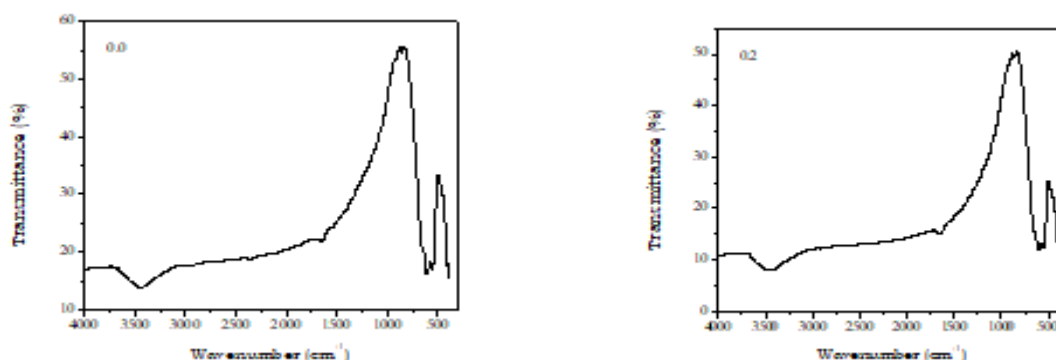


Fig-4: IR spectra of $\text{Y}_3\text{In}_x\text{Fe}_{5-x}\text{O}_{12}$ of samples $x = 0.0$ and 0.2

ANALYSIS OF ELECTRICAL RESISTIVITY

The D. C. electrical resistivity (ρ) measurements for all the samples of $Y_3In_xFe_{5-x}O_{12}$ garnet system were carried out in the temperature range of 300-725 K. Plots of $\log \rho$ Vs $1000/T$ are shown in Fig.5. It is observed from resistivity plots that, D.C. electrical resistivity decreases with increase in temperature. The plot exhibits a relatively sharp kink, which divides the curve in two parts. The resistivity plots obeys Arrhenius relation given by the equation,

$$\rho = \rho_0 e^{\frac{\Delta E}{KT}} \quad \dots 1$$

Using the above relation and from the resistivity plot, the activation energy for two regions that is ferrimagnetic and paramagnetic was calculated and the values are given in table 3. It is observed from table 3 that, activation energy decreases with increase in In^{3+} ions. The experimental results on D.C. electrical resistivity studies closely matches with those reported in the literature [12].

Table-3: Activation energy (ΔE) in paramagnetic (E_p) and ferrimagnetic (E_f) region of $Y_3In_xFe_{5-x}O_{12}$.

x	E_p (eV)	E_f (eV)	ΔE (eV)
0.0	0.25	0.13	0.12
0.2	0.19	0.10	0.09
0.4	0.13	0.06	0.07

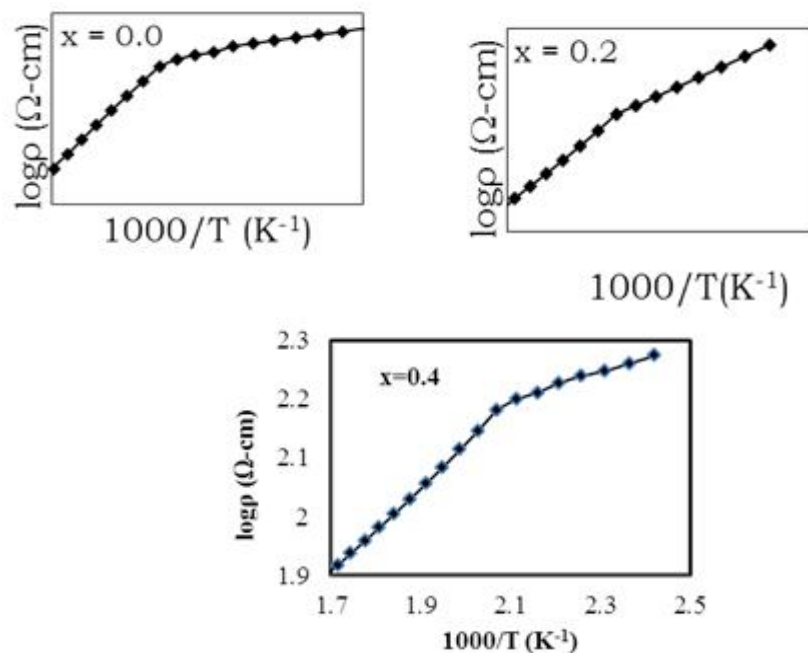


Fig-5: Variation of $\log \rho$ versus $1000/T$ of $Y_3In_xFe_{5-x}O_{12}$. ($x = 0.0, 0.2$ and 0.4).

CONCLUSION

The garnet system In-YIG was prepared by a solid-state sintering method. The parameter lattice constant increases slightly with In^{3+} substitution. IR spectra show typical absorption bands indicating the garnet nature of the samples. It is observed from resistivity plots that, D.C. electrical resistivity decreases with increase in temperature and activation energy decreases with increase in In^{3+} ions.

REFERENCES

1. E. E. Anderson, E. E. (1962), *J. Phys. Soc. Japan Suppl.* 17, 365.
2. Guo Cuijing, Zhang Wei, Ji Rongjin, Zeng Yanwei. (2011) *J. Magn. Magn. Mater.* 323-611
3. Gilileo, M. A. (1960), *J. Phys. Chem. Solids* 13, 33.
4. Gilileo, M. A. and Geller S. (1958), *Phys. Rev.* 110, 73.
5. Geller, S. and Gilileo, M.A. (1957), *J. Phys. chem. Solids* 3, 30.
6. Hongjie Zhao Ji Zhou Yang Bai Zhilun Gui Longtu Li (2004), *J. Magn. Magn. Mater.* 280, 208.
7. Hotmeister, A. M., Campbell, K.R. (1992), *J. Appl. Phys.* 72, 638.

-
8. Ibetombi Soibam, Sumitra phanjoubam, Sharma, H. B., Sharma, H. N. K. and Chandra Prakash. (2009), *Ind. J. Phys.* 83 (3) 285.
 9. Iwauchi, K. (1971), *Jap. Appl. Phys.* 10, 1520.
 10. Kuanr, B.K., Singh, P. K., Kisan, P., Kumar, N., Rao, S.L.N., Srivastava, G.P. (1986) *J. Appl. Phys.* 8, 63.
 11. Kenneth, A., Wickersheim, (1961) *J. Appl. Phys.* 32205S.
 12. Lomako, I. D., Pavlov, V. I., and Shishkin, N. Ya., (2003) *Crystallo. Reports*, 48, 116.
 13. Lax, B. and Button, K., (1962), "Microwave ferrites and ferri-magnetics", *McGraw-Hill Book Co. Inc New York*.
 14. Ristic, M., Nowik, I., Popovic, S., Felner, I., Music, S., (2003) *J. Mater, Lett.* 57, 2584.
 15. Richard J. Cunningham and Elmer E. Anderson, ,(1961), *J.Appl.Phys.*32S388.
 16. Smit, J. and Wijn, H. P. J.1959, *Ferrites, New York, Wiley*.
 17. Zhongjun Cheng, Hua Yang, Lianxiang Yu, Yuming Cui, Shouhua Feng, (2006), *J. Magn. Magn. Mater.* 302259.

MANUSCRIPT SUBMISSION

GUIDELINES FOR CONTRIBUTORS

1. Manuscripts should be submitted preferably through email and the research article / paper should preferably not exceed 8 – 10 pages in all.
2. Book review must contain the name of the author and the book reviewed, the place of publication and publisher, date of publication, number of pages and price.
3. Manuscripts should be typed in 12 font-size, Times New Roman, single spaced with 1” margin on a standard A4 size paper. Manuscripts should be organized in the following order: title, name(s) of author(s) and his/her (their) complete affiliation(s) including zip code(s), Abstract (not exceeding 350 words), Introduction, Main body of paper, Conclusion and References.
4. The title of the paper should be in capital letters, bold, size 16” and centered at the top of the first page. The author(s) and affiliations(s) should be centered, bold, size 14” and single-spaced, beginning from the second line below the title.

First Author Name1, Second Author Name2, Third Author Name3

1Author Designation, Department, Organization, City, email id

2Author Designation, Department, Organization, City, email id

3Author Designation, Department, Organization, City, email id

5. The abstract should summarize the context, content and conclusions of the paper in less than 350 words in 12 points italic Times New Roman. The abstract should have about five key words in alphabetical order separated by comma of 12 points italic Times New Roman.
6. Figures and tables should be centered, separately numbered, self explained. Please note that table titles must be above the table and sources of data should be mentioned below the table. The authors should ensure that tables and figures are referred to from the main text.

EXAMPLES OF REFERENCES

All references must be arranged first alphabetically and then it may be further sorted chronologically also.

• Single author journal article:

Fox, S. (1984). Empowerment as a catalyst for change: an example for the food industry. *Supply Chain Management*, 2(3), 29–33.

Bateson, C. D.,(2006), ‘Doing Business after the Fall: The Virtue of Moral Hypocrisy’, *Journal of Business Ethics*, 66: 321 – 335

• Multiple author journal article:

Khan, M. R., Islam, A. F. M. M., & Das, D. (1886). A Factor Analytic Study on the Validity of a Union Commitment Scale. *Journal of Applied Psychology*, 12(1), 129-136.

Liu, W.B, Wongcha A, & Peng, K.C. (2012), “Adopting Super-Efficiency And Tobit Model On Analyzing the Efficiency of Teacher’s Colleges In Thailand”, *International Journal on New Trends In Education and Their Implications*, Vol.3.3, 108 – 114.

- **Text Book:**

Simchi-Levi, D., Kaminsky, P., & Simchi-Levi, E. (2007). *Designing and Managing the Supply Chain: Concepts, Strategies and Case Studies* (3rd ed.). New York: McGraw-Hill.

S. Neelamegham," Marketing in India, Cases and Reading, Vikas Publishing House Pvt. Ltd, III Edition, 2000.

- **Edited book having one editor:**

Raine, A. (Ed.). (2006). *Crime and schizophrenia: Causes and cures*. New York: Nova Science.

- **Edited book having more than one editor:**

Greenspan, E. L., & Rosenberg, M. (Eds.). (2009). *Martin's annual criminal code: Student edition 2010*. Aurora, ON: Canada Law Book.

- **Chapter in edited book having one editor:**

Bessley, M., & Wilson, P. (1984). Public policy and small firms in Britain. In Levicki, C. (Ed.), *Small Business Theory and Policy* (pp. 111–126). London: Croom Helm.

- **Chapter in edited book having more than one editor:**

Young, M. E., & Wasserman, E. A. (2005). Theories of learning. In K. Lamberts, & R. L. Goldstone (Eds.), *Handbook of cognition* (pp. 161-182). Thousand Oaks, CA: Sage.

- **Electronic sources should include the URL of the website at which they may be found, as shown:**

Sillick, T. J., & Schutte, N. S. (2006). Emotional intelligence and self-esteem mediate between perceived early parental love and adult happiness. *E-Journal of Applied Psychology*, 2(2), 38-48. Retrieved from <http://ojs.lib.swin.edu.au/index.php/ejap>

- **Unpublished dissertation/ paper:**

Uddin, K. (2000). A Study of Corporate Governance in a Developing Country: A Case of Bangladesh (Unpublished Dissertation). Lingnan University, Hong Kong.

- **Article in newspaper:**

Yunus, M. (2005, March 23). Micro Credit and Poverty Alleviation in Bangladesh. *The Bangladesh Observer*, p. 9.

- **Article in magazine:**

Holloway, M. (2005, August 6). When extinct isn't. *Scientific American*, 293, 22-23.

- **Website of any institution:**

Central Bank of India (2005). *Income Recognition Norms Definition of NPA*. Retrieved August 10, 2005, from <http://www.centralbankofindia.co.in/home/index1.htm>, viewed on

7. The submission implies that the work has not been published earlier elsewhere and is not under consideration to be published anywhere else if selected for publication in the journal of Indian Academicians and Researchers Association.

8. Decision of the Editorial Board regarding selection/rejection of the articles will be final.



INDIAN ACADEMICIANS & RESEARCHERS ASSOCIATION

Major Objectives

- To encourage scholarly work in research
- To provide a forum for discussion of problems related to educational research
- To conduct workshops, seminars, conferences etc. on educational research
- To provide financial assistance to the research scholars
- To encourage Researcher to become involved in systematic research activities
- To foster the exchange of ideas and knowledge across the globe

Services Offered

- Free Membership with certificate
- Publication of Conference Proceeding
- Organize Joint Conference / FDP
- Outsource Survey for Research Project
- Outsource Journal Publication for Institute
- Information on job vacancies

Indian Academicians and Researchers Association

Shanti Path ,Opp. Darwin Campus II, Zoo Road Tiniali, Guwahati, Assam

Mobile : +919999817591, email : info@iaraedu.com www.iaraedu.com



EMPYREAL PUBLISHING HOUSE

- Assistant in Synopsis & Thesis writing
- Assistant in Research paper writing
- Publish Thesis into Book with ISBN
- Publish Edited Book with ISBN
- Outsource Journal Publication with ISSN for Institute and private universities.
- Publish Conference Proceeding with ISBN
- Booking of ISBN
- Outsource Survey for Research Project

Publish Your Thesis into Book with ISBN “Become An Author”

EMPYREAL PUBLISHING HOUSE

Zoo Road Tiniali, Guwahati, Assam

Mobile : +919999817591, email : info@editedbook.in, www.editedbook.in